

University of Alberta

Large Deformation Analysis of Flexible Rods

by

Donald Wayne Raboud



A thesis submitted to the Faculty of Graduate Studies and Research in
partial fulfillment of the requirements for the degree of Doctor of Philosophy

Department of Mechanical Engineering

Edmonton, Alberta
Fall 1996



National Library
of Canada

Acquisitions and
Bibliographic Services Branch

395 Wellington Street
Ottawa, Ontario
K1A 0N4

Bibliothèque nationale
du Canada

Direction des acquisitions et
des services bibliographiques

395, rue Wellington
Ottawa (Ontario)
K1A 0N4

Your file Votre référence

Our file Notre référence

The author has granted an irrevocable non-exclusive licence allowing the National Library of Canada to reproduce, loan, distribute or sell copies of his/her thesis by any means and in any form or format, making this thesis available to interested persons.

L'auteur a accordé une licence irrévocable et non exclusive permettant à la Bibliothèque nationale du Canada de reproduire, prêter, distribuer ou vendre des copies de sa thèse de quelque manière et sous quelque forme que ce soit pour mettre des exemplaires de cette thèse à la disposition des personnes intéressées.

The author retains ownership of the copyright in his/her thesis. Neither the thesis nor substantial extracts from it may be printed or otherwise reproduced without his/her permission.

L'auteur conserve la propriété du droit d'auteur qui protège sa thèse. Ni la thèse ni des extraits substantiels de celle-ci ne doivent être imprimés ou autrement reproduits sans son autorisation.

ISBN 0-612-18096-4

Canada

University of Alberta

Library Release Form

Name of Author: Donald Wayne Raboud


Title of Thesis: Large Deformation Analysis of Flexible Rods

Degree: Doctor of Philosophy

Year this Degree Granted: 1996

Permission is hereby granted to the University of Alberta Library to reproduce single copies of this thesis and to lend or sell such copies for private, scholarly, or scientific research purposes only.

The author reserves all other publication and other rights in association with the copyright in the thesis, and except as hereinbefore provided, neither the thesis nor any substantial portion thereof may be printed or otherwise reproduced in any material form whatever without the author's prior written permission.



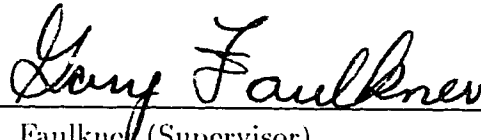
Donald Wayne Raboud
#101, 10645 80 Ave.,
Edmonton, Alberta, Canada
T6E 1V6

Date: Aug 9, 1996

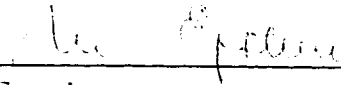
University of Alberta

Faculty of Graduate Studies and Research

The undersigned certify that they have read, and recommend to the Faculty of Graduate Studies and Research for acceptance, a thesis entitled **Large Deformation Analysis of Flexible Rods** submitted by **Donald Wayne Raboud** in partial fulfillment of the requirements for the degree of Doctor of Philosophy



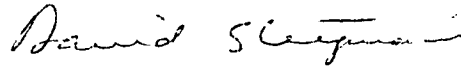
Dr. Faulkner (Supervisor)



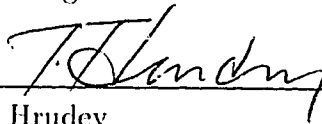
Dr. Epstein



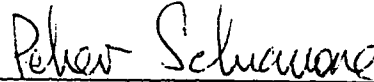
Dr. Lipsett



Dr. Steigmann



Dr. Hudey



Dr. Schiavone

Date: July 29, 1996

To my parents...

Abstract

The equations of equilibrium for large three-dimensional inextensible deformations of rods are solved using an iterative shooting technique which essentially converts the original two-point boundary value problem into a sequence of initial value problems which converge to the desired solution. This method can be used efficiently and accurately on a personal computer, mainly due to the fact that the load and deformations can be applied in their entirety so that incremental methods are avoided.

The technique is applied to a variety of example problems in which linear elastic materials are considered. Where previous analytical, numerical or experimental results are available, the present technique is shown to compare favorably. The shooting technique employed is found to be well suited to finding multiple equilibrium solutions which are investigated for a cantilever beam under dead tip and uniform distributed loads.

This initial value approach is combined with a method for considering the rod using a number of segments. The use of segments in this fashion is found to be useful for modeling complex rod structures as well as having practical numerical advantages. This is used to advantage in determining the force systems produced by a variety of orthodontic retraction appliances. Both planar and non-planar appliances and activations are considered.

The numerical procedure is then modified to include the analysis of nonlinear elastic materials. Constitutive relationships are employed which qualitatively model the behavior of shape memory alloys in planar situa-

tions. Qualitative agreement with the limited experimental results available is demonstrated using the assumed constitutive behavior. This assumed shape memory behavior is then employed to investigate and compare the behavior of planar orthodontic retraction appliances to those made of linear elastic materials. The shape memory alloy appliances are shown to deliver relatively constant force systems which is a desirable characteristic in this application.

Acknowledgments

I am especially grateful to Dr. M.G. Faulkner, Dr. A.W. Lipsett and Dr. D.J. Steigmann without whom this work would not have been possible. Their patience and understanding through some tough times is sincerely appreciated.

I would also like to take this opportunity to thank some other people who have contributed in some form or other to this work:

Victor del Valle — constant computer updates and making me buy things I really didn't need

Pat Flemming — along with Vic, much needed distractions

Bill Peck — help with \LaTeX .

I would also like to thank Tina, Bob, Vic, Carrie (and others in the office) for help at various times. Thanks also to the entire Mexpos organization (or lack thereof) and others too numerous to mention for helping to make my stay here enjoyable.

Contents

1	Introduction	1
1.1	Literature Review	2
1.1.1	Rod Theories	3
1.1.2	Analytical Solutions	5
1.1.3	Numerical Results	6
1.1.4	Nonlinear Elastic Materials	7
1.2	Thesis Outline	9
2	Background Theory	11
2.1	Kinematics	12
2.2	Equilibrium Equations	12
2.3	Constitutive Assumptions	13
3	Numerical Procedure and Verification	16
3.1	Solution for the Rod	17
3.1.1	Solution for an Individual Segment	17
3.1.2	Solution for the Complete Rod	23
3.2	Verification of Results	25
3.2.1	Initially Straight Rods	26
3.2.1.1	Initially Straight Circular Rod Deformed Into a Helix	26
3.2.1.2	Initially Straight Orthotropic Rod Deformed Into a Helix	34
3.2.1.3	Initially Straight Orthotropic Rod Deformed Into A Möbius Strip	40
3.2.1.4	Initially Straight Cantilever Beam Loaded in a Non-Principal Direction By a Dead Tip Load	47
3.2.2	Initially Curved Rods	51

3.2.2.1	Initially Helical Orthotropic Rod Bent and Twisted Into Another Helix	51
3.2.2.2	Initially Curved Cantilever Loaded Out of the Initial Plane of Curvature by a Dead Tip Load	56
4	Multiple Solutions For Cantilever Beams Under Dead Loads	60
4.1	Buckling of Planar Shapes	62
4.1.1	Development of Multiple Planar Snapes	62
4.1.2	Buckling of Planar Shapes Out of the Plane	65
4.2	Non-Buckled Three-Dimensional Shapes	71
4.2.1	Deep Cantilever Beams Under Dead Tip Loads	71
4.2.1.1	Potential Energies of Deformed Configurations	76
4.2.2	Shallow Cantilevers	78
4.3	Some Final Remarks	82
5	Three-Dimensional Effects in Orthodontic Retraction Appliance Design	83
5.1	Introduction to the Problem	83
5.1.1	Tooth Retraction in the Lateral Plane	85
5.1.2	Tooth Retraction in the Occlusal Plane	87
5.2	Boundary Value Problem Description	88
5.3	Vertical Loops	92
5.3.1	Force Systems From Planar Vertical Loops Undergoing Planar Activations	92
5.3.2	Force Systems From Initially Non-Planar Vertical Loops Undergoing Planar Activations	95
5.4	T-Springs	101
5.4.1	Force Systems From T-Springs With Out-of-Plane Modifications Undergoing Planar Activations	101
5.4.2	Force Systems From Planar T-Springs Undergoing Non-Planar Activations	106
5.5	Concluding Remarks	111
6	Nonlinear Elastic Materials: Shape Memory Alloys	112
6.1	Constitutive Model For Shape Memory Alloys	113
6.1.1	Bilinear Constitutive Model	118
6.2	Numerical Procedure For the Planar Situation	121
6.2.1	Kinematics and Equilibrium	121

6.2.2	Modifications To Include Bilinear Constitutive Models	123
6.2.3	Integration Procedure	123
6.3	Numerical Results	128
6.3.1	Clamped-Slider Problem	129
6.3.2	Initially Curved Cantilever Beam	132
6.3.3	Orthodontic Retraction Appliances	136
6.3.3.1	Vertical Loop	136
6.3.3.2	T-Spring	139
7	Concluding Remarks	148
7.1	Summary	148
7.2	Future Work	150
	References	152

APPENDICES

A	Shooting Procedure	158
B	Analytical Solution for an Initially Straight Circular Rod Deformed into a Helix	161
C	Use of Contour Maps For Two Parameter Shooting Problems	165
D	Evaluation of Elastic Limit	169

List of Tables

3.1	Flap (w) and Chordwise (v) Deflections For a Uniform Cantilever Beam Loaded in Various Non-Principal Directions . . .	50
3.2	Geometry at the End of a Curved Cantilever Under the Action of a Dead Tip Load	58
3.3	Geometry at the End of a Curved Cantilever Under the Action of a Dead Uniform Distributed Load	59
4.1	Number of Planar Equilibrium Solutions as a Function of the Load Parameter α	63
4.2	Potential Energies of Various Equilibrium Configurations for a Deep Cantilever (Aspect Ratio = 1/1.7) at a Load $\beta = 64$.	77
4.3	Potential Energies of Various Equilibrium Configurations for a Shallow Cantilever (Aspect Ratio =1.7) at a Load $\beta = 45$. .	80
5.1	Details of Segments Used to Model Planar T-Spring	102
6.1	Material Properties	128
6.2	Details of Segments Used to Model Planar T-Spring	140

List of Figures

3.1	Arbitrary Rod Segment	17
3.2	Position Coordinates Along Rod Segment	20
3.3	Initially Straight Rod Deformed Into a Helix	26
3.4	Geometry of Helix Centerline, $M_z = 200 \text{ Nm}$, $F_z = 100 \text{ N}$, $\alpha = 45^\circ$	29
3.5	Twist/Unit Length (κ_1) Along Rod	30
3.6	Energy Integral Along Rod	30
3.7	Geometry of Helix Centerline, $\alpha = 5^\circ$	32
3.8	Geometry of Helix Centerline, $\alpha = 85^\circ$	33
3.9	Initially Straight Orthotropic Rod Deformed Into a Helix . . .	35
3.10	Geometry of Orthotropic Helix Centerline, $R = 0.05\text{m}$, $\alpha = 45^\circ$, $a/b = 10$	37
3.11	Twist/Unit Length (κ_1) Along Helix, $R = 0.05\text{m}$, $\alpha = 45^\circ$, $a/b = 10$	38
3.12	Energy Integral Along Helix, $R = 0.05\text{m}$, $\alpha = 45^\circ$, $a/b = 10$.	38
3.13	Deformed Helices For the Case Aspect Ratio = 10 for Various Pitch Angles	39
3.14	Geometry of Möbius Strip Centerline for Various Aspect Ratios	42
3.15	Three-Dimensional Views of Deformed Möbius Strip for Vari- ous Aspect Ratios	43
3.16	Variation of κ_1 Along the Deformed Möbius Strip as a Func- tion of Aspect Ratio	44
3.17	Variation of the Energy Integral Along the Deformed Möbius Strip as a Function of Aspect Ratio	44
3.18	Geometry of Möbius Strip Centerline	45
3.19	Three-Dimensional Views of Möbius Strip Solutions	46
3.20	Variation of κ_1 Along the Deformed Möbius Strip	47

3.21	Cantilever Beam Loaded at Various Angles To Principal Directions	48
3.22	Geometry of Deformed Helix Centerline, $R = 0.1\text{m}$, $\alpha = 45^\circ$. Aspect Ratio = 10	53
3.23	Twist/Unit Length (κ_1) Along Deformed Helix	54
3.24	Energy Integral Along Deformed Helix	54
3.25	Initial Orthotropic Helix Deformed Into a Straight Rod	55
3.26	Initially Curved Cantilever Beam Loaded Out of the Plane of Initial Curvature	56
4.1	Cantilever Beam With Dead Tip Load, P	61
4.2	Planar Equilibrium Configurations Corresponding to $\alpha = 3.214$	64
4.3	Planar Equilibrium Configurations Corresponding to $\alpha = 5.0$	64
4.4	Fixed End Moment Component M_3 Required to Maintain Planar Equilibrium Configurations	65
4.5	Dimensionless Buckling Loads as a Function of the Aspect Ratio for Dead Tip and Uniform Distributed Loads	66
4.6	M_1 Component Required to Maintain Buckled Equilibrium Configurations, $a/b = 1/1.7$	68
4.7	M_3 Component Required to Maintain Buckled Equilibrium Configurations, $a/b = 1/1.7$	69
4.8	Geometry of Buckled Shapes #2 ($\beta = 64$) and #3 ($\beta = 44$), $a/b = 1/1.7$	70
4.9	M_1 Components Required to Maintain Equilibrium Configurations Far Removed from the Original Plane and the Associated Potential Energies (Nm) For an Aspect Ratio of $1/1.7$	72
4.10	Development of Multiple Three-Dimensional Equilibrium Shapes A and B, $a/b = 1/1.7$	73
4.11	Three Views of Shape B, Aspect Ratio = $1/1.7$, $\beta = 25$	74
4.12	M_3 Components Required to Maintain Equilibrium Configurations Far Removed from the Original Plane, $a/b = 1/1.7$	75
4.13	Variation in κ_1 Along the Deformed Rod for Shapes A, B, C and D at a Load of $\beta = 35$	75
4.14	M_1 Components Required to Maintain Equilibrium Configurations Far Removed from the Original Plane, $a/b = 1.7$	79
4.15	M_3 Components Required to Maintain Equilibrium Configurations, $a/b = 1.7$	80

4.16	Oblique Views of Deformed Geometries for the Same Rod Loaded as a Deep and Shallow Cantilever at the Same Absolute Load	81
5.1	Undeformed, Neutral Position and Activated Position for a T-Spring Appliance in a Plane	84
5.2	Lateral View of an Orthodontic Retraction Appliance Used for Space Closure	86
5.3	Occlusal View of an Orthodontic Retraction Appliance Used for Space Closure	88
5.4	Boundary Value Problem for the Case in which the Brackets Are in the E_1 - E_2 Plane and are Collinear	90
5.5	Boundary Value Problem for the Case in which the Brackets Do Not Remain in the Same Plane	91
5.6	Results for Planar Vertical Loops Undergoing Planar Activations	93
5.7	Lateral and Occlusal Views of Undeformed Vertical Loop With Out-of-Plane Modifications	96
5.8	Lateral and Occlusal Views of Vertical Loop With Out-of-Plane Modifications in Fully Activated Configuration	96
5.9	Comparison of Force-Activation Relationship Between Planar Vertical Loops and Vertical Loops with Out-of-Plane Modifications	97
5.10	Comparison of M/F Ratios Generated By Planar Vertical Loops and Vertical Loops with Out-of-Plane Modifications	99
5.11	Comparison of M^*/F Ratios Generated By Planar Vertical Loops and Vertical Loops with Out-of-Plane Modifications	100
5.12	Geometry of Planar T-Spring	102
5.13	Lateral and Occlusal Views of Undeformed Preactivated T-Spring With Out-of-Plane Modifications	103
5.14	Lateral and Occlusal View of Preactivated T-Spring With Out-of-Plane Modifications in Fully Activated Configuration	103
5.15	Comparison of Force-Activation Relationship For Planar T-Springs and T-Springs With Out-of-Plane Modifications	104
5.16	Comparison of M/F Ratios Generated By Planar T-Springs and T-Springs With Out-of-Plane Modifications	105
5.17	Comparison of M^*/F Ratios Generated By Planar T-Springs and T-Springs With Out-of-Plane Modifications	105
5.18	Occlusal View of Typical Non-Planar Situation	107

5.19	Directions of Forces and Moments Acting on Spring and Anterior Tooth in Non-Planar Situation	108
5.20	Occlusal Force F_3 as a Function of Angular Difference Between Brackets	109
5.21	Occlusal M^*/F Ratio as a Function of Angular Difference Between Brackets	110
5.22	Torquing Moment M_1 as a Function of Angular Difference Between Brackets	110
6.1	Comparison of Moment-Curvature Relationships	114
6.2	Typical Strain Energy Function for Nonlinear Elastic Materials	115
6.3	Loading/Unloading Behavior of Shape Memory Alloys	116
6.4	M_3 - γ_3 Relationship Following Maxwell's Equal Area Rule	118
6.5	Bilinear Constitutive Model for Shape Memory Alloys	119
6.6	Cantilever of Shape Memory Alloy Under a Dead Tip Load	124
6.7	Cantilever of Shape Memory Alloy Under Dead Tip Load, Loaded to P_1	125
6.8	Cantilever of Shape Memory Alloy Under Dead Tip Load, Loaded to P_2	126
6.9	Cantilever of Shape Memory Alloy Under Dead Tip Load, Unloaded to P_1	127
6.10	Clamped-Slider Problem	129
6.11	Vertical Deflections at Center of Beam for Clamped-Slider Problem	131
6.12	Moment and Curvature Distribution in Bilinear Clamped-Slider Problem at the Maximum Load 12.26 N	132
6.13	Initially Curved Cantilever Beam With Tip Load	133
6.14	Initial Angle at Free End for Initially Curved Cantilever Beam	134
6.15	Moment and Curvature Distribution in Bilinear Curved Cantilever Problem at the Maximum Load 2.06 N	135
6.16	Results for Planar Vertical Loop Problem	137
6.17	Moment and Curvature Distribution in Bilinear Vertical Loop Problem at the Maximum Activation 2.3mm	138
6.18	Geometry of Standard T-Spring	139
6.19	Results for Planar T-Spring Problem	141
6.20	Moment and Curvature Distribution in Bilinear T-Spring Problem at the Maximum Activation 6.7mm	142
6.21	Curvature Distribution Along T-Spring During De-activation	143

6.22	Moment-Curvature Relationship For Bilinear Material Governed by Maxwell's Equal Area Rule	144
6.23	Results for Planar T-Spring Problem With Bilinear Material Following Maxwell's Equal Area Rule	145
6.24	Moment and Curvature Distribution in Bilinear (Maxwell's Equal Area Rule) T-Spring Problem at the Maximum Activation 6.7mm	146
6.25	Energy Integral Along T-Spring with Bilinear Shape Memory Material	147
B.1	Initially Straight Circular Rod Deformed Into a Helix	162
C.1	Free End versus Fixed End Moment for a Cantilever Undergoing Planar Deformations for a Load $\alpha = 5.0$	166
C.2	Contour Map of Free End $M_1 = 0$ and $M_3 = 0$ as Functions of Fixed End M_1 and M_3 Components for a Cantilever Beam Undergoing Out-of-Plane Deformations for a Load $\beta = 62$. . .	167
D.1	Locations on the Cross Section Used to Evaluate the Yielding Criterion	170

Chapter 1

Introduction

There is a large variety of structures which can be modelled as rods. Applications as diverse as

- a pipeline being installed in an offshore oil and gas facility,
- retraction appliances used to reposition teeth during orthodontic treatment,
- helical springs to provide controlled stiffness variations for automobiles,
- highly deformable space structures,
- variable stiffness fishing poles,

can be adequately represented by a one dimensional (rod) continuum model. In all of these instances it is important to be able to determine the forces and moments developed when structures are deformed or, alternatively, to determine the deformations which occur due to application of the loads. The pipeline must be properly supported during installation or it may be damaged. Orthodontic retraction appliances must deliver appropriate systems of forces and moments within certain ranges to produce the desired type of tooth movement without causing tissue damage or producing unwanted side effects. The force-deflection relationships of helical springs, such as those used in automotive suspension systems, are often of critical importance in many applications.

The types of structures listed above (and many others), though they can take on a wide variety of complex initial shapes, all share a common geometric similarity. They are all slender bodies having lengths much greater

than typical cross sectional dimensions. Such structures are termed *rods*. In addition, the structures listed above all undergo large deformations. A large deformation is one in which the initial geometry is changed significantly during the loading. As a result, the problem of determining the forces and/or deflections which arise is *geometrically nonlinear*. The fact that these rod problems are *geometrically nonlinear* greatly complicates the solution as compared to problems in which the geometry changes are infinitesimal.

Apart from the *geometric nonlinearity* due to the inherently large deformations these structures can undergo, nonlinearity may be introduced into the problem through the materials used. Most engineering structures are constructed of linearly elastic materials, or more precisely materials used in their linearly elastic ranges¹. However increasing use is being made of materials which do not exhibit this type of linear elastic behavior. Such structures could also have a *material nonlinearity* which adds complexity to the problem.

The *geometric nonlinearity* which is present in these problems makes them very difficult to solve analytically. This is further complicated by the variety of complex initial shapes these structures may assume as well as the wide variety of boundary conditions to which these structures may be subjected. As a result, numerical methods are usually employed to obtain approximate solutions to the governing equations. This thesis is concerned with the development and application of a particular numerical procedure to obtain solutions for rod-like structures undergoing large (nonlinear) three-dimensional deformations. The rods under consideration will have general three-dimensional initial shapes. Due to the nonlinearity inherent in the problem, the existence of multiple equilibrium solutions is a possibility and will be investigated. Further, different materials will be considered, including some exhibiting nonlinear elastic behavior.

1.1 Literature Review

Investigations concerning the deflections of rods have been around for over 250 years since the time of Euler (see Love 1944 for a historical account). The problem continues to be investigated to this day for several reasons. One

¹This is still a reasonable assumption despite the fact that the rods under consideration may undergo large deformations. Many rod-like structures can undergo large deformations while still experiencing only small strains everywhere in the material.

of the major reasons for studying solutions is that, as suggested above, they have numerous practical applications in problems as diverse as the laying of offshore pipelines (Faulkner and Stredulinsky 1976) and the development of orthodontic retraction springs (Lipsett et al. 1990). A second, very different reason is that the formulation of rod problems is an example of a one-dimensional² continuum theory which can be used to investigate non-linear phenomena including questions of stability (Steigmann and Faulkner 1993) and multiplicity of solutions Navaee and Elling (1991, 1992). As a result, a great deal of work has been done dealing with theories of rods as well as with methods for obtaining solutions. Thus a very extensive literature has accumulated on the subject and it would be impossible to recount all of it. It is therefore not the purpose here to present a complete review of the pertinent literature but rather to give an indication of what is available and to refer to previous reviews of the subject.

1.1.1 Rod Theories

A theory which governs the behaviour of rods under loading is required in order to predict the forces which are developed as rod-like structures (such as those listed above) are deformed. Such a theory of rods is defined by Antman (1995) as

...the characterization of the motion of slender solid bodies by a finite number of equations in which there is but one independent spatial variable,

which in this case is the arclength. There are several important classifications of rod theories which characterize how the theories are developed. The first, termed *intrinsic* or *Cosserat* theories, are developed by assuming the rod to be a spatial curve and attributing this curve with sufficient kinematical structure to account for the desired modes of deformation (which in the literature for rods are usually a combination of bending, torsion, extension and shear). In the other main type of theory, referred to as *induced* theories, the equations governing three-dimensional elasticity are applied to rod-like bodies and specialized to account for the fact that the cross sectional dimensions are much less than the length (see Green et al. 1974a, for example).

² All quantities are functions of only one independent variable, in this case the arclength.

Both types of theory exist in varying degrees of complexity regarding the types of deformations considered.

Intrinsic rod theories are usually begun by considering the centerline of the rod to be a space curve comprised of material points to each of which is assigned a triad of orthogonal unit vectors (Green and Laws 1966, Cohen 1966, Kafadar 1972, Green et al. 1974b, and Antman 1974 are just several examples). Such a curve is often referred to as a *directed space curve*. These vectors are usually directed along the tangent to the centerline and along the principal directions in the cross section. This triad is used to account for the kinematics of the deformation. If extension is considered, the vector directed along the tangent to the rod is allowed to extend and shorten. If shear is considered, the triad does not remain orthogonal but rather the angles between the vectors can change. Bending and torsion produce only rigid body transformations of this triad which allows for a much simpler analysis as only two of the unit vectors are strictly required. The third can be expressed as a cross product of the other two (Green and Laws 1973).

The works of Kirchhoff (1859) and Clebsch (1862) (see Love 1944) are examples of induced theories. Dill (1992) has revisited these works and re-examines their ideas using more modern developments in three-dimensional elasticity theory. In this work Dill performs an order of magnitude analysis based on characteristic length parameters of the rod (length, cross section) as well as on typical lengths characteristic of the curvature and twist in the rod³. The theory of rods deals only with the cases in which certain ratios of these parameters are much less than unity. Based on this analysis, Dill concludes that in a first order rod theory “the dominant modes of deformation must be a global bending and twisting with small axial extension”. Dill goes on to say that the small extension in the rod can be considered to be zero in the momentum balance equations with sufficient accuracy. He also points out that, while the shears due to torsion of the cross section appear in the equations of motion, shears due to transverse loading are second order effects and therefore do not appear. As a result, bending and twisting are therefore the only modes of deformation considered in this thesis. Note that this is not to say that extensional or shear deformations do not play an important role in some types of problems, but should rather be seen as a limitation on the

³Dill used a generalized radius of curvature, defined as $1/\kappa$ where κ is the curvature or rate of change of angle per unit length, as the characteristic length. It was generalized in the sense that it included the twist along the rod as a ‘curvature’.

types of problems to which a first order rod theory should be applied. There are still, however, a wide variety of practical problems in which bending and torsion are the dominant modes of deformation. This ongoing interest is evidenced by the amount of current work devoted to the subject (see Banan et al. 1991; Koenig and Bolle 1993; Raboud et al. 1996a, 1996b; Raboud et al. 1996 and Pai and Palazotto 1996 for some recent examples).

1.1.2 Analytical Solutions

The equations of equilibrium governing the three-dimensional deformations of long slender rods are well known. In his treatise, Love (1944) presents a derivation of these equations based on that of Kirchhoff. Landau and Lifshitz (1970) derive the equations of equilibrium of the rod based on an analysis of an arbitrary infinitesimal section of the rod. Steigmann and Faulkner (1993) obtained the equilibrium equations using variational calculus to minimize the potential energy of the deformed rod.

However, due to the inherent geometric nonlinearity of the equilibrium equations, analytical solutions to problems are rarely obtainable. A notable exception is the case when an initially straight rod is bent and twisted into a helix through the action of axial end moments and forces. Both Love (1944) and Landau and Lifshitz (1970) derive analytical solutions for this problem for inextensible rods with circular cross sections (i.e. isotropic rods). Faulkner and Steigmann (1993) consider the inextensible case for cross sections characterized by two distinct principal directions (i.e. orthotropic rods). Whitman and DeSilva (1974) obtain solutions for rods with circular cross sections which take extensibility into account.

Apart from these examples, very few analytical solutions for truly three dimensional problems exist. Mahadevan and Keller (1993), in considering the geometries of Möbius strips, use an analytical solution for an isotropic rod as the starting point for a homotopy continuation procedure (Keller 1968). However, as this solution is essentially a planar deformation with twist, the resulting geometries are not truly three-dimensional.

When the discussion is limited to planar problems, the situation simplifies considerably. The number of equilibrium equations is reduced to one as there is bending about only one axis and there is no twisting of the cross section. These problems are typically referred to as *elastica* problems. In this case a number of analytical solutions have been obtained (see Mitchell 1959; Frisch-Fay 1962; Antman 1968 for example) which often express the

solutions in terms of elliptic integrals. However, even for the planar case these solutions are generally limited to rods with uniform cross sections, simple initial geometries and subjected to particular loading and boundary conditions.

1.1.3 Numerical Results

To consider more general problems (including complex initial geometries, non-uniform cross sections as well as complex loads and boundary conditions) numerical techniques must be used. There is an extensive literature for numerical solutions of planar problems (Schmidt and DaDeppo 1971; Gorski 1976). In the literature a wide range of loading conditions have been studied, including consideration given to beams deflecting under their own weight, the so called *heavy elastica* (Wang 1986). Beams with non-uniform cross sections (Faulkner and Stredulinsky 1976; Lee et al. 1993) and a variety of boundary conditions (Chucheepsakul et al. 1995, for example) have also been studied.

There has likewise been much work done to develop numerical solutions for three-dimensional problems. Again, a wide variety of loads, boundary conditions and initial geometries (including pretwisted rods (Rosen 1991)) have been considered.

The numerical techniques used typically involve finite element or finite difference procedures (Greif et al. 1982; Surana 1983; Surana and Soren 1989). Due to the large displacements which can occur, nonlinear formulations must be used. This includes the concept of applying the loads in increments which greatly increases computational effort. This is required because, in a nonlinear problem, the stiffness matrix is a function of the deformation and must be updated as the solution progresses. If the possibility of multiple solutions is of interest, the finite element formulation is not well suited and the loading path must be modified as done by Fried (1981) for example. More recent finite element approaches (Jiang and Chernuka 1993; Pai and Palazotto 1996 are just a couple of examples) use so called co-rotational formulations which attempt to reduce the number of load increments required by decomposing the element deformations into rigid body motions and motions which produce strain. The rigid body motions then account for the large displacements and rotations which occur.

Other approaches have also been considered. For example, Navace and Elling (1991, 1992) have employed two different approaches to study multiple

solutions of planar cantilever beams. One approach utilizes elliptic integrals and uses a procedure similar to the one developed by Frisch-Fay (1962). The other approach employs a predictor-corrector scheme with an initial value formulation.

Another approach that has been applied to determine static deformations is the method of *dynamic relaxation* (Alwar et al. 1974; Belytschko and Hughes 1983; Ramesh and Krishnamoorthy 1993). In this approach, the static equations governing the deformations are augmented by dynamical terms including the effects of inertia and damping. The steady state solution to the dynamics problem is thus the static solution to the original problem. Since only the static solution is of interest, the inertia and damping terms can be chosen to improve the convergence of the dynamical problem to the static equilibrium solution as discussed by Papadrakakis (1981).

An alternative approach for planar problems, dubbed the *segmental shooting technique*, was developed for applications including the laying of offshore pipelines (Faulkner and Stredulinsky 1976) and the prediction of force systems produced by orthodontic retraction appliances (Lipsett et al. 1990; Faulkner et al. 1991). This technique avoids the direct solution of the nonlinear boundary value problem by considering the rod as being comprised of a large number of segments, each of which experiences only small displacements so that a linear solution can be applied over each segment. The total nonlinear solution is obtained by assembling the segments together. This solution converts the original boundary value problem into a sequence of initial value problems which converge to the required boundary conditions through the use of a shooting procedure. This formulation was found to be well suited to investigate the development of multiple solutions (Faulkner et al. 1993; Lipsett et al. 1993). This segmental approach has been recently modified to take fully three-dimensional deformations into account (Raboud et al. 1996b). This modified procedure was used to investigate the development of multiple three-dimensional equilibrium solutions for cantilever beams under dead tip and distributed loads (Raboud et al. 1996a). As well, three-dimensional deformations of orthodontic appliances, with complex initial shapes, were investigated (Raboud et al. 1996).

1.1.4 Nonlinear Elastic Materials

Constitutive relationships, which relate the kinematics of the deformation to the forces and moments generated in the material, play an important

role in applying the theory. Most commonly in the literature, the materials considered are assumed to be linearly elastic with the moments produced being related to the differences between initial and final curvatures along the rod⁴ (Love 1944). Similarly, the force components developed in the rod may also be determined through constitutive relationships although this isn't always the case. For example, when extensibility is considered, the tension in the rod is usually expressed as $F_1 = EA\varepsilon$ where F_1 is the axial tension which acts along the tangent to the rod's centerline, ε is the axial strain, E is the Young's modulus of the material and A is the area of the cross section. Similarly when shears are considered they are related to the shear forces F_2 and F_3 through constitutive relationships (see Antman 1995 for example). When shears (or extensibility) are not considered, F_2 and F_3 (or F_1) are not given by any constitutive relationship but are rather determined by a balance of momentum as in the usual linear theory of elasticity.

However, linear elastic materials are obviously not the only type available. Nonlinear elastic materials, because of their unique properties, are seeing increasing use in a number of rod-like structures. A number of authors have considered rod theories with general nonlinear elastic and plastic behaviors.

Shape Memory Alloys (SMA) are an example of such a material which exhibits nonlinear elastic behavior due to changes in both temperature and strain. A typical alloy which demonstrates such behavior is NiTi (nickel titanium). Shape memory alloys get their name from their observed behavior of, after being deformed at a low temperature, returning to a specific 'remembered' shape upon heating above a suitable transition temperature⁵. This is termed the *shape memory effect*. Even at constant temperatures, shape memory alloys can also exhibit nonlinear elastic behaviors such as hysteresis and *pseudoelasticity*⁶ which results in large nonlinear elastic ranges over which relatively constant forces are applied.

The shape memory effect is manifested through a phase change in internal crystalline structure between the *martensite* and *austenite* phases due to changes in temperature (Duering et al. 1990). At low temperatures, the martensitic phase of the material is stable. In this phase the material is easily deformed due to the fact that several energetically equivalent config-

⁴Note that curvatures here is meant to include both the usual bending curvatures as well as the rate of twist along the rod.

⁵The specific shape must be 'learned' by the material through a series of heat treatments (Duering et al. 1990).

⁶Also referred to as *super-elasticity* in the literature.

urations of the crystal structure (called *variants*), which are rotations and mirror images of one another, exist randomly distributed throughout the material (Shaw and Kyriakides 1995). During deformation the essentially randomly distributed variants are reoriented to one variant in particular to accommodate the deformation. Thus the application of stress causes one of the variants to be favored over the others. At higher temperatures, austenite is the stable phase. The austenitic phase has no variants, due to its highly symmetric crystal lattice (Shaw and Kyriakides 1995) so that upon heating the deformed martensite lattice ‘springs back’ to the austenitic phase and the deformation is recovered.

Pseudoelastic behavior (at constant temperature) results from deformations which occur at temperatures such that the material is initially in the austenite phase. As loads are applied, the martensite phase can become stable, even at the higher temperatures, due to the strain in the material. This is termed *stress induced martensite*. As in the shape memory effect, one variant of the induced martensite phase predominates during the deformation to accommodate the large shape changes. As the loads are removed, the martensite becomes unstable. A transition back to austenite occurs and the original shape is recovered.

Shape memory alloys have been employed in a number of applications including use for eyeglass frames, medical devices, fire detection equipment and military applications (Duering et al. 1990). They are also used for ‘smart’ structures due to their ability to change shape in a controlled manner through temperature changes. One application for which these materials seem particularly suited is in the area of orthodontics where Miura et al. (1986) and Kapila and Sachdeva (1989) have evaluated this material and compared it to others commonly used in orthodontics. This material’s particular mechanical properties (large elastic springback, low stiffness and the ability to provide relatively constant forces over large ranges) are characteristics which are desirable in orthodontic applications.

1.2 Thesis Outline

Chapter 2 describes some of the background theory concerning inextensible rods. The kinematical basis used to characterize the rod deformations is described and the equations of equilibrium are presented. Constitutive assumptions are discussed for linear elastic materials. As well, some general

results are presented which can be used as a check of the numerical procedure to be subsequently developed.

Chapter 3 presents the development of a numerical procedure in which the two point boundary value rod problem is solved as a sequence of initial value problems which converge to the required boundary conditions. The nonlinear equilibrium equations for rods made of linearly elastic materials are applied to a segment of the rod and direct numerical integration is used to obtain a solution from the initial values. A method for assembling the various segments to maintain geometric and force compatibility is described. Numerical results are then presented for a variety of problems. These are compared with previous analytical, numerical or experimental results to assess the effectiveness of the numerical technique.

In Chapter 4 the numerical procedure is used to investigate the emergence of multiple three-dimensional equilibrium solutions for a cantilever beam loaded by dead tip and uniform distributed loads. The results for multiple planar solutions as well as for out-of-plane buckling are compared to previous results. The appearance and development of several classes of multiple solutions for fully three-dimensional situations is described. The dependence of this behavior on the aspect ratio of the cross section is discussed.

The numerical technique is then used to evaluate the three-dimensional force systems produced by orthodontic retraction appliances in Chapter 5. A variety of segments are required to model these appliances since they have complex initial shapes. Results for several planar appliance designs are presented. In an effort to better control tooth response, out-of-plane modifications to these planar designs are introduced. The force systems delivered by the modified designs are compared to those from the original appliances.

Chapter 6 considers a modified application of the numerical technique to include materials with nonlinear elastic behavior. Constitutive models for materials which exhibit the *shape memory effect* are considered. Results are presented for a variety of planar problems which simulate the qualitative behavior of these materials. Planar orthodontic appliances are revisited and the behavior of several designs using shape memory alloys are investigated.

Chapter 7 summarizes the results of the work, discussing the advantages and limitations of the numerical technique developed in this work. Some of the areas which warrant future consideration are also discussed.

Chapter 2

Background Theory

In this chapter, the kinematics, equilibrium equations and constitutive assumptions used to characterize the rods considered are described. While the theory concerning such rods has been developed and presented by a number of authors (Love 1944; Landau and Lifshitz 1970), a reformulation of the theory in a variational setting has been recently presented in detail by Steigmann and Faulkner (1993) and their work is closely followed here. After a description of the kinematical basis used, their results will be referred to as required.

For the purposes of this thesis, a rod is defined to be a one-dimensional continuum (a directed spatial curve¹) which deforms only through bending and twisting as it is assumed to be inextensible. As well, following the Bernoulli-Euler hypotheses, under any deformation initially plane cross sections remain plane, experience no strain and are everywhere normal to the space curve tangent. The rods considered here are assumed to have the shear center everywhere coincident with the centroid of the cross section. Both rods which are transversely isotropic² and transversely orthotropic³ will be considered.

¹Directed in the sense that each point on the curve has associated with it a particular orientation. By orientation it is meant not only the tangent direction, but a particular rotation about that tangent as well.

²Transversely isotropic in the sense that the properties of the cross section are independent of orientation (i.e. any axis in the cross section is a principal axis). In all cases material isotropy is assumed.

³i.e. distinct principal directions exist in the cross section.

2.1 Kinematics

A configuration of the rod is characterized by a set of position functions and an orthonormal basis $\{\mathbf{r}(s), \mathbf{e}_i(s)\}$ which define the location and orientation of any point on the rod in terms of the arclength parameter s : $s \in [0, L]$. The vector $\mathbf{e}_1(s)$ is a unit vector which is everywhere in the tangent direction of increasing arclength. The vectors $\mathbf{e}_2(s)$ and $\mathbf{e}_3(s)$ are unit vectors embedded in the material which define the orientation of the cross section. In the case of transversely orthotropic rods, $\mathbf{e}_2(s)$ and $\mathbf{e}_3(s)$ are in the principal directions of the cross section. For rods which are transversely isotropic, $\mathbf{e}_2(s)$ and $\mathbf{e}_3(s)$ are any orthogonal unit vectors which span the cross section since all such pairs will be in the principal directions. This orthonormal basis $\{\mathbf{e}_i(s)\}$ will be referred to as the *material basis*. In the undeformed state, $\{\mathbf{r}(s), \mathbf{e}_i(s)\}$ take on the values $\{\hat{\mathbf{x}}(s), \hat{\mathbf{E}}_i(s)\}$ which serves as a reference configuration from which to measure all kinematical quantities. The material basis $\{\mathbf{e}_i(s)\}$ differs from the Frenet basis (Hay 1953) in that the latter depends only on the shape of the centerline of the rod and does not take the orientation of the cross sections into account. The material basis has the advantage of being uniquely determined, once the material basis in the reference configuration $\{\hat{\mathbf{E}}_i(s)\}$ has been specified, even in the situation where the rod remains straight in which case the Frenet basis is undefined.

The rate of change of the material basis $\{\mathbf{e}_i(s)\}$ with respect to arclength is determined by the vector $\boldsymbol{\kappa}(s)$ ($\boldsymbol{\kappa}(s) = \kappa_j(s)\mathbf{e}_j(s)$), i.e.

$$\mathbf{e}_i' = \boldsymbol{\kappa} \times \mathbf{e}_i \quad (2.1)$$

where the $'$ notation indicates differentiation with respect to arclength. The κ_1 component is the twist per unit length along the rod while κ_2 and κ_3 are the components of curvature in the respective principal directions. In the rod's undeformed configuration, which may be initially curved and twisted, $\kappa_i(s)$ takes on the values $\kappa_i^0(s)$.

2.2 Equilibrium Equations

The equations of equilibrium which govern the deformations of rods of the type considered here can be derived from variational principles (see Steigmann and Faulkner (1993) for example) or from more elementary considerations

(Love 1944; Landau and Lifshitz 1970) and are

$$\mathbf{F}' + \mathbf{b} = \mathbf{0} \quad (2.2a)$$

$$\mathbf{M}' = \mathbf{F} \times \mathbf{e}_1 \quad (2.2b)$$

where \mathbf{b} is the body force per unit length acting on the rod while \mathbf{F} and \mathbf{M} are, respectively, the force and moment resultant over the cross section acting on the material in the part $[0, s]$ due to the material in the part $(s, L]$.

It has been shown by Steigmann and Faulkner (1993) that for rods which are uniformly curved and twisted in the reference configuration, the classical *energy integral* (Love 1944) can be generalized to give

$$U - \boldsymbol{\kappa} \cdot \mathbf{M} - \mathbf{e}_1 \cdot \mathbf{F} - \mathbf{r} \cdot \mathbf{b} = \text{const} \quad (2.3)$$

where U is the strain energy per unit length along the rod and \mathbf{b} is now a uniform dead body force. This expression, which is a first integral of the equilibrium equations, is a necessary condition which must hold at every point along the rod and therefore can serve as an accuracy check which must be approximately satisfied by any numerical solution developed in subsequent chapters.

2.3 Constitutive Assumptions

In order to determine the deformed configuration of the rod, some information is needed specifying how the rod reacts to loading. This information is contained in constitutive relations which, for the rods considered here, identify how the curvatures and twist along the rod are related to the moments acting at each arclength. This information, along with the equations of equilibrium (2.2a) and (2.2b) and appropriate boundary conditions (which vary from problem to problem), is used to obtain the solution to each individual rod problem.

The rods considered in this thesis for the most part will be assumed to be linearly elastic and have a quadratic strain energy function U . (Alternate strain energy functions for nonlinear elastic materials will be considered in Chapter 6.) It is usually further assumed that U depends only on the difference in curvatures⁴ between the deformed and undeformed (reference)

⁴Curvatures here is meant to include both the physical curvature components of the rod (i.e. κ_2 and κ_3) as well as the twist per unit length κ_1 .

configurations (Love 1944). If the vector $\gamma(s)$ is defined as

$$\gamma(s) = \kappa(s) - \kappa^0(s) \quad (2.4)$$

so that

$$\gamma_i(s) = \kappa_i(s) - \kappa_i^0(s) \quad (2.5)$$

then the strain energy U is given by

$$U(\gamma) = \frac{1}{2} \left[GJ\gamma_1^2 + EI_2\gamma_2^2 + EI_3\gamma_3^2 \right] \quad (2.6)$$

where GJ is the torsional rigidity of the rod and EI_2 and EI_3 are the flexural rigidities about the principal \mathbf{e}_2 and \mathbf{e}_3 axes respectively. As shown by Steigmann and Faulkner (1993), the moment can be obtained using

$$\mathbf{M} = \frac{\partial U}{\partial \kappa_i} \mathbf{e}_i \quad (2.7)$$

which along with (2.5) and (2.6) results in

$$\mathbf{M} = GJ\gamma_1\mathbf{e}_1 + EI_2\gamma_2\mathbf{e}_2 + EI_3\gamma_3\mathbf{e}_3. \quad (2.8)$$

Note that when non-circular cross sections are considered, J is not the usual polar moment of inertia but must rather take into account the contribution to torsional rigidity attributable to warping of the cross section (Dill 1992)⁵. For example, if a rectangular cross section with dimensions a and b ($b > a$) is considered, the torsional rigidity is given by Timoshenko and Goodier (1970) as

$$GJ = \frac{1}{3} G(2a)^3(2b) \left[1 - \frac{192}{\pi^5} \frac{a}{b} \sum_{n=1,3,5,\dots}^{\infty} \frac{1}{n^5} \tanh \frac{n\pi b}{2a} \right]. \quad (2.9)$$

⁵Note that while this may appear to be in contradiction with the previously stated assumption that initially plane cross sections remain plane and experience no strain, in the present theory the cross sections do in fact remain plane. The present approach is to endow a space curve (the rod centerline) with sufficient kinematical structure to account for the desired modes of deformation, namely bending and torsion. Thus, essentially, the centerline is given flexural and torsional rigidities to resist bending and twisting. To be a valid model of reality, the values for the rigidities are chosen to most closely approximate observed behavior. St. Venant's solution to the torsion problem (see Love 1944) shows that warping has a significant effect on the torsional rigidity and must be taken into account in the value for J . As discussed by Dill (1992), this is the only effect that warping of the cross section should have in a first order rod theory.

Note that the expressions (2.6) and (2.8) are simply a superposition of results for torsion and bending about a principal axis obtainable from elementary strength of materials theory.

When initially straight, transversely isotropic rods are considered, $\kappa_i^0 = 0$, $El_2 = El_3 = EI$ so that (2.8) simplifies to

$$\mathbf{M} = GJ\kappa_1\mathbf{e}_1 + EI[\kappa_2\mathbf{e}_2 + \kappa_3\mathbf{e}_3]. \quad (2.10)$$

Using the fact that

$$\kappa_2\mathbf{e}_2 + \kappa_3\mathbf{e}_3 = \mathbf{e}_1 \times [-\kappa_2\mathbf{e}_3 + \kappa_3\mathbf{e}_2] \quad (2.11)$$

and noting, from (2.1) with $i = 1$, that

$$\mathbf{e}'_1 = -\kappa_2\mathbf{e}_3 + \kappa_3\mathbf{e}_2. \quad (2.12)$$

equation (2.10) becomes

$$\mathbf{M} = GJ\kappa_1\mathbf{e}_1 + EI\mathbf{e}_1 \times \mathbf{e}'_1. \quad (2.13)$$

This particular constitutive relationship supplies an additional first integral which any solution to the rod problem in this class must satisfy. This can be obtained by differentiating (2.13) with respect to arclength and using (2.2a) to get

$$\mathbf{F} \times \mathbf{e}_1 = GJ\kappa'_1\mathbf{e}_1 + GJ\kappa_1\mathbf{e}'_1 + EI\mathbf{e}_1 \times \mathbf{e}''_1. \quad (2.14)$$

Taking the dot product of (2.14) with \mathbf{e}_1 and recalling from (2.1) that \mathbf{e}'_1 is perpendicular to \mathbf{e}_1 gives the result that $GJ\kappa'_1 = 0$, or

$$\kappa_1 = \text{constant} \quad (2.15)$$

where κ_1 is the twist per unit length along the rod. Thus (2.14) becomes

$$\mathbf{F} \times \mathbf{e}_1 = GJ\kappa_1\mathbf{e}'_1 + EI\mathbf{e}_1 \times \mathbf{e}''_1. \quad (2.16)$$

Equation (2.15) shows that the twist will remain constant along the entire length of the rod as has been pointed out previously by several authors (Love 1944; Landau and Lifshitz 1970). This condition can again serve as an accuracy check for certain numerical solutions developed in subsequent chapters.

Chapter 3

Numerical Procedure and Verification

In the previous chapter, the equations of equilibrium for inextensible rods were developed. These equations were then combined with constitutive assumptions for the rod to obtain the equations which describe the rod's deformations. These equations are highly nonlinear and as such are often very difficult to solve analytically. Also, due to the nonlinearity involved, the problems being investigated may exhibit multiple equilibrium configurations which further complicates the situation (Navaee and Elling 1991, 1992; Faulkner et al. 1993)

In this chapter a numerical solution is developed to solve these equations. The procedure involves two important concepts. First, the nonlinear equilibrium equations are applied to a segment of the rod and direct numerical integration is used to obtain a solution from the initial values. Force and geometric compatibility conditions are then used to assemble the various segments to obtain a solution over the entire rod in terms of the initial values at one end of the rod. Segmenting the rod in this fashion has several advantages which are discussed in Section 3.1.2. The solution for the rod is therefore treated as an initial value problem which depends on the conditions at one end of the rod. These conditions will not in general be completely known *a priori* and any unknown conditions will need to be estimated initially. This leads to the second major concept which is that a shooting procedure is used to iteratively modify the initial estimates to ensure that all boundary conditions for the rod are satisfied. Thus the solution proceeds as a sequence of initial value problems which converge to the appropriate boundary condi-

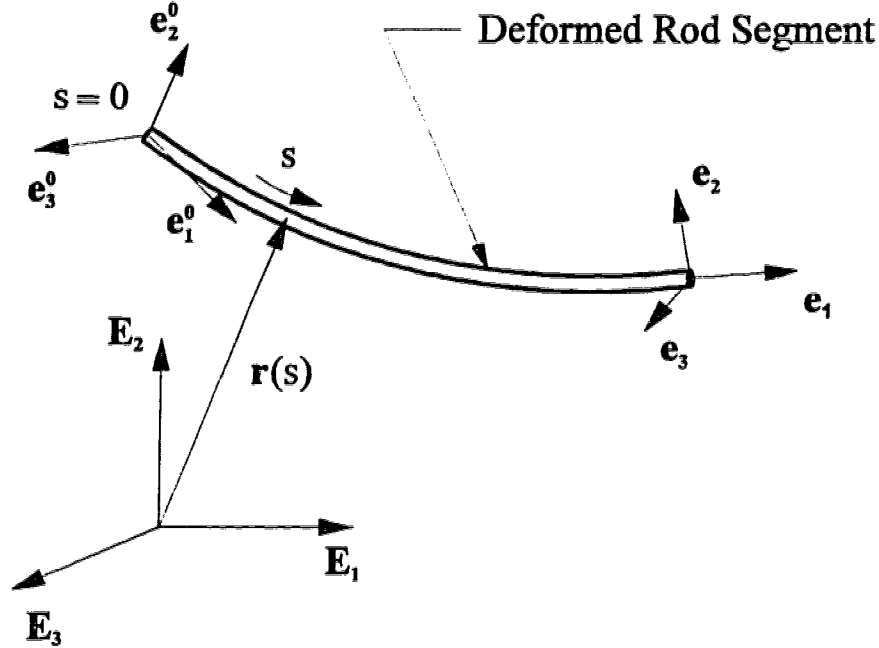


Figure 3.1: Arbitrary Rod Segment

tions.

Previous authors (Faulkner and Stredulinsky 1976; Lipsett et al. 1990; Lipsett et al. 1993; Faulkner et al. 1993) have applied this technique to analyze the bending of rods in two dimensions. The extension of this work to include fully three-dimensional deformations (as discussed in Raboud et al. 1996b) is presented in this chapter. Using the procedure developed, numerical results are obtained for a variety of problems and compared with previous analytical, numerical and experimental results to assess the effectiveness of the present technique.

3.1 Solution for the Rod

3.1.1 Solution for an Individual Segment

Consider a segment of the rod as shown in Figure 3.1. (As will be discussed in Section 3.1.2, a number of these segments will be assembled together to form the complete rod). In this figure, $\{\mathbf{E}_i\}$ is a fixed global orthonormal

basis, in which the particular rod problem is formulated. For example, if gravity loading were included in the problem it may act in the negative \mathbf{E}_2 direction. Note that $\{\mathbf{E}_i\}$ is the same for *all* segments in a particular rod. $\{\mathbf{e}_i(s)\}$ is the embedded *material basis* which changes orientation along the length of the rod segment. At the start of the segment (corresponding to an arclength $s = 0$) the values of $\{\mathbf{e}_i(s)\}$ are $\{\mathbf{e}_i^0\}$ which will serve as a fixed (independent of arclength) orthonormal basis over a particular segment of the rod. The basis $\{\mathbf{e}_i^0\}$ will be referred to as the *local basis*.

The orientation of the *material basis* in terms of the *local basis* is most conveniently expressed using Euler angles. Love (1944) uses a set of Euler angles which suffers from the fact that a singularity occurs for a null rotation. For convenience, the set of Euler angles commonly referred to as the yaw (ϕ), pitch (θ) and roll (ψ) angles (Goldstein 1980) are chosen which move the singularity away from the null rotation. In terms of these angles the components of the *material basis* $\{\mathbf{e}_i\}$ are

$$\begin{Bmatrix} \mathbf{e}_1 \\ \mathbf{e}_2 \\ \mathbf{e}_3 \end{Bmatrix} = [\mathbf{R}] \begin{Bmatrix} \mathbf{e}_1^0 \\ \mathbf{e}_2^0 \\ \mathbf{e}_3^0 \end{Bmatrix}, \quad (3.1)$$

where

$$[\mathbf{R}] = \begin{bmatrix} c_\theta c_\phi & c_\theta s_\phi & -s_\theta \\ s_\psi s_\theta c_\phi - c_\psi s_\phi & s_\phi s_\theta s_\phi + c_\psi c_\phi & c_\theta s_\psi \\ c_\psi s_\theta c_\phi + s_\psi s_\phi & c_\psi s_\theta s_\phi - s_\psi c_\phi & c_\theta c_\psi \end{bmatrix}, \quad (3.2)$$

where c and s represent cosine and sine respectively. Therefore the Euler angles at the start of the segment are $\{0, 0, 0\}$ (i.e. a null rotation).

The components of curvature and twist along the segment, which are shown by Steigmann and Faulkner (1993) to be

$$\kappa_i = \frac{1}{2} \epsilon_{ijk} \mathbf{e}_k \cdot \mathbf{e}'_j, \quad (3.3)$$

where ϵ_{ijk} is the permutation symbol, can then be expressed in terms of the Euler angles and their derivatives as

$$\begin{Bmatrix} \kappa_1 \\ \kappa_2 \\ \kappa_3 \end{Bmatrix} = \begin{bmatrix} -s_\theta & 0 & 1 \\ c_\theta s_\psi & c_\psi & 0 \\ c_\theta c_\psi & -s_\psi & 0 \end{bmatrix} \begin{Bmatrix} \phi' \\ \theta' \\ \psi' \end{Bmatrix}. \quad (3.4)$$

The moment acting at any arclength can then be expressed in terms of Euler angles, their derivatives and the initial curvatures using (3.4), (2.8) and (2.5) as

$$\mathbf{M} = M_i \mathbf{e}_i, \quad (3.5)$$

where

$$\begin{aligned} M_1 &= GJ(-s_\theta \phi' + \psi' - \kappa_1^0), \\ M_2 &= EI_2(c_\theta s_\psi \phi' + c_\psi \theta' - \kappa_2^0), \\ M_3 &= EI_3(c_\theta c_\psi \phi' - s_\psi \theta' - \kappa_3^0). \end{aligned} \quad (3.6)$$

Note that equation (3.4) can be inverted to determine the Euler angle derivatives (with respect to arclength) in terms of the curvature components provided

$$\begin{vmatrix} -s_\theta & 0 & 1 \\ c_\theta s_\psi & c_\psi & 0 \\ c_\theta c_\psi & -s_\psi & 0 \end{vmatrix} = -c_\theta \neq 0. \quad (3.7)$$

This then indicates that a singularity occurs, for this particular set of Euler angles, at $\theta = \pm n\pi/2$, $n = 1, 3, 5, \dots$ and it is not possible at these points to determine the Euler angle derivatives from the curvatures. This behavior causes stability problems in numerical schemes using Euler angles. However, as will be discussed in Section 3.1.2, considering the rod in segments allows for a rather simple method to overcome this difficulty.

As shown in Figure 3.2, the coordinates along the rod segment $\{\mathbf{r}(s)\}$, expressed in the *global basis*, are $(X(s), Y(s), Z(s))$. At the start of the segment ($s = 0$) the coordinates in the *global basis* are $\{\mathbf{r}(0)\} = (X(0), Y(0), Z(0))$. Expressed in terms of the *local basis*, the coordinates at each point along the rod segment are $\mathbf{x}(s) = (x(s), y(s), z(s))$ and the segment begins at the origin of the *local basis*, (i.e. $\mathbf{x}(0) = (x(0), y(0), z(0)) = (0, 0, 0)$). Therefore the coordinates at any arclength can be expressed as

$$\mathbf{r}(s) = \mathbf{r}(0) + \mathbf{x}(s). \quad (3.8)$$

Since $\mathbf{e}_1(s)$ is the unit tangent vector (i.e. $\mathbf{e}_1(s) = \mathbf{r}'(s)$), equations (3.1), (3.2) and (3.8) result in the coordinates of the centerline of the rod in the *local basis* satisfying the differential equations

$$x' = c_\theta c_\phi, \quad y' = c_\theta s_\phi, \quad z' = -s_\theta. \quad (3.9)$$

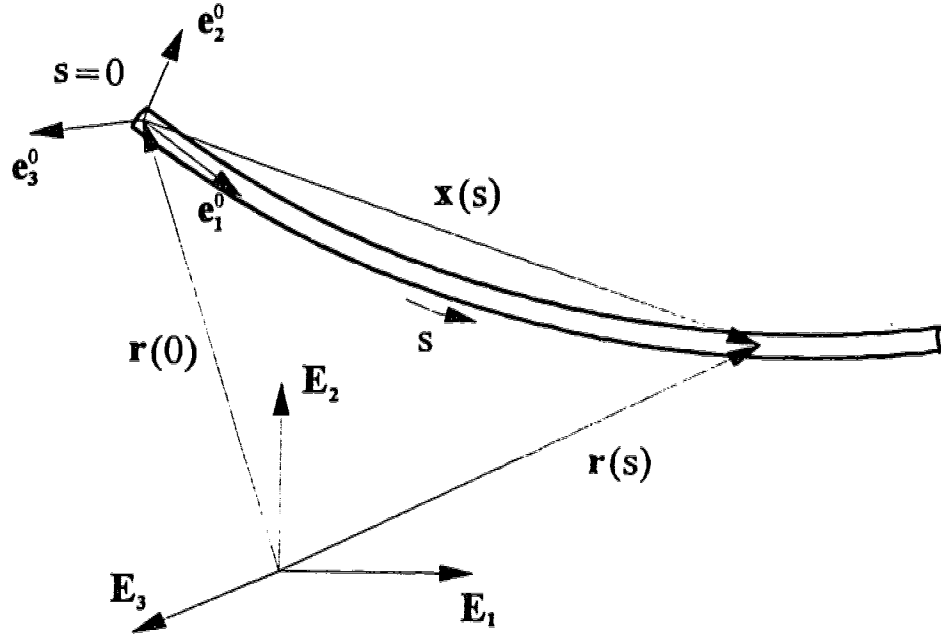


Figure 3.2: Position Coordinates Along Rod Segment

The force vector \mathbf{F} at the start of the segment can be expressed as

$$\mathbf{F} = F_i^0 \mathbf{e}_i^0 \quad (3.10)$$

where F_1^0 is the initial tension acting on the rod while F_2^0 and F_3^0 are the initial shear components in the \mathbf{e}_2^0 and \mathbf{e}_3^0 directions. For the purpose of illustration consider that a dead uniform distributed load \mathbf{b} acts on the segment. The components of \mathbf{b} can be expressed in terms of $\{\mathbf{e}_i^0\}$, since this is a valid orthonormal basis, as

$$\mathbf{b} = b_i \mathbf{e}_i^0 \quad (3.11)$$

where the b_i are constants. The equilibrium equation (2.2a) can be integrated to give

$$\mathbf{F}(s) = \mathbf{F}(0) - \int_0^s \mathbf{b} ds \quad (3.12)$$

which for the special case of uniform loading becomes

$$\mathbf{F}(s) = [F_i^0 - b_i s] \mathbf{e}_i^0. \quad (3.13)$$

Note that the components of the force vector in equation (3.13) are no longer the tension and shear components because they are expressed in terms of the fixed (for the segment) basis $\{\mathbf{e}_i^0\}$. The true tension and shear components must necessarily be expressed in terms of the material basis which changes along the segment. Equation (3.13) can be combined with equations (3.1) and (3.2) to give

$$\mathbf{F} = F_i \mathbf{e}_i, \quad (3.14)$$

where

$$\begin{Bmatrix} F_1 \\ F_2 \\ F_3 \end{Bmatrix} = [\mathbf{R}] \begin{Bmatrix} F_1^0 - b_1 s \\ F_2^0 - b_2 s \\ F_3^0 - b_3 s \end{Bmatrix}. \quad (3.15)$$

The force components in equations (3.14) and (3.15) are now the true tension and shear components and will be used in the subsequent work.

The constitutive relation (2.8) can now be differentiated with respect to arclength and combined with the equilibrium equation (2.2b) to give

$$\begin{aligned} \mathbf{F} \times \mathbf{e}_1 &= GJ \kappa_1' \mathbf{e}_1 + EI_2 \kappa_2' \mathbf{e}_2 + EI_3 \kappa_3' \mathbf{e}_3 \\ &+ GJ (\kappa_1 - \kappa_1^0) \mathbf{e}_1' + EI_2 (\kappa_2 - \kappa_2^0) \mathbf{e}_2' + EI_3 (\kappa_3 - \kappa_3^0) \mathbf{e}_3', \end{aligned} \quad (3.16)$$

which can be written as three component equations

$$\begin{aligned} GJ \kappa_1' &= (EI_2 - EI_3) \kappa_2 \kappa_3 + EI_3 \kappa_2 \kappa_3^0 - EI_2 \kappa_3 \kappa_2^0, \\ EI_2 \kappa_2' &= (EI_3 - GJ) \kappa_1 \kappa_3 + GJ \kappa_3 \kappa_1^0 - EI_3 \kappa_1 \kappa_3^0 + F_3, \\ EI_3 \kappa_3' &= (GJ - EI_2) \kappa_1 \kappa_2 + EI_2 \kappa_1 \kappa_2^0 - GJ \kappa_2 \kappa_1^0 - F_2, \end{aligned} \quad (3.17)$$

where equation (2.1) has been used and only rod segments which have constant initial curvatures and twists have been considered. Note that the tension F_1 is not involved directly since the rod is assumed to be inextensible. There is no constitutive relationship to determine the tension from the deformation and it does not appear explicitly in the equilibrium equations, but rather it is determined by an overall equilibrium balance.

By taking the derivatives of (3.4) and substituting these into (3.17), the

component equations can be rewritten as

$$\begin{aligned}\phi'' &= \frac{C_1 EI_2 c_\psi + C_2 EI_3 s_\psi}{EI_2 EI_3 c_\theta}, \\ \theta'' &= \frac{C_2 EI_3 c_\psi - C_1 EI_2 s_\psi}{EI_2 EI_3}, \\ \psi'' &= \frac{C_3 + GJ s_\theta \phi''}{GJ},\end{aligned}\tag{3.18}$$

where

$$\begin{aligned}C_1 &= (GJ - EI_2)\kappa_1 \kappa_2 + EI_2 \kappa_2^0 \kappa_1 - GJ \kappa_1^0 \kappa_2 \\ &\quad + EI_3 (s_\theta c_\psi \phi' \theta' + c_\theta s_\psi \phi' \psi' + c_\psi \theta' \psi') - F_2, \\ C_2 &= (EI_3 - GJ)\kappa_1 \kappa_3 + GJ \kappa_1^0 \kappa_3 - EI_3 \kappa_3^0 \kappa_1 \\ &\quad + EI_2 (s_\theta s_\psi \phi' \theta' - c_\theta c_\psi \phi' \psi' + s_\psi \theta' \psi') + F_3, \\ C_3 &= (EI_2 - EI_3)\kappa_2 \kappa_3 + EI_3 \kappa_3^0 \kappa_2 - EI_2 \kappa_2^0 \kappa_3 + GJ c_\theta \phi' \theta',\end{aligned}\tag{3.19}$$

To nondimensionalize these equations, the dimensionless parameters

$$\begin{aligned}\rho &= \frac{s}{L}, \quad \hat{\kappa}_i = \kappa_i L, \quad \nu_i = \frac{F_i L^2}{EI}, \quad \lambda_i = \frac{b_i L^3}{EI}, \\ \Omega &= \frac{GJ}{EI}, \quad \beta = \frac{EI_2}{EI}, \quad \gamma = \frac{EI_3}{EI},\end{aligned}\tag{3.20}$$

are introduced where L is the length of the segment and EI is taken to be the larger of EI_2 and EI_3 . Equations (3.18) and (3.19) then become

$$\begin{aligned}\ddot{\phi} &= \frac{\hat{C}_1 \beta c_\psi + \hat{C}_2 \gamma s_\psi}{\beta \gamma c_\theta}, \\ \ddot{\theta} &= \frac{\hat{C}_2 \gamma c_\psi - \hat{C}_1 \beta s_\psi}{\beta \gamma}, \\ \ddot{\psi} &= \frac{\hat{C}_3 + \Omega s_\theta \ddot{\phi}}{\Omega},\end{aligned}\tag{3.21}$$

and

$$\begin{aligned}\hat{C}_1 &= (\Omega - \beta)\hat{\kappa}_1 \hat{\kappa}_2 + \beta \hat{\kappa}_2^0 \hat{\kappa}_1 - \Omega \hat{\kappa}_1^0 \hat{\kappa}_2 \\ &\quad + \gamma (s_\theta c_\psi \dot{\phi} \dot{\theta} + c_\theta s_\psi \dot{\phi} \dot{\psi} + c_\psi \dot{\theta} \dot{\psi}) - \nu_2, \\ \hat{C}_2 &= (\gamma - \Omega)\hat{\kappa}_1 \hat{\kappa}_3 + \Omega \hat{\kappa}_1^0 \hat{\kappa}_3 - \gamma \hat{\kappa}_3^0 \hat{\kappa}_1 \\ &\quad + \beta (s_\theta s_\psi \dot{\phi} \dot{\theta} - c_\theta c_\psi \dot{\phi} \dot{\psi} + s_\psi \dot{\theta} \dot{\psi}) + \nu_3, \\ \hat{C}_3 &= (\beta - \gamma)\hat{\kappa}_2 \hat{\kappa}_3 + \gamma \hat{\kappa}_3^0 \hat{\kappa}_2 - \beta \hat{\kappa}_2^0 \hat{\kappa}_3 + \Omega c_\theta \dot{\phi} \dot{\theta},\end{aligned}\tag{3.22}$$

where the dot notation indicates differentiation with respect to ρ . Similarly, using equation (3.20), (3.4) and (3.24) become

$$\begin{Bmatrix} \dot{\kappa}_1 \\ \dot{\kappa}_2 \\ \dot{\kappa}_3 \end{Bmatrix} = \begin{bmatrix} -s_\theta & 0 & 1 \\ c_\theta s_\psi & c_\psi & 0 \\ c_\theta c_\psi & -s_\psi & 0 \end{bmatrix} \begin{Bmatrix} \dot{\phi} \\ \dot{\theta} \\ \dot{\psi} \end{Bmatrix} \quad (3.23)$$

and

$$\begin{Bmatrix} \nu_1 \\ \nu_2 \\ \nu_3 \end{Bmatrix} = [\mathbf{R}] \begin{Bmatrix} \nu_1^0 - \chi_1 \rho \\ \nu_2^0 - \chi_2 \rho \\ \nu_3^0 - \chi_3 \rho \end{Bmatrix} \quad (3.24)$$

while (3.9) simply becomes

$$\frac{\dot{x}}{L} = c_\theta c_\phi, \quad \frac{\dot{y}}{L} = c_\theta s_\phi, \quad \frac{\dot{z}}{L} = -s_\theta. \quad (3.25)$$

Equations (3.20) - (3.25) along with (3.4) completely describe the deformation of the rod segment in terms of the conditions at the beginning of that segment. The force, moment, position and orientation at the end of the segment can therefore be determined by the force, moment, position and orientation at the start of the segment by direct numerical integration. The Bulirsch-Stoer method is used, rather than the more common Runge-Kutta methods, to perform the integration because it is significantly more computationally efficient when high accuracy is required (see Press et al. 1992 for a description of the method).

3.1.2 Solution for the Complete Rod

In the previous section a method of solution for an individual segment of the rod was presented¹. To solve the entire rod, which can be comprised of a

¹Note that a similar segmental approach has been used previously (Faulkner and Stredulinsky 1976; Lipsett et al. 1990; Lipsett et al. 1993; Faulkner et al. 1993) to solve planar elastica problems where large deflections are involved. In those cases the rod was considered using a large number of segments so that each individual segment undergoes only small relative deformations. This was required so that a linearized equilibrium equation could be applied and a power series solution was obtained. This is not the case in the current work where the fully nonlinear equations are applied to each segment so that maintaining small relative deformations is not required. Individual segments may therefore be quite long and the use of a single segment may be sufficient to solve a given rod problem.

number of segments (or possibly just one), the individual segments are assembled in such a way that force and geometric compatibility are maintained. This is accomplished by using the force, moment, position and orientation obtained at the end of one segment as the starting values for the next segment. That is the forces and moments obtained at the end of the k^{th} segment are used as the inputs to the $k + 1^{\text{th}}$ segment. Similarly, the material basis $\{\mathbf{e}_i\}$ at the end of the k^{th} segment becomes the local basis $\{\mathbf{e}_i^0\}$ for the $k + 1^{\text{th}}$ segment. As well, the global coordinates at the end of one segment, obtained using (3.25) and (3.8), become the starting coordinates $\mathbf{r}(0)$ for the next segment. This procedure is continued from segment to segment until a solution is obtained for the entire rod. In this way, the forces, moments, position and orientation at the end of the rod are completely determined by the forces, moments, position, and geometry at the start of the rod.

One of the main reasons for solving the rod in this manner is that many rod-like structures of interest have complicated initial geometries in their undeformed configuration. These rods can often be modelled as a number of segments of simple geometric types. Since each individual segment has a simple geometry (with constant initial curvatures) it can be considered much more readily. Complex loading conditions, non-constant initial curvatures and varying material properties can be similarly handled in a straightforward manner.

A further advantage to using a segmented solution in this manner, even for rods which have simple initial geometries, is that for many problems large rotations occur and the Euler angles used to describe the deformation can pass through a singular point ($\theta = \pm n\pi/2$, $n = 1, 3, 5, \dots$ as discussed previously for the set of Euler angles used here). By introducing new segments along the rod, new local bases are established at the beginning of each new segment. The Euler angles which describe the material basis in terms of these local bases are all reset to zero at the start of each segment. This can be done often enough along the rod to avoid the singularities inherent in the Euler angle representations and the resulting numerical difficulties.

The solution as presented above is an initial value approach in that the solution to the rod problem is determined from the conditions (force, moment, position and orientation) at one end of the rod which must be completely specified in order to obtain a solution. However, most rod problems are actually two-point boundary value problems where some of the boundary conditions are known at each end of the rod. In general not all of the conditions will be known at one end *a priori*, but rather some will be unknown and

a corresponding number of conditions will be known at the other end of the rod. The unknowns at the start of the rod must be initially estimated to start the numerical procedure. From these initial estimates the solution for the rod is obtained using the procedure described previously. The values obtained at the end of the rod are compared to known boundary conditions at that end. The initial estimates are then modified iteratively using a Newton-Raphson secant method algorithm. This procedure is repeated until the values at the end of the rod converge, to within a specified tolerance, to the desired boundary conditions to give the appropriate solution. The Newton-Raphson method used is discussed in more detail in Appendix A.

3.2 Verification of Results

In this section the numerical procedure developed previously is used to solve several problems which have known analytical or numerical solutions. This is done to allow a determination of the accuracy and efficiency of the method. The problems considered are:

Initially Straight Rods

- Initially straight circular rod bent and twisted into a helix by the action of forces and moments along the initial axis of the rod.
- Initially straight orthotropic rod bent and twisted into a helix by the action of forces and moments along the initial axis of the rod.
- Initially straight orthotropic rod deformed into a Möbius strip.
- Cantilever beam loaded in a non-principal direction by a dead tip load.

Initially Curved Rods

- Initially helical orthotropic rod bent and twisted into another helix.
- Initially curved cantilever loaded out of the initial plane of curvature by a dead tip load.

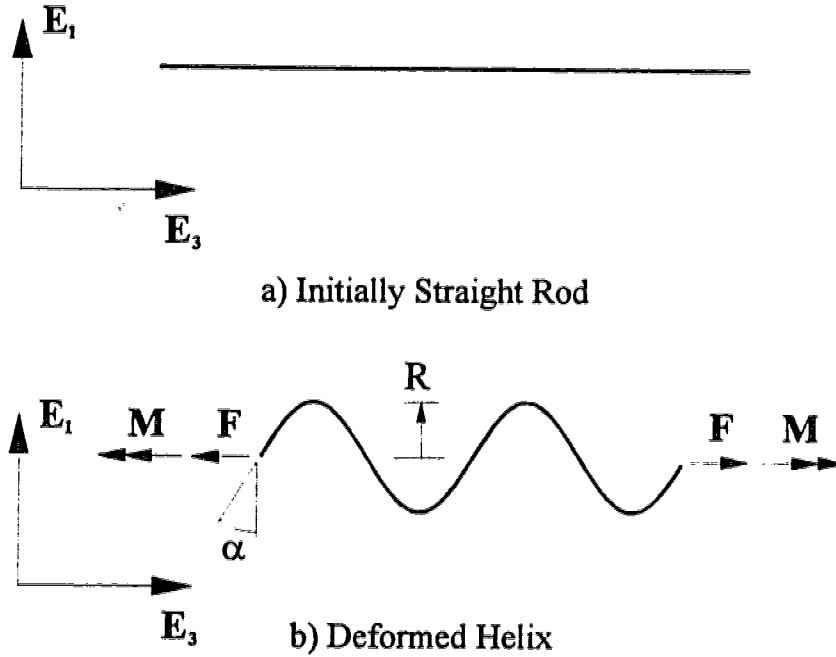


Figure 3.3: Initially Straight Rod Deformed Into a Helix: (a) Undeformed Configuration, (b) Deformed Configuration

3.2.1 Initially Straight Rods

3.2.1.1 Initially Straight Circular Rod Deformed Into a Helix

The first problem considered is an initially straight circular rod with constant material properties bent and twisted into a helix of radius R and pitch angle α as shown in Figure 3.3. The analytical solution for this problem has been considered by previous authors (Love 1944; Landau and Lifshitz 1970) and is also presented in Appendix B for completeness. This problem is one of the few truly three-dimensional problems which combines bending and twisting and has a known analytical solution to allow comparison with the numerical results.

The analytical solution shows that specifying the helix centerline (i.e. R and α given) is not enough to determine the forces and moments required to maintain the deformation. This is because R and α only specify the geometry of the helix centerline while κ_1 is also required to determine the rate at which the orientation of the cross section changes along the helix. For

each value of κ_1 there exists a force-moment combination which will support that particular deformation so that an infinite number of solutions exist for a specified helix centerline. Therefore, rather than specifying the geometry of the helix centerline, a different approach will be taken. The problem is posed with the axial force \mathbf{F} , axial moment \mathbf{M} and pitch angle α specified. With these values specified, the radius R and twist per unit length κ_1 of the resulting helix can be determined from equations (B.7b), (B.7c) and (B.11) to be

$$R = \frac{\cos \alpha}{2F_z \sin \alpha} \left[M_z \pm \sqrt{M_z^2 - 4EI F_z \sin \alpha} \right], \quad (3.26)$$

with the corresponding value of κ_1 determined from either of equations (B.7b) or (B.7c). Therefore, for $F_z \neq 0$, there may be two solutions for the radius (each with a corresponding κ_1) or there may be no solution at all for the combination of force, moment and pitch angle specified. Note that the solution in equation (3.26) is undefined when $F_z = 0$ or $\alpha = 0$. However, when $F_z = 0$, κ_1 and R are given by (B.13) and (B.14) respectively. When $\alpha = 0$ (which implies that the centerline remains in the \mathbf{E}_1 - \mathbf{E}_2 plane), equations (B.7b), (B.7c) and (B.11) simplify to

$$R = \frac{EI}{M_z}, \quad (3.27)$$

$$\kappa_1 = \frac{F_z R}{GJ} = \frac{F_z EI}{M_z GJ}. \quad (3.28)$$

To begin the numerical procedure, the position and geometry at the start of the rod must be specified. For a helix of radius R and pitch angle α the coordinates of the starting position in the global basis are assumed to be

$$X = R, \quad Y = 0, \quad Z = 0. \quad (3.29)$$

while the initial material basis is given by

$$\begin{Bmatrix} \mathbf{e}_1 \\ \mathbf{e}_2 \\ \mathbf{e}_3 \end{Bmatrix} = \begin{bmatrix} 0 & \cos \alpha & \sin \alpha \\ 1 & 0 & 0 \\ 0 & \sin \alpha & -\cos \alpha \end{bmatrix} \begin{Bmatrix} \mathbf{E}_1 \\ \mathbf{E}_2 \\ \mathbf{E}_3 \end{Bmatrix}. \quad (3.30)$$

The components of the force and moment vectors ($\mathbf{F} = F_i \mathbf{e}_i$ and $\mathbf{M} = M_i \mathbf{e}_i$) in this material basis are then given by

$$\begin{aligned} F_1 &= F_z \sin \alpha, \\ F_2 &= 0, \\ F_3 &= -F_z \cos \alpha, \end{aligned} \quad (3.31)$$

and

$$\begin{aligned} M_1 &= M_z \sin \alpha + M_\zeta \cos \alpha, \\ M_2 &= 0, \\ M_3 &= -M_z \cos \alpha + M_\zeta \sin \alpha, \end{aligned} \tag{3.32}$$

where equations (B.7a)-(B.7d) and (B.10) have been used. These are now the initial tension, shear forces and moment components (twisting and bending) acting at the start of the rod which are the values required to begin the numerical procedure.

To compare the numerical and analytical solutions, an initially straight steel rod ($E = 207$ GPa, $G = 70$ GPa) one metre long and with a cross sectional diameter of 6 mm is subjected to an axial force and moment of 100 N and 200 Nm respectively with the pitch angle selected to be 45° . This particular choice of force system allows two analytical solutions from equation (3.26) as

$$\text{Solution \#1: } R \approx 0.04769610\text{m} \quad \kappa_1 = 16.25726757\text{m}^{-1}, \tag{3.33a}$$

$$\text{Solution \#2: } R \approx 1.95230390\text{m} \quad \kappa_1 = 31.37851470\text{m}^{-1}. \tag{3.33b}$$

From the first set of values, M_ζ , which depends on both the axial force and the radius R , is 4.769610 Nm while for the second solution it is 195.230390 Nm. Then, with the forces and moments at the start of the rod specified, the corresponding components in the initial material basis are determined as shown in equations (3.31)-(3.32). Note that since all of the initial conditions are completely specified, no shooting is required to solve this problem. It will simply serve as an accuracy check on the integration portion of the numerical solution. An evaluation of the shooting part of the solution will be performed in subsequent sections.

Figure 3.4 shows the resulting geometry of the centerline of the rod obtained using the numerical solution as well as the analytical solution. The numerical results can be seen to be indistinguishable from the analytical solutions. While the first solution (3.33a) indicates a helix with more than two complete turns, (3.33b) is only a small fraction of one turn at a much larger radius. Note that despite the simple initial geometry, five segments were used to generate the numerical solutions. This is due to the fact that a singularity in the Euler angles used would occur at an arclength of approximately 0.211 m and cause numerical difficulties. This clearly demonstrates the usefulness of a segmented solution as presented here.

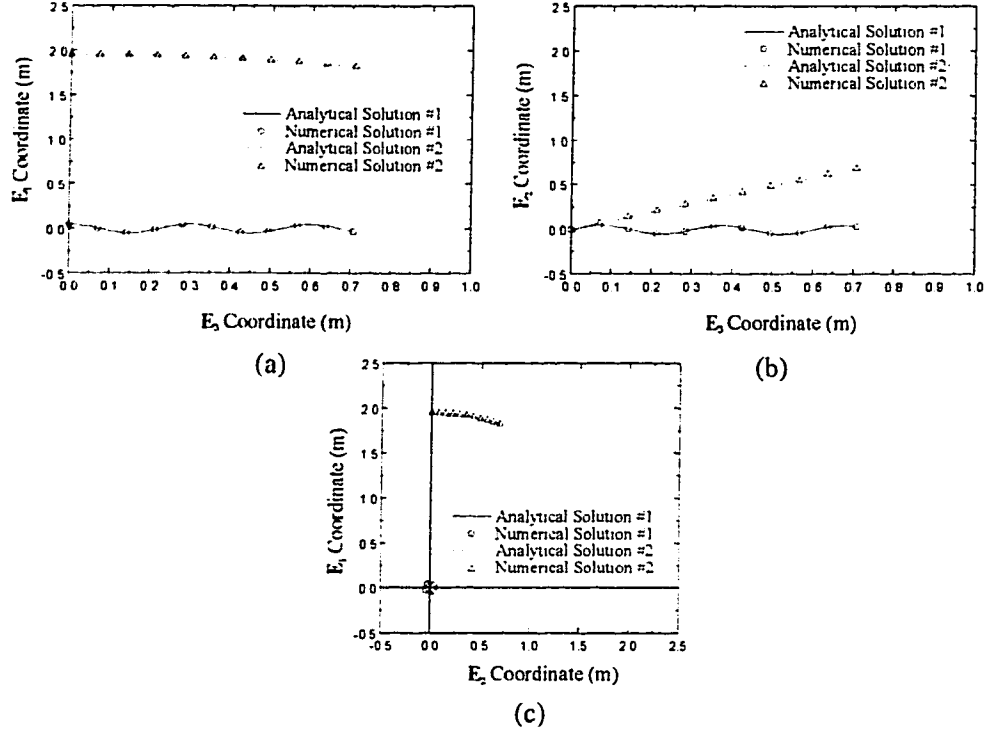


Figure 3.4: Geometry of Helix Centerline, $M_z = 200$ Nm, $F_z = 100$ N, $\alpha = 45^\circ$: (a) E_3 - E_1 Plane, (b) E_3 - E_2 Plane, (c) E_2 - E_1 Plane

As well as comparing the deformed shapes as above, two further checks on the accuracy of the numerical solution were used. The energy integral in equation (2.3) should remain constant. In addition, as this is a circular rod (i.e. transversely isotropic), equation (2.15) is applicable which states that the twist per unit length κ_1 should remain constant along the rod. Figures 3.5 and 3.6 show κ_1 and the energy integral respectively as functions of arclength. These two quantities can be seen to be constant along the rod. In fact, no change in either quantity was noticed to at least seven significant digits for either solution. Note that the analytical results are available and are exactly equal to the numerical results at the start of the rod. These results are available since the conditions at the start are completely specified which allows the values of the twist and energy integral to be computed.

As a further test of the robustness of the numerical solution, the pitch angle of the resulting helix was changed from 45° to first 5° and then 85°

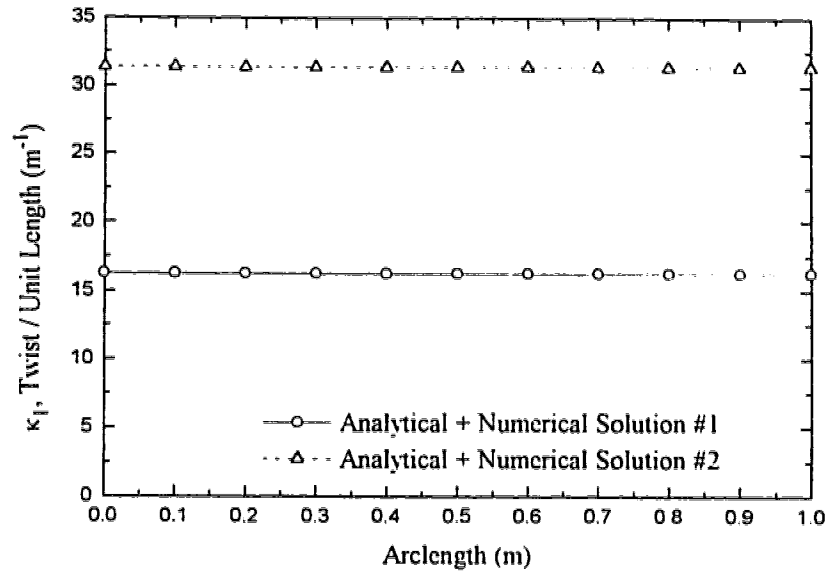


Figure 3.5: Twist/Unit Length (κ_1) Along Rod

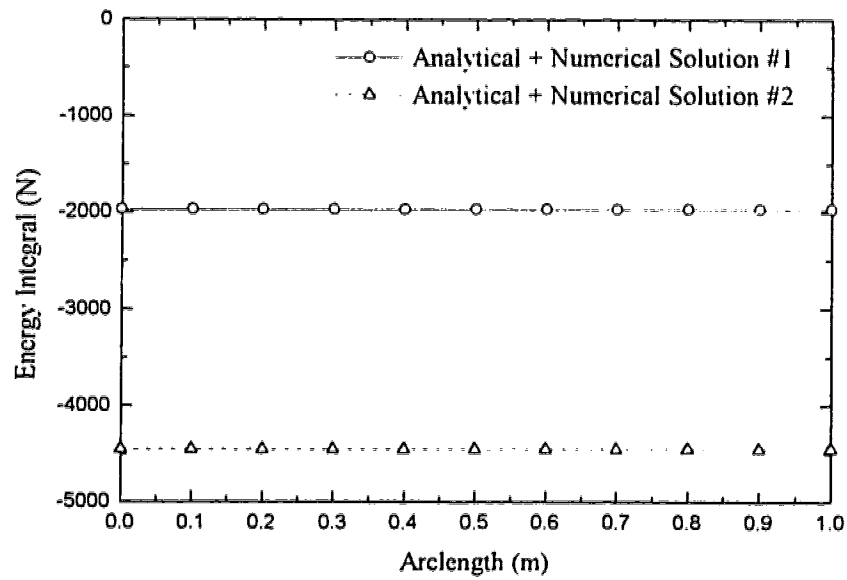


Figure 3.6: Energy Integral Along Rod

while the values for the axial moment and force were held fixed. This has the effect of changing the relative amounts of bending and twisting in the resulting deformation. When α approaches zero there is almost pure bending with little twist, while a value of α near 90° indicates a nearly straight rod with considerable twist and little bending. For both $\alpha = 5^\circ$ and $\alpha = 85^\circ$, equation (3.26) still indicates that multiple solutions exist and the results for $\alpha = 5^\circ$ are

$$\text{Solution \#1: } R = 0.06578260\text{m} \quad \kappa_1 = 2.6929327\text{m}^{-1}, \quad (3.34a)$$

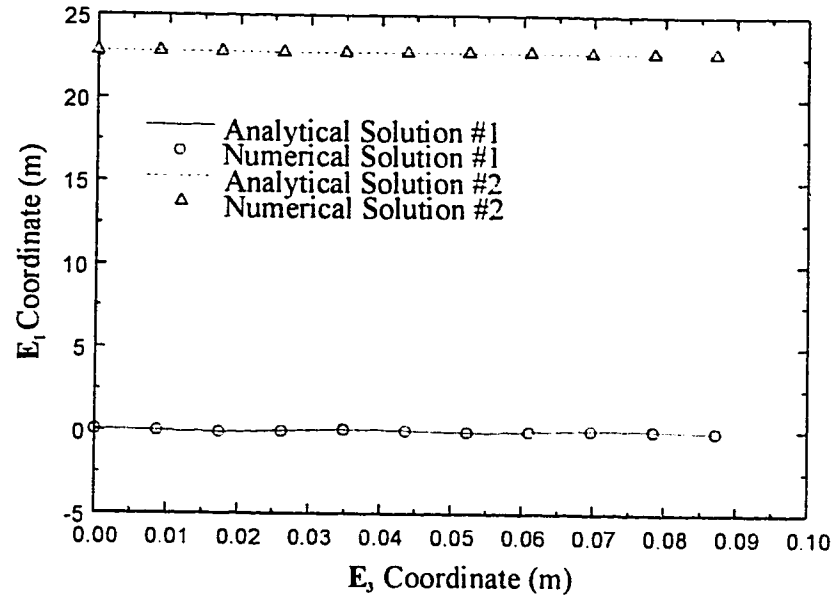
$$\text{Solution \#2: } R = 22.79432201\text{m} \quad \kappa_1 = 256.9147493\text{m}^{-1}, \quad (3.34b)$$

while for $\alpha = 85^\circ$ they are

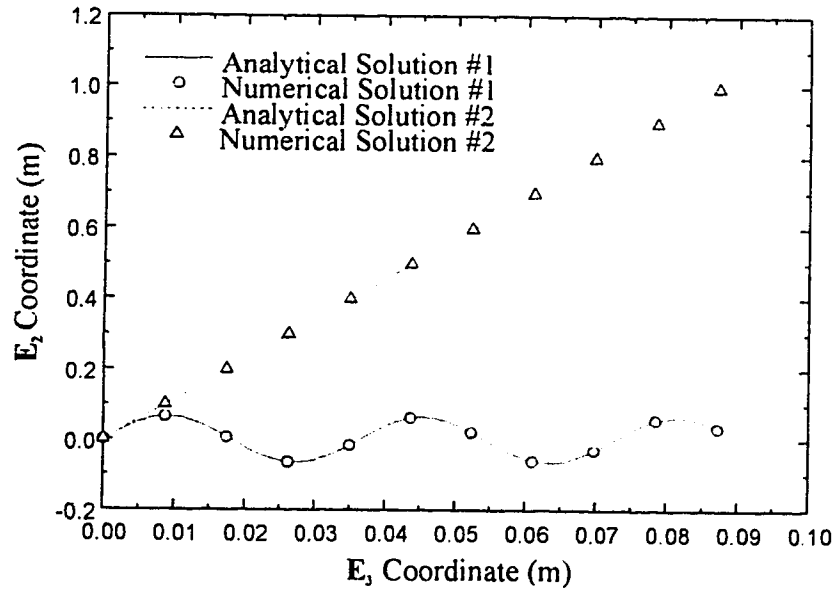
$$\text{Solution \#1: } R = 0.00594034\text{m} \quad \kappa_1 = 22.37608614\text{m}^{-1}, \quad (3.34c)$$

$$\text{Solution \#2: } R = 0.16903699\text{m} \quad \kappa_1 = 22.53568806\text{m}^{-1}. \quad (3.34d)$$

Figures 3.7 and 3.8 show the resulting geometries for each of these cases. (Note that the geometries in the \mathbf{E}_2 - \mathbf{E}_1 plane are circular arcs and are not shown). As can be seen, there is again excellent agreement between the analytical and numerical solutions. The numerical solution is again able to generate all of the multiple analytical solutions. As well, the checks using both κ_1 and the energy integral, not shown here, were found to be similarly consistent as with the $\alpha = 45^\circ$ case.

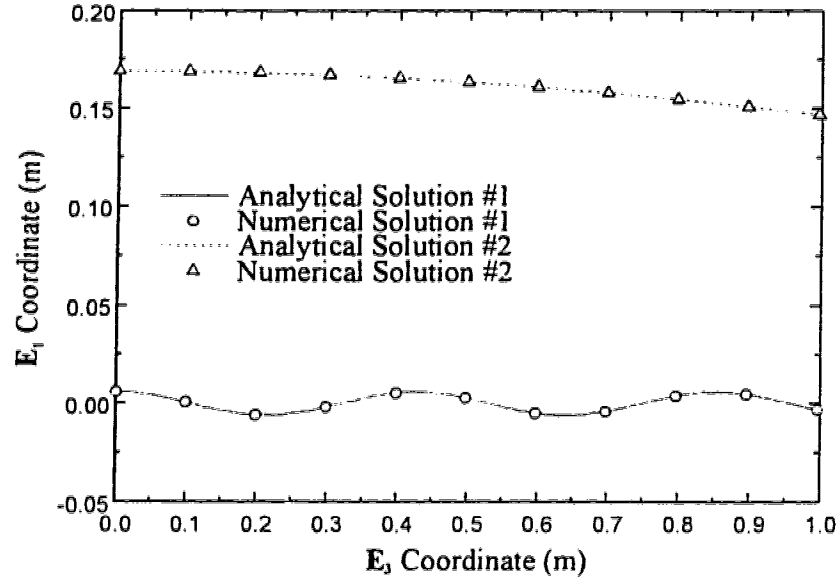


(a)

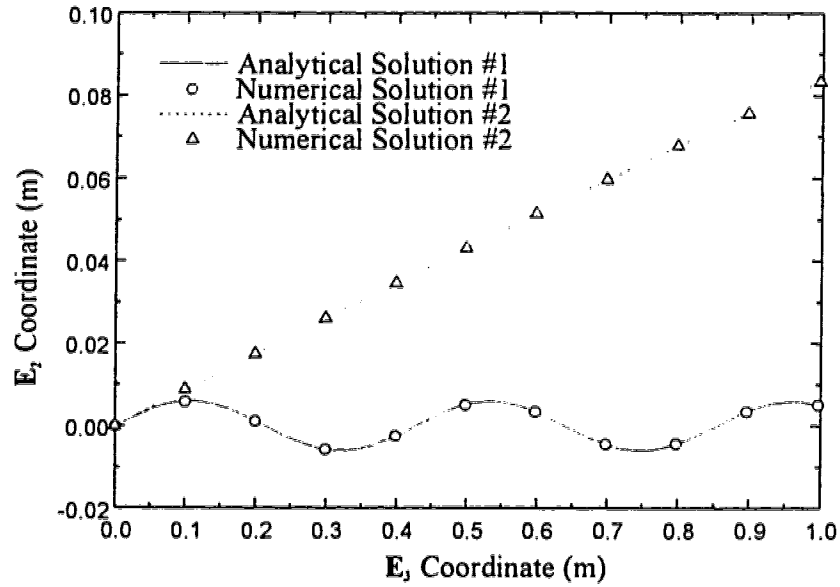


(b)

Figure 3.7: Geometry of Helix Centerline, $\alpha = 5^\circ$: (a) E_3 - E_1 Plane, (b) E_3 - E_2 Plane



(a)



(b)

Figure 3.8: Geometry of Helix Centerline, $\alpha = 85^\circ$: (a) E_3 - E_1 Plane, (b) E_3 - E_2 Plane

3.2.1.2 Initially Straight Orthotropic Rod Deformed Into a Helix

To investigate rods with non-circular cross sections, the next problem considered is an initially straight orthotropic rod bent and twisted into a helix again with a radius R and pitch angle α as shown in Figure 3.9. Faulkner and Steigmann (1993) have considered this problem and have derived analytical solutions². Their solution to this problem shows that all bending along the rod is about only one principal axis so that the curvature about that axis is equal to the curvature of the helix centerline κ_c . Further, the twist per unit length along the rod is required to be equal to the geometric torsion τ of the centerline of the helix, where these quantities are defined as

$$\tau = \frac{\cos \alpha \sin \alpha}{R}, \quad (3.35a)$$

$$\kappa_c = \frac{\cos^2 \alpha}{R}. \quad (3.35b)$$

Thus, a major difference between this case and the isotropic case is that for orthotropic rods there are no multiple solutions for a given helix (i.e. specified R and α). In the isotropic case with R and α given, κ_1 could still be selected arbitrarily and the forces and moments required to maintain the deformation could then be determined from equations (B.7a)-(B.7d). In the orthotropic case, κ_1 is no longer arbitrary but is equal to τ , defined in equation (3.35a), so that only one solution exists for each set of R and α .

The initial conditions for this problem, as with the isotropic case, are again set with the initial position coordinates in the global basis given by

$$X = R, \quad Y = 0, \quad Z = 0, \quad (3.36)$$

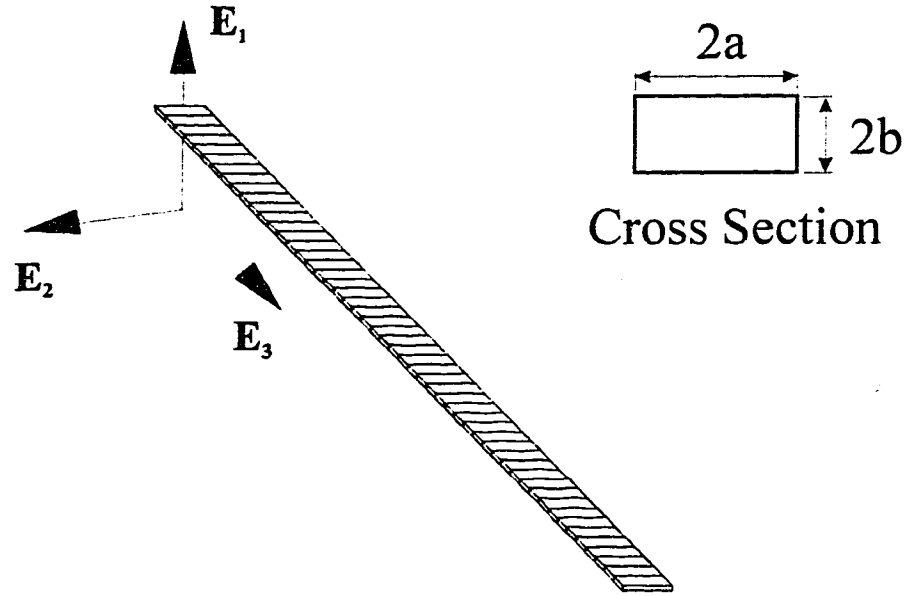
while the initial material basis is again given by

$$\begin{Bmatrix} \mathbf{e}_1 \\ \mathbf{e}_2 \\ \mathbf{e}_3 \end{Bmatrix} = \begin{bmatrix} 0 & \cos \alpha & \sin \alpha \\ 1 & 0 & 0 \\ 0 & \sin \alpha & -\cos \alpha \end{bmatrix} \begin{Bmatrix} \mathbf{E}_1 \\ \mathbf{E}_2 \\ \mathbf{E}_3 \end{Bmatrix}. \quad (3.37)$$

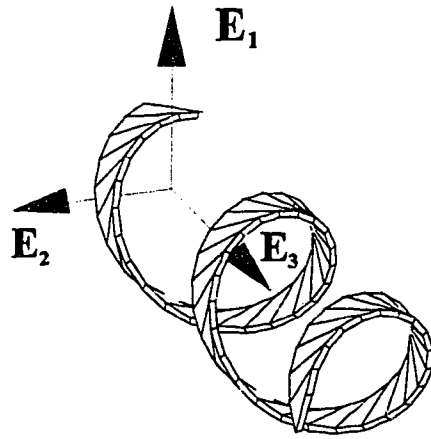
Faulkner and Steigmann (1993) show that the moments and forces necessary to maintain this deformed configuration are given by

$$\mathbf{M} = GJ\tau\mathbf{e}_1 + EI_3\kappa_c\mathbf{e}_3 \quad (3.38)$$

²These are so called controllable deformations because they can be maintained by surface forces alone in any material of a particular class.



(a)



(b)

Figure 3.9: Initially Straight Orthotropic Rod Deformed Into a Helix: (a) Un-deformed Configuration, (b) Deformed Helix

and

$$\mathbf{F} = (GJ - EI_3)\tau^2 \mathbf{e}_1 + (GJ - EI_3)\kappa_s \tau \mathbf{e}_3 \quad (3.39)$$

which are already expressed in the initial material basis at the start of the rod. Note that all the initial conditions are again specified so that shooting is not required to solve this problem.

To compare the numerical and analytical solutions, an initially straight steel rod ($E = 207$ GPa, $G = 70$ GPa) one metre long is considered. The centerline of the deformed helix is specified with a radius of $R = 0.05$ m while the pitch angles are chosen to be 5° , 45° , and 85° . The aspect ratio of the cross section, a/b as shown in Figure 3.9, is allowed to vary from one to ten by letting a vary and keeping b fixed at 3mm.

Figure 3.10 shows three views for both the numerical and analytical solutions of the centerline geometry for the case where $\alpha = 45^\circ$ and the aspect ratio $a/b = 10$. As can be seen, there is again excellent agreement with no noticeable difference between the numerical and analytical results.

Figures 3.11 and 3.12 show the twist per unit length and the energy integral respectively for this case as well. As can be seen, there is once again excellent agreement between the analytical and numerical solutions. In particular, κ_1 agrees with the values predicted by equation (3.35a) with $R = 0.05$ m and $\alpha = 45^\circ$. Note that equation (2.15), which requires that κ_1 remain constant, is only applicable in the case of isotropic rods, while the rods with rectangular cross sections considered here are orthotropic³. Thus, the fact that κ_1 is a constant is not a constitutive requirement in this case, but merely a result of the particular boundary value problem (in this case initial value problem since all initial conditions are known) being considered.

Similar results were found for the other pitch angles and aspect ratios considered. Excellent agreement was observed in the shapes as well as in the twist per unit length and energy integral values. To give a better indication of the relative amounts of bending and twisting, Figure 3.13 shows the deformed configurations for a rod with an aspect ratio of 10 in which the pitch angles considered are 5° , 45° and 85° . Note that the solutions delivered by the numerical procedure are smooth and continuous even though the shapes

³Note that in the special case where $a = b$, $EI_2 = EI_3$. The rod is thus considered isotropic within the limits of the present theory despite the fact that a rod with a square cross section is not truly isotropic in a fully three-dimensional linear elasticity framework. In particular, equation (2.15) applies and κ_1 should remain constant.

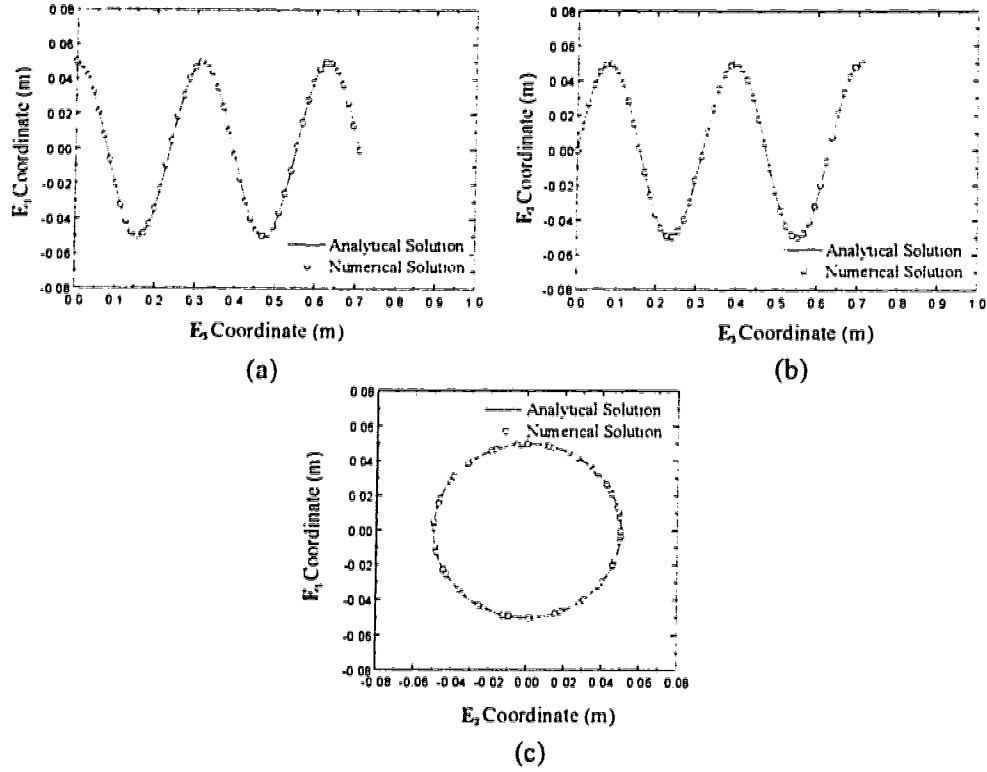


Figure 3.10: Geometry of Orthotropic Helix Centerline. $R = 0.05\text{m}$. $\alpha = 45^\circ$. $a/b = 10$: (a) E_3 - E_1 Plane. (b) E_3 - E_2 Plane. (c) E_2 - E_1 Plane

shown in Figures 3.13a-c do not appear to be smooth. This is due to the fact that the three-dimensional pictures (here and elsewhere in this thesis) were created using straight segments. 50 segments were used to generate these figures which in some cases (such as Figure 3.13a) are not enough to produce a smooth appearance. However, despite the appearance in these figures, the solutions delivered by the numerical procedure are smooth.

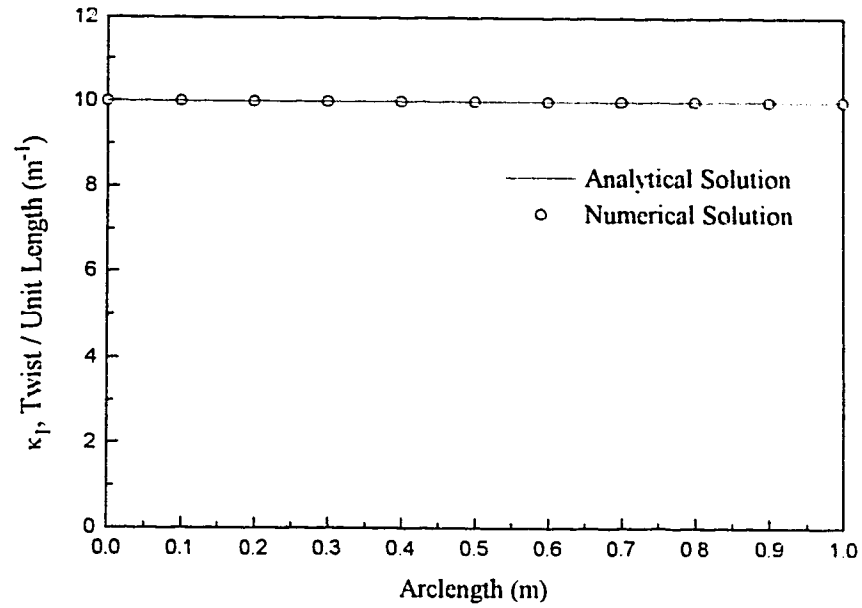


Figure 3.11: Twist/Unit Length (κ_1) Along Helix. $R = 0.05\text{m}$, $\alpha = 45^\circ$, $a/b = 10$

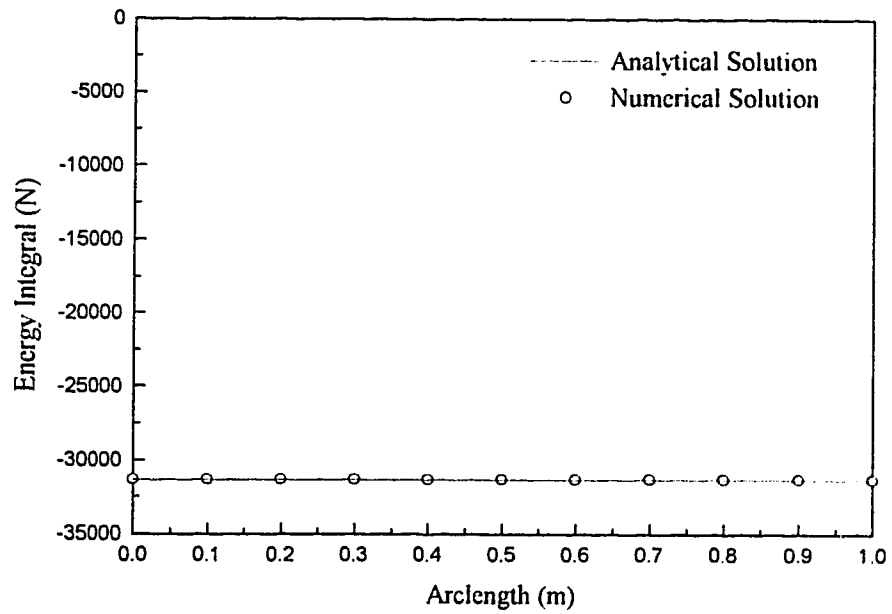
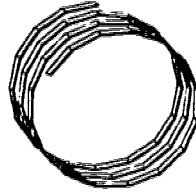
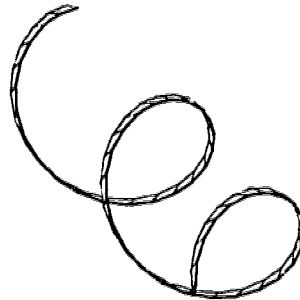


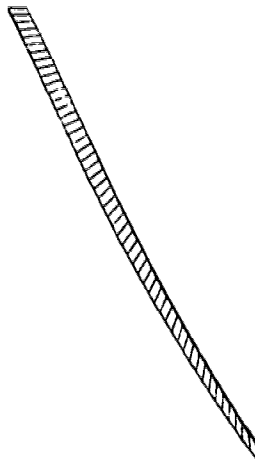
Figure 3.12: Energy Integral Along Helix, $R = 0.05\text{m}$, $\alpha = 45^\circ$, $a/b = 10$



(a)



(b)



(c)

Figure 3.13: Deformed Helices For the Case Aspect Ratio = 10 for Various Pitch Angles: (a) $\alpha = 5^\circ$. (b) $\alpha = 45^\circ$. (c) $\alpha = 85^\circ$

3.2.1.3 Initially Straight Orthotropic Rod Deformed Into A Möbius Strip

To further investigate rods with non-circular cross sections, the next problem considered is a thin rectangular rod deformed into a Möbius strip. To make such a strip, the ends of the rod are joined together after undergoing a 180° twist about the centerline. In this case, not all of the initial values at the start of the rod are known *a priori* so shooting is required to satisfy all of the boundary conditions. The location and orientation at the start of the rod may be specified and is given here to be

$$X = 0, \quad Y = 0, \quad Z = 0, \quad (3.40)$$

while the initial material basis is given by

$$\begin{Bmatrix} \mathbf{e}_1 \\ \mathbf{e}_2 \\ \mathbf{e}_3 \end{Bmatrix} = \begin{bmatrix} 1 & 0 & 0 \\ 0 & 0 & -1 \\ 0 & 1 & 0 \end{bmatrix} \begin{Bmatrix} \mathbf{E}_1 \\ \mathbf{E}_2 \\ \mathbf{E}_3 \end{Bmatrix}, \quad (3.41)$$

which corresponds to Euler angles of $(\phi, \theta, \psi) = (0, 0, -\pi/2)$. The force and moment at the start of the rod required to maintain the deformed Möbius strip are not known *a priori*, however, and must be determined. This means that this is a six parameter shooting problem (three components for the force and three for the moment). Thus six conditions are required at the end of the rod to complete the boundary value problem and use the shooting technique. Since the deformed Möbius strip is continuous, the end of the rod is located at the same point as the start coordinates which furnishes three conditions, i.e.

$$X_{end} = 0, \quad Y_{end} = 0, \quad Z_{end} = 0. \quad (3.42)$$

The remaining condition comes from the fact that the cross section at the end of the rod is rotated 180° about the centerline with respect to the orientation of the initial cross section at the start of the rod. This fact requires that

$$\begin{Bmatrix} \mathbf{e}_1 \\ \mathbf{e}_2 \\ \mathbf{e}_3 \end{Bmatrix} = \begin{bmatrix} 1 & 0 & 0 \\ 0 & 0 & 1 \\ 0 & -1 & 0 \end{bmatrix} \begin{Bmatrix} \mathbf{E}_1 \\ \mathbf{E}_2 \\ \mathbf{E}_3 \end{Bmatrix} \quad (3.43)$$

at the end of rod which corresponds to Euler angles of $(\phi, \theta, \psi) = (0, 0, \pi/2)$. (Thus the π radians angular difference between the cross sections at the

start and end of the rod is accounted for by a $\pi/2$ rotation at the start of the rod about the \mathbf{E}_1 axis and another $\pi/2$ at the other end.) These are the six known boundary conditions which are required to use the shooting technique described previously.

Mahadevan and Keller (1993) have recently investigated this problem and presented numerical results for various aspect ratios of the cross section. An analytical solution available for rods with square cross sections (aspect ratio = 1) was used as the starting point for a continuation scheme to obtain the results for higher aspect ratios.

A rod 2π meters long with a constant thickness was used which has its width varied to produce aspect ratios in the range from 1 to 10. Figure 3.14 shows the geometry of the centerline obtained using the current approach while Figure 3.15 shows a three-dimensional view of the deformed configurations. These results for the centerline are in close agreement with the graphical results presented by Mahadevan and Keller (1993). For an aspect ratio of one, the deformed shape of the centerline is circular and remains planar. As the aspect ratio is increased, the centerline deforms more out of the initial \mathbf{E}_2 - \mathbf{E}_1 plane and loses its circular shape as shown in Figures 3.14b-c. For very large aspect ratios, Mahadevan and Keller (1993) demonstrated that the centerline approached a limiting shape which was nearly indistinguishable from the results for an aspect ratio of ten. As a result, higher aspect ratios were not investigated here.

When a square cross section is used (aspect ratio = 1), the flexural rigidities EI_2 and EI_3 are equal. The rod is therefore considered to be transversely isotropic in the present theory and as a result κ_1 should remain constant. At any other aspect ratio, however, the rod is transversely orthotropic and κ_1 need not remain constant. This behavior is evident in Figure 3.16 which shows the variation of κ_1 along the rod as a function of the aspect ratio. Figure 3.17 shows the variation of the energy integral along the rod for various aspect ratios. As before, these results show excellent consistency for each aspect ratio considered.

Since these problems are geometrically nonlinear, it is possible to have more than one solution which satisfies all of the given boundary conditions. In the context of the Möbius strip problem, each of the multiple solutions (if they exist) would have to satisfy the conditions specified in equations (3.40)-(3.43). In order to find these multiple solutions using the present numerical technique it is therefore necessary to change the initial estimates of the unknown force and moment components. If these new initial estimates are "close" enough

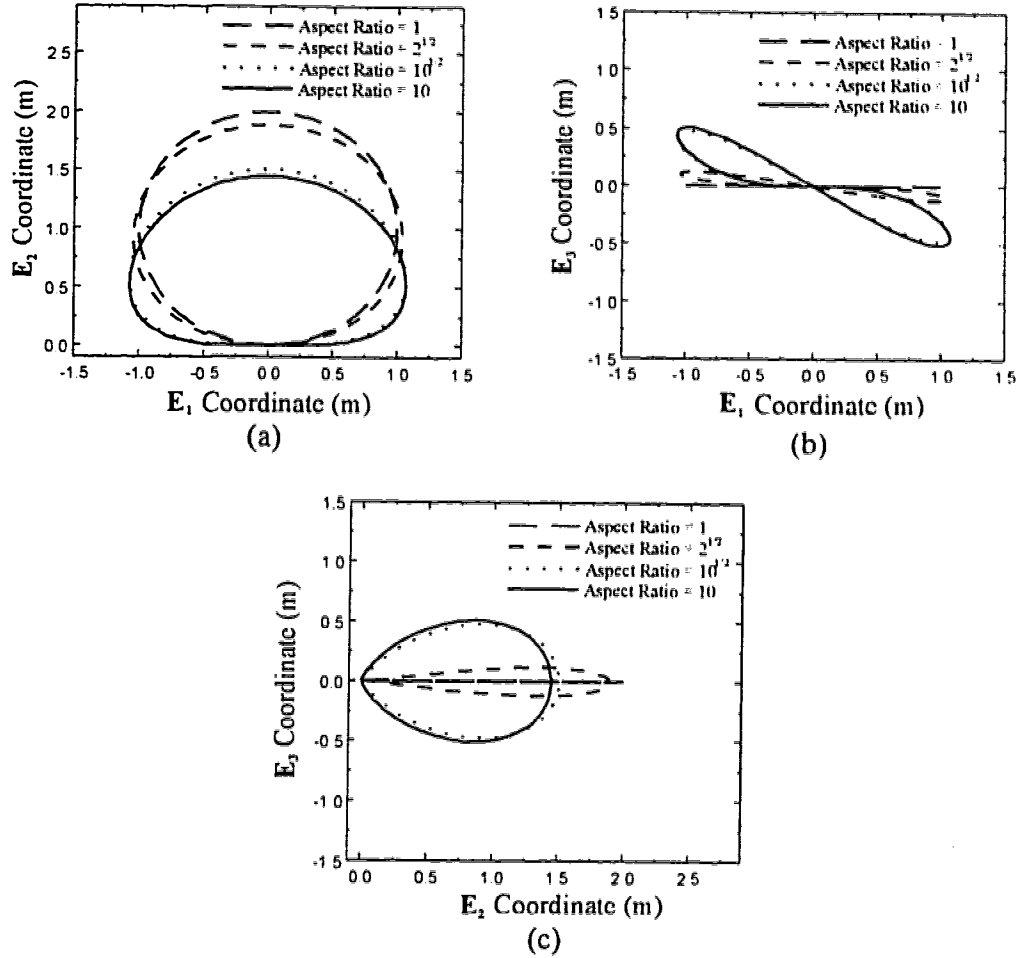
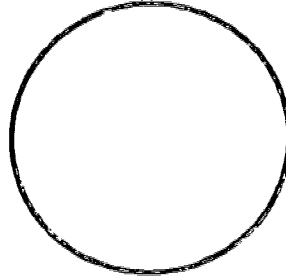


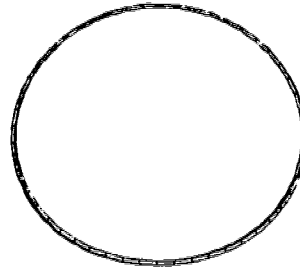
Figure 3.14: Geometry of Möbius Strip Centerline for Various Aspect Ratios: (a) E_1 - E_2 Plane, (b) E_1 - E_3 Plane, (c) E_2 - E_3 Plane

to another solution (if it exists), the numerical procedure may converge to that solution. To demonstrate this idea a rod with an aspect ratio of $\sqrt{2}$ was reconsidered. Figures 3.18 and 3.19 show a particular solution which satisfies the required boundary conditions (i.e. equations (3.40)-(3.43)) for this rod. This solution is different from the solution presented previously for a rod with an aspect ratio of $\sqrt{2}$. In this case, the rod has undergone a 540° rotation about the centerline rather than a 180° rotation as before. Of particular interest here is the fact that the twist remains constant in this

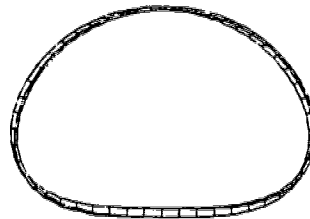
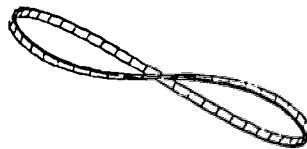
Aspect Ratio = 1



Aspect Ratio = $2^{1/2}$



Aspect Ratio = $10^{1/2}$



Aspect Ratio = 10

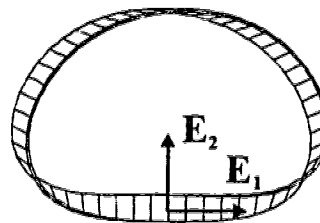
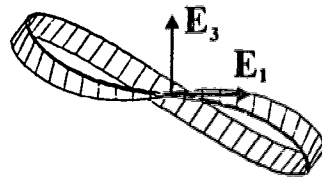


Figure 3.15: Three-Dimensional Views of Deformed Möbius Strip for Various Aspect Ratios

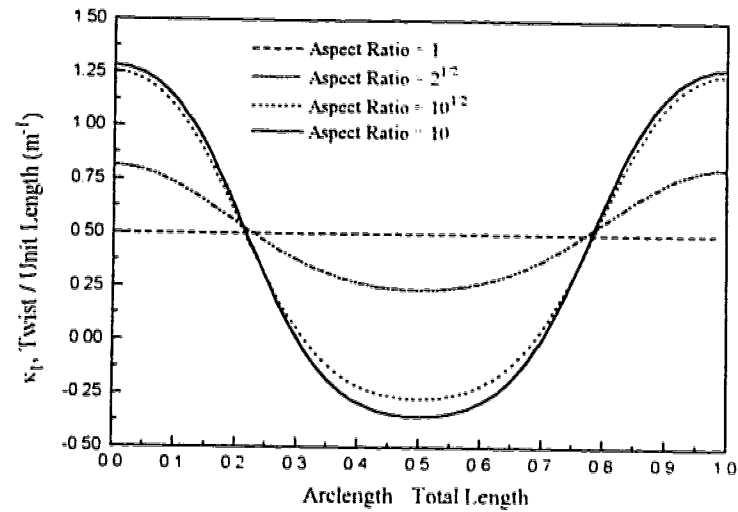


Figure 3.16: Variation of κ_1 Along the Deformed Möbius Strip as a Function of Aspect Ratio

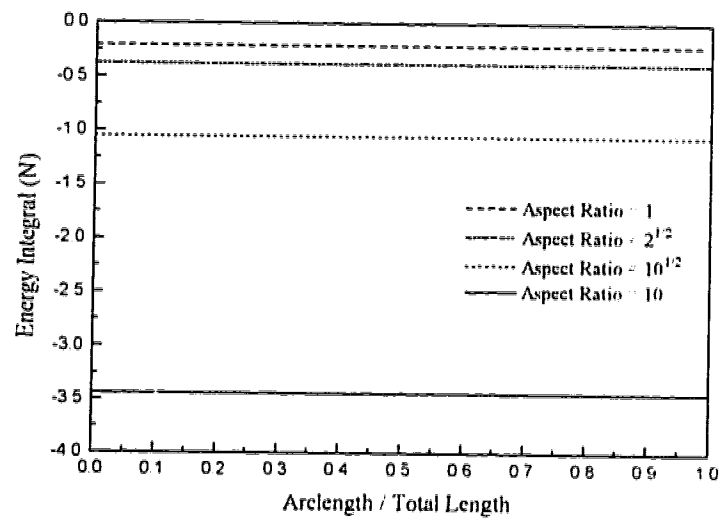


Figure 3.17: Variation of the Energy Integral Along the Deformed Möbius Strip as a Function of Aspect Ratio

solution while it varied in the previous case (see Figure 3.20).

The results shown for the multiple solutions to the Möbius strip problem are not exhaustive. They are included here only to demonstrate that multiple solutions may exist for these nonlinear problems and that the present numerical technique is well suited to finding them when they exist.

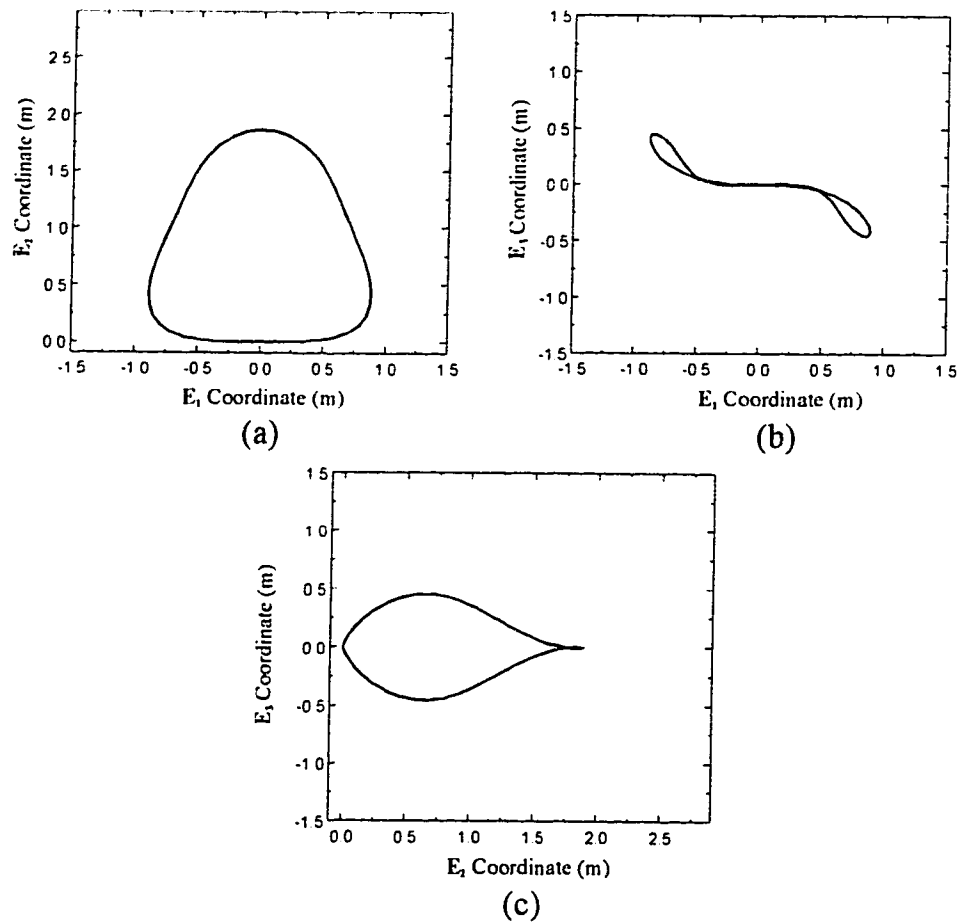


Figure 3.18: Geometry of Möbius Strip Centerline: (a) E_1 - E_2 Plane, (b) E_1 - E_3 Plane, (c) E_2 - E_3 Plane

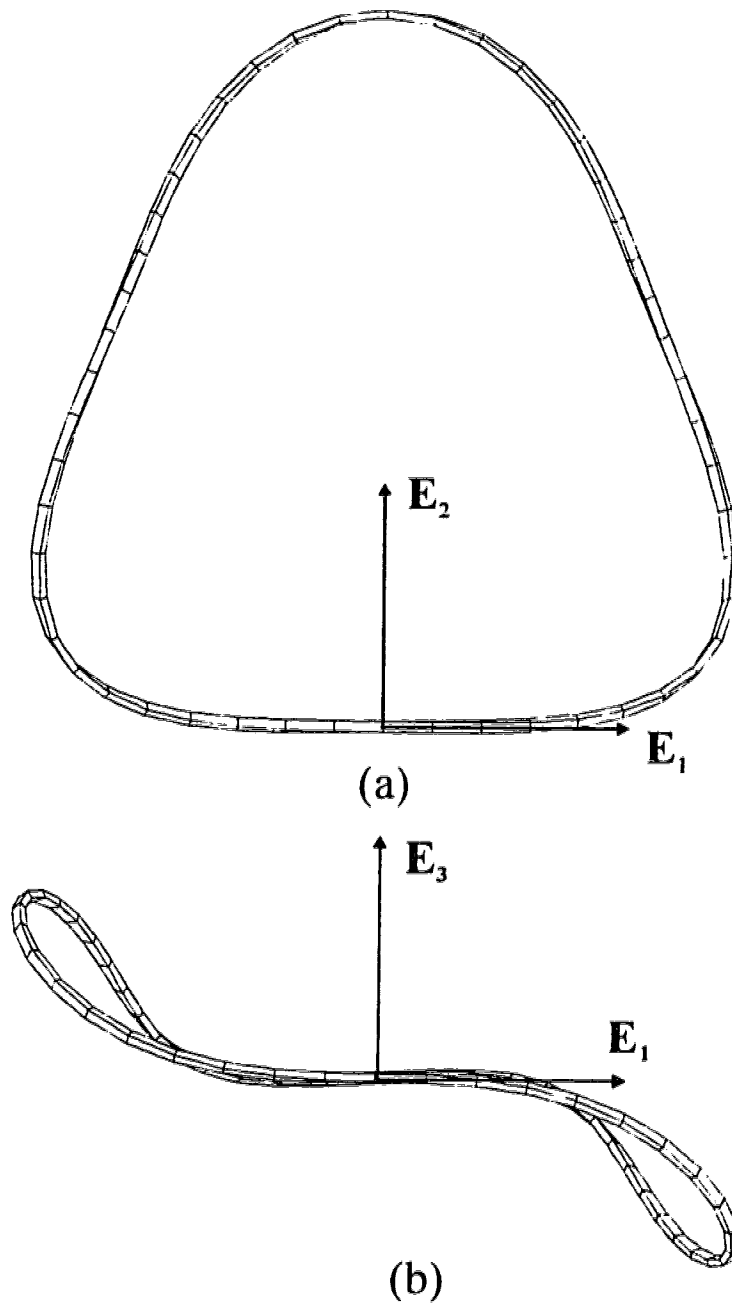


Figure 3.19: Three-Dimensional Views of Möbius Strip Solutions: (a) E_1 - E_2 Plane, (b) E_1 - E_3 Plane

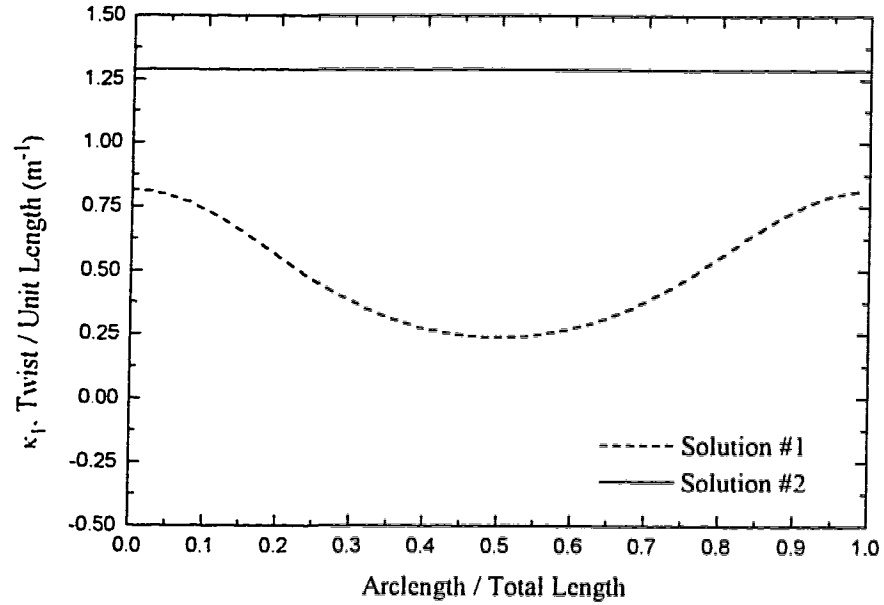


Figure 3.20: Variation of κ_1 Along the Deformed Möbius Strip

3.2.1.4 Initially Straight Cantilever Beam Loaded in a Non-Principal Direction By a Dead Tip Load

The final problem considered involving initially straight rods is the case in which a cantilever beam is loaded by a dead tip load in a non-principal direction. This problem has been considered both experimentally and theoretically by Dowell et al. (1977). In their experimental investigation, a 20 inch long beam of 7075 aluminum with a $1/2 \times 1/8$ inch cross section was loaded by dead tip loads at various angles relative to the principal directions as shown in Figure 3.21. The angle θ was varied from 0° to 90° in 15° increments. At each θ , dead tip loads were applied and the deflections v and w were measured in the chordwise (stiffer) and flap (more flexible) directions respectively. The geometric twist angle $\tilde{\phi}$ was also measured which Dowell et al. (1977) define as

...the angle determined by the projection of the elastic axis and leading edge of the cross-section at the beam tip on a plane perpendicular to the undeformed cross section.

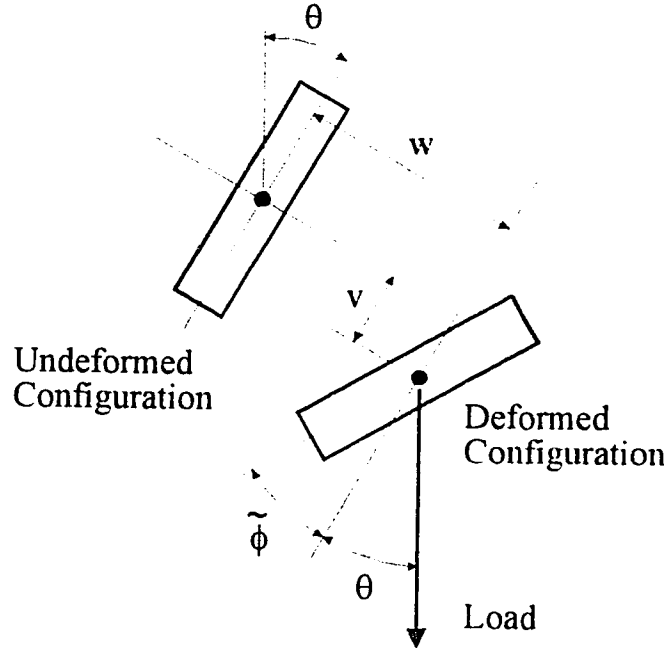


Figure 3.21: Cantilever Beam Loaded at Various Angles To Principal Directions

Dowell et al. (1977) give an expression for $\tilde{\phi}$ at the tip of the beam as

$$\tilde{\phi} = \phi + \int_0^L v' w'' dx \quad (3.44)$$

where ϕ is the angle of twist measured relative to the deformed central axis (equivalent to κ_1). $\tilde{\phi}$ is used (instead of ϕ) to measure the overall effect of twist along the beam since the large deflections which occur make ϕ itself difficult to measure.

To start the current numerical procedure, the global basis for each θ is chosen to be aligned with the initial tangent vector and the principal directions such that

$$\mathbf{E}_i = \mathbf{e}_i \quad (3.45)$$

while the starting coordinates of the centerline are

$$X = 0, \quad Y = 0, \quad Z = 0. \quad (3.46)$$

In the material basis, the components of the force vector become

$$\begin{aligned} F_1 &= 0, \\ F_2 &= -P \cos \theta, \\ F_3 &= -P \sin \theta, \end{aligned} \tag{3.47}$$

where only the tip load has been considered. However, this ignores the weight of the beam. The weight may be easily taken into account with the present numerical method by replacing equation (3.47) with

$$\begin{aligned} F_1 &= 0, \\ F_2 &= -(P + wL) \cos \theta, \\ F_3 &= -(P + wL) \sin \theta, \end{aligned} \tag{3.48}$$

where w is the weight per unit length and L is the overall length of the beam. Whether or not the weight of the beam is included, the components for the moment are all unknown. As a result this is a three parameter shooting problem⁴.

The results using the current numerical technique are shown in Table 3.1. The results for the geometric twist angle $\tilde{\phi}$ shown for the current procedure were obtained using equation (3.44). As can be seen, there is very good agreement with the experimental results of Dowell et al. for all of the values of θ considered. When $\theta = 0^\circ$ or $\theta = 90^\circ$ no twist was observed experimentally as is expected since in these cases the loading is about one of the principal axes. For the other values of θ considered, the chordwise deflections are all very near the lower range of the experimental values reported while the flap deflections and geometric twist angle consistently fall within the experimental ranges given. The results including the weight of the beam are also in slightly better agreement with the observed experimental behavior than are those which ignore the weight of the beam.

⁴Note that since there must be no moment component about the vertical axis, a relationship between M_2 and M_3 could have been obtained which would reduce this to a two parameter shooting problem. Either method will produce the desired results.

Table 3.1: Flap (w) and Chordwise (v) Deflections For a Uniform Cantilever Beam Loaded in Various Non-Principal Directions

Horizontal Cantilever ($\theta = 15^\circ$) w,v - inches, $\tilde{\phi}$ - degrees									
Load (lbs)	Weight Neglected			Weight Included			Experimental		
	w	v	$\tilde{\phi}$	w	v	$\tilde{\phi}$	w	v	$\tilde{\phi}$
1	0.80	0.19	0.2	0.84	0.20	0.2	0.75 - 1.00	0.19 - 0.20	0.1 - 1.2
2	1.62	0.38	0.9	1.66	0.39	0.9	1.5 - 1.75	0.40 - 0.41	0.6 - 1.7
3	2.48	0.60	2.0	2.53	0.61	2.1	2.5 - 2.75	0.64 - 0.65	2.2 - 2.5
4			3.8			3.8			3.5 - 4.1
Horizontal Cantilever ($\theta = 30^\circ$)									
1	1.54	0.17	0.4	1.61	0.18	0.4	1.50 - 1.75	0.19 - 0.20	0.3 - 0.8
2	3.06	0.37	1.5	3.14	0.38	1.5	3.0 - 3.25	0.40 - 0.43	1.5 - 1.9
3	4.55	0.61	3.3	4.62	0.62	3.4	4.5 - 4.75	0.64 - 0.69	3.3 - 3.7
4			5.9			6.0			5.7 - 6.5
Horizontal Cantilever ($\theta = 45^\circ$)									
1	2.16	0.14	0.4	2.26	0.15	0.5	2.25 - 2.50	0.15 - 0.25	0.3 - 0.7
2	4.21	0.32	1.7	4.30	0.33	1.7	4.25 - 4.50	0.33 - 0.38	1.6 - 2.0
3	6.06	0.56	3.6	6.14	0.57	3.7	6.0 - 6.25	0.60 - 0.63	3.5 - 3.8
Horizontal Cantilever ($\theta = 60^\circ$)									
0.5			0.1			0.1			0.1 - 0.2
1.0	2.63	0.10	0.4	2.75	0.11	0.4	2.50 - 2.75	0.11 - 0.14	0.1 - 0.5
1.5			0.8			0.8			0.7 - 1.0
2.0	5.02	0.24	1.4	5.13	0.25	1.4	5.00 - 5.25	0.27 - 0.29	1.4 - 1.6
Horizontal Cantilever ($\theta = 75^\circ$)									
0.5			0.05			0.06			0.01 - 0.16
1.0	2.92	0.05	0.21	3.05	0.06	0.22	2.75 - 3.25	0.05 - 0.17	0.20 - 0.37
1.5			0.46			0.48			0.52 - 0.60

3.2.2 Initially Curved Rods

3.2.2.1 Initially Helical Orthotropic Rod Bent and Twisted Into Another Helix

Section 3.2.1.2 dealt with the problem in which an initially straight orthotropic rod is bent and twisted into a helix. This section discusses the related problem in which an orthotropic rod, already helical in its undeformed state, is bent and twisted into another helix. Faulkner and Steigmann (1993) have considered this class of problems and have demonstrated that this is the most general statically controllable deformation possible for inextensible elastic rods⁵. As discussed in section 3.2.1.2, the initial twist per unit length along the rod, κ_1^0 , is equal to the geometric torsion defined in (3.35a). As well, the initial curvature of the centerline, κ_c^0 , is given by (3.35b). These are required so that the deformation can be maintained by end forces and moments alone. Faulkner and Steigmann (1993) show that the moment ($\mathbf{M} = M_i \mathbf{e}_i$) and force ($\mathbf{F} = F_i \mathbf{e}_i$) necessary to maintain a deformation in which this initially helical rod is bent and twisted into another helix (subjected to the same restrictions regarding the twist per unit length κ_1) are given by

$$\begin{aligned} M_1 &= GJ (\tau - \tau^0), \\ M_2 &= 0, \\ M_3 &= EI_3 (\kappa_c - \kappa_c^0), \end{aligned} \tag{3.49}$$

and

$$\begin{aligned} F_1 &= (\tau - \tau^0) \left[GJ (\tau - \tau^0) - EI_3 (\kappa_c - \kappa_c^0) \frac{\tau}{\kappa_c} \right], \\ F_2 &= 0, \\ F_3 &= (\tau - \tau^0) \left[GJ (\tau - \tau^0) \frac{\kappa_c}{\tau} - EI_3 (\kappa_c - \kappa_c^0) \right], \end{aligned} \tag{3.50}$$

where

$$\begin{aligned} \kappa_c &= \sqrt{\kappa_2^2 + \kappa_3^2}, \\ \kappa_c^0 &= \sqrt{(\kappa_2^0)^2 + (\kappa_3^0)^2}. \end{aligned} \tag{3.51}$$

⁵In the case of orthotropic rods, a restriction is that all of the bending must be about only one principal direction in the cross section. This implies that for both the initial and deformed helices, the twist per unit length along the rod be equal to the geometric torsion of the centerline (as discussed in section 3.2.1.2).

These results assume that all the bending is around the \mathbf{e}_3 axis throughout the entire rod⁶. Note that if the rod were initially straight ($\tau^0 = 0$, $\kappa_c^0 = 0$) equations (3.49) and (3.50) reduce to equations (3.38) and (3.39) respectively.

To begin the numerical procedure, a rod with an initial helical shape is chosen by specifying R^0 and α^0 . These values thus determine the initial centerline curvature and torsion of the undeformed helix. This rod will then be deformed into another helix with another specified R and α . As before, the starting coordinates in the global basis are therefore given by

$$X = R, \quad Y = 0, \quad Z = 0, \quad (3.52)$$

while the initial material basis is again given by

$$\begin{Bmatrix} \mathbf{e}_1 \\ \mathbf{e}_2 \\ \mathbf{e}_3 \end{Bmatrix} = \begin{bmatrix} 0 & \cos \alpha & \sin \alpha \\ 1 & 0 & 0 \\ 0 & \sin \alpha & -\cos \alpha \end{bmatrix} \begin{Bmatrix} \mathbf{E}_1 \\ \mathbf{E}_2 \\ \mathbf{E}_3 \end{Bmatrix}. \quad (3.53)$$

Note that all of the conditions at the start of the rod are completely determined so that shooting will not be required.

To compare numerical and analytical results, a steel rod with an aspect ratio of ten and an initial helical shape ($R^0 = 0.05$ m, $\alpha^0 = 45^\circ$) is chosen. This rod is then deformed into another helix with a radius selected to be 0.1m while maintaining the initial pitch angle of 45° . Figure 3.22 shows both the numerical and analytical results for the geometry of the deformed shape. As can be seen, there is once again excellent agreement with no noticeable difference between the two solutions.

Figures 3.23 and 3.24 show the twist per unit length and the energy integral respectively along the rod for this particular deformation. κ_1 remains constant at 5 m^{-1} which is the expected value for this case from equation (3.35a). The energy integral also shows excellent consistency with no noticeable variation from the initial value.

Similar results (not shown) were found for the same initial helix deformed into a variety of other helices. In all cases investigated there was again excellent agreement between numerical and analytical results for the geometry of the deformed helix as well as in the values obtained for κ_1 and the energy

⁶Note that it would also be possible to have all bending about the \mathbf{e}_2 axis instead. In that case, $F_3 = 0$ and $M_3 = 0$ while F_2 and M_2 would be nonzero. Bending about the \mathbf{e}_3 axis is chosen here to maintain some consistency with results for helices presented previously.

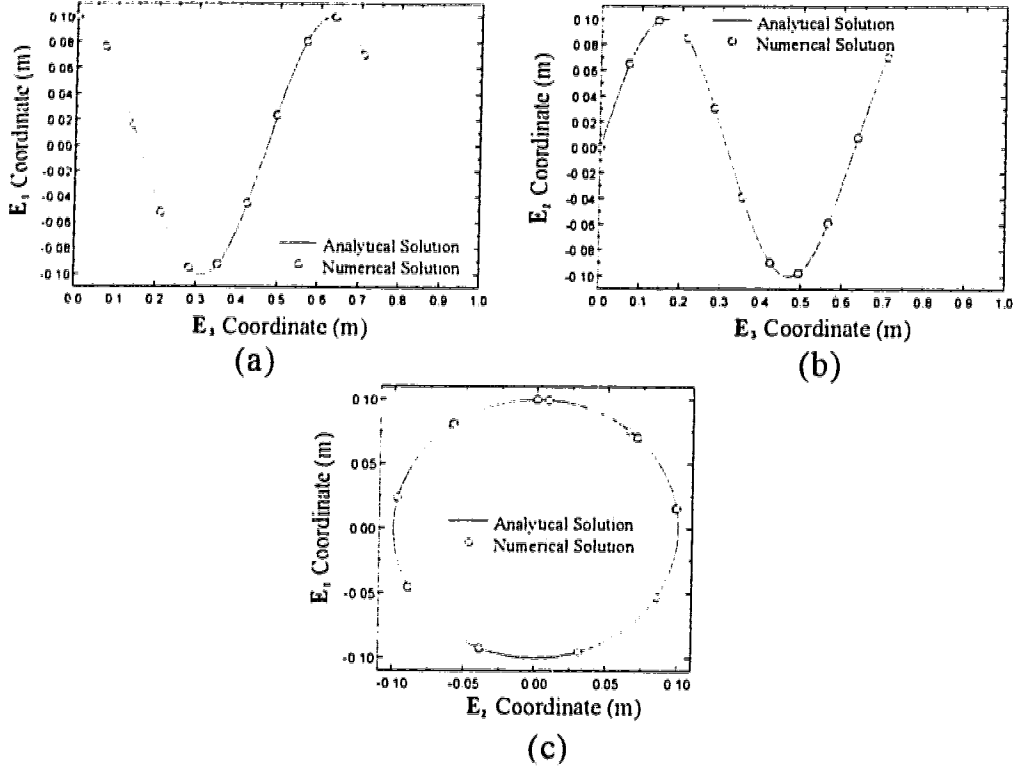


Figure 3.22: Geometry of Deformed Helix Centerline. $R = 0.1\text{m}$. $\alpha = 45^\circ$. Aspect Ratio = 10: (a) E_3 - E_1 Plane, (b) E_3 - E_2 Plane, (c) E_2 - E_1 Plane

integral. Of particular interest is the special case in which the final deformed helix is a straight rod with no twist for which both the curvature and the torsion are zero. Figure 3.25 shows the initial and final geometries which result. Note that this is essentially the inverse problem of the straight rod deformed into a helix shown in Figure 3.9. In the former case, both forces and moments are required to maintain the deformed configuration. In the present case, no forces are necessary while the moments required are equal and opposite to those in the former case.

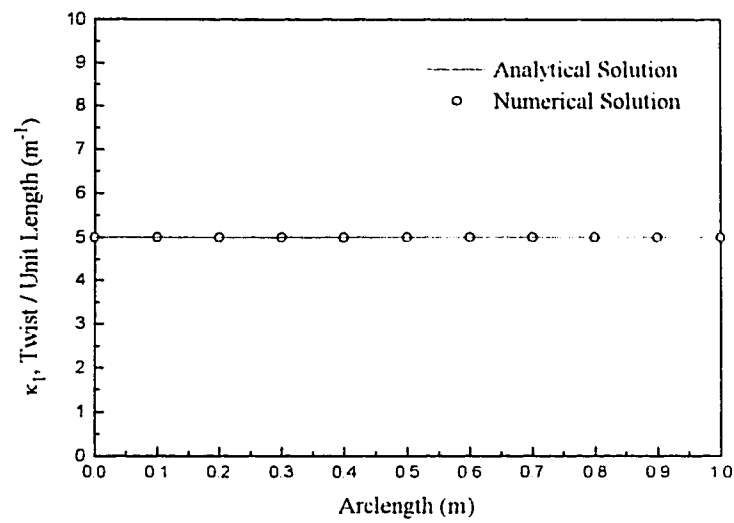


Figure 3.23: Twist/Unit Length (κ_1) Along Deformed Helix

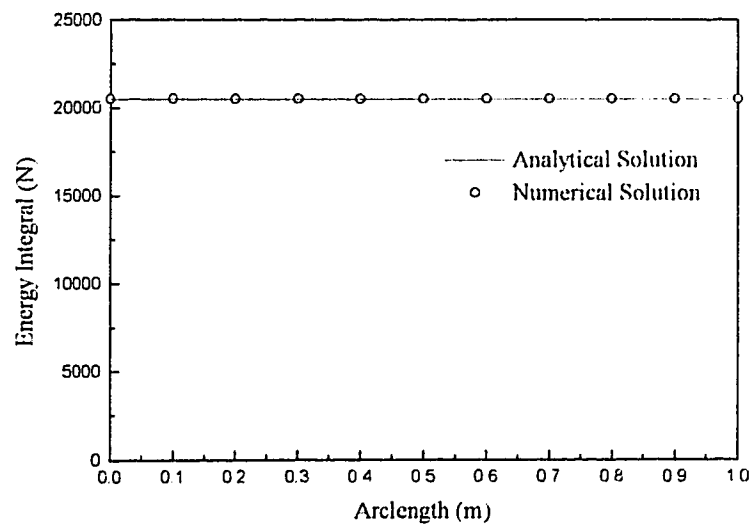
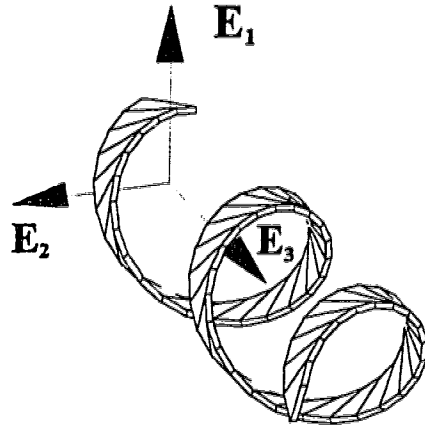
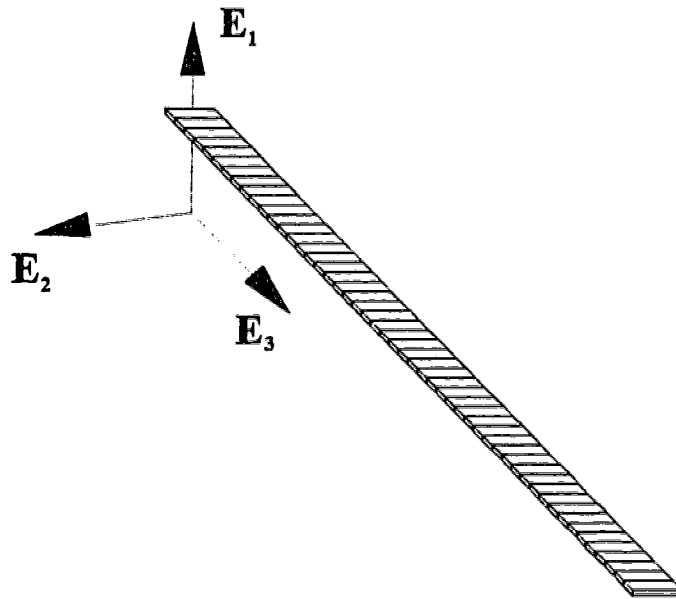


Figure 3.24: Energy Integral Along Deformed Helix



(a)



(b)

Figure 3.25: Initial Orthotropic Helix Deformed Into a Straight Rod: (a) Undeformed Helix, (b) Deformed Configuration

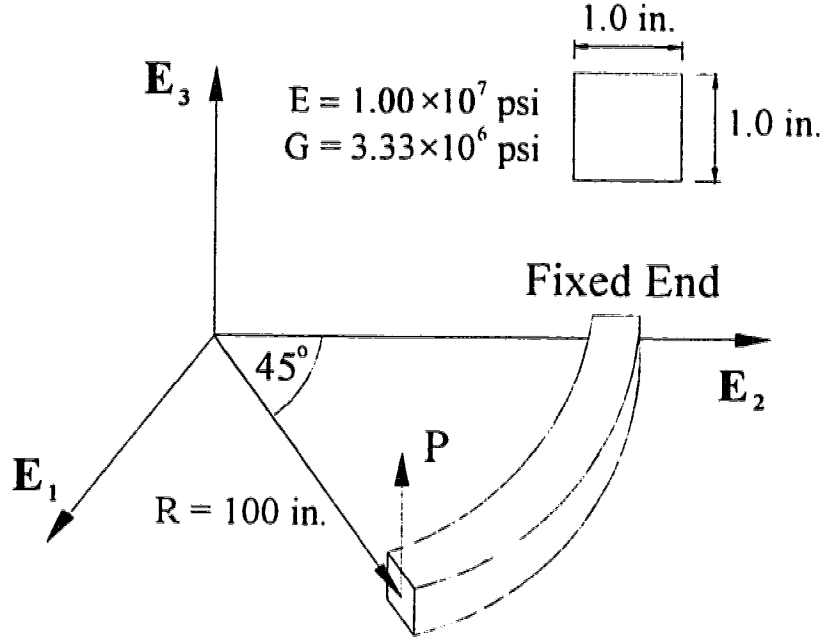


Figure 3.26: Initially Curved Cantilever Beam Loaded Out of the Plane of Initial Curvature

3.2.2.2 Initially Curved Cantilever Loaded Out of the Initial Plane of Curvature by a Dead Tip Load

The final problem considered is that in which an initially curved cantilever beam is acted upon by a dead tip load out of the plane of initial curvature as shown in Figure 3.26. The numerical procedure is started at the fixed end of the beam where the global coordinates are

$$X = 0, \quad Y = 100 \text{ in}, \quad Z = 0. \quad (3.54)$$

and the initial material basis is given by

$$\begin{Bmatrix} \mathbf{e}_1 \\ \mathbf{e}_2 \\ \mathbf{e}_3 \end{Bmatrix} = \begin{bmatrix} 1 & 0 & 0 \\ 0 & 0 & 1 \\ 0 & -1 & 0 \end{bmatrix} \begin{Bmatrix} \mathbf{E}_1 \\ \mathbf{E}_2 \\ \mathbf{E}_3 \end{Bmatrix}. \quad (3.55)$$

The initial forces are therefore given by

$$\begin{aligned} F_1 &= 0, \\ F_2 &= -P, \\ F_3 &= 0. \end{aligned} \tag{3.56}$$

while the moment components at the start of the rod are

$$\begin{aligned} M_1 &= \text{unknown}, \\ M_2 &= 0, \\ M_3 &= \text{unknown}. \end{aligned} \tag{3.57}$$

The M_1 and M_3 components are unknown since these will depend on the resulting deflection once the load is specified. $M_2 = 0$ since the load is acting in the initial \mathbf{e}_2 direction and no moment will be produced about this axis. This problem is therefore a two parameter shooting problem. At the other end of the rod, the two corresponding known boundary conditions arise from the fact that this is a free end and therefore the M_1 and M_3 components must vanish.

Table 3.2 shows the predicted coordinates of the tip of the cantilever for various dimensionless loads k where

$$k = \frac{PR^2}{EI} \tag{3.58}$$

and $El_2 = El_3 = EI$. These values show excellent agreement with those reported by Surana and Sorem (1989) where a nonlinear finite element procedure was used.

To consider a more complicated loading condition and to demonstrate the suitability of the numerical procedure for dealing with such a load, the tip load in Figure 3.26 was replaced with dead uniform distributed load acting in the same plane. Table 3.3 shows the results for various k_d values where

$$k_d = \frac{wR^3}{EI} \tag{3.59}$$

and w is the magnitude of the distributed load. Note that a comparison with previous solutions was not possible in this case since no other solutions to this particular problem were found in the literature. Also note that for all the loads considered in this section (both tip loads and uniform distributed loads) the energy integral was once again found to show excellent consistency with no noticeable variation to at least seven significant figures.

Table 3.2: Geometry at the End of a Curved Cantilever Under the Action of a Dead Tip Load

k	Current Method			Surana and Sorem (1989)		
	E_1 (in.)	E_2 (in.)	E_3 (in.)	E_1 (in.)	E_2 (in.)	E_3 (in.)
1.0	69.1362	71.6529	15.2722	69.1975	71.6195	15.0119
2.0	65.4006	73.8728	27.5836	65.5727	73.7796	27.2169
3.0	61.0592	76.4225	36.4615	61.3109	76.2900	36.1061
4.0	56.9396	78.8072	42.7314	57.2323	78.6598	42.4276
5.0	53.2915	80.8861	47.2451	53.6011	80.7386	46.9963
6.0	50.1288	82.6567	50.5950	50.4428	82.5185	50.3935
7.0	47.3945	84.1679	53.1595	47.7069	84.0353	52.9962
8.0	45.0206	85.4561	55.1786	45.3285	85.3319	55.0458
9.0	42.9451	86.5639	56.8080	43.2471	86.4472	56.6994
10.0	41.1167	87.5240	58.1511	41.4120	87.4136	58.0621
11.0	39.4935	88.3625	59.2787	39.7818	88.2572	59.2056
12.0	38.0422	89.1002	60.2404	38.3233	88.9990	60.1806
13.0	36.7359	89.7536	61.0719	37.0097	89.6557	61.0232
14.0	35.5530	90.3359	61.7994	35.8195	90.2407	61.7600
15.0	34.4758	90.8580	62.4427	34.7351	90.7649	62.4112

Table 3.3: Geometry at the End of a Curved Cantilever Under the Action of a Dead Uniform Distributed Load

k_d	\mathbf{E}_1 (in.)	\mathbf{E}_2 (in.)	\mathbf{E}_3 (in.)
1.0	70.5656	70.7751	4.6391
2.0	70.1384	70.9649	9.1990
3.0	69.4515	71.2698	13.6082
4.0	68.5387	71.6746	17.8090
5.0	67.4398	72.1613	21.7603
6.0	66.1964	72.7111	25.4381
7.0	64.8482	73.3063	28.8330
8.0	63.4307	73.9303	31.9474
9.0	61.9738	74.5716	34.7920
10.0	60.5020	75.2177	37.3826
11.0	59.0343	75.8606	39.7381
12.0	57.5852	76.4940	41.8786
13.0	56.1654	77.1135	43.8238
14.0	54.7824	77.7156	45.5930
15.0	53.4411	78.2985	47.2038

Chapter 4

Multiple Solutions For Cantilever Beams Under Dead Loads

In the previous chapter a numerical solution of the nonlinear equilibrium equations governing the three-dimensional deformations of rods was developed and presented. The two point boundary value problem was solved by using an initial value approach coupled with an iterative shooting technique to ensure that the required boundary conditions at the end of the rod are satisfied. This procedure was combined with a method of considering the rod as a number of segments which are assembled in such a way as to maintain continuity and compatibility. Numerical results for several problems were obtained and compared with previous analytical, numerical or experimental solutions to verify the current numerical results. Further, the suitability of the shooting procedure to finding multiple equilibrium solutions, when they exist, was shown.

In this chapter the numerical procedure previously developed is used to investigate the problem in which a cantilever beam is loaded by dead tip and uniform distributed loads (Raboud et al. 1996a). Previous authors (Navaee and Elling 1991, 1992) have detailed the development and geometry of multiple planar equilibrium shapes as the load is increased. It is interesting to note that in their experimental verification of these multiple shapes (which used orthotropic rods), it was difficult to maintain some of the planar shapes as the rod had a tendency to twist out of the plane. This suggests that the full three-dimensional problem needs to be considered.

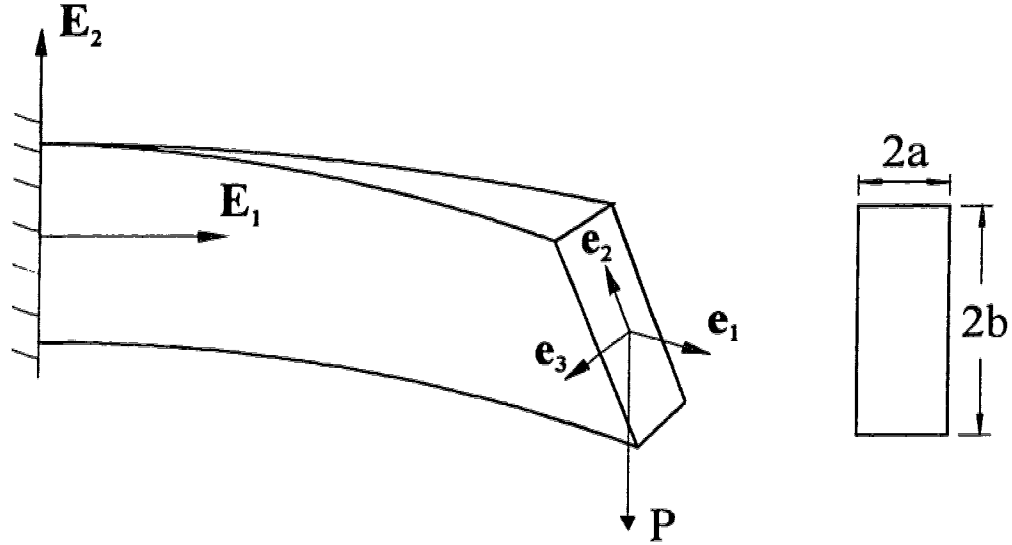


Figure 4.1: Cantilever Beam With Dead Tip Load, P

The problem of the buckling of a deep cantilever beam (ie: an orthotropic rod) due to tip loading has been considered by Hodges and Peters (1975). In particular, they consider the loads necessary for out-of-plane buckling for rods with rectangular cross sections and various width to height (aspect) ratios. The analysis does not provide the post-buckled shapes but considers only the loading necessary to maintain the deformed shape.

The problem considered is the deformation of a cantilever beam due to a dead tip load as shown in Figure 4.1. The cross section is rectangular with an aspect ratio a/b . In the undeformed configuration the longitudinal axis of the beam is aligned with the global \mathbf{E}_1 axis while the principal directions of the cross section are in the \mathbf{E}_2 and \mathbf{E}_3 directions. The load P is applied in the negative \mathbf{E}_2 direction. The numerical procedure is begun at the fixed end of the beam with the initial geometry and orientation given by

$$X = 0, \quad Y = 0, \quad Z = 0, \quad (4.1)$$

and

$$\begin{aligned} \mathbf{e}_1 &= \mathbf{E}_1, \\ \mathbf{e}_2 &= \mathbf{E}_2, \\ \mathbf{e}_3 &= \mathbf{E}_3. \end{aligned} \quad (4.2)$$

respectively, while the force and moment components are

$$\begin{aligned} F_1 &= 0, \\ F_2 &= P, \\ F_3 &= 0, \end{aligned} \tag{4.3}$$

and

$$\begin{aligned} M_1 &= \text{unknown}, \\ M_2 &= 0, \\ M_3 &= \text{unknown}. \end{aligned} \tag{4.4}$$

This is therefore a two parameter shooting problem with the M_1 and M_3 components of the moment at the fixed end of the beam unknown. (Note that planar deformations correspond to the situation in which the initial M_1 component is set to zero). The corresponding known conditions at the other end of the rod are that both M_1 and M_3 are zero at the free end¹.

4.1 Buckling of Planar Shapes

4.1.1 Development of Multiple Planar Shapes

For the case of planar deformations, it has been shown previously (Navace and Elling 1991, 1992; Faulkner et al. 1993) that for a tip load the number of equilibrium shapes is a function of the load parameter

$$\alpha = \sqrt{\frac{PL^2}{EI_3}}. \tag{4.5}$$

where P is the magnitude of the load and L is the length of the beam. The number of equilibrium shapes for various ranges of α is given Table 4.1.

¹Note that M_2 must also be zero at the free end. However, this particular loading combined with the initial values at the fixed end given by equations (4.1)-(4.4) will result in a moment at the free end with no component in the \mathbf{E}_2 direction for any initial M_1 or M_3 . Thus a relationship exists between the three moment components at the free end and care must be exercised when choosing which two to use as boundary conditions as not all combinations will work for all situations. For example, both M_1 and M_2 will remain zero at free end (and throughout the rod in fact) if the initial M_1 component is zero (since this corresponds to a planar deformation with no twist). The choice of M_1 and M_3 works for all the deformations discussed in this chapter.

Table 4.1: Number of Planar Equilibrium Solutions as a Function of the Load Parameter α

Load Parameter	# of Equilibrium Configurations
$0 < \alpha < 3.214$	1
$\alpha = 3.214$	2
$3.214 < \alpha < 7.142$	3
$\alpha = 7.142$	4
$7.412 < \alpha < 10.935$	5
\vdots	\vdots

When multiple shapes first develop (ie: at $\alpha = 3.214$) one additional shape is possible but this shape immediately splits into two as the load is increased above the bifurcation point. These bifurcation values and the corresponding shapes can be reproduced using the present numerical technique by setting $M_1 = 0$ at the fixed end of the beam to ensure planar deformations (which reduces the problem to a one parameter shooting problem). Figure 4.2 shows the deformed configurations for a one meter long beam corresponding to a load $\alpha = 3.214^2$. This figure shows the original equilibrium configuration (Shape #1) as well as the second configuration possible at this load (Shape #1a). Figure 4.3 shows the three resulting planar shapes corresponding to a load $\alpha = 5$. It can be seen how the second equilibrium configuration in Figure 4.2 (Shape #1a) bifurcates into two different shapes (Shapes #2 and #3 in Figure 4.3) as the load is increased. Note that these computed shapes show excellent agreement with previously published results.

The development of multiple solutions can also be seen in Figure 4.4 which shows the M_3 component at the fixed end required to maintain equilibrium as a function of the load parameter α . The M_3 component for Shape #1 begins at 0 at a load of $\alpha = 0$ and increases as the load is increased. This is the only solution which exists below $\alpha = 3.214$. At a load of $\alpha = 3.214$ a new equilibrium configuration exists as shown by the fact that a new curve begins at this point. As the load increases, this new solution bifurcates

²For these and all other numerical results generated by the numerical procedure in this chapter, the energy integral (equation (2.3)) was found to be constant in each case. Further, an overall equilibrium balance was observed in each case.

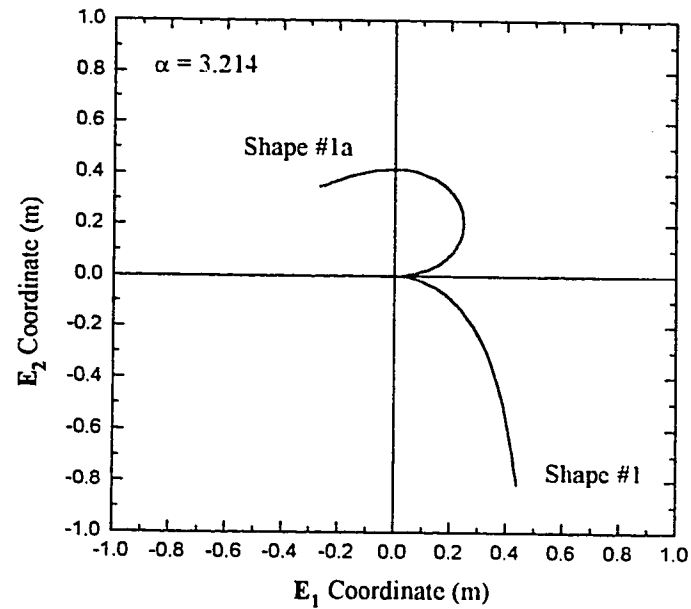


Figure 4.2: Planar Equilibrium Configurations Corresponding to $\alpha = 3.214$

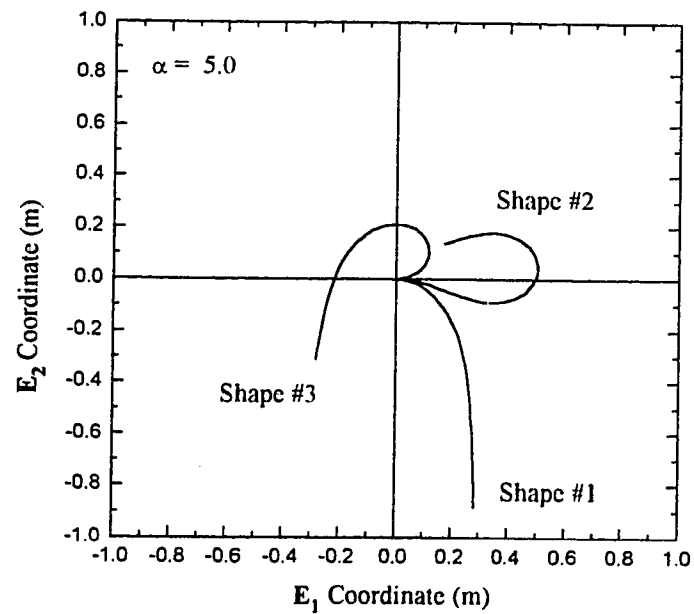


Figure 4.3: Planar Equilibrium Configurations Corresponding to $\alpha = 5.0$

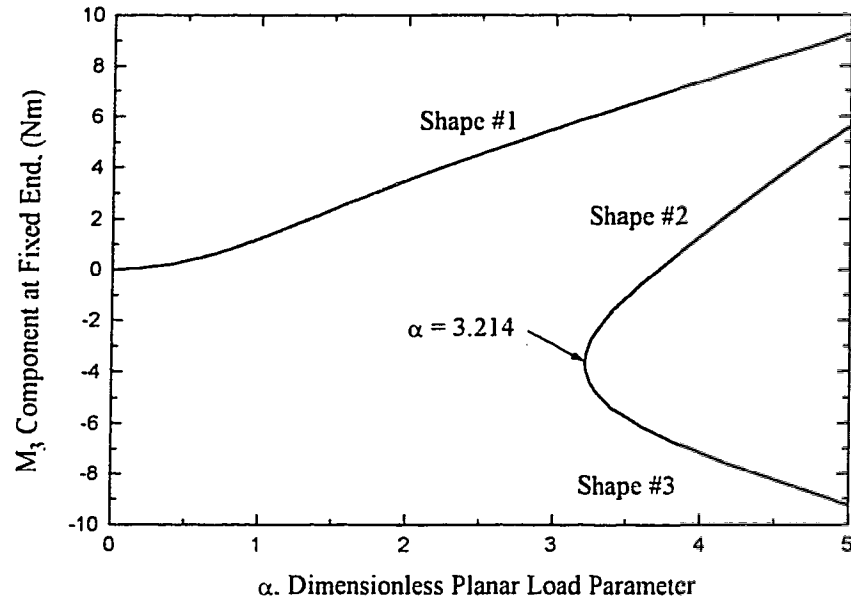


Figure 4.4: Fixed End Moment Component M_3 Required to Maintain Planar Equilibrium Configurations

into two shapes (Shape #2 and Shape #3) with distinct M_3 components required to maintain equilibrium. Note that the sign of the M_3 component only indicates whether the tip of the beam has a positive or negative E_1 coordinate. As the load is further increased, new equilibrium configurations (not shown here) would appear in the same manner. This type of figure will be useful in the following discussion of multiple three-dimensional solutions. In the three-dimensional case both M_1 and M_3 can be considered.

4.1.2 Buckling of Planar Shapes Out of the Plane

Hodges and Peters (1975) considered the problem in which a cantilever beam under the action of a dead tip load buckles out of the plane. (In what follows buckling is referred to as the transition from a planar equilibrium state to an infinitesimally nearby out-of-plane solution.) In particular, they used a perturbation approach and presented numerical results for the buckling loads as a function of the aspect ratio (a/b) of the cross section³. Using

³For their numerical values, Hodges and Peters (1975) considered materials with a Poisson's ratio $\nu = 0.3$.

the present technique with $M_1 \neq 0$ allows the determination of the buckling loads as shown in Figure 4.5 where the dimensionless loading parameter is given by

$$\beta = \frac{PL^2}{\sqrt{GJ} \times EI_2}. \quad (4.6)$$

(Note that this problem is a two parameter shooting problem, unlike the planar cases, since M_1 may now be non-zero and is unknown.) These results show excellent agreement with those of Hodges and Peters (1975). For example, when the results are extrapolated to an aspect ratio of zero (which is equivalent to ignoring the out-of-plane flexural rigidity of the rod), the dimensionless buckling load approaches

$$\beta_0 = 4.0126 \quad (4.7)$$

which is also the result given by Landau and Lifshitz (1970). Further, when the curve is extrapolated to the horizontal axis, the load increases without limit as the aspect ratio approaches 0.607 indicating that at higher aspect

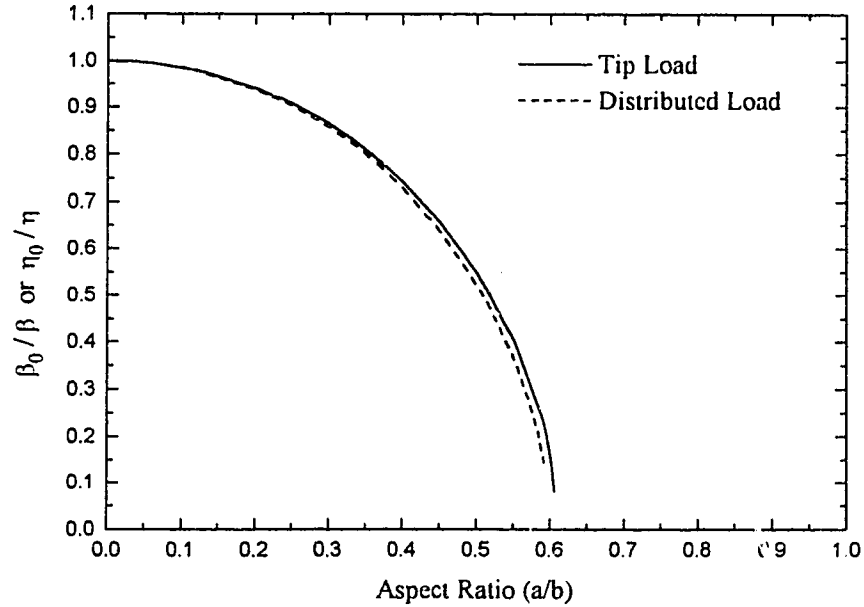


Figure 4.5: Dimensionless Buckling Loads as a Function of the Aspect Ratio for Dead Tip and Uniform Distributed Loads

ratios the rod does not have a perturbed out of the plane solution which agrees very closely with the results of Hodges and Peters (1975).

Figure 4.5 also shows the dimensionless loads which provide nearby out-of-plane equilibrium shapes if the tip load is replaced with a uniformly distributed dead load acting in the same plane. Again, as the aspect ratio approaches zero, the loading parameter approaches

$$\eta_0 = 12.85, \quad (4.8)$$

where

$$\eta = \frac{w_y L^3}{\sqrt{GJ \times EI_2}} \quad (4.9)$$

and w_y is the magnitude of the distributed load per unit length. It can be seen that the load rises indefinitely as the aspect ratio approaches 0.603. This illustrates that, relative to β_0 and η_0 , the buckling loads for the tip and uniformly distributed loads at any aspect ratio are close, but not identical, to each other. It is especially interesting that both cases have a very similar limit on the aspect ratio above which buckling will not occur despite being different loading conditions.

The results shown in Figure 4.5 for the distributed load case were verified experimentally using an aluminum cantilever beam with an aspect ratio of 0.260 loaded under its own weight. By varying the length, it was found that the beam buckled out of the plane between a length of 3.38 and 3.40 m. This agrees closely with the predicted length of 3.398 m.

The results of Hodges and Peters (1975) and those above in Figure 4.5 indicate only the loads at which out-of-plane deformations begin through the buckling of a planar equilibrium shape (Shape #1 as shown in Figures 4.2 and 4.3). However, as has been discussed previously, more than one planar equilibrium shape can exist for certain load ranges. The question naturally arises whether or not these other planar equilibrium configurations may also buckle out of the plane in a manner similar to the buckling behavior discussed so far. To illustrate, consider a cantilever with a tip load and an aspect ratio of 1/1.7. For this aspect ratio, out-of-plane buckling occurs for $\beta_0/\beta = 0.248$ or $\beta = 16.18$ (from Figure 4.5). Below this load only planar Shape #1 (Figure 4.3) exists and the M_1 component for equilibrium is therefore zero as shown in Figure 4.6. Increasing the load beyond this value results in the moment component M_1 increasing from zero as shown in Figure 4.6. (Recall

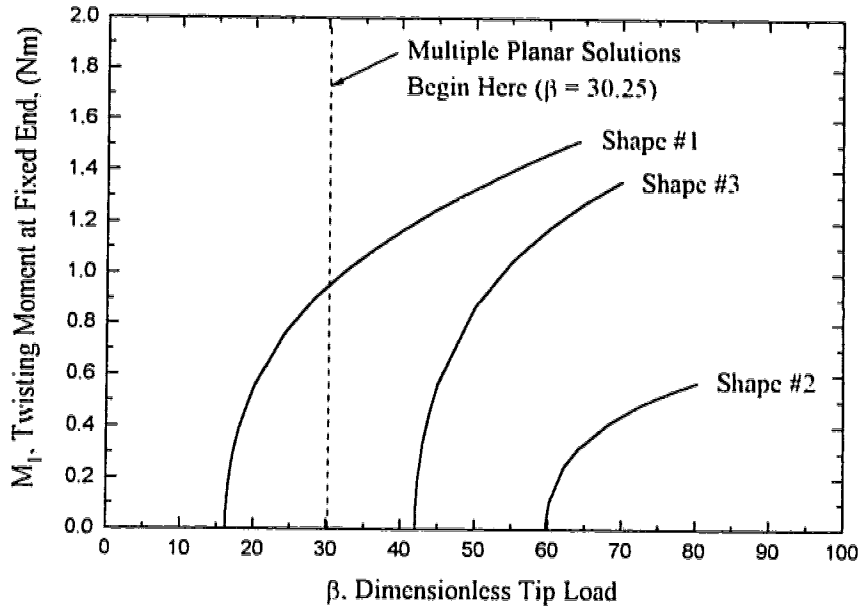


Figure 4.6: M_1 Component Required to Maintain Buckled Equilibrium Configurations. $a/b = 1/1.7$

that a non-zero M_1 component implies that the tip of the beam has moved away from the original \mathbf{E}_1 - \mathbf{E}_2 plane of the rod.) The twisting moment M_1 continues to increase as β is increased due to a combination of the load getting larger and the tip of the beam moving further away from the original plane of the rod. The load at which multiple planar solutions begin to occur, $\beta = 30.25$ (which is equivalent to $\alpha = 3.214$ in Table 4.1), is also indicated in Figure 4.6. Out-of-plane buckled loads are therefore possible at lower loads than are the multiple planar solutions. For loads above $\beta = 30.25$ it was found that each of the two new planar solutions can also buckle out of the plane. These are indicated in Figure 4.6 which shows that above $\beta = 59.76$ (Shape #2, Figure 4.3) and $\beta = 42.02$ (Shape #3, Figure 4.3) the other two planar solutions exhibit buckled equilibrium configurations similar to the behaviour described above. As the load is further increased above these values, the moment component M_1 necessary to maintain equilibrium also increases. Note that Figure 4.6 shows the twisting moment for the buckled shapes assuming the rod moves to only one side of the \mathbf{E}_1 - \mathbf{E}_2 plane. There is a second half which is symmetric about the $M_1 = 0$ axis which would consider shapes on the other side of the original plane where the beam tip

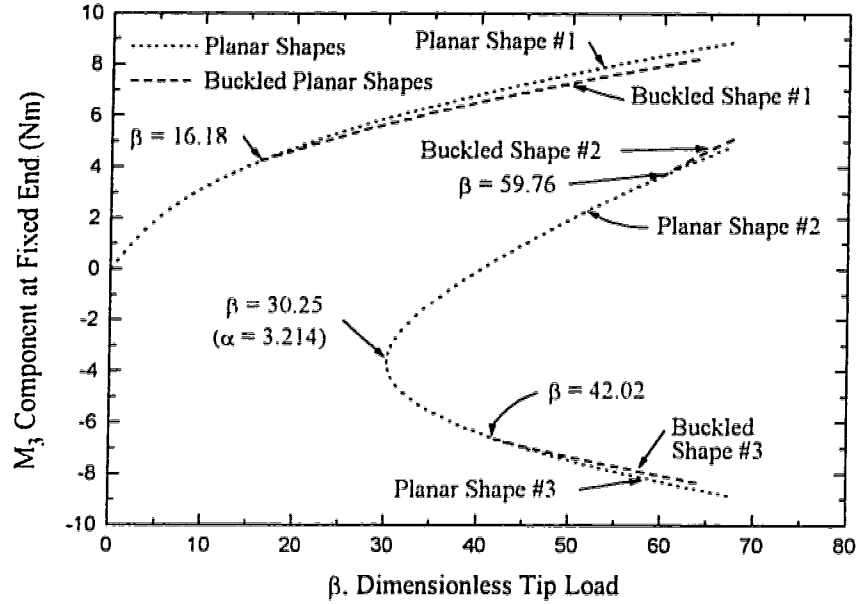


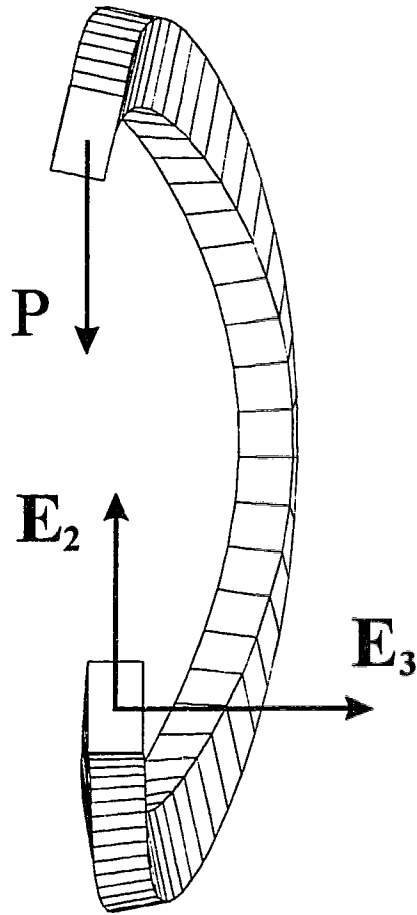
Figure 4.7: M_3 Component Required to Maintain Buckled Equilibrium Configurations, $a/b = 1/1.7$

has the opposite \mathbf{E}_3 coordinate.

A similar behavior can be seen in Figure 4.7 which shows the M_3 component required for equilibrium. The planar Shapes #1 - #3 are shown as the dotted curves and are equivalent to the curves shown in Figure 4.4. The new buckled shapes are indicated by the new branches which develop from the planar curves. The main difference between Figures 4.6 and 4.7 is that, as mentioned, the M_1 component is identically zero for the planar shapes. Thus these all collapse onto the same line (the $M_1 = 0$ axis) in Figure 4.6. Another difference is that, as mentioned previously, Figure 4.6 has symmetry about the $M_1 = 0$ line (since the tip of the beam could buckle equally to either side of the original \mathbf{E}_1 - \mathbf{E}_2 plane). Figure 4.7 shows no such symmetry since the buckled shapes, regardless of which side they buckle to, will have the same M_3 coordinate. Thus the dashed lines in Figure 4.7, which represent the buckled configurations, each represent a pair of buckled shapes (one on each side of the original plane).

To appreciate the deformed shapes of these rods, Figure 4.8 illustrates the deformed shape of a 1-m long rod with loads of $\beta = 64$ corresponding to Shape #2 and $\beta = 44$ corresponding to Shape #3. These loads are just

Shape #2
 $\beta = 64$



Shape #3
 $\beta = 44$

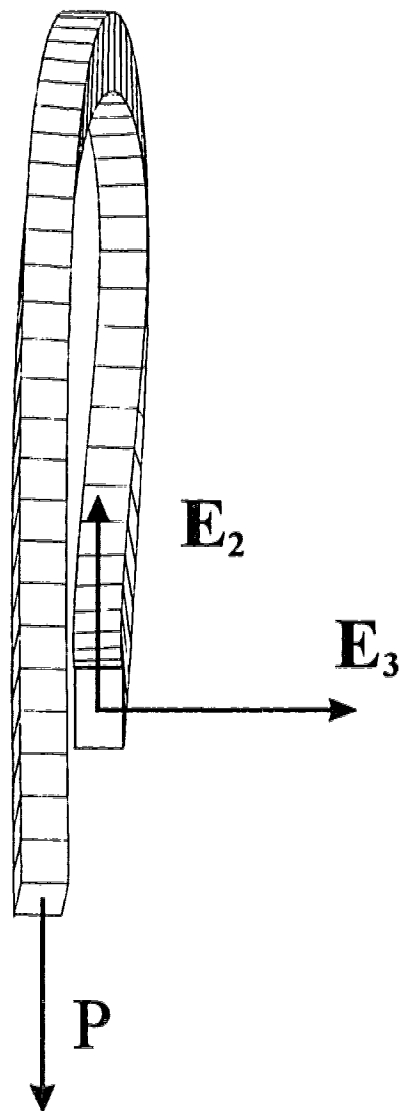


Figure 4.8: Geometry of Buckled Shapes #2 ($\beta = 64$) and #3 ($\beta = 44$), $a/b = 1/1.7$

above those required for buckling in each case. In both cases the deformed shapes are observed looking down the \mathbf{E}_1 axis in the positive \mathbf{E}_1 direction. Also, the cross sections here, and in all such figures in this chapter, have been expanded by a factor of ten for clarity.

4.2 Non-Buckled Three-Dimensional Shapes

4.2.1 Deep Cantilever Beams Under Dead Tip Loads

All of the above analysis only considers the development of out-of-plane solutions as the buckling of planar shapes (ie: an equilibrium path exists between the out-of-plane solution and a planar shape). A larger question is whether or not other three-dimensional equilibrium shapes exist which do not develop as buckled planar ones similar to development of multiple solutions in the plane. This may mean that the moment component M_1 for these new solutions may be considerably above zero. Using the shooting procedure described previously, larger initial estimates for M_1 can be used as input to the numerical procedure to search for these solutions. Since this involves a two parameter shooting problem, the actual technique used was a more systematic approach involving the use of contour maps as described by Lipsett et al. (1993). Details and limitations of the procedure are described in more detail in Appendix C. Figure 4.9 shows the non-zero M_1 values which result in equilibrium being satisfied. (The numbers shown beside each figure will be discussed later.) This figure indicates that the development of these new shapes is qualitatively similar to the development of multiple equilibrium solutions in the plane. At the critical load where $\beta = 18.87$, shown as point I in Figure 4.9, a new equilibrium shape is possible (far removed and with no connection to the original planar solution). As the load is increased, this shape bifurcates into two others (Shape A and Shape B) which represent distinct equilibrium configurations. Figure 4.10 illustrates the development of Shapes A and B as the load increases from the original bifurcation point.

It is somewhat surprising that this occurs at loads below those at which multiple planar solutions are possible ($\beta = 30.25$) and yet the shapes taken by these equilibrium configurations look similar to the planar shapes. As an example, Figure 4.11 shows the three views of the centerline of Shape B at a load of $\beta = 25$. In the \mathbf{E}_1 - \mathbf{E}_2 plane the shape of the centerline appears similar to planar Shape #2 shown in Figure 4.3 even though there

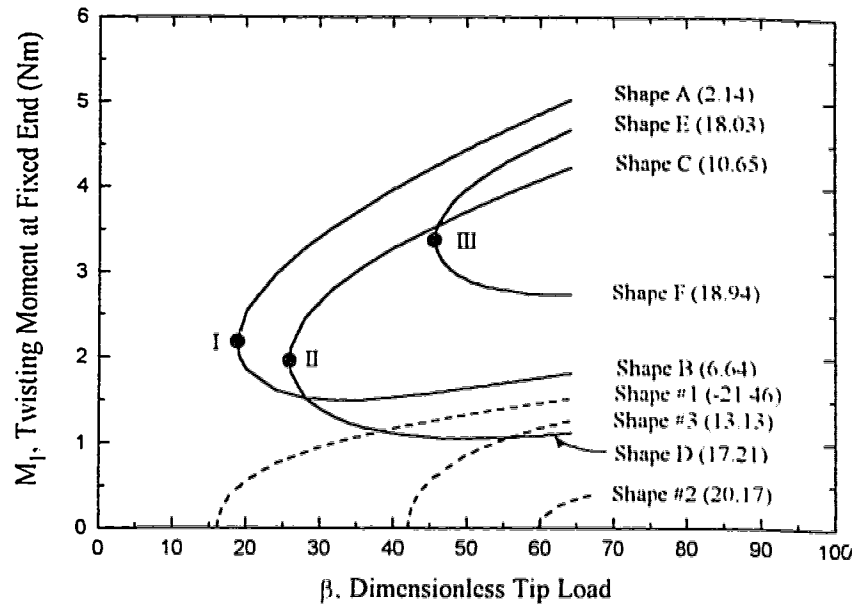


Figure 4.9: M_1 Components Required to Maintain Equilibrium Configurations Far Removed from the Original Plane and the Associated Potential Energies (Nm) For an Aspect Ratio of 1/1.7

is a relatively large out-of-plane movement of the tip of the beam.

As well as the two branches which develop from point I, there are additional shapes which develop from points II and III shown in Figure 4.9. These are again distinct equilibrium configurations. Where the branches seem to cross each other and the M_1 components are equal, the M_3 components required to maintain equilibrium are different (as demonstrated in Figure 4.12) so that the shapes are all distinct. Notice also from Figure 4.12 that there appears to be no fundamental difference between the development of these shapes far removed from the plane and the development of the multiple planar equilibrium configurations. The difference is only apparent when the M_1 components are considered. These shapes are fundamentally different from those which develop as buckled planar shapes (shown in Figure 4.6 and as the dashed curves in Figure 4.9). These are not buckled shapes since they do not develop from planar shapes. They are not related to the planar shapes at all since no equilibrium path exists between these shapes and any planar configuration.

The difference in the various configurations can also be seen by consider-

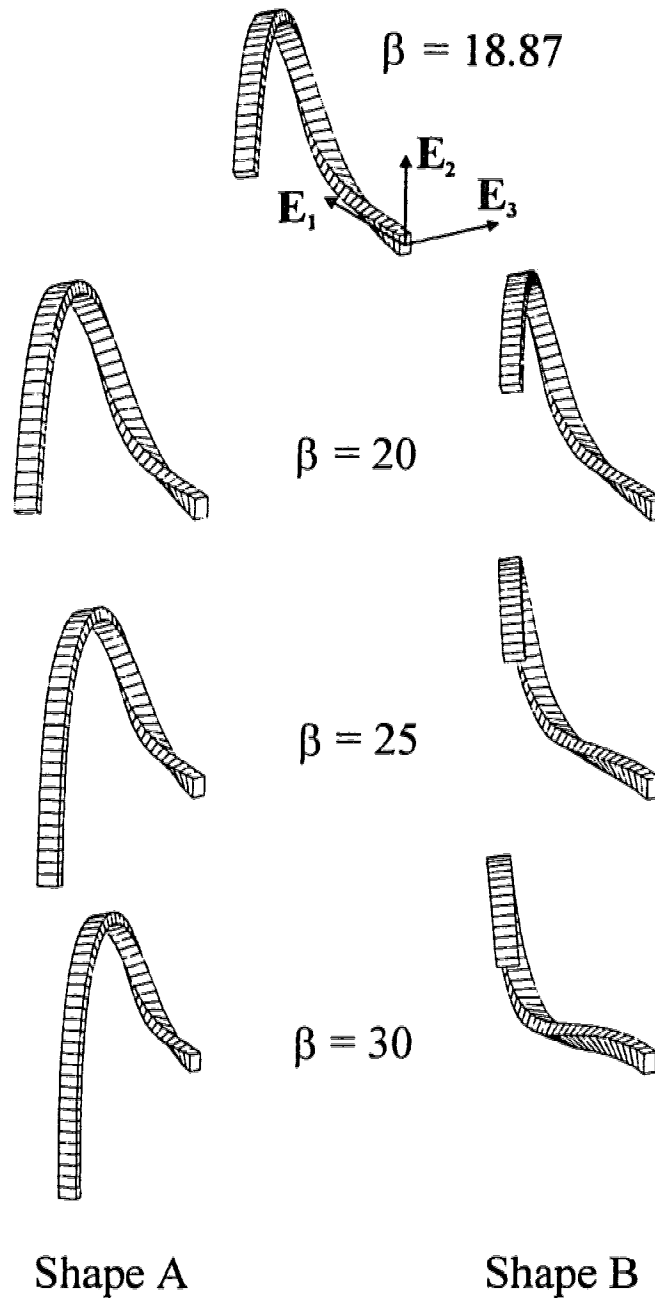


Figure 4.10: Development of Multiple Three-Dimensional Equilibrium Shapes A and B, $a/b = 1/1.7$

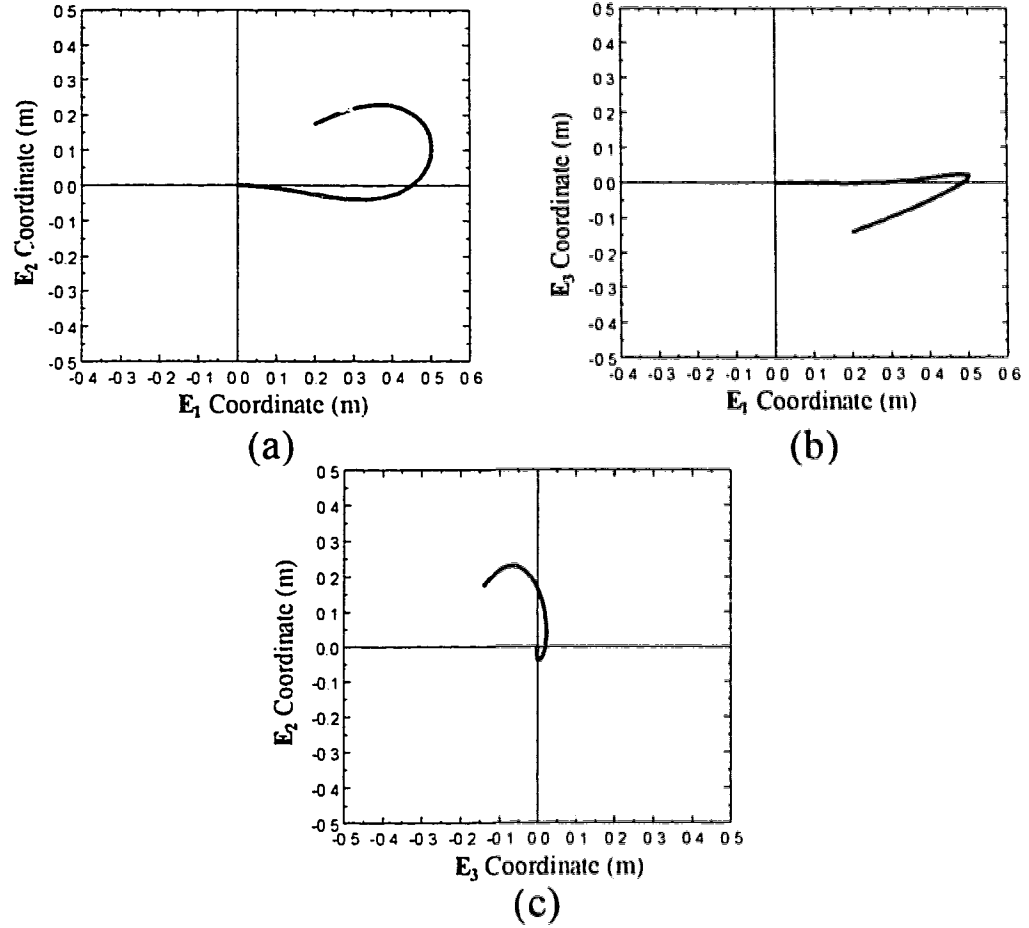


Figure 4.11: Three Views of Shape B, $a/b = 1/1.7$, $\beta = 25$: (a) E_1 - E_2 Plane. (b) E_1 - E_3 Plane. (c) E_3 - E_2 Plane

ing the twist per unit length along the deformed configurations. For example, Figure 4.13 shows the variation of κ_1 along the length of the rod corresponding to Shapes A, B, C and D at a load of $\beta = 35$. Shapes A and B, which develop from the same configuration (point I, Figure 4.9), show a similar pattern in which all of the twist is in one direction. Also, since Shape A requires a larger M_1 component at the fixed end for equilibrium (as shown in Figure 4.9), κ_1 is therefore larger at the fixed end ($s = 0$) as well. However, Shapes C and D, which develop from point II (Figure 4.9) show a different pattern in which the twist changes orientation along the rod (some of the

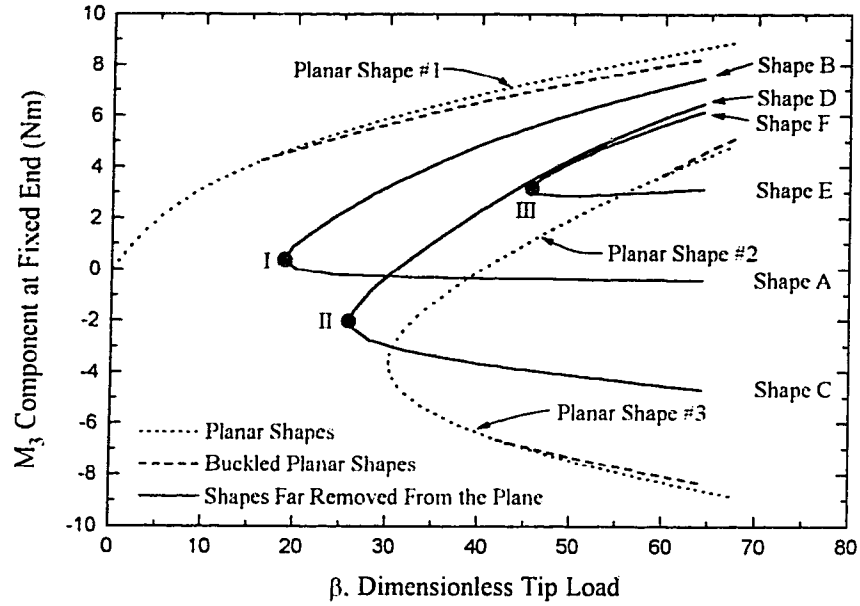


Figure 4.12: M_3 Components Required to Maintain Equilibrium Configurations Far Removed from the Original Plane. $a/b = 1/1.7$

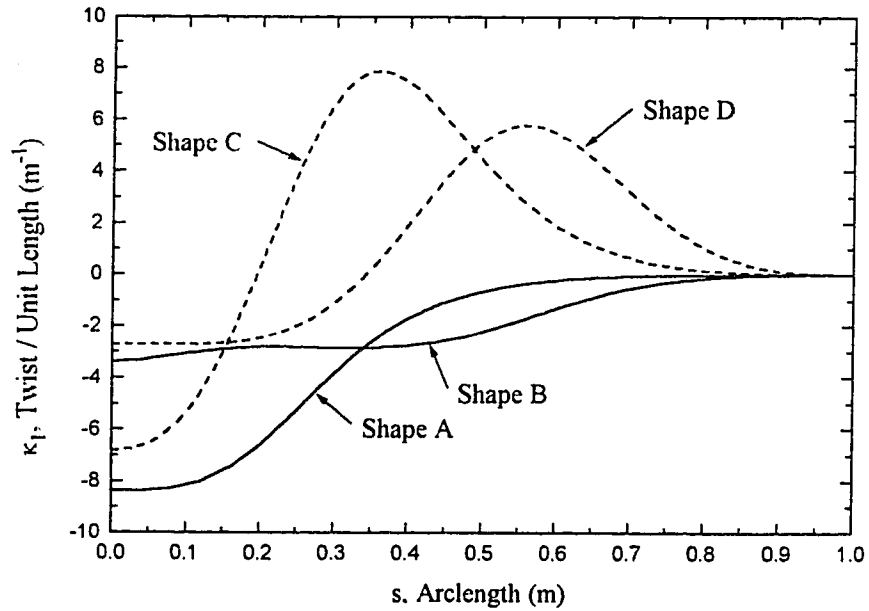


Figure 4.13: Variation in κ_1 Along the Deformed Rod for Shapes A, B, C and D at a Load of $\beta = 35$

twist is in a positive direction and some is in a negative sense). Also, in comparison to Shapes A and B where most of the twist is concentrated near the fixed end of the beam, Shapes C and D have more of the twist occurring near the middle of the beam with the peak values of κ_1 occurring away from the fixed end (and in the opposite sense of the value at $s = 0$). Note also that κ_1 vanishes at the point $s = 1$ for all of the configurations considered since this corresponds to the free end of the beam.

4.2.1.1 Potential Energies of Deformed Configurations

It is also of interest to consider the potential energies associated with the various shapes considered. Since a stable equilibrium state is a minimizer of the potential energy function, consideration of the potential energies allows a global comparison of the shapes obtained. However, this gives no indication of the local stabilities of these configurations. A more complete stability analysis would require the generation of all kinematically admissible displacement fields which satisfy the required boundary conditions to ensure that the energy is actually a minimum. This is difficult to do in the present context of using this initial value numerical solution and is not attempted here.

The potential energy E is defined as

$$E(\boldsymbol{\kappa}, \mathbf{r}) = S(\boldsymbol{\kappa}) - P(\mathbf{r}) \quad (4.10)$$

where

$$S(\boldsymbol{\kappa}) = \int_0^L U(\boldsymbol{\kappa}) ds \quad (4.11)$$

is the strain energy stored along the rod (with $U(\boldsymbol{\kappa})$ given by equation (2.6)) and

$$P(\mathbf{r}) = \mathbf{P} \cdot \mathbf{r}(L) \quad (4.12)$$

is the load potential associated with the dead tip load $\mathbf{P} = -P \mathbf{E}_2$. Table 4.2 shows the potential energies for the various shapes considered in Figure 4.9 for a steel rod ($E = 200$ GPa, $\nu = 0.3$) 1-m long with a 2.0 mm by 3.4 mm cross section (aspect ratio = 1/1.7) at a load of $\beta = 64$. (Some of these values are also shown in Figure 4.9.) At this load three planar shapes exist, for which the M_1 component is zero, and each of these will have an associated

Table 4.2: Potential Energies of Various Equilibrium Configurations for a Deep Cantilever (Aspect Ratio = 1/1.7) at a Load $\beta = 64$

Shape	Potential Energy (Nm)
Planar ($M_1 = 0$)	Shape #1
	Shape #2
	Shape #3
Buckled	Shape #1
	Shape #2
	Shape #3
Far Removed From the Plane	Shape A
	Shape B
	Shape C
	Shape D
	Shape E
	Shape F

buckled configuration as well (shown as the dashed curves in Figure 4.9). Shape #1 has the lowest absolute potential energy. The potential energies of the buckled Shapes #1 – #3 are all lower than those of their associated planar shapes, however there is only a small difference in the energies. Of the shapes far removed from the plane, branches AB from point I, which starts at the lowest load, has the lowest energies followed by branches CD from point II and EF from point III. It can also be seen that the branches corresponding to Shapes A, C and E. (which have the higher M_1 components from Figure 4.9 and lower M_3 components from Figure 4.12) consistently have potential energies lower than the associated branches B, D, and F. Also note that branches AB have potential energies substantially lower than either of the planar Shapes #2 or #3 or their buckled configurations while the other branches (CD and EF) have energies which are comparable to these shapes. It should be emphasized again that a solution with a low potential energy is not necessarily stable, and one with a high energy unstable, with respect to small perturbations. A more complete stability analysis would need to be

completed before any definite assertions could be made about the stabilities of these equilibrium configurations.

4.2.2 Shallow Cantilevers

To this point only rods with aspect ratios less than one (ie: deep cantilevers) have been considered. When the aspect ratio is greater than one (a shallow cantilever) a similar behavior is seen to occur. Figure 4.14 shows the results for the M_1 component required for equilibrium, similar to Figure 4.9, for a rod with an aspect ratio of 1.7. Figure 4.15 shows the M_3 components for the same beam. As can be seen from these figures, there are again numerous equilibrium configurations possible. There are, however, some interesting differences between the two sets of figures. One aspect to note is that in the shallow cantilever case there are now five planar shapes shown versus three in the deep cantilever case. This is due to differences in the definitions for the dimensionless load parameters α (for planar results) and β (for out-of-plane results). In the shallow case, values of β correspond to higher values of α so that more planar shapes can exist as shown in Table 4.1. Another significant difference is that for the shallow cantilever there are no longer any three-dimensional shapes ($M_1 \neq 0$) which develop as planar shapes buckle out of the original plane (the dashed curves in Figures 4.9 and 4.12). This is expected for Shape #1 (Figure 4.3) since it was shown that this planar configuration would not buckle above an aspect ratio of 0.607. It was also found that the planar Shapes #2 and #3 would not buckle above aspect ratios of approximately 0.7 and 0.6, respectively. Therefore the only shapes indicated in Figure 4.14 are those far removed from the plane while Figure 4.15 shows both those far removed from the plane as well as the planar shapes. Note that, as before, Figure 4.14 only indicates shapes which deform on one side of the original plane. There are another set of curves (symmetric about the $M_1 = 0$ axis) corresponding to shapes which buckle on the other side of the plane.

As an example of a deformed configuration, Figure 4.16a shows an oblique view of the deformed configuration corresponding to branch A in Figure 4.14 at a load of $\beta = 20$. Figure 4.16b shows the same view for the same rod loaded as a deep cantilever with the same absolute load (corresponding in this case to $\beta = 34$). Note that the two shapes are somewhat similar despite being loaded as shallow and deep cantilevers, respectively.

The potential energies for the various equilibrium configurations are also

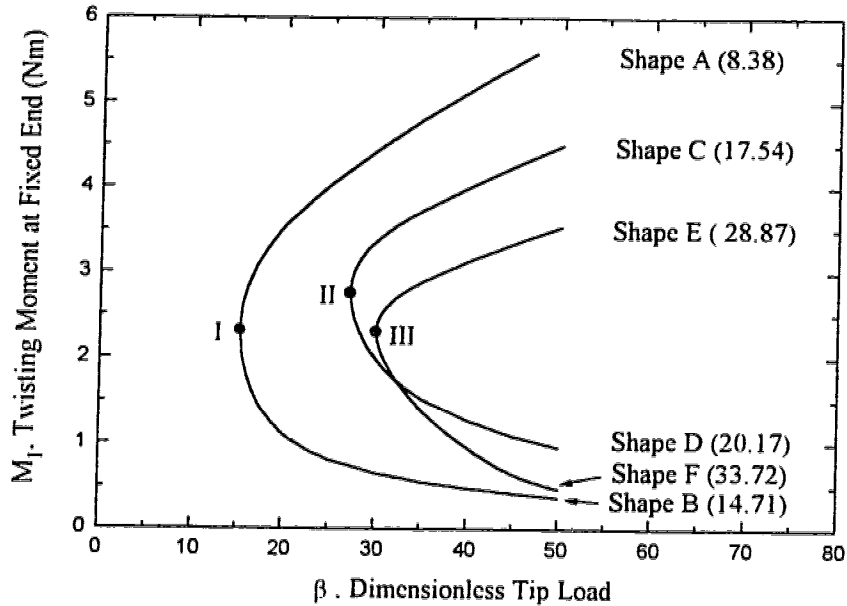


Figure 4.14: M_1 Components Required to Maintain Equilibrium Configurations Far Removed from the Original Plane, $a/b = 1.7$

shown in Figure 4.14, as well as in Table 4.3. corresponding to a load of $\beta = 45$. Note that this corresponds to a load of $\alpha = 8.688$ so that five planar shapes will exist as indicated in Table 4.1. The usual three planar shapes considered thus far (similar to those of Figure 4.3) have the lowest potential energies, with Shape #1 having by far the lowest. As mentioned previously there are no associated buckled configurations for these planar shapes at this aspect ratio. Of the shapes far removed from the plane, branches AB again have the lowest potential energies followed by branches CD and EF. All these shapes have potential energies significantly higher than the three planar ones. This is in contrast to the deep cantilever case shown in Figure 4.9 where some of these shapes had lower potential energies than several of the first three planar shapes. In this case, these shapes are closer in potential energies to planar Shapes #4 and #5 (not shown) which in turn have much higher energies than the other planar shapes.

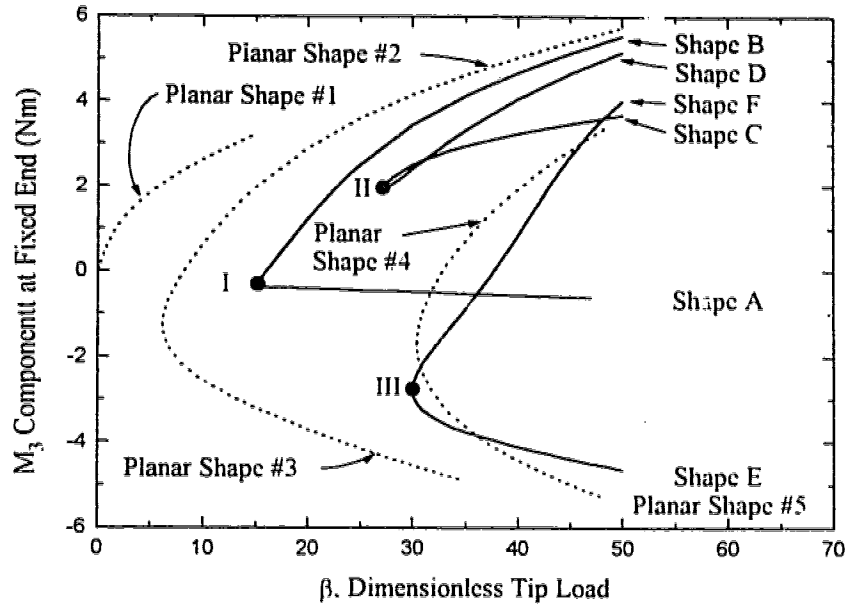


Figure 4.15: M_3 Components Required to Maintain Equilibrium Configurations, $a/b = 1.7$

Table 4.3: Potential Energies of Various Equilibrium Configurations for a Shallow Cantilever (Aspect Ratio = 1.7) at a Load $\beta = 45$

Shape		Potential Energy (Nm)
Planar ($M_1 = 0$)	Shape #1	-29.60
	Shape #2	1.58
	Shape #3	-7.32
	Shape #4	26.14
	Shape #5	23.08
Far Removed From the Plane	Shape A	8.38
	Shape B	14.71
	Shape C	17.54
	Shape D	20.17
	Shape E	28.87
	Shape F	33.72

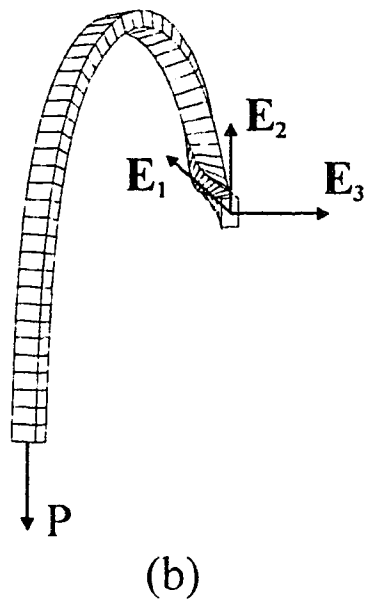
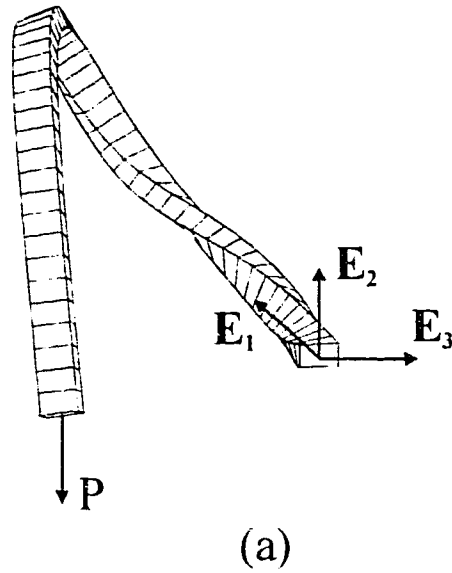


Figure 4.16: Oblique Views of Deformed Geometries for the Same Rod Loaded as a Deep and Shallow Cantilever at the Same Absolute Load: (a) Shallow Cantilever (Aspect Ratio = 1.7, Shape A, $\beta = 20$), (b) Deep Cantilever (Aspect Ratio = $1/1.7$, Shape B, $\beta = 34$)

4.3 Some Final Remarks

The existence of several classes of multiple equilibrium configurations for cantilever beams under dead tip loads in a fully three-dimensional setting has been established. The most well known of these are the multiple planar shapes which have been detailed previously (Navaee and Elling 1991, 1992; Faulkner et al. 1993). Another well known class is the three-dimensional configurations which result as planar shapes buckle out of the initial plane. While this has been investigated previously for one particular planar shape (Hodges and Peters 1975) it has been shown here that other planar shapes can also buckle out of the plane in a similar manner. The third class described here are the fully three-dimensional shapes which appear far removed from the original plane of loading. The appearance and development of these shapes is qualitatively similar to the multiple planar solutions. At some critical load, one of these shapes appears (not buckled from a planar shape) and then immediately bifurcates into two as the load is increased. Somewhat surprisingly, it was found that these new shapes could emerge at loads below those required for the multiple planar shapes. Further, it is not known whether or not the out-of-plane shapes suggested by Figures 4.9, 4.12, 4.14 and 4.15 are exhaustive. However, the possibility for numerous equilibrium shapes has certainly been demonstrated.

As a final note, it should be stressed that the results presented are highly dependent upon the aspect ratio used. (The aspect ratios used were chosen to illustrate some of the different types of behavior possible.) This is especially true of the relative magnitudes of the loads required for the various shapes to occur. For example, while some of the shapes far removed from the plane were found to emerge at loads below those required for multiple planar solutions, this was for a specific aspect ratio and will not be true for all aspect ratios. In particular, if a square cross section is considered (aspect ratio = 1) then there would not be any out-of-plane equilibrium shapes (buckled planar shapes or those appearing far removed from the original plane) possible. This is due to the fact that a rod with $EI_2 = EI_3$ is considered to be transversely isotropic and, since only initially straight rods are considered in this section, equation (2.15) applies. Thus, since M_1 (and therefore κ_1) must be zero at the free end of the beam, equation (2.15) requires that κ_1 be zero at the fixed end as well so that M_1 would be zero there also. As discussed previously, requiring $M_1 = 0$ at the fixed end of the beam implies that only planar equilibrium will exist.

Chapter 5

Three-Dimensional Effects in Orthodontic Retraction Appliance Design

Up to this point, the numerical procedure developed in Chapter 3 has been used to solve a variety of problems. In Chapter 3 the segmental approach (considering the rod as being comprised of several shorter rod segments) was used to avoid the numerical difficulties which arise when a singularity in the Euler angles used is encountered. In this chapter the segmental approach will be used to advantage in modeling complex rod structures. The specific problem analyzed is an orthodontic retraction appliance used to reposition teeth in the dental arch. These appliances have complex initial geometries and can undergo large three-dimensional deformations so that a nonlinear three-dimensional analysis is required (Raboud et al. 1996).

5.1 Introduction to the Problem

One aspect of orthodontic treatment involves space closure where a single anterior tooth or group of teeth (segment) is retracted to close a space in the dental arch. Often the space to be closed (6–9 mm typically) has been created through the extraction of a tooth (typically an canine) to make room in a crowded dental arch. This treatment is done to improve occlusion and/or for purely cosmetic reasons.

Several methods exist for achieving this space closure. One such method is

referred to as the segmented approach¹ (Burstone 1982; Braun and Marcotte 1995) in which these spaces are closed through the use of specialized retraction appliances. These appliances consist of 'springs' which are attached to brackets fixed to the teeth. A number of different types of appliances are used of which the vertical loop and T-spring are the most common.

Figure 5.1 illustrates the use of a T-spring in a plane. The unloaded shape is first brought to the neutral position, in which the ends of the appliance are collinear with no applied axial force (Burstone 1982), essentially through the application of couples to its ends. The appliance is then 'activated' by pulling the ends apart a specified distance. The fully activated spring is then held in this shape by means of brackets which are mounted on the outer

¹Here the segmented approach refers to joining several teeth together and moving the *segments* as one unit. This should not be confused with the numerical segmental approach which is involved in modeling the rod as a number of segments.

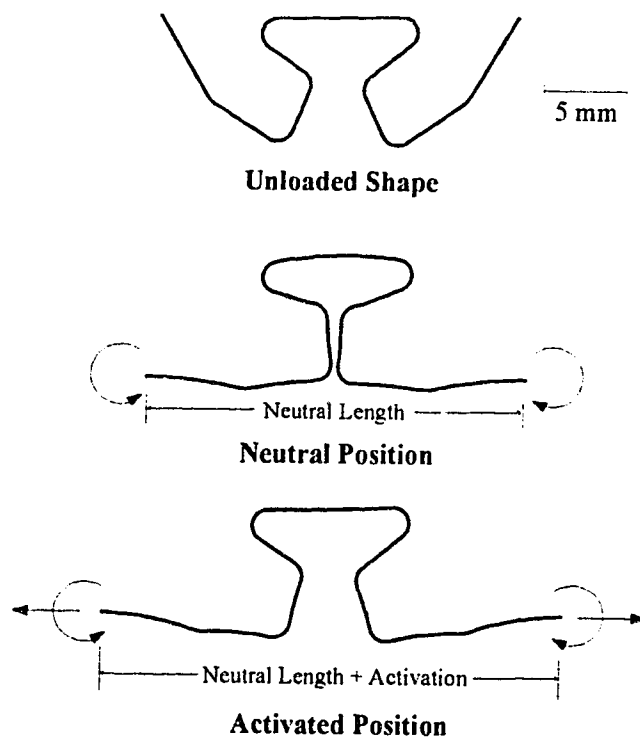


Figure 5.1: Undeformed, Neutral Position and Activated Position for a T-Spring Appliance in a Plane

surfaces of the teeth.

When these springs are activated (deformed and then fixed to the brackets) they apply forces and moments only to the brackets at each of its ends. The relative amounts of force and moment applied by the appliance will determine the resulting type of tooth movement. Therefore the appliances must be able deliver appropriate levels of both force and moment to obtain the desired tooth movement. As a result many of the appliance designs have been evaluated either experimentally, analytically (Chaconas et al. 1974; Burstone and Koenig 1976; Faulkner et al. 1989) or numerically (Lipsett et al. 1990; Faulkner et al. 1991). However, all of these evaluations have been limited to describing the force systems under the assumption that the appliance is mounted and remains in the plane of one of the tooth surfaces. Because these force systems are usually applied to the buccal (towards the cheeks or lips) surfaces and because these tooth surfaces can be in different planes (Isaacson et al. 1993), they can result in three-dimensional effects which are undesirable and cause tooth movements which require further corrective treatment in the future. By initially understanding these effects, they can be minimized and it may also be possible to include modifications to the spring designs which can essentially counteract the undesired effects.

5.1.1 Tooth Retraction in the Lateral Plane

To appreciate and predict the type of tooth movement that will occur from a specific force system (forces and moments), the effective resistance of the supporting tissue around the root of a tooth is described in terms of a center of resistance C_{res} . The center of resistance is defined as the point at which a single applied force would cause the tooth to translate in the direction of that force. When the force system is not equivalent to a single force applied at the C_{res} the tooth will both translate and rotate. This combined movement (translation and rotation) is described by the center of rotation C_{rot} , which is the axis about which the tooth rotates during application of a specific force system².

Figure 5.2a illustrates a typical situation in which forces and moments from an activated vertical loop retraction appliance are applied by means of a typical segmented system. The forces and moments applied to the brackets

²The center of rotation C_{rot} is equivalent to the *instantaneous center* of the tooth in this instance.

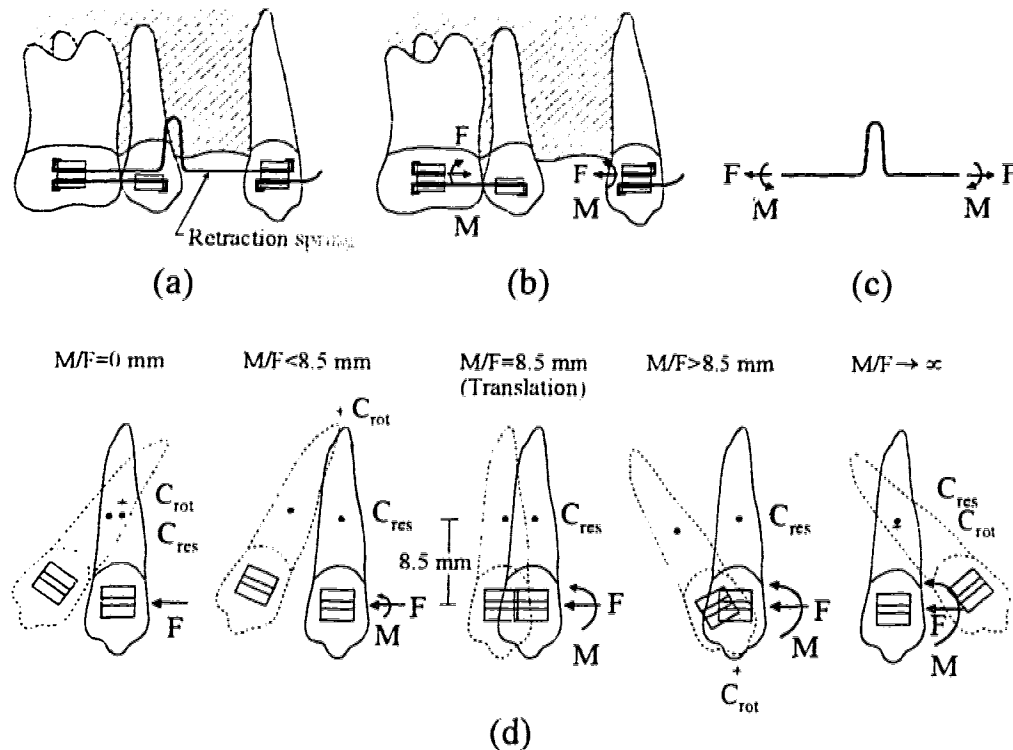


Figure 5.2: Lateral View of an Orthodontic Retraction Appliance Used for Space Closure: (a) Typical Installation. (b) Forces and Moments Applied to Brackets in Lateral Plane. (c) Forces and Moments Applied to Appliance in Lateral Plane. (d) Resulting Tooth Movement as a Function of M/F Ratio

by the appliance are as indicated in Figure 5.2b while the equal and opposite forces and moments which act on the spring are shown in Figure 5.2c. The activation of the appliance must provide the appropriate level of force and moment to force (M/F) ratio if a particular type of tooth movement is to occur (Quinn and Yoshikawa 1985; Tanne et al. 1988). Figure 5.2d illustrates the predicted movements of the anterior tooth including the position of C_{res} and C_{rot} which are believed to occur in the lateral plane of the appliance.

If the force system at the bracket is just a force ($M = 0$ and $M/F = 0$), the resulting tooth displacement is described by a center of rotation which is apical (towards the tip of the root) to the center of resistance. Increasing the M/F ratio can dramatically alter the C_{rot} of the tooth or tooth segment. The center of rotation moves apically as the M/F ratio is increased from zero

translation occurs. With tooth translation, there is no rotation and C_{rot} is located infinitely far from C_{res} . While there is some uncertainty about the specific value (Tanne et al. 1988), it is generally accepted that a M/F ratio of approximately 8.5 mm will result in translation for a single rooted tooth such as a canine. The M/F ratio of 8.5 mm is equal to the distance between the point of application of the force system at the bracket and the center of resistance. Increasing the M/F ratio further now results in rotation in the opposite direction because C_{rot} is now incisal (towards the crown of the tooth) to C_{res} . Further increases in the M/F ratio cause C_{rot} to move towards C_{res} from the incisal side. As a final limiting case when there is a very large M/F ratio (caused by either $M \rightarrow \infty$ or possibly a very small force), C_{rot} is essentially coincident with C_{res} .

5.1.2 Tooth Retraction in the Occlusal Plane

A similar analysis to that described above for the lateral plane can be applied in the occlusal plane³ (perpendicular to lateral plane) as shown in Figure 5.3. The forces applied to the brackets are shown in Figure 5.3a while those applied to the appliance⁴ are shown in Figure 5.3b. If the appliance is mounted on the buccal side as shown then the activation force F alone will tend to rotate the attached tooth not about the C_{res}^* (which in this plane is near the tooth axis) but about a C_{rot}^* which is lingual (towards the tongue) to the center of resistance as shown in Figure 5.3c. To inhibit this longitudinal axis rotation and effect translation, the application of a moment M^* as shown in Figure 5.3d is required. The M^*/F ratio required in this situation (canine retraction) is approximately 3.5 mm which is again the distance from the point of application of the appliance to the C_{res}^* . Increasing the M^*/F ratio above this value will change the direction of tooth rotation so that C_{rot}^* is now buccal to C_{res}^* as shown in Figure 5.3e. Note that the force F acting on a tooth in both the lateral and occlusal planes is the same, however, the lateral moment M is different from the moment M^* acting in the occlusal plane.

³The occlusal plane is approximately the plane containing the tops of the teeth in the dental arch.

⁴The appliance shown is now a T-spring which is another common retraction appliance.

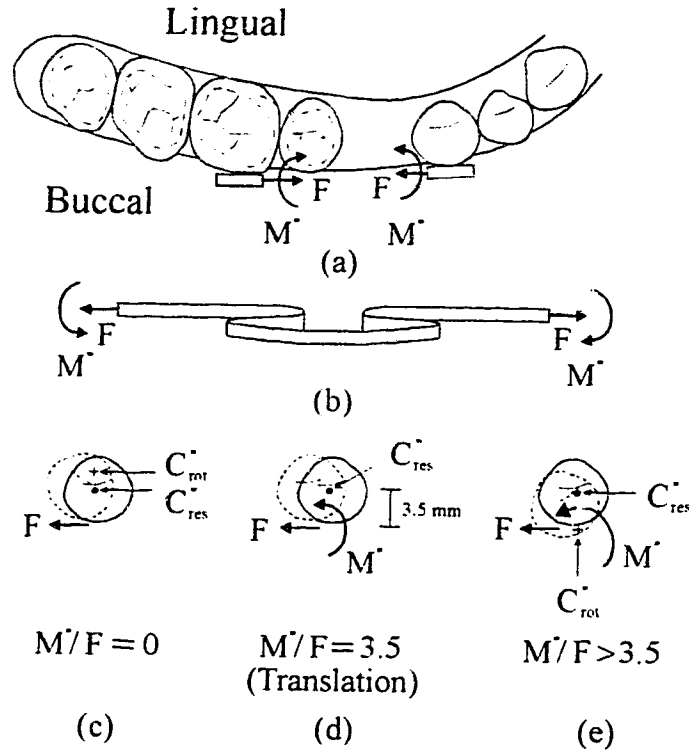


Figure 5.3: Occlusal View of an Orthodontic Retraction Appliance Used for Space Closure: (a) Forces and Moments Applied to Brackets in Occlusal Plane, (b) Forces and Moments Applied to Appliance in Occlusal Plane, (c) Resulting Tooth Movement in Occlusal Plane for $M^*/F = 0$, (d) Tooth Translation in Occlusal Plane, (e) Resulting Tooth Movement in Occlusal Plane for $M^*/F > 3.5$ mm

5.2 Boundary Value Problem Description

In order to analyze the appliances using the numerical technique developed in Chapter 3, boundary conditions for the problem must be established. In all of the problems considered in this chapter, the geometry (position and orientation) of both ends of the appliance will be taken as known. (This arises from the fact that the brackets to which the appliance will be attached are fixed to the teeth and their position and orientation relative to each other is assumed to be known.) However, the components of the force and moment acting at each end of the appliance are unknown so that this becomes a

six parameter shooting problem. Starting at the posterior (left) end of the appliance (see Figure 5.4), the initial position and orientation are

$$X = 0, \quad Y = 0, \quad Z = 0, \quad (5.1)$$

where

$$\begin{aligned} \mathbf{e}_1 &= \mathbf{E}_1. \\ \mathbf{e}_2 &= \mathbf{E}_2. \\ \mathbf{e}_3 &= \mathbf{E}_3. \end{aligned} \quad (5.2)$$

All the forces and moments which act at this end (F_1 , F_2 , F_3 , M_1 , M_2 , M_3) are to be determined so that there are six initial unknowns. The six known boundary conditions at the anterior (right) end⁵ of the appliance are the geometry and orientation of the bracket at that end. Several different types of boundary conditions at this end will be considered. In the usual case, illustrated in Figure 5.4, both brackets are in the same plane and are collinear. The boundary conditions at the anterior end become

$$X = \text{IBD}, \quad Y = 0, \quad Z = 0, \quad (5.3)$$

and

$$\begin{aligned} \mathbf{e}_1 &= \mathbf{E}_1. \\ \mathbf{e}_2 &= \mathbf{E}_2. \\ \mathbf{e}_3 &= \mathbf{E}_3, \end{aligned} \quad (5.4)$$

where the Interbracket Distance (IBD) is simply the distance between the inside edges of the two brackets and is defined as (see Figure 5.1)

$$\text{IBD} = \text{Neutral Length} + \text{Activation}. \quad (5.5)$$

In the other case considered the two brackets no longer remain in the same plane but rather are located as shown in Figure 5.5. The location of the anterior bracket has been moved out of the \mathbf{E}_1 - \mathbf{E}_2 plane by a rotation through an angle α about the \mathbf{E}_2 axis and maintaining the same distance between the two brackets. Essentially the inside edge of the anterior bracket is located

⁵Note that left (posterior) and right (anterior) as shown in Figure 5.4 are only valid for the left side of the dental arch.

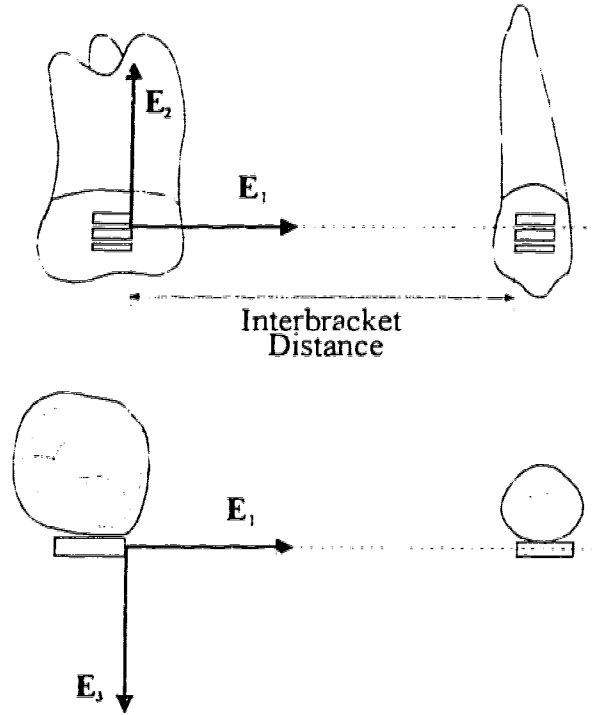


Figure 5.4: Boundary Value Problem for the Case in which the Brackets Are in the \mathbf{E}_1 - \mathbf{E}_2 Plane and are Collinear

at a position on an arc with radius IBD centered about the origin of the coordinate system. The anterior bracket is then further rotated by an angle α as shown in Figure 5.5 in order to maintain a symmetric spring deformation. Thus the total angular difference between the brackets measured in the \mathbf{E}_1 - \mathbf{E}_3 plane is 2α . The resulting boundary conditions at the anterior end of the appliance are

$$X = \text{IBD} \cos \alpha, \quad Y = 0, \quad Z = -\text{IBD} \sin \alpha. \quad (5.6)$$

while the local unit vectors are

$$\begin{Bmatrix} \mathbf{e}_1 \\ \mathbf{e}_2 \\ \mathbf{e}_3 \end{Bmatrix} = \begin{bmatrix} \cos 2\alpha & 0 & -\sin 2\alpha \\ 0 & 1 & 0 \\ -\sin 2\alpha & 0 & \cos 2\alpha \end{bmatrix} \begin{Bmatrix} \mathbf{E}_1 \\ \mathbf{E}_2 \\ \mathbf{E}_3 \end{Bmatrix}. \quad (5.7)$$

Note that with the spring orientation relative to the brackets and teeth as defined above, the planar moment M , occlusal moment M^* and force F are

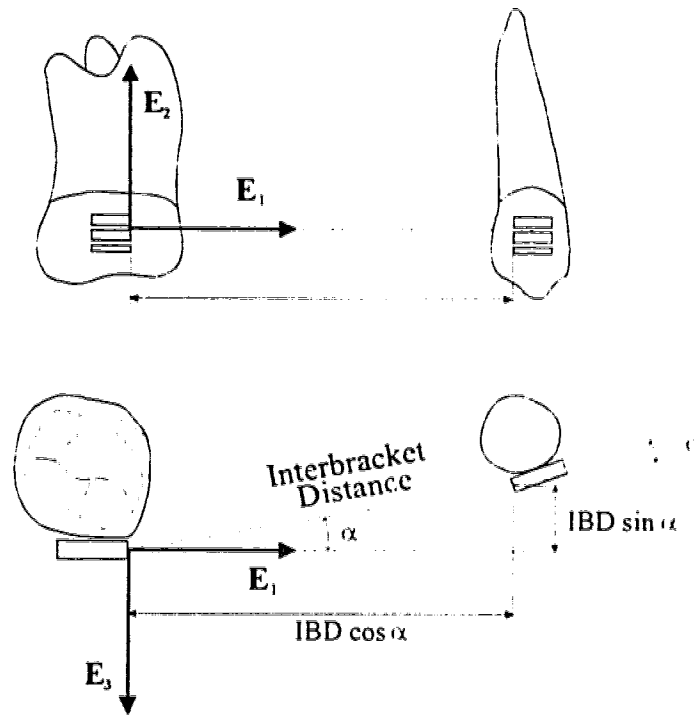


Figure 5.5: Boundary Value Problem for the Case in which the Brackets Do Not Remain in the Same Plane

equal to the moment components M_3 , M_2 and axial force F_1 respectfully. A positive M_3 component *acting on the spring* is as shown in Figure 5.2c while a positive M_2 component *acting on the spring* is as shown in Figure 5.3b. A positive F_1 component is shown in both figures.

In this chapter several appliances will be analyzed. One particular point of interest will be the activations at which the elastic limit is reached for each specific appliance. Only activations at or below this value are investigated. No consideration is given to deformations into the plastic range beyond the elastic limit (Burstone and Goldberg 1983) which would cause the appliance to become permanently deformed. Appendix D contains a detailed description of the criteria used to establish when the elastic limit has been reached. The discussion of the force systems produced by these appliances will follow the conventions used in Section 5.1. In the lateral plane, the axial force F_1 will be referred to as simply F while the moment component (M_3) will be referred to as M . This is to maintain consistency with the orthodontic litera-

ture. In the occlusal plane the M_2 moment component will be referred to as M^* . The other force and moment components will be referred to as required.

5.3 Vertical Loops

5.3.1 Force Systems From Planar Vertical Loops Undergoing Planar Activations

One of the most common retraction appliances used is the vertical loop. Four different planar vertical loop designs were evaluated. The dimensions of the typical vertical loop (Appliance #1) are shown in Figure 5.6a. In addition to this standard vertical loop design, one with an apical helix (Appliance #2) was also considered. Another modification to the standard vertical loop in which the ends of the spring are given an initial 10° gabling bend⁶ in the \mathbf{E}_1 - \mathbf{E}_2 plane is shown as Appliance #3 in Figure 5.6a. The final planar vertical loop considered (Appliance #4) is another modified version consisting of both an apical helix and gabling bends of 10° .

When the discussion is limited to planar appliances undergoing planar activations, the boundary conditions described in Section 5.2 are simplified considerably. The shear force component F_3 and the moment components M_1 and M_2 are required to be zero in this situation. Further, since the appliances considered are symmetric about the vertical centerline, the vertical shear force F_2 is also zero. Thus, instead of six unknowns in the general case, there are only two unknown values at the left end of the appliance (F and M). The two required conditions at the end of the spring are given by

$$X = \text{IBD}, \quad Y = 0. \quad (5.8)$$

The other boundary conditions discussed in Section 5.2 will be satisfied automatically with $F_2 = F_3 = M_1 = M_2 = 0$ specified at the start of the numerical procedure.

The wire for these vertical loops was assumed to have a 0.406×0.559 mm (0.016×0.022 inch) cross section and be constructed of stainless steel with a Young's modulus of 177 GPa (25.7×10^6 psi) and a yield strength of 1400 MPa (200×10^3 psi) (Lipsett et al. 1990; Faulkner et al. 1991). Because of the material used and the size of the wire, the elastic activation range for these

⁶Also referred to as a pre-activation.

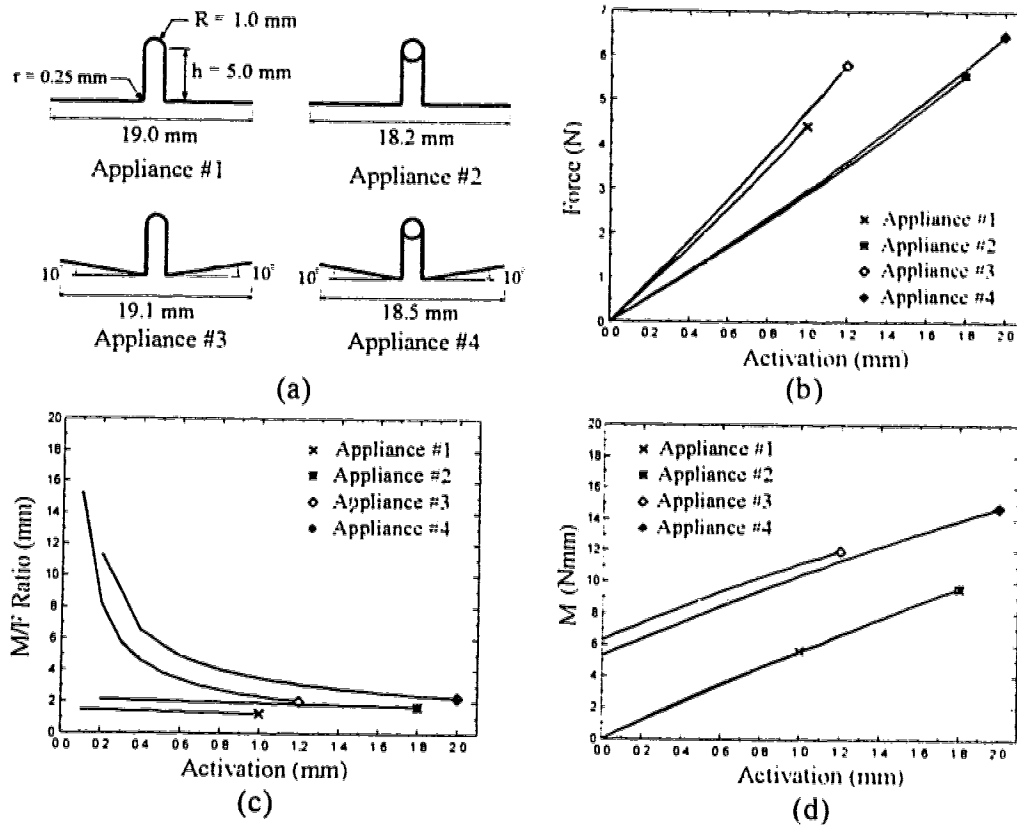


Figure 5.6: Results for Planar Vertical Loops Undergoing Planar Activations: (a) Dimensions. (b) Forces. (c) M/F Ratios. (d) M

vertical loops is limited to the values shown (Figures 5.6b-d) for each of the four designs. In each case, the IBD at the maximum activation is required to be 20 mm for comparison between the various designs. For example, since Appliance #1 has a 1.0 mm maximum activation, its neutral position is 19 mm as shown in Figure 5.6a. (Note that in this case the undeformed shape of the spring is also the neutral position.) Similarly, since Appliance #4 has a maximum activation of 2.0 mm, the neutral position is 18.0 mm.

A comparison of the results in Figure 5.6b shows the effect of the addition of a single wound apical helix to the simple vertical loop. The maximum elastic activation is increased to 1.8 mm for Appliance #2 as compared to 1.0 mm for Appliance #1. A larger activation range is desirable since the appliance will need fewer re-activations to close the same amount of space.

Another effect of the addition of the apical helix is that the force-activation rate (slope in Figure 5.6b) is "softened". This is also advantageous from the orthodontist's perspective since a low force-activation rate allows a more constant force to be applied as the teeth (and therefore the brackets and the ends of the appliance) move closer together. A constant force is thought to be more efficient at moving teeth than are variable forces (Quinn and Yoshikawa 1985) so a low force-activation rate is desirable. Note that the addition of an apical helix produces very little change in either the M/F ratio or the moment M (apart from the increase in the elastic range) as shown in Figures 5.6c and d respectively.

The effect of preactivating the simple vertical loop by gabbling the ends 10° (Appliance #3) can be seen in Figures 5.6c and d. The main difference is the additional moment (approximately 6 Nmm) required to initially bring the preactivated appliance to the neutral position before activation. (This is not required for the simple vertical loop since the undeformed position is the neutral position in that case.) The additional moment has the effect of increasing the M/F ratio especially for low activations. However, at higher activations this effect is diminished. Figure 5.6c shows that at a 1.0 mm activation, the M/F ratio for Appliance #3 is only marginally higher than the simple vertical loop (Appliance #1). The preactivation has little effect on the force-activation rate as shown in Figure 5.6b.

The combination of both the apical helix and the preactivation (Appliance #4) produces a combination of the above effects as shown in Figure 5.6b-d. Compared to the original vertical loop there has been a doubling of the elastic range from 1.0 to 2.0 mm, a softening of the force-activation rate and an increase in the M/F ratio at all activations (approximately doubled at a 1.0 mm activation).

In summary, the planar vertical loops described provide a relatively high level of force for a small activation (ie: high force-activation rate). However, the M/F ratios generated are considerably lower than those required for translation in the lateral plane (approximately 8.5 mm) except for the very last portion of the deactivation. The simple vertical loop can be modified by the addition of apical helicies and/or by gabbling of the ends. The addition of apical helicies allows for larger elastic activations while the gabbling of the ends introduces higher M values and increased M/F ratios. While the force levels are certainly sufficient to produce tooth movement, the M/F ratios at or near the maximum activations are still well below those suggested to produce translation (Tanne et al. 1988).

5.3.2 Force Systems From Initially Non-Planar Vertical Loops Undergoing Planar Activations

To illustrate the effects of design parameters which are out of the lateral plane and create force systems which have the potential to cause out-of-plane tooth displacement, the vertical loops discussed above were modified by an additional bend at each of the lower bends seen in Figure 5.6a. Each of these lower radii (which are modelled as plane curves for the planar vertical loops) are replaced with initially helical segments to give each of the ends of the appliance an additional 10° out-of-plane preactivation⁷. The total angular difference between the two ends in the $\mathbf{E}_1\text{-}\mathbf{E}_3$ plane is therefore 20° . This was done for all of the vertical loops shown in Figure 5.6a while maintaining the same preactivation in the $\mathbf{E}_1\text{-}\mathbf{E}_2$ plane for each of these appliances.

Since the vertical loops are now initially non-planar, the full force system discussed in Section 5.2 must be considered. However, as with the initially planar appliances, the vertical shear force F_2 must again be zero due the symmetry of the appliance about the vertical centerline. This symmetry also requires that F_3 and M_1 be zero as well so that there are three initial unknowns (F , M and M^*) for the springs considered in this section. The three boundary conditions required at the other end of the spring are then given by equation (5.3). The conditions given in equation 5.4 follow from the symmetry when $F_2 = F_3 = M_1 = 0$ at the start of the numerical procedure.

Figure 5.7 shows both a lateral and an occlusal view of the shape of the spring (Appliance #1) with these additional bends before activation while Figure 5.8 shows the activated shape at maximum activation. Note that the activation causes the appliance to return to being almost planar. Figure 5.9 shows a comparison of the force-activation relationship for the original planar appliances to those with the additional out-of-plane modifications. In each case the maximum activations to allow only elastic behavior are shown. In Figure 5.9a the original vertical loop (Appliance #1) and the vertical loop with preactivation (Appliance #3) are compared to the modified designs

⁷The helices used had the same radius as the initial plane curve. The pitch angle and total included angle were chosen to produce the desired preactivations in both the $\mathbf{E}_1\text{-}\mathbf{E}_2$ and $\mathbf{E}_1\text{-}\mathbf{E}_3$ planes. Note that specifying the radius and pitch angle only determines the shape of the centerline of the helix. The twist per unit length (κ_1^0) is arbitrary at this point. However, since the procedure developed in Chapter 3 only considers the case of constant initial curvatures and twist, κ_1^0 was required to be equal to the geometric torsion which would satisfy these conditions.

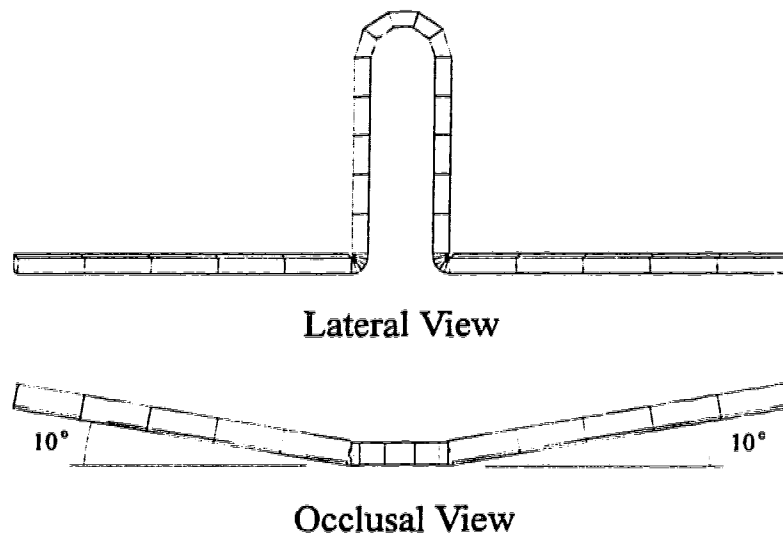


Figure 5.7: Lateral and Occlusal Views of Undeformed Vertical Loop With Out-of-Plane Modifications

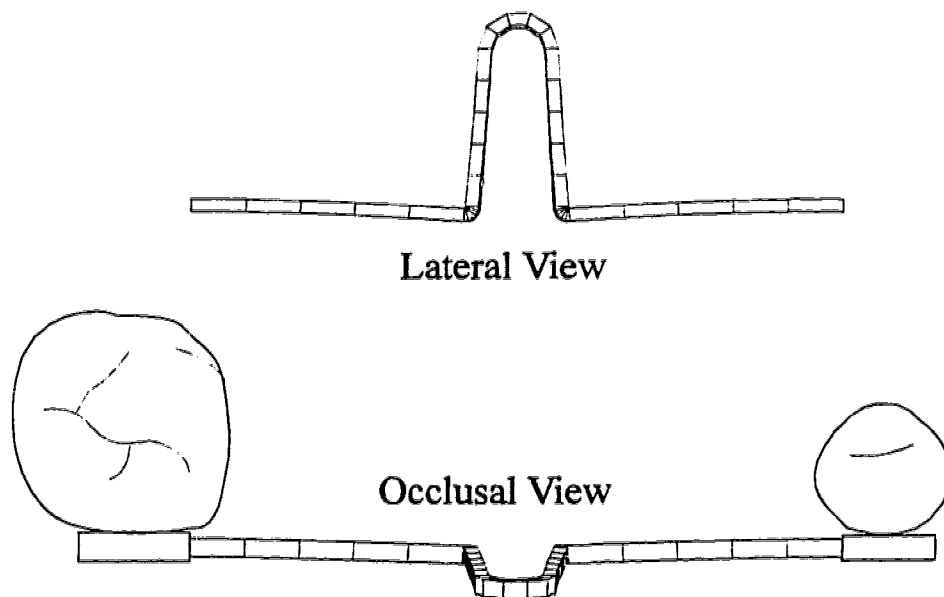
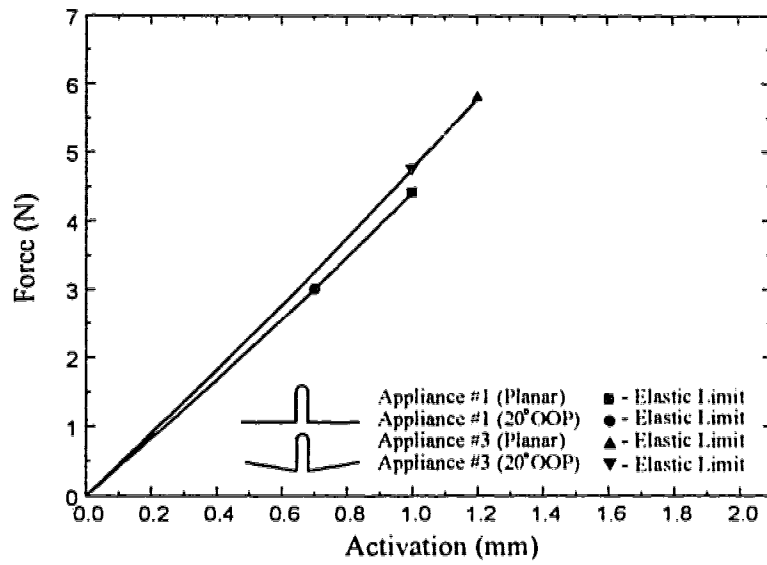
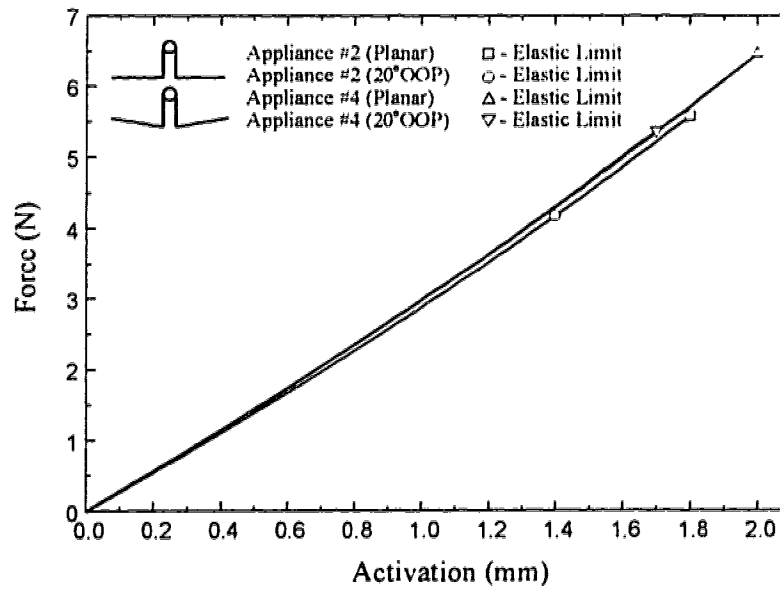


Figure 5.8: Lateral and Occlusal Views of Vertical Loop With Out-of-Plane Modifications in Fully Activated Configuration



(a)



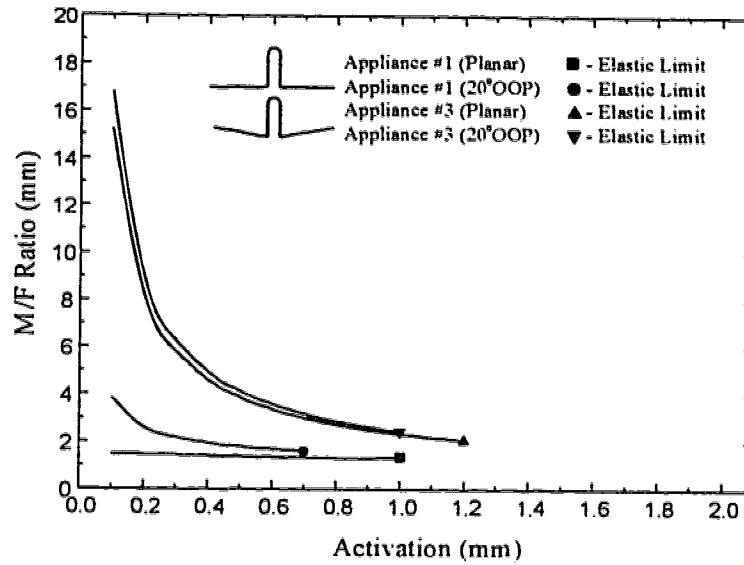
(b)

Figure 5.9: Comparison of Force-Activation Relationship Between Planar Vertical Loops and Vertical Loops with Out-of-Plane Modifications: (a) Appliances #1 and #3, (b) Appliances #2 and #4

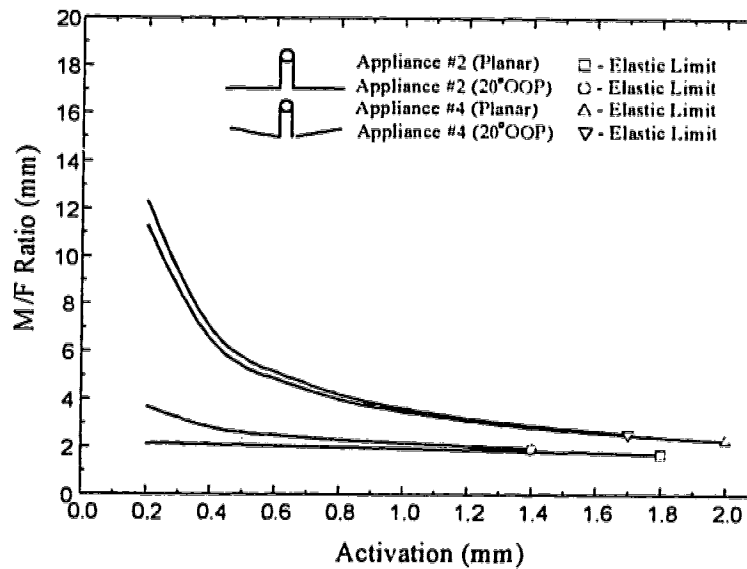
which have the additional 10° out-of-plane (OOP) bends. It is seen that the out-of-plane bends do not significantly influence the original force-activation relationships so that the out-of-plane design modifications can be applied without any appreciable change to the force applied when activated. In Figure 5.9b the comparison is for the vertical loop with apical helicies (Appliance #2) and the vertical loop with both the apical helix and 10° preactivation (Appliance #4). Note that as indicated in the previous section, the appliances with the apical helicies allow considerably more activation than the original design. The force-activation relationship in the lateral plane again demonstrates that the addition of the out-of-plane bends does not have any appreciable effect on the original force-activation rate. However, the introduction of the out-of-plane bends does reduce the maximum elastic activation possible. In the case of the original vertical loop (Appliance #1) this reduction is from 1.0 mm to 0.7 mm with a total 20° out-of-plane bend.

While the force-activation relationships are essentially unaffected by the additional out-of-plane bends, the M/F ratios in the original lateral plane are influenced to some degree. Figure 5.10 compares the M/F ratios for the various out-of-plane designs with the planar ones. The original loop (Appliance #1) and the preactivated loop (Appliance #3) are compared in Figure 5.10a while the other two designs with apical helicies (Appliance #2 and Appliance #4) are shown in Figure 5.10b. The effect of the out-of-plane bends on the original M/F ratio is evident only at small activations where the additional bends cause a slight increase in the M/F ratio. Near the maximum activation possible for a particular spring design there is no significant difference.

The major influence of the out-of-plane bends is the introduction of the additional moment M^* in the occlusal plane which is not present in for the planar vertical loops. The M^*/F ratios for the four appliances considered are shown in Figure 5.11. The qualitative behavior of the M^*/F ratios are very similar to that seen in the lateral plane in that the M^*/F ratio decreases as the activation is increased. The out-of-plane bends cause a large increase in the generation of an occlusal moment M^* . The M^*/F ratio at the maximum elastic activation varies up to approximately 2.0 mm for the 20° out-of-plane Appliance #1. However, this maximum activation now occurs at only 0.7 mm compared with a 1.0 mm maximum activation for the original appliance. Comparing the M^*/F ratios at a particular activation, say 0.7 mm, shows that Appliance #4 (apical helix and preactivation) provides a M^*/F ratio of approximately 3.0 mm. This is close to the value previously discussed



(a)



(b)

Figure 5.10: Comparison of M/F Ratios Generated By Planar Vertical Loops and Vertical Loops with Out-of-Plane Modifications: (a) Appliances #1 and #3, (b) Appliances #2 and #4

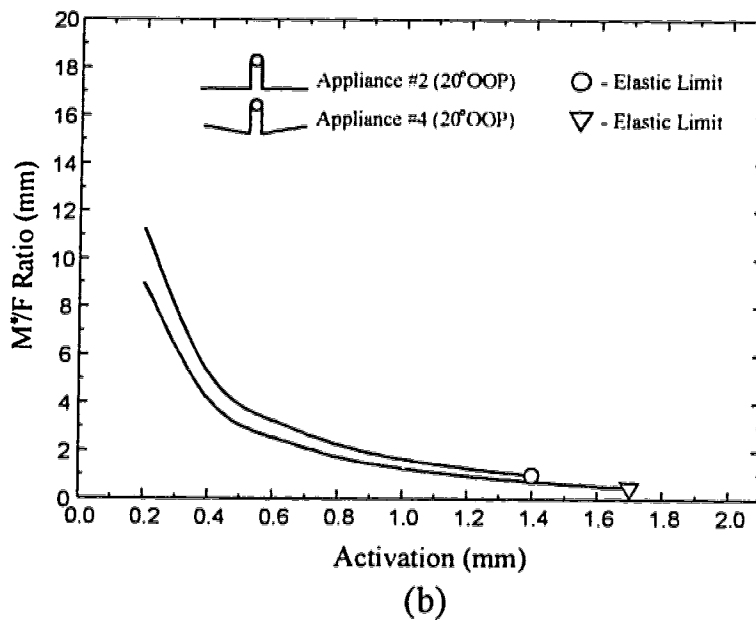
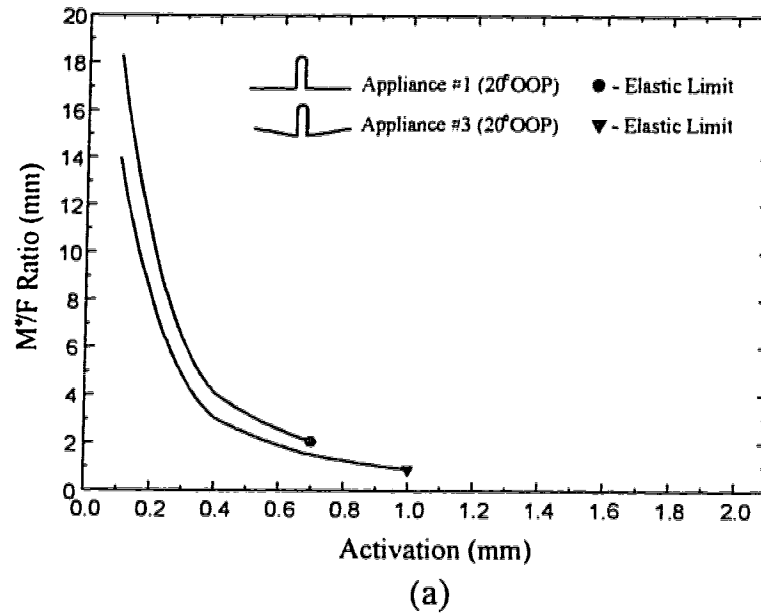


Figure 5.11: Comparison of M^*/F Ratios Generated By Planar Vertical Loops and Vertical Loops with Out-of-Plane Modifications: (a) Appliances #1 and #3, (b) Appliances #2 and #4

to prevent longitudinal axis rotation for a single rooted tooth (a canine for example).

Overall the vertical loop and three variations discussed (Appliances #1-#4) can be modified to introduce moments which counteract the tendency for a retracting tooth to rotate about its longitudinal axis. The introduction of a three-dimensional design, while showing this possibility, again reveals the extreme sensitivity of this particular loop to what would clinically be relatively small variations. The out-of-plane bends of 10° each are relatively small but because of the high load-deflection rate which is characteristic of the vertical loop the result is large variations in the M^*/F ratios produced. In addition, the total elastic activation possible is small (from only 0.7 mm to less than 2.0 mm in the best case).

5.4 T-Springs

5.4.1 Force Systems From T-Springs With Out-of-Plane Modifications Undergoing Planar Activations

As a comparison with the vertical loops discussed previously and as an alternative which is less sensitive to small variations, a preactivated T-spring design in which the material is 0.432×0.635 mm (0.017×0.025 inch) Titanium Molybdenum Alloy (TMA) with a Young's modulus of 69 GPa (10×10^6 psi) and a yield stress of 1240 MPa (180×10^3 psi) is also analyzed (Faulkner et al. 1989; Lipsett et al. 1990). The dimensions of the planar design are shown in Figure 5.12. Details of the segments used to model this appliance are given in Table 5.1. As well as this basic design an additional one with out-of-plane bends, similar to those for the vertical loops considered in the previous section, was also analyzed. The appliance was modified to the initial shape shown in Figure 5.13 by introducing 10° out-of-plane bends at the positions marked 4, 6, 12 and 14 in Figure 5.12. This results in a total angular difference of 40° between the ends of the appliance in the occlusal plane. The shape of the appliance when activated to the elastic limit is shown in Figure 5.14. The activation causes the appliance to return to being almost planar, similar to vertical loops previously considered. Note that, due to the symmetry in the appliance, the problems considered in this section have the same boundary conditions as the vertical loops discussed previously. Thus when the planar appliance is considered, a two parameter shooting problem

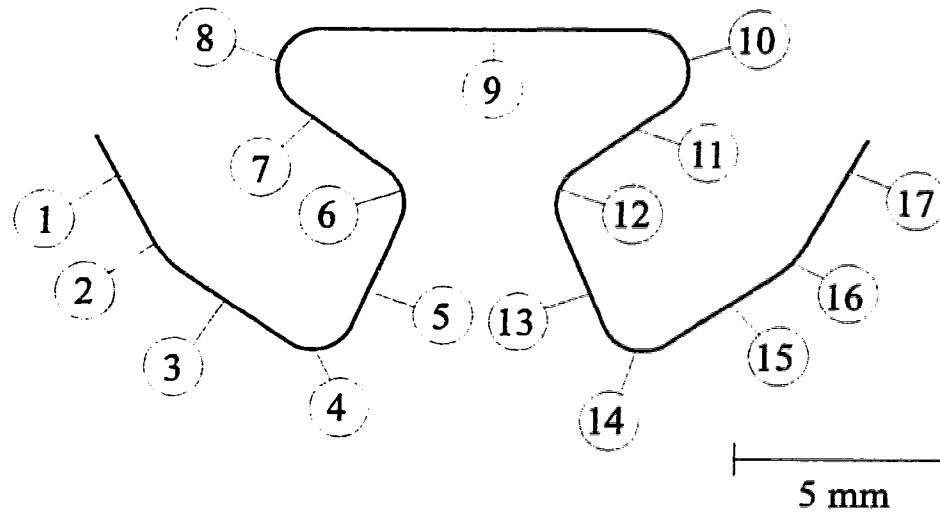


Figure 5.12: Geometry of Planar T-Spring

Table 5.1: Details of Segments Used to Model Planar T-Spring

Segment	Type	Length (mm)	Angle (°)	Radius (mm)
1	Straight	2.809	—	—
2	Curved	—	27.5	2.453
3	Straight	3.000	—	—
4	Curved	—	100	1.000
5	Straight	2.765	—	—
6	Curved	—	78	1.000
7	Straight	2.743	—	—
8	Curved	—	144.5	1.000
9	Straight	7.725	—	—
10	Curved	—	144.5	1.000
11	Straight	2.743	—	—
12	Curved	—	78	1.000
13	Straight	2.765	—	—
14	Curved	—	100	1.000
15	Straight	3.000	—	—
16	Curved	—	27.5	2.453
17	Straight	2.809	—	—

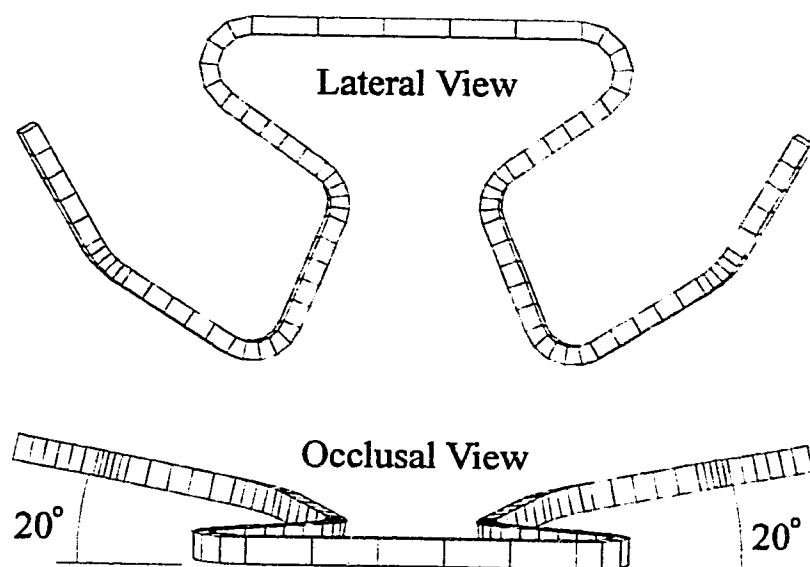


Figure 5.13: Lateral and Occlusal Views of Undeformed Preactivated T-Spring With Out-of-Plane Modifications

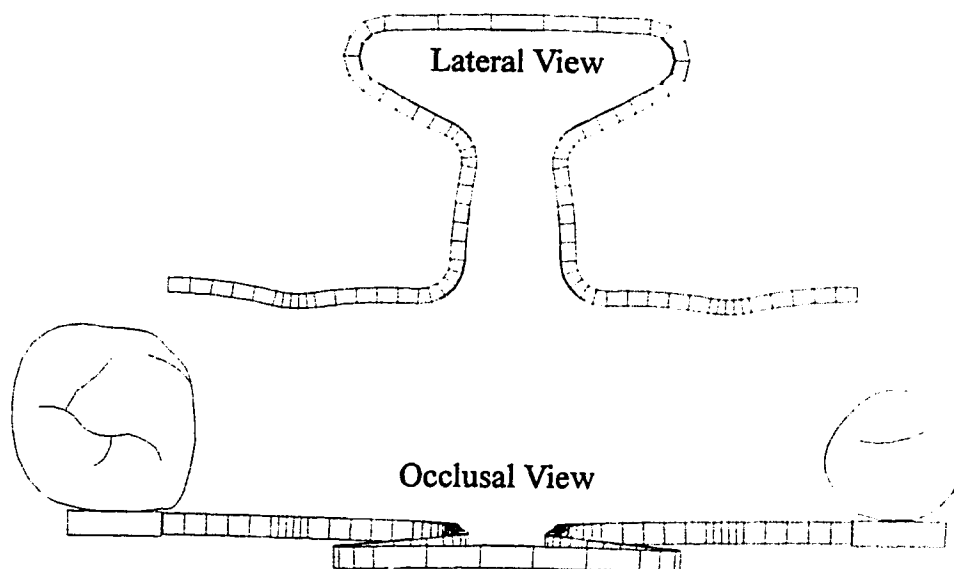


Figure 5.14: Lateral and Occlusal View of Preactivated T-Spring With Out-of-Plane Modifications in Fully Activated Configuration

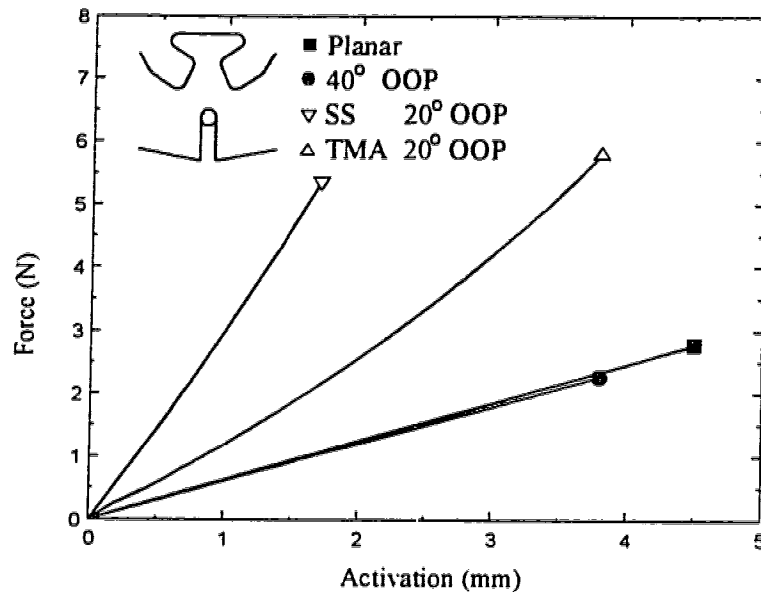


Figure 5.15: Comparison of Force-Activation Relationship For Planar T-Springs and T-Springs With Out-of-Plane Modifications

is required while the initially non-planar T-spring requires a three parameter shooting problem.

Figures 5.15, 5.16 and 5.17 illustrate the results for both the planar T-spring design as well as the T-spring with the out-of-plane modifications. As a comparison with the vertical loops discussed previously, results for Appliance #4 (vertical loop with an apical helix and preactivation), made of both stainless steel and TMA, with the out-of-plane modifications are included. Appliance #4 was chosen since it produced the best results (large elastic activation range, higher M^*/F and M/F ratios) of the vertical loops considered. Again, these springs are all compared based on the same interbracket distance (20 mm) at the maximum elastic activation for each design and material.

As is evident from Figures 5.15–5.17, the use of TMA dramatically increases the maximum elastic activation. The elastic range of the vertical loop increased from 1.7 mm with stainless steel to 3.8 mm with TMA for the same spring design. The force levels generated at the maximum elastic activation remain approximately the same so that the force-activation rate is ‘softened’ with the use of TMA. The material used, however, has little effect on the

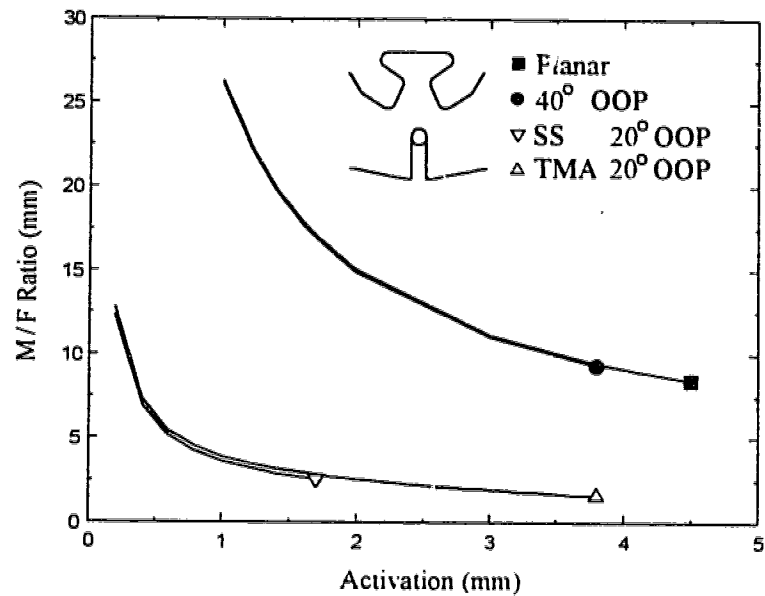


Figure 5.16: Comparison of M/F Ratios Generated By Planar T-Springs and T-Springs With Out-of-Plane Modifications

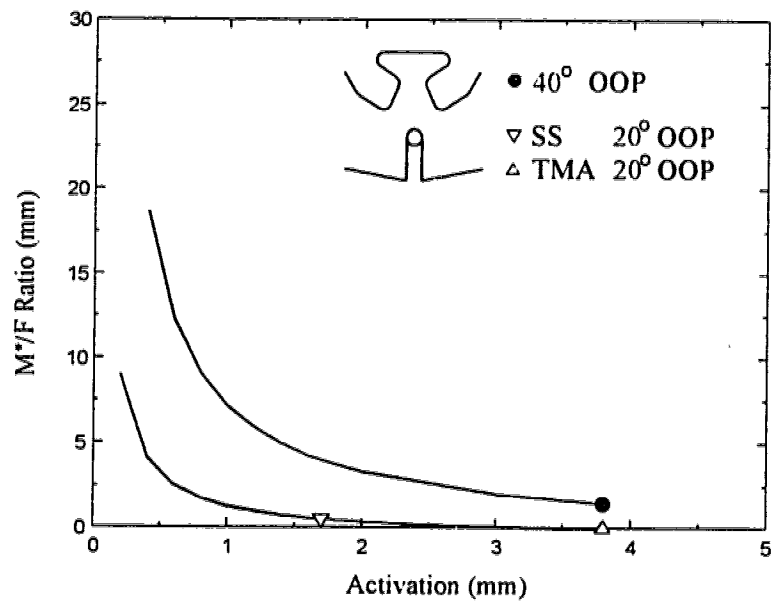


Figure 5.17: Comparison of M*/F Ratios Generated By Planar T-Springs and T-Springs With Out-of-Plane Modifications

M/F and M^*/F ratios other than the increased range of activation as can be seen in Figures 5.16 and 5.17. Note that the TMA vertical loop, due to its larger activation range, has shorter straight sections at the ends to maintain a 20 mm interbracket distance at maximum activation. This difference in initial geometry accounts for the slight difference between the two curves for activations below 1.7 mm. If both vertical loops had exactly the same initial geometry, the M/F and M^*/F ratios would be identical over this range.

The results for the T-spring in Figure 5.15 show a much softer force-activation relationship than for either of the vertical loops. The introduction of the out-of-plane modifications again has very little effect on this behavior apart from a change in the elastic range (from 4.5 mm for the planar appliance to 3.8 mm with the out-of-plane modifications). The forces generated at the maximum elastic activations are about half of those for the vertical loops.

The most significant difference is in the M/F and M^*/F ratios as seen in Figures 5.16 and 5.17. These values are considerably higher than those for the vertical loops over all activations. The M/F ratio at the maximum activation is approximately 8.5 mm which is very close to the value suggested to produce translation. As well, this behavior is essentially unaffected by the out-of-plane modifications. However, the out-of-plane bends generate a significant occlusal M^*/F ratio. At the maximum activation, the 40° out-of-plane T-spring produces a M^*/F ratio of approximately 1.4 mm. At a more intermediate activation, say 3.0 mm, this appliance produces lateral M/F and occlusal M^*/F ratios of approximately 12 mm and 2.5 mm respectively. At this activation, this design has the advantage of providing the appropriate force system in the lateral E_1 - E_2 plane as well as generating an occlusal system which helps prevent the tooth being retracted from rotating about its longitudinal axis.

5.4.2 Force Systems From Planar T-Springs Undergoing Non-Planar Activations

All of the above analysis has assumed that the two brackets which transfer the force system to the teeth are in the same lateral E_1 - E_2 plane. This is somewhat unrealistic for larger interbracket distances. As illustrated in Figure 5.18, with an interbracket distance of 20 mm the attachment points on the buccal surfaces could be at angles which are approximately 20° apart when measured in the occlusal plane. The use of an initially planar appliance in

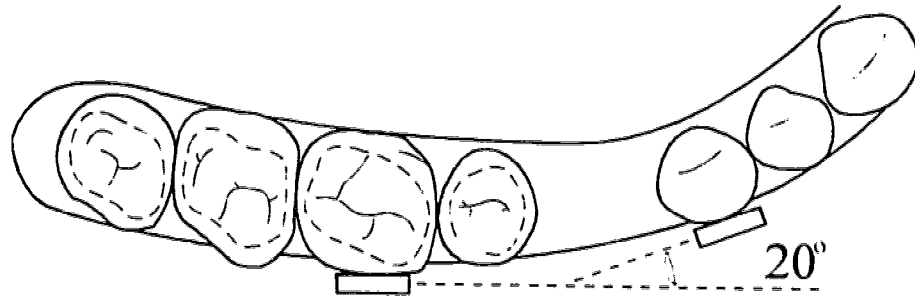


Figure 5.18: Occlusal View of Typical Non-Planar Situation

this situation affects the forces and moments produced when the appliance is inserted and activated. It can also produce clinically significant out-of-plane forces when the original planar appliance is brought first to the neutral position and then bent out of the plane to allow insertion into the non-aligned brackets. This occlusal E_1 - E_3 plane bend causes additional forces in the occlusal plane, an occlusal M^* moment and a torquing moment M_1 about the longitudinal axis of the appliance. These forces are in addition to the forces shown in Figures 5.15 and 5.16 for the planar appliance. The directions of these forces and moments (caused by the activation) applied to the appliance as well as to the anterior maxillary (upper front) tooth are shown in Figure 5.19. (Note that for a symmetric appliance placed symmetrically, $F_2 = 0$ which is the case being considered here.) Figures 5.20, 5.21 and 5.22 illustrate the force F_3 , the occlusal M^*/F ratio and the torquing moment M_1 produced when a planar symmetrically mounted T-spring is bent, inserted and activated (to an interbracket distance of 20 mm) with various angular differences between the ends measured in the occlusal plane. (Note that the boundary conditions for this problem are assumed to be as illustrated in Figure 5.5 and given by equations (5.6) and (5.7) with $F_2 = 0$.) The results indicate that bending of a planar design to fit a non-planar situation can generate clinically important forces and moments in ways which have not been previously discussed. As an example, the M^*/F ratio generated for an occlusal plane angular difference of 20° is approximately 1.7 mm. However, it is in the opposite to the direction of those discussed above so that it actually promotes rotation of the tooth about its longitudinal axis rather than inhibiting it. The occlusal force F_3 is not large (0.38 N for a 20° angular difference) but the torquing moment is approximately the same magnitude as

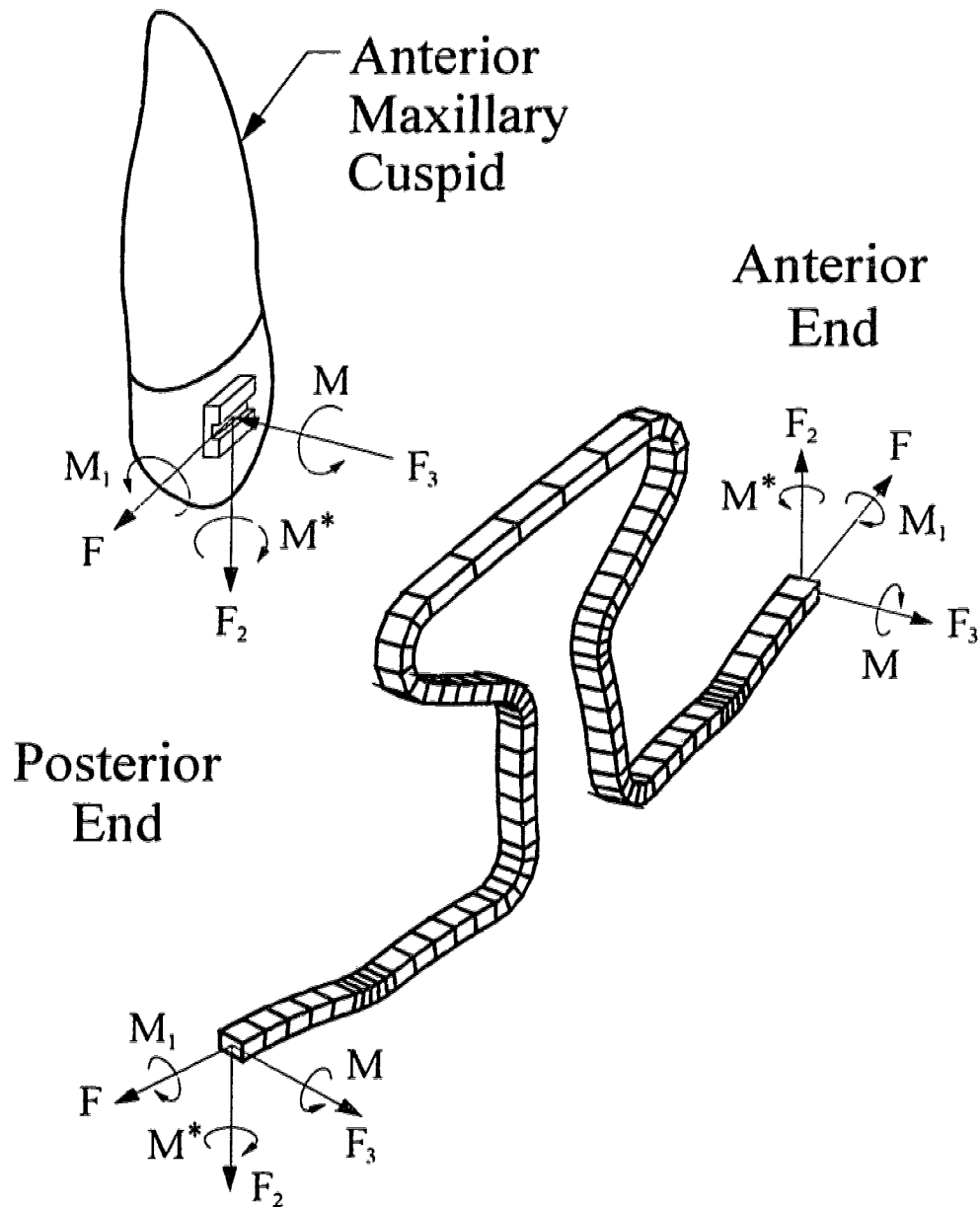


Figure 5.19: Directions of Forces and Moments Acting on Spring and Anterior Tooth in Non-Planar Situation

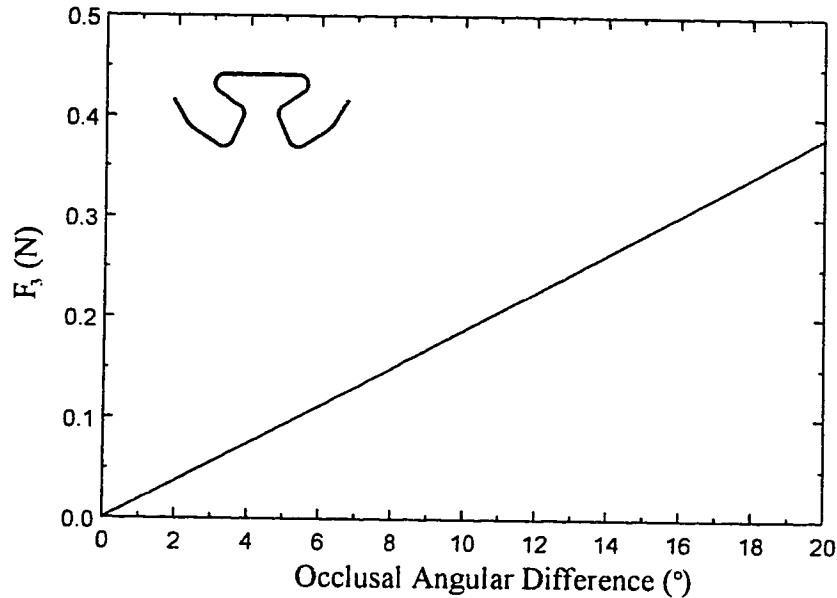


Figure 5.20: Occlusal Force F_3 as a Function of Angular Difference Between Brackets

the occlusal moment M_2 . Note that the torquing moment in this case would create a tendency for the crown of the tooth to rotate labially (towards the lips and cheeks) and the root lingually (towards the tongue). The net result of F_3 and M_1 is a possible labial-lingual rotation of the anterior tooth. It is difficult to determine the direction of this rotation or translation of the anterior tooth generally since it is highly dependent on the exact angle between the two ends of the bracket as well as the offset of the two brackets in the \mathbf{E}_1 - \mathbf{E}_3 plane as discussed previously in the lateral case for specific cases (Burstone and Koenig 1974). In the case considered here, the combination of F_3 and M_1 would tend to promote a translation of the anterior tooth towards the tongue. However, since the force level involved is quite low, not much movement would be expected. The out-of-plane preactivated bends discussed in Section 5.4.1 would counteract the effect of the M^* component developed by the occlusal plane angular difference between the brackets and help to prevent rotation of the anterior tooth about its longitudinal axis. Note again that, while not shown, the planar force system shown in Figures 5.15 and 5.16 (F and M/F ratio) remains virtually unchanged.

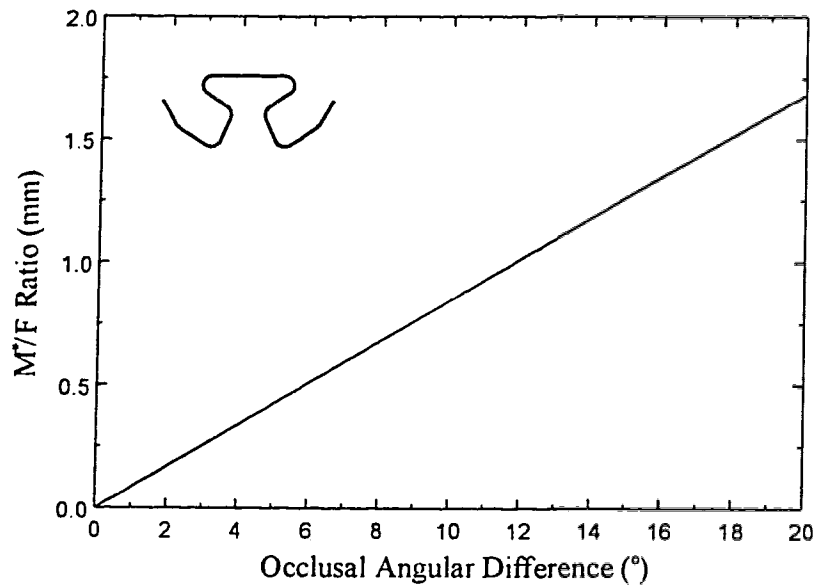


Figure 5.21: Occlusal M^*/F Ratio as a Function of Angular Difference Between Brackets

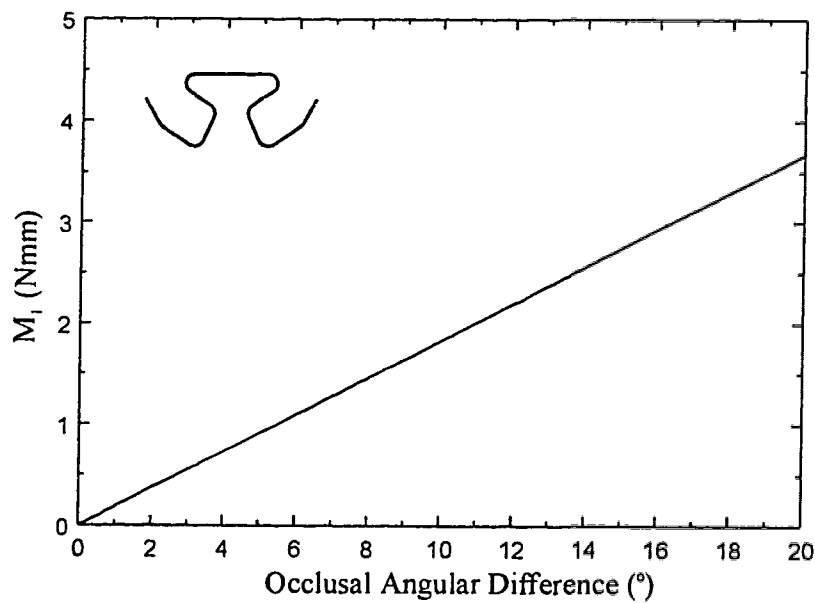


Figure 5.22: Torquing Moment M_1 as a Function of Angular Difference Between Brackets

5.5 Concluding Remarks

The numerical procedure developed in Chapter 3 has been used to analyze orthodontic retraction appliances undergoing large three-dimensional deformations. Appliances with both planar and non-planar initial configurations undergoing both planar and non-planar activations were considered. The use of a number of segments facilitated modeling of the complex initial geometries of the appliances investigated.

Vertical loops were found to have higher force-activation relationships than did the T-springs. Further, stainless steel vertical loops were found in general to be more sensitive to small changes in design, both in and out of the initial plane of the spring. The maximum elastic activation possible was mostly a function of the material used but also depends somewhat on the geometry. The out-of-plane design modifications introduced would partially counteract the tendency for the tooth to rotate about its longitudinal axis.

T-springs were found to have lower force-activation relationships and produce higher M/F ratios, both of which are desirable characteristics in a retraction appliance. TMA T-springs are far less sensitive to small changes in design and therefore to inaccuracies in the actual clinical manufacture and installation of these appliances. A total out-of-plane bend of 40° produces a force system which tends to promote tooth translation and inhibit rotation about its longitudinal axis. The necessity of using these out-of-plane bends was illustrated for a planar spring installed in typical non-planar situations. This unaltered spring would result in an increased tendency for longitudinal axis rotation.

Chapter 6

Nonlinear Elastic Materials: Shape Memory Alloys

In the previous chapters, a numerical procedure has been developed and implemented to solve three-dimensional rod problems. The method used was a shooting procedure which converted the original boundary problem into a sequence of initial value problems which converge to the desired boundary conditions. The rods were assumed to consist of materials with linearly elastic behavior. In this chapter, the numerical procedure is modified to account for materials which exhibit nonlinear elastic behavior. In particular, materials which show the shape memory effect will be considered. These materials have been shown to demonstrate such nonlinear effects as pseudoelasticity and hysteresis.

Although these shape memory alloys (such as NiTi) have been studied in the past, most of the work has been directed towards investigating the uniaxial extensional behavior of these materials (Shaw and Kyriakides 1995). Very little work appears to have been done with regards to quantifying the bending and torsional behavior of rods constructed with these materials. Further, no work has been done to investigate the coupling between these modes of deformation. Due to this lack of experimental results for verification, there are no accurate models which can quantitatively predict results for specific situations in which rods with shape memory alloys experience a combination of bending, torsion and extensional deformations. As a result, constitutive models which demonstrate *qualitative* agreement with the limited experimental results available will be proposed and implemented in the numerical procedure. The goal in this chapter will be to demonstrate that the numeri-

cal procedure developed in the preceding chapters for linear elastic materials is adaptable to consider nonlinear elastic materials as well.

To simplify this task and avoid unnecessary detail, the discussion will be limited to planar problems with bending as the only mode of deformation. Constitutive models, which in a qualitative sense model behaviors (i.e. pseudoelasticity and hysteresis) observed in these materials, will be described and modifications to the numerical procedure required to implement these models will be discussed. A number of examples will be discussed which show qualitative agreement with the limited planar results available. Two planar orthodontic retraction appliances will then be considered to take advantage of the ability of this material to deliver relatively constant force systems over a large elastic range which is a desirable characteristic for orthodontic wires.

Note that the decision to limit the investigation to include only planar results is made to simplify the discussion. It would be equally possible to consider fully three-dimensional deformations which demonstrate similar nonlinear behavior. However there is no known experimental work which has been done that encompasses all of these effects in three dimensions. Further, a planar analysis is sufficient to achieve the stated goal of demonstrating the adaptability of the numerical technique to include nonlinear elastic materials.

6.1 Constitutive Model For Shape Memory Alloys

Figure 6.1a shows the moment-curvature ($M_3 - \gamma_3$) relationship for linear elastic materials while Figure 6.1b illustrates a typical moment-curvature relationship assumed for the nonlinear materials considered in this work. As with the linear case, the dependence of the strain energy function (and therefore the moment) on the initial curvature of the rod (κ_3^0 only in the planar case) is assumed to be a function of the difference between the initial and final curvatures γ_3 only. Both figures show an anti-symmetry about the origin (i.e. $M_3(\gamma_3) = -M_3(-\gamma_3)$).

There are some important differences to note between these two figures. In the linear case, the slope of the $M_3 - \gamma_3$ relationship is constant with a slope of EI (the flexural rigidity of the beam). In the nonlinear case, this slope is not only variable with γ_3 but there are regions where the slope of the $M_3 - \gamma_3$ curve is negative. Equilibrium configurations which contain regions

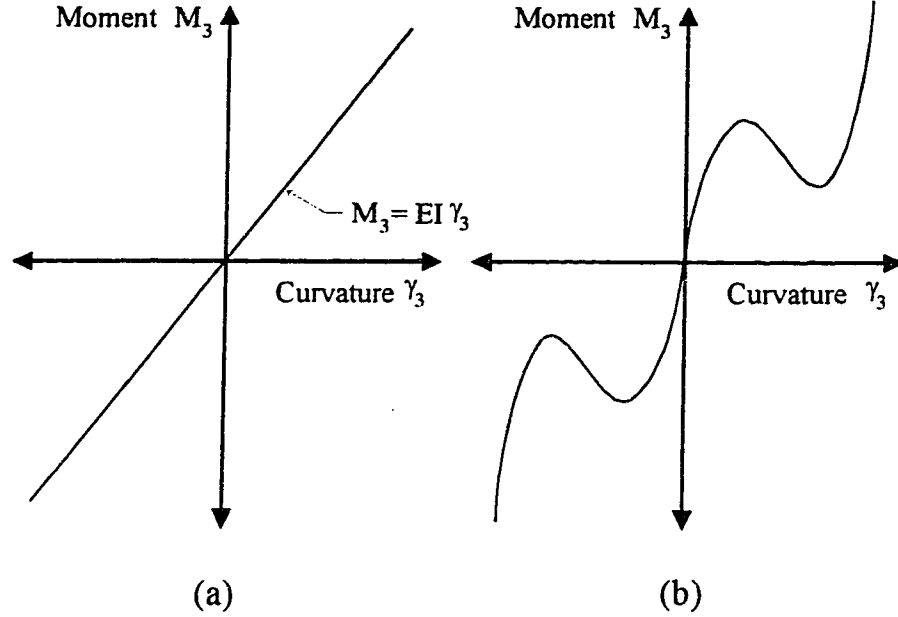


Figure 6.1: Comparison of Moment-Curvature Relationships: (a) Rods with Linear Elastic Materials. (b) Rods with Nonlinear Elastic Materials

with these curvatures could not be observed physically since they are unstable. In these regions, the material has violated the condition of convexity of the strain energy function which is required for stability (Fosdick and James 1981; James 1981; Steigmann and Faulkner 1993). For the planar case this convexity condition reduces to

$$\frac{\partial^2 U}{\partial \gamma_3^2} \geq 0 \quad (6.1)$$

or, using equation (2.7),

$$\frac{\partial M_3}{\partial \gamma_3} \geq 0. \quad (6.2)$$

Figure 6.2 illustrates a typical strain energy function from which the $M_3 - \gamma_3$ relationship in Figure 6.1b is obtained through equation (2.7). The dashed portions of this curve indicate regions where the strain energy function is non-convex (from equation (6.1)) and deformed configurations containing

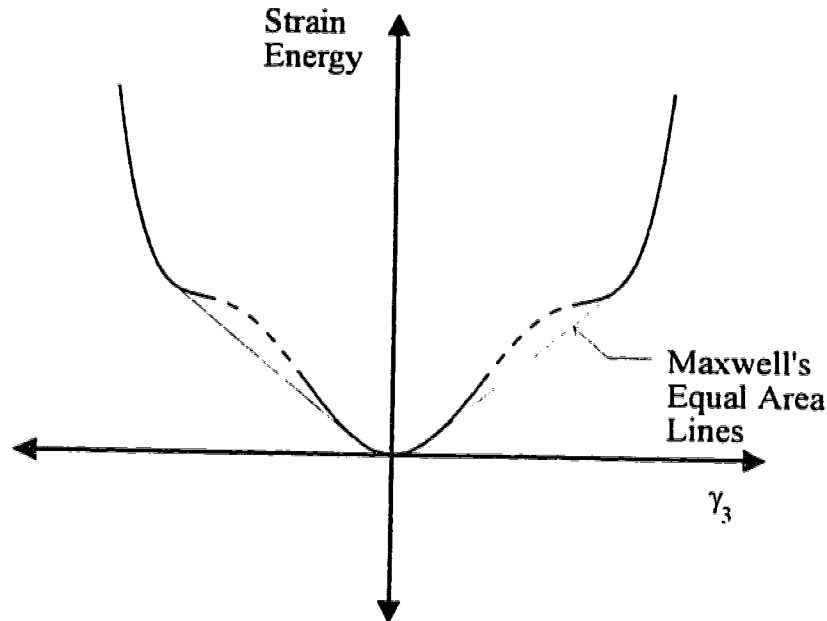


Figure 6.2: Typical Strain Energy Function for Nonlinear Elastic Materials

the associated curvatures are unstable. Also shown in Figure 6.2 are the *Maxwell's equal area lines* (James 1981) which will be discussed shortly.

In Figure 6.3, the region of unstable curvatures in the M_3 - γ_3 relationship (shown for $\gamma_3 \geq 0$ only) is indicated by the dashed portion of the curve. For equilibrium configurations to exist, it is possible for the curvatures to have discontinuities at a number of points along the rod. At such points, the curvature 'jumps' from one value to another value to exclude any curvatures which are in the unstable regions. Points at which this jumping behavior occurs are commonly referred to as *corners*¹. At these points of discontinuity, there are certain necessary conditions which must be satisfied for equilibrium. Steigmann and Faulkner (1993) have investigated this requirement for three-dimensional inextensible deformations of rods while Fosdick and James (1981) and James (1981) have considered this type of behavior for the planar inextensible case. Fosdick and James (1981) and James (1981) show that at

¹However, this does not imply that at these points there are kinks in the rod with sharp changes in direction. Even though there are step discontinuities in the curvature, the position coordinates and tangent direction of the rod remain smooth so that the term *corner* in this respect is somewhat misleading.

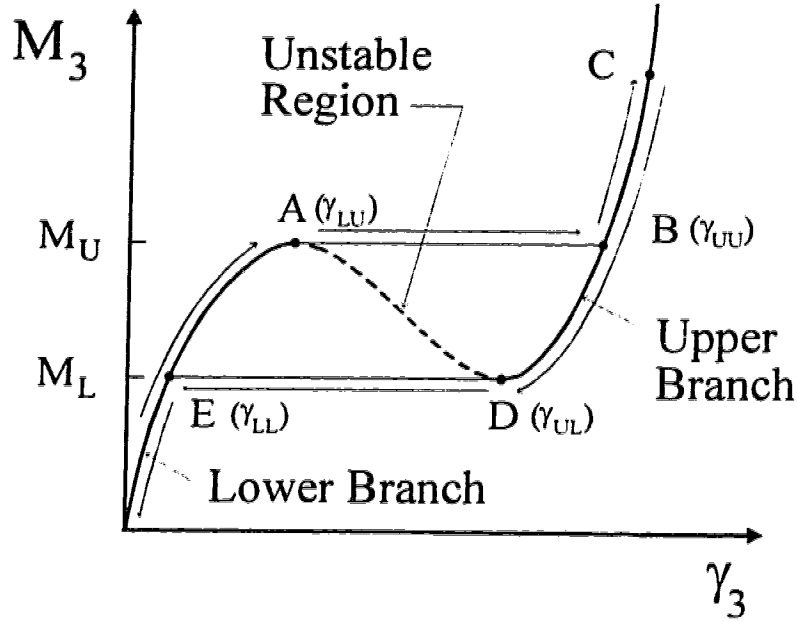


Figure 6.3: Loading/Unloading Behavior of Shape Memory Alloys

such points the moment must be continuous, i.e.

$$\Delta M_3 = 0 \quad (6.3)$$

where ΔM_3 is the difference between the moments on either side of the discontinuity. Thus in Figure 6.3 the solid lines joining points A–B and E–D (which are the points at which the discontinuities in curvature would occur to exclude the unstable regions) are horizontal so that a constant moment is maintained across the discontinuity.

To illustrate the behavior of this material, in particular the hysteresis effects, consider a material point undergoing a cycle of loading and unloading as shown in Figure 6.3. As the moment applied to the material is increased from zero, the curvature increases towards point A in Figure 6.3. Once the moment reaches the value M_U which occurs at a curvature value of γ_{LU} ², a further increase results in a jump to point B on the upper branch (indicated by a solid line) since this is the only curvature region associated with moment

²The first subscript refers to the branch (*Upper* or *Lower*). The second refers to the moment value at the discontinuity (*Upper* or *Lower*).

values above M_U . Increasing the moment further results in the curvature increasing to point C. Now as the moment is reduced, the curvature reduces as well. When the moment falls below M_U the curvature does not jump to the lower branch at point A, but rather continues along the upper branch until point D is reached. At this point the curvature jumps back to the lower branch at point E where further reductions in the moment cause the curvature to approach zero. Thus for moments in the ranges $M_3 < M_L$ or $M_3 > M_U$ there is only one associated curvature value. In the range $M_L < M_3 < M_U$ there are two stable curvatures (plus one unstable value which will never exist in a physical situation) associated with each moment. In this range, the particular curvature value which the material will adopt depends upon the loading history of the material. Note that the hysteresis described above is such that in a loading and unloading cycle, energy will be dissipated by the material. The loop could not be in the other direction (i.e. counterclockwise) or energy would be created by the material.

Maxwell's equal area lines, shown in Figure 6.2, are called "equal area" lines since they divide equal areas in the $M_3 - \gamma_3$ plot as shown in Figure 6.4 for $\gamma_3 > 0$. The slope of these lines in Figure 6.2 are the constant moments at which the discontinuities occur as shown in Figure 6.4. These lines define the behavior of a particular material which is absolutely stable in the sense that only curvatures whose tangent in Figure 6.2 is below the *entire* curve are allowed³ (note that this excludes some of the solid line in Figure 6.2 which would correspond to weakly stable configurations (James 1981)). When this type of behavior is observed, discontinuities in the curvature are still allowed (as shown in Figure 6.4) but there will be no hysteresis since the loading and unloading curves will be the same.

The behavior of the SMA material is very dependent upon the temperature. Below a certain temperature, the nonlinear effects of hysteresis and pseudoelasticity will be present. At higher temperatures, a nonlinear moment-curvature relationship (i.e. variable flexural rigidity) is still present, but curvature discontinuities will not occur since all regions of the strain energy function will be regions of convexity. Falk (1980) has proposed a sixth order polynomial Helmholtz free energy function to model shape memory effects concerning shear deformations of single crystals which models this temperature dependency. There are four polynomial coefficients which can be varied independently to model specific materials. Temperature appears

³Such points are called points of *super-convexity* (Fosdick and James 1981).

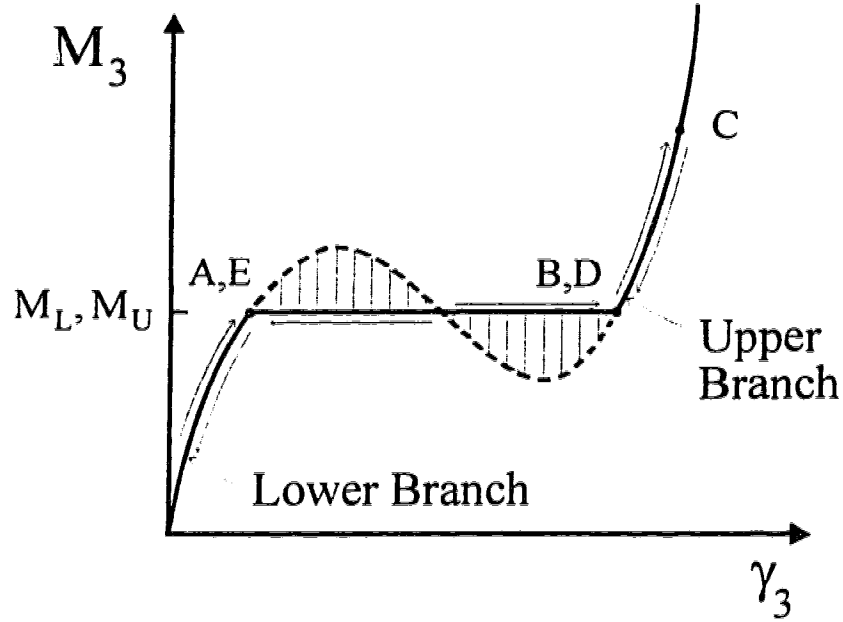


Figure 6.4: $M_3 - \gamma_3$ Relationship Following Maxwell's Equal Area Rule

as a separate parameter which affects the shape of the free energy function and the position of the stress-strain relationship. A similar form could be used to model the nonlinear $M_3 - \gamma_3$ relationship which takes the temperature effect into account. However, since the purpose in this work is only to demonstrate qualitative agreement with experimental results, a somewhat simpler relationship, referred to here as a *bilinear* model will be employed. In this model, the effects of temperature are not included explicitly as this is not required for the present objectives.

6.1.1 Bilinear Constitutive Model

An example of a moment-curvature relationship considered for *bilinear* materials in this work is shown in Figure 6.5. In this model, two separate linear moment-curvature relationships exist. There are critical moment and curvature values which define regions of unstable curvatures and divide the moment-curvature relationship into *lower* and *upper* branches as shown. The

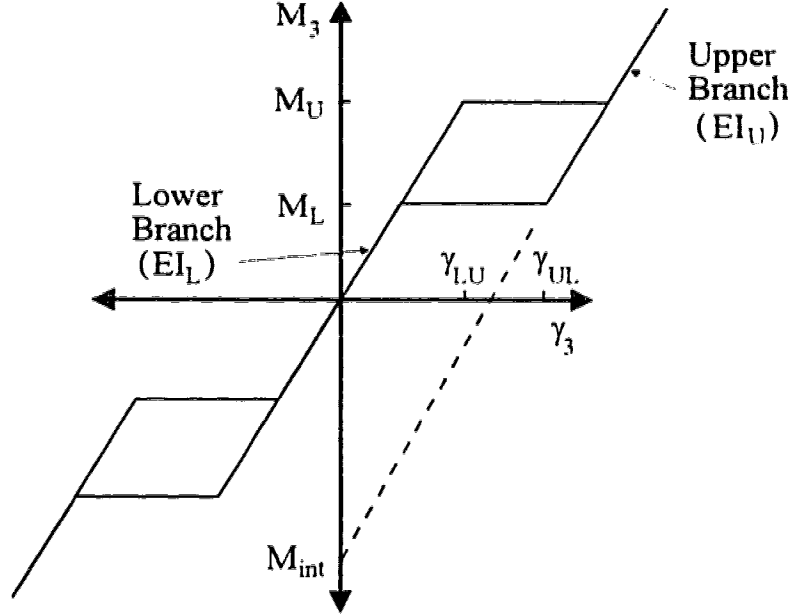


Figure 6.5: Bilinear Constitutive Model for Shape Memory Alloys

moment-curvature relationship on each of these branches is given by

$$M_3 = \begin{cases} EI_L \gamma_3 & \text{Lower Branch,} \\ EI_U \gamma_3 + \hat{M}_{\text{int}} & \text{Upper Branch,} \end{cases} \quad (6.4)$$

where

$$\hat{M}_{\text{int}} = \begin{cases} M_{\text{int}} & \gamma_3 > 0, \\ -M_{\text{int}} & \gamma_3 < 0. \end{cases} \quad (6.5)$$

M_{int} is a negative number which fixes the position of the upper branch vertically as shown in Figure 6.5. The definitions in equation (6.5) are necessary because the two upper branches (one on either side of the origin) have moment intercepts with the opposite sign. In this model the parameters which must be specified include the slope of each of the two branches (EI_L and EI_U), the moment intercept ($M_{\text{int}} < 0$) which translates the upper branches vertically as well as the lower and upper critical moment values (M_L and M_U respectively) at which the discontinuities occur. Note that from equations (2.7), (6.1) and (6.4) convexity of the strain energy function is satisfied

provided $EI_L > 0$ and $EI_U > 0$ for the regions $\gamma_{LU} < |\gamma_3|$ and $|\gamma_3| > \gamma_{UL}$. In the region $\gamma_{LU} > |\gamma_3| < \gamma_{UL}$ the curvatures are assumed to be unstable so that it is unnecessary to define the M_3 - γ_3 relationship specifically over this region.

The strain energy function for this material becomes, upon integration of equation (2.7),

$$U = \begin{cases} \frac{1}{2}EI_L(\kappa_3^2 - 2\kappa_3\kappa_3^0) + c_L & \text{Lower Branch,} \\ \frac{1}{2}EI_U(\kappa_3^2 - 2\kappa_3\kappa_3^0) + \hat{M}_{int}\kappa_3 + c_U & \text{Upper Branch.} \end{cases} \quad (6.6)$$

where c_L and c_U are constants of integration. However, since the reference configuration (from which κ_3 is measured) is taken to be the undeformed shape (with no strain energy), the integration constant for the lower branch becomes

$$c_L = \frac{1}{2}EI_L(\kappa_3^0)^2 \quad (6.7)$$

so that equation (6.6) becomes

$$U = \begin{cases} \frac{1}{2}EI_L\gamma_3^2 & \text{Lower Branch,} \\ \frac{1}{2}EI_U(\kappa_3^2 - 2\kappa_3\kappa_3^0) + \hat{M}_{int}\kappa_3 + c_U & \text{Upper Branch.} \end{cases} \quad (6.8)$$

This is referred to as a *natural* reference configuration (Fosdick and James 1981). However, c_U cannot in general be fixed using similar arguments.

Using equations (6.4) and (6.8), the energy integral (I_E) defined in equation (2.3) becomes

$$I_E = \begin{cases} \frac{1}{2}EI_L(\kappa_3^{02} - \kappa_3^2) - F_1 - (Xb_1 + Yb_2) & \text{Lower Branch,} \\ -\frac{1}{2}EI_U\kappa_3^2 - F_1 - (Xb_1 + Yb_2) + c_U & \text{Upper Branch.} \end{cases} \quad (6.9)$$

Note that if the discontinuities follow Maxwell's equal area rule as discussed previously, the energy integral is required to be constant across the discontinuity (Fosdick and James 1981; James 1981) which would then fix the value of c_U . In such a case, M_L and M_U would be the same and there would be no hysteresis during loading/unloading although there would still be a discontinuity in the M_3 - γ_3 relationship.

6.2 Numerical Procedure For the Planar Situation

In this section the kinematics and equilibrium equations presented in Chapter 3 will be simplified for the planar case where there is only bending about one principal axis and no twist. The development described in section 3.1.1 will be followed and specialized for planar results. As well, the numerical technique developed in Chapter 3 will be adapted to include the bilinear constitutive model discussed in Section 6.1.1 which will be used to model the shape memory materials.

6.2.1 Kinematics and Equilibrium

When the discussion is limited to planar problems, equation (3.1) becomes

$$\begin{Bmatrix} \mathbf{e}_1 \\ \mathbf{e}_2 \\ \mathbf{e}_3 \end{Bmatrix} = [\mathbf{R}_p] \begin{Bmatrix} \mathbf{e}_1^0 \\ \mathbf{e}_2^0 \\ \mathbf{e}_3^0 \end{Bmatrix}, \quad (6.10)$$

where

$$[\mathbf{R}_p] = \begin{bmatrix} \cos \phi & \sin \phi & 0 \\ -\sin \phi & \cos \phi & 0 \\ 0 & 0 & 1 \end{bmatrix}. \quad (6.11)$$

$[\mathbf{R}_p]$ is the rotation matrix for planar problems. In the planar case only two material vectors deform since the orientation of \mathbf{e}_3 remains constant in the \mathbf{E}_3 direction. As a result only one angle is necessary to specify the orientation of the *material basis* in terms of the *local basis* (whereas three Euler angles are required in the three-dimensional situation⁴) and there are therefore no problems with singularities in the planar representation as with the Euler angles in three dimensions.

Only bending (about the \mathbf{e}_3 axis which never changes orientation) is considered so the curvature along the rod reduces to

$$\kappa_3 = \phi' \quad (6.12)$$

which is obtained from equations (3.3), (6.10) and (6.11) and where the $'$ notation again indicates differentiation with respect to arclength.

⁴Note that equations (3.2) and (6.11) are equivalent when $\theta = 0$ and $\psi = 0$.

The coordinates of the rod segment in the *global basis* can again be expressed using equation (3.8) where now $\{\mathbf{r}(s)\} = \{X(s), Y(s), 0\}$, $\{\mathbf{r}(0)\} = \{X(0), Y(0), 0\}$ and $\{\mathbf{x}(s)\} = \{x(s), y(s), 0\}$ since only planar deformations are considered. The coordinates of the centerline of the rod then satisfy

$$x'(s) = \cos \phi, \quad y'(s) = \sin \phi, \quad z'(s) = 0 \quad (6.13)$$

in the *local basis*.

The first equation of equilibrium, given in equation (2.2a), can again be integrated for the planar case to yield

$$\mathbf{F} = F_i \mathbf{e}_i. \quad (6.14)$$

where

$$\begin{Bmatrix} F_1 \\ F_2 \\ F_3 \end{Bmatrix} = [\mathbf{R}_p] \begin{Bmatrix} F_1^0 - b_1 s \\ F_2^0 - b_2 s \\ 0 \end{Bmatrix} \quad (6.15)$$

following a development similar to that in Section 3.1.1 but limited to planar results. The right hand side of equation (2.2b) then becomes

$$\mathbf{F} \times \mathbf{e}_1 = -F_2 \mathbf{e}_3 \quad (6.16)$$

so that the second equilibrium equation can be written as

$$\mathbf{M}' = -F_2 \mathbf{e}_3. \quad (6.17)$$

As a result, only the \mathbf{e}_3 component of this equation is nonzero. Equation (6.17) can therefore be written as a single scalar equation

$$M'_3 = (F_1^0 - b_1 s) \sin \phi - (F_2^0 - b_2 s) \cos \phi. \quad (6.18)$$

where equations (6.11) and (6.15) have been used.

Constitutive relationships are required to specify the function M'_3 and complete the governing equation (6.18). The next section discusses the implementation of the constitutive model presented in Section 6.1.1 into the numerical procedure.

6.2.2 Modifications To Include Bilinear Constitutive Models

When bilinear constitutive models (see section 6.1.1) are specified, the moment-curvature relationship is defined separately for each of the two distinct curvature regions, referred to here as the *lower* and *upper* branches. The model employed here is

$$M_3 = \begin{cases} EI_L \gamma_3 & \text{Lower Branch,} \\ EI_U \gamma_3 + \hat{M}_{im} & \text{Upper Branch,} \end{cases} \quad (6.19)$$

where \hat{M}_{im} is defined in equation (6.5). The equilibrium equation (6.18) for this material then becomes

$$\begin{aligned} EI_L \phi'' &= (F_1^0 - b_1 s) \sin \phi - (F_2^0 - b_2 s) \cos \phi & \text{Lower Branch,} \\ EI_U \phi'' &= (F_1^0 - b_1 s) \sin \phi - (F_2^0 - b_2 s) \cos \phi & \text{Upper Branch,} \end{aligned} \quad (6.20)$$

which, using the dimensionless parameters

$$\begin{aligned} \rho &= \frac{s}{L}, \quad \kappa_3 = \kappa_3 L, \quad \gamma_3 = \gamma_3 L \\ \nu_i &= \frac{F_i L^2}{EI_L}, \quad \lambda_i = \frac{b_i L^3}{EI_L}, \quad \Gamma = \frac{EI_U}{EI_L}, \end{aligned} \quad (6.21)$$

can be written as

$$\ddot{\phi} = \begin{cases} (\nu_1^0 - \lambda_1 \rho) \sin \phi - (\nu_2^0 - \lambda_2 \rho) \cos \phi & \text{Lower Branch,} \\ \frac{1}{\Gamma} [(\nu_1^0 - \lambda_1 \rho) \sin \phi - (\nu_2^0 - \lambda_2 \rho) \cos \phi] & \text{Upper Branch.} \end{cases} \quad (6.22)$$

6.2.3 Integration Procedure

When the bilinear constitutive model for shape memory alloys is implemented, the numerical procedure proceeds in a similar fashion as previously described in Chapter 3 with one significant difference. As shown in Figure 6.3 shape memory materials can, over a certain range of moments, demonstrate hysteresis in which the particular curvature assumed by the material depends on whether the moment is increasing or decreasing at that point so that the loading history of the material must be taken into account. It is therefore

necessary to take a previous state of the material into consideration to determine which branch (lower or upper) of $M_3 - \gamma_3$ relationship should be used in the integration at each material point in the rod.

This previous state of the material is recorded in the form of a moment distribution, at a particular load, in which the moment and branch (lower or upper) at each arclength is recorded. In the undeformed reference state, this moment distribution is simply a zero moment (on the lower branch) everywhere in the rod. The numerical integration proceeds along the rod as before until a discontinuity in the curvature is encountered. When a discontinuity in the curvature is approached, the step size of the integration is continually reduced until it falls below a minimum tolerance. At this point, the discontinuity is considered to have been reached, and the curvature is changed accordingly. The integration then proceeds as before using the appropriate branch in equation (6.22). A simple example is presented here to illustrate the application of these concepts.

A cantilever beam, of shape memory alloy, under the action of a dead tip load is shown in Figure 6.6a. Figure 6.6b shows the constitutive model used for this material. Only one half of the $M_3 - \gamma_3$ relationship is shown for convenience since all the curvatures in this problem will be in the same (negative) sense. Seven distinct points (A-F) are labeled along the cantilever for reference. Points B and C' are immediately next to each other. In the unloaded state shown, there is no moment or curvature change anywhere

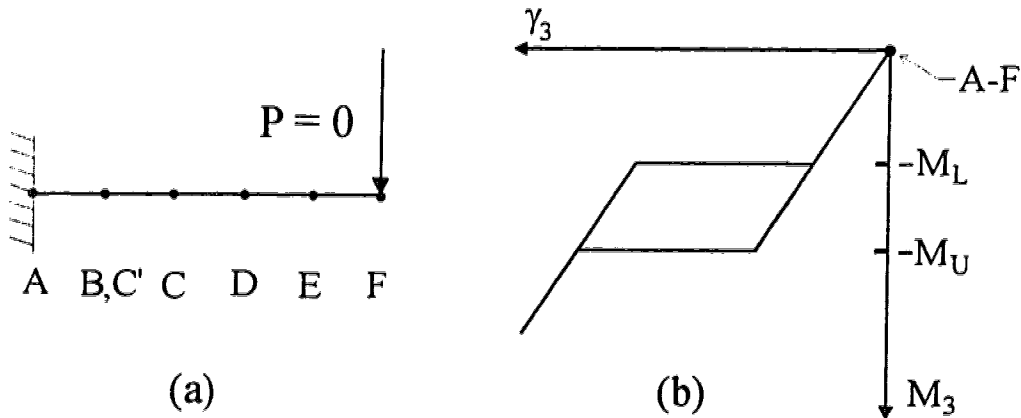


Figure 6.6: Cantilever of Shape Memory Alloy Under a Dead Tip Load: (a) Problem Definition, (b) Constitutive Model of Material in Unloaded Configuration

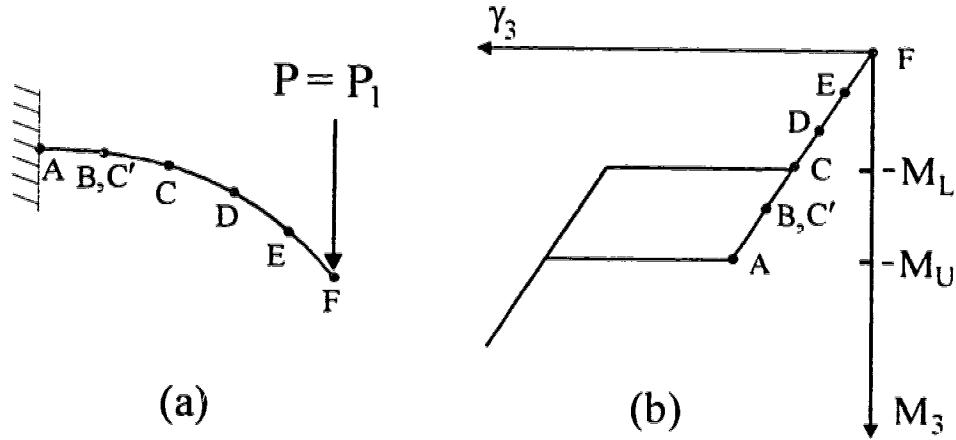


Figure 6.7: Cantilever of Shape Memory Alloy Under Dead Tip Load. Loaded to P_1 : (a) Deformation of Beam, (b) Location of Material Points on Constitutive Diagram

along the cantilever so all of the material points indicated (A–F) are on the origin in the $M_3 - \gamma_3$ curve as shown in Figure 6.6b.

As the load P is increased, to P_1 say, the cantilever deforms as shown in Figure 6.7a. The individual material points A–F experience the moments and curvatures as indicated in Figure 6.7b. Point F, which is at the free end of the cantilever and therefore experiences no moment, remains at the origin of the $M_3 - \gamma_3$ curve. Point A is the fixed end of the beam and thus is subjected to the largest moment in this problem. At the load shown, the magnitude of the moment at this location is immediately below M_U so that all of the curvatures remain on the lower branch. If the load P is then increased slightly, the moment at the fixed end increases to M_U at which point a jump to the upper branch (high curvature region) occurs for a very small region near the fixed end of the beam.

As the load is again increased (to a value P_2) the deformed shape is as shown in Figure 6.8a. More material near the fixed end jumps to the high curvature region as this material experiences moments greater than M_U as shown in Figure 6.8b. Note that, since the high curvature region is located in the material near the fixed end of the beam, the result is a large movement of the beam tip (free end). Let the value of P_2 be such that all of the material between points A and B inclusive is in the high curvature region. Point C' is immediately next to point B but is in the low curvature region (i.e. lower

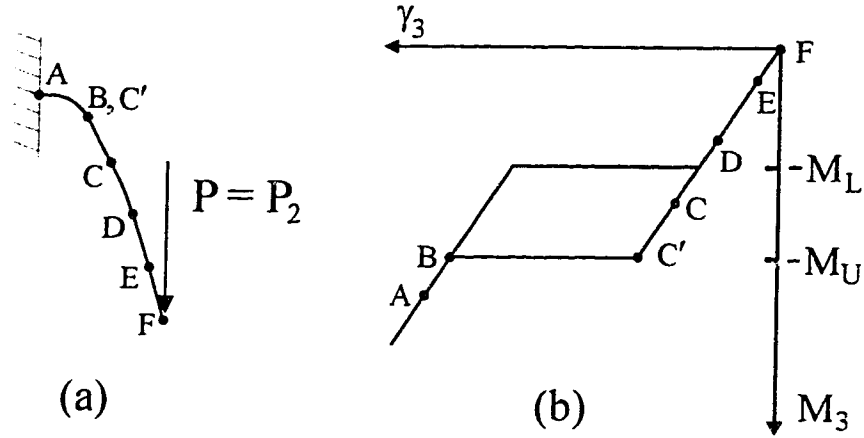


Figure 6.8: Cantilever of Shape Memory Alloy Under Dead Tip Load. Loaded to P_2 : (a) Deformation of Beam. (b) Location of Material Points on Constitutive Diagram

branch). (Note that between points B and C' there is a discontinuity in the curvature although the tangent at these points remains smooth.) This is demonstrated in Figure 6.8b which shows that the material between points A and B is in the high curvature region while the material between points C' and F is in the low curvature region.

The load P_2 will be the maximum load for this problem. Now the load will be reduced back to zero. Since the beam is being unloaded from this reference load, the moment distribution (including the appropriate branch) along the beam corresponding to the load P_2 is recorded. This information is to be used to determine which branch should be used in the integration procedure for each material point in the beam. Note that when the load was being applied to the beam, the reference moment configuration was simply no moment anywhere in the beam.

Consider the situation in which the load is reduced back to $P = P_1$. Figure 6.9a shows the resulting deformation of the beam while Figure 6.9b illustrates the curvatures and moments experienced by the material points. Although the curvatures between points A and B have been reduced somewhat as the load has been reduced, the material between these points is still in the high curvature region. Recall that this material was in the low curvature region when the beam was loaded to this same load value as shown in Figure 6.7b. This difference is due to the hysteresis in this material as

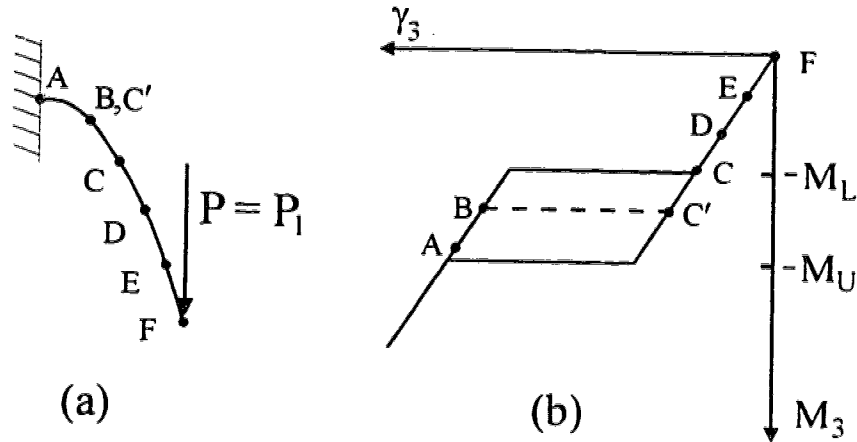


Figure 6.9: Cantilever of Shape Memory Alloy Under Dead Tip Load, Unloaded to P_1 : (a) Deformation of Beam, (b) Location of Material Points on Constitutive Diagram

described in Section 6.1 and results in a much larger tip deflection than when the same load P_1 was applied originally (as opposed to being removed) as in Figure 6.7a. This is because the material near the fixed end is still in the high curvature region. The material between points C' and F experienced no discontinuities upon loading and remained in the low curvature region at the maximum load P_2 as shown in Figure 6.8b. Therefore, no hysteresis will occur in this material region as the load is removed so that Figures 6.7b and 6.9b are identical over the material region C'-F.

As a result of the above behavior, the discontinuity in curvature, which occurred at a moment of M_U when the load was being applied, now occurs at a moment below this value (but above M_L). However, the moment is still continuous across the discontinuity as indicated by the dashed line in Figure 6.9b. This situation continues until the load P is lowered to the point where the moment at point B reaches M_L . As the load is then reduced slightly below this value, the material at point B jumps back to the lower branch as discussed previously. Thus slightly less material is in the high curvature region and slightly more material is now on the lower branch. As the load is further reduced, more material from the upper branch jumps to the low curvature region which causes the moment at which the curvature discontinuity occurs to reduce further. This continues until the load is reduced to a value (say P_L) such that the moment at point A reaches M_L which

causes the last bit of material at the fixed end to jump back to low curvature region. Thus there are no discontinuities in curvature and the deformed shapes of the beam are identical for both loading and unloading to the same value below P_L .

6.3 Numerical Results

In this section numerical results will be presented for four separate problems. The predicted behavior of shape memory alloys (SMA) in these situations using the constitutive model described above will be compared to two linear elastic materials, stainless steel (SS) and Titanium Molybdenum Alloy (TMA). Rectangular wires with 0.406×0.559 mm (0.016×0.022 inch) cross sections will be considered in each case. Again, the goal is to show that qualitative agreement with experimental results can be obtained and to demonstrate the differences in behavior from linear elastic materials.

The properties of the materials considered in this section are shown in Table 6.1. The material properties for the stainless steel and TMA are discussed in Chapter 5. The Young's modulus for the shape memory alloy is taken from the tensile results of Miura et al. (1986). For the bilinear model two elastic moduli are needed. In the examples which follow it will be assumed that $EI_U = EI_L$ for the shape memory alloys considered. The critical lower and upper moments at which the discontinuities in curvature occur are selected to be $M_L = 5$ Nmm and $M_U = 10$ Nmm while the intercept value for the upper branch is assumed to be $M_{int} = -20$ Nmm. These values are arbitrary (i.e. not selected to represent any particular material) but are chosen so that the problems to be discussed in subsequent sections will experience discontinuous curvatures.

Table 6.1: Material Properties

Material	Young's Modulus	Yield Strength
	(GPa)	(MPa)
SS	177	1400
TMA	69	1240
SMA	50	N/A

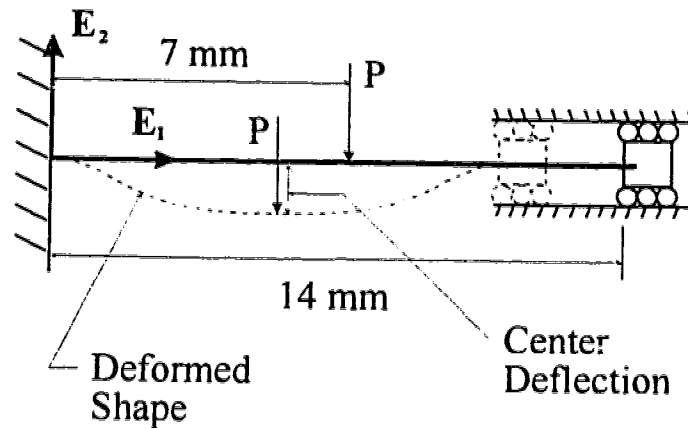


Figure 6.10: Clamped-Slider Problem

The yield strength, as it is defined for linear elastic materials, has no real meaning when shape memory alloys are considered. The yield strength will only be used to determine approximate elastic ranges, using the procedure outlined in Appendix D simplified to consider only planar deformations, for the stainless steel and TMA materials for each of the problems considered. This will serve as a guide as to how much load to apply to the shape memory alloys since no other better indication is available.

6.3.1 Clamped-Slider Problem

The first problem considered is shown in Figure 6.10. The initially straight beam is rigidly fixed at one end. The other end is constrained to have a horizontal slope but is free to move in the \mathbf{E}_1 direction. The load P is applied at the center of the beam in the negative \mathbf{E}_2 direction. This problem was chosen since it closely approximates a three-point bending situation for which there are previous experimental results.

When the analysis is limited to planar problems, the boundary conditions which must be specified simplify considerably. A single angle (ϕ) and only two spatial coordinates (X and Y in the \mathbf{E}_1 and \mathbf{E}_2 directions respectively) are all that are required to specify the orientation and location at a material point. Further, the shear force F_3 and the moment components M_1 and M_2 must be zero for planar problems. The result is that only six initial values (compared to twelve for the three dimensional case) must be specified.

Due to the symmetry in this problem only one half of the beam needs to

be considered. At the fixed end of the beam the initial coordinates are given by

$$X = 0, \quad Y = 0, \quad (6.23)$$

while the initial material basis is

$$\begin{Bmatrix} \mathbf{e}_1 \\ \mathbf{e}_2 \end{Bmatrix} = \begin{bmatrix} 1 & 0 \\ 0 & 1 \end{bmatrix} \begin{Bmatrix} \mathbf{E}_1 \\ \mathbf{E}_2 \end{Bmatrix}, \quad (6.24)$$

which corresponds to $\phi = 0$. At the fixed end the force components are

$$\begin{aligned} F_1 &= 0, \\ F_2 &= \frac{P}{2}, \end{aligned} \quad (6.25)$$

due to the symmetry. The initial moment M_3 is unknown so this becomes a one parameter shooting problem. The known boundary condition comes from the fact that, due to the symmetry, the slope at the center of the beam must be zero so that

$$\phi_{\text{center}} = 0. \quad (6.26)$$

The vertical deflection at the center of the beam for the three materials considered are shown in Figure 6.11. Both the stainless steel and the titanium molybdenum alloy beams show linear load-deflection relationships with the stainless steel beam having a higher slope due to the material's larger modulus of elasticity. The maximum elastic deflection at the center of the beam is limited to 0.316 mm for the stainless steel. The deflection of the TMA beam is considerably larger at 0.714 mm although the maximum elastic load is slightly less (10.89 N versus 12.26 N for the stainless steel beam).

When the shape memory alloy is considered, the load is applied up to the maximum elastic load for the stainless steel (since this is the larger of the two elastic materials). At the maximum load, the deflection of the center of the beam is much larger at 2.14 mm. The load-deflection relationship is linear up to a deflection of approximately 0.4 mm. At this point a plateau is reached over which the slope flattens out over a considerable range and then increases again. As the load is removed the load-deflection curve is again linear down to a deflection of about 1.65 mm where another plateau is reached until a deflection of about 0.25 mm where the unloading plateau joins

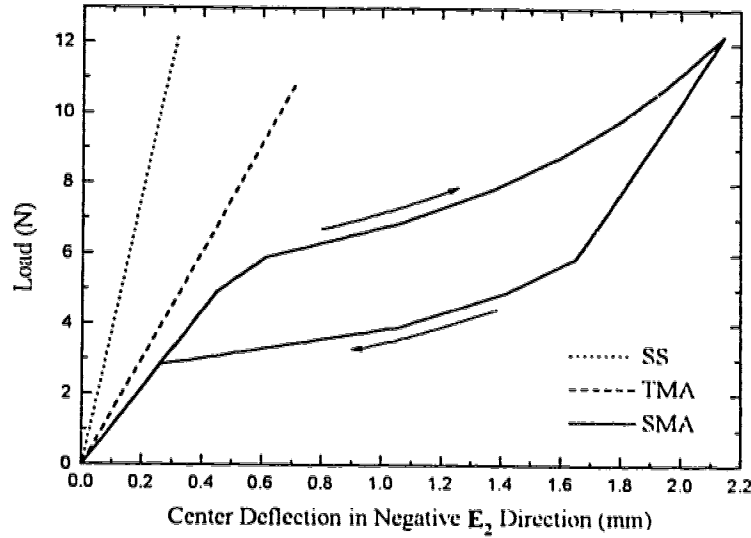


Figure 6.11: Vertical Deflections at Center of Beam for Clamped Slider Problem

the loading curve. Over the loading and unloading plateaus the slope of the load-deflection curves are reduced so that the load remains relatively constant over a large range of deflections. This qualitative behavior is consistent with results for three point bending tests reported by Miura et al. (1986) and Duerling et al. (1990)⁵.

Figures 6.12a–d illustrates the response of the clamped-slider beam with the bilinear shape memory alloy material at the maximum load considered. As can be seen in these figures nearly half of the beam is in the high curvature region (indicated by the thick lines in Figure 6.12a) which is evenly divided between the two ends. In fact, the deformation of the half beam considered in Figure 6.12a is itself symmetric so that it would have been only necessary to consider 1/4 of the beam. The smoothness of the moment at the discontinuous curvatures can be clearly seen in Figures 6.12c and d.

⁵Note that the boundary conditions modelled in the present work were chosen for simplicity. The descriptions in the works mentioned did not give clear indications of what the boundary conditions were in the actual experimental setup.

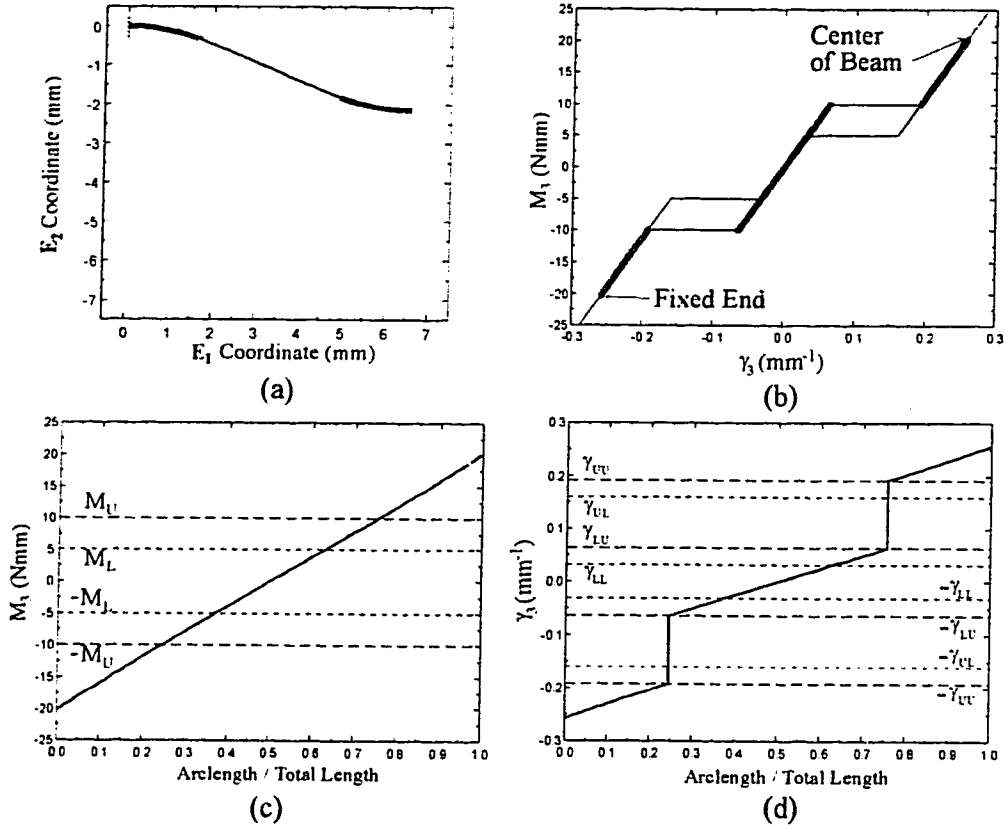


Figure 6.12: Moment and Curvature Distribution of Bilinear Clamped-Slider Problem at the Maximum Load 12.26 N: (a) Deflected Shape. (b) Constitutive Diagram, (c) Moment Distribution. (d) Curvature Distribution

6.3.2 Initially Curved Cantilever Beam

Figure 6.13 illustrates the next problem considered. An initially curved cantilever beam (initially in the \mathbf{E}_1 - \mathbf{E}_2 plane) is acted upon by a dead tip load in the \mathbf{E}_1 direction.

At the free end of the beam the initial material basis is

$$\begin{Bmatrix} \mathbf{e}_1 \\ \mathbf{e}_2 \end{Bmatrix} = \begin{bmatrix} \cos \phi_0 & \sin \phi_0 \\ -\sin \phi_0 & \cos \phi_0 \end{bmatrix} \begin{Bmatrix} \mathbf{E}_1 \\ \mathbf{E}_2 \end{Bmatrix}, \quad (6.27)$$

which is in terms of the initial angle ϕ_0 which is unknown. (In the undeformed position $\phi_0 = 90^\circ$.) At the free end the moment M_3 must be identically zero

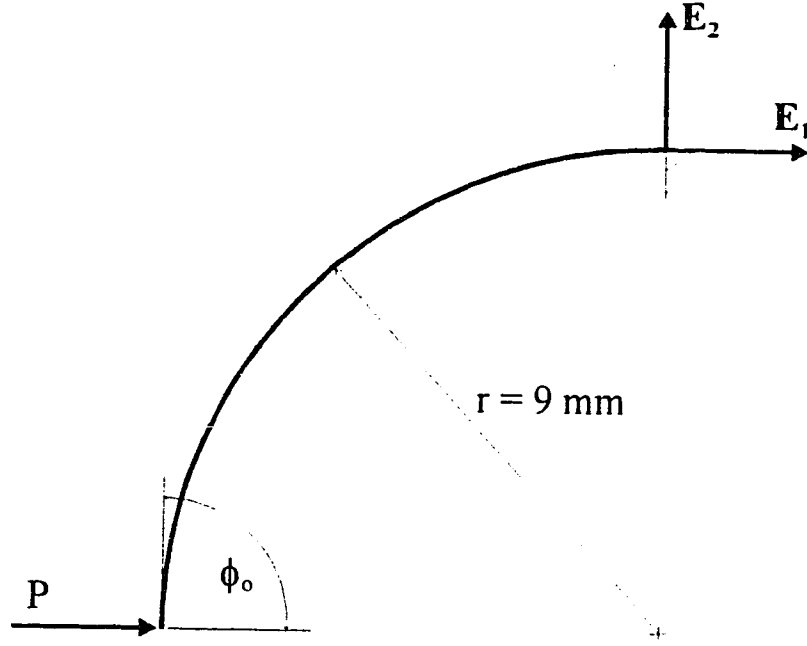


Figure 6.13: Initially Curved Cantilever Beam With Tip Load

while the force components are given by

$$\begin{aligned} F_1 &= P \cos \phi_0, \\ F_2 &= -P \sin \phi_0, \end{aligned} \quad (6.28)$$

so that all of the unknowns at the free end of the beam are a function of the unknown initial angle. This is therefore once again a one parameter shooting problem. The known boundary condition comes from the fact that at the fixed end of the beam the slope must be zero so that

$$\phi_{\text{fixed end}} = 0. \quad (6.29)$$

Note that, as shown in Figure 6.13, the fixed end of the cantilever is at the coordinates

$$X = 0, \quad Y = 0, \quad (6.30)$$

while the coordinates at the start of the beam (free end) are unknown initially. This could, therefore, be posed as a three parameter shooting problem

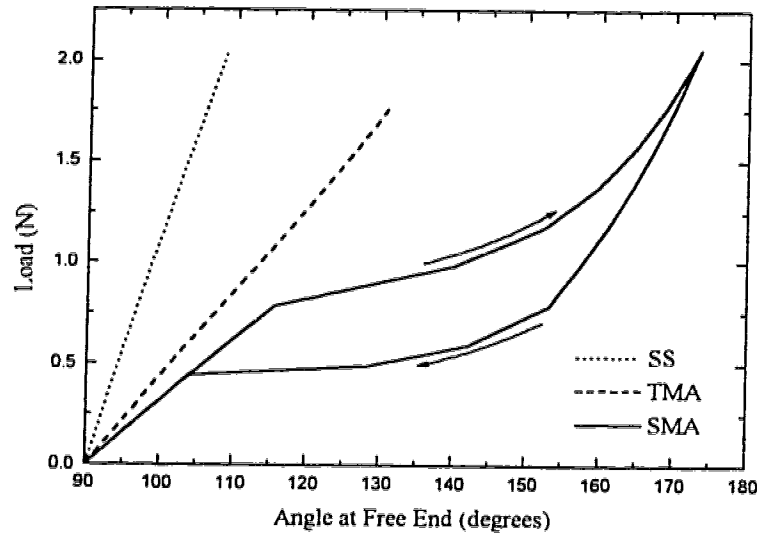


Figure 6.14: Initial Angle at Free End for Initially Curved Cantilever Beam

with ϕ_0 , X and Y at the free end as the initial unknowns and ϕ , X and Y at the fixed end as the known boundary conditions. However, the choice of initial position X and Y simply translates the entire beam without affecting the forces applied or the resulting deformation. Thus, the problem is posed as a one parameter shooting problem as specified above. After the solution is obtained a rigid body transformation is applied to the coordinates to move the fixed end of the beam to the origin. This is done because shooting problems with fewer parameters generally have a faster and more well behaved convergence (Faulkner et al. 1993). In this particular case the convergence would very likely have been well behaved in the three parameter problem, but it is usually good practice to reduce the number of unknowns as much as possible.

Figure 6.14 shows the results for this problem in terms of the initial angle at the free end of the beam as a function of the load applied for the three materials considered. This figure appears very similar to the results shown for the clamped-slider problem. The stainless steel material once again undergoes a smaller elastic displacement while supporting the greater load than does the TMA material. This can be explained by the much higher elastic modulus of the stainless steel.

The response of the SMA beam is also very similar qualitatively to that for the clamped-slider problem. The tip deflection at maximum load is once

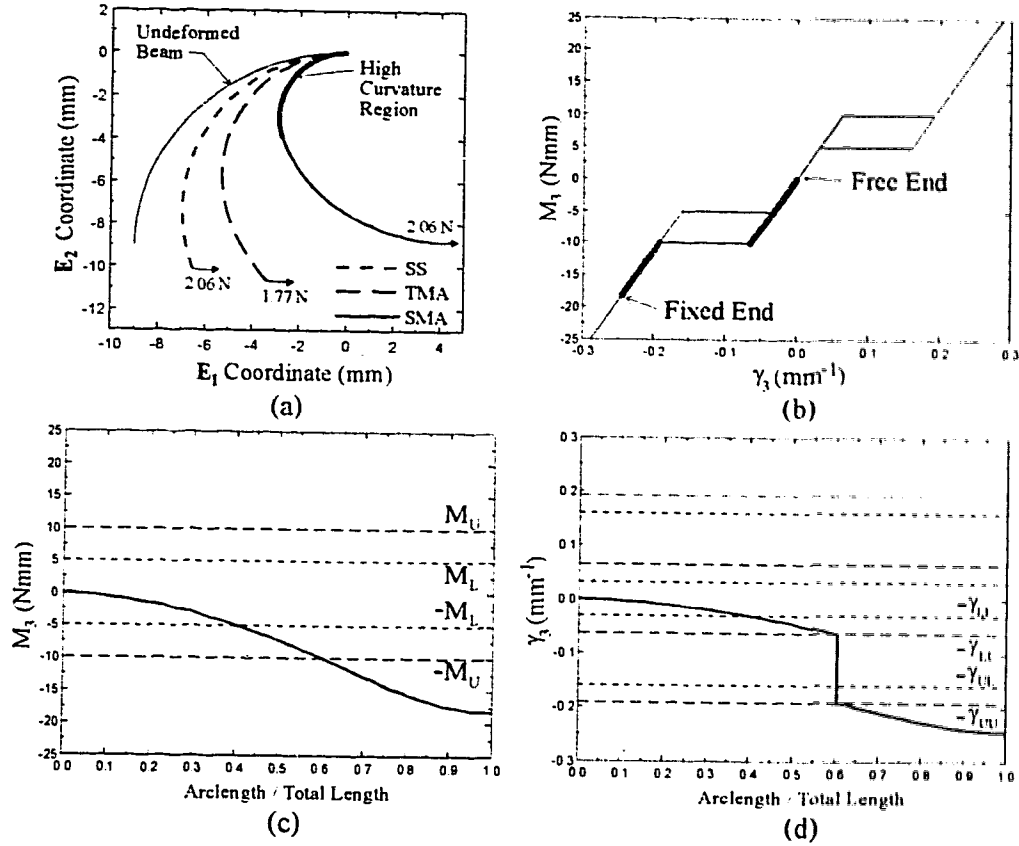


Figure 6.15: Moment and Curvature Distribution in Bilinear Curved Cantilever Problem at the Maximum Load 2.06 N: (a) Deflected Shape, (b) Constitutive Diagram, (c) Moment Distribution, (d) Curvature Distribution

again much higher than for either the stainless steel or TMA materials as shown in Figure 6.15a. (Note that the tip loads at the maximum elastic activation are once again different for the two linearly elastic materials.) There are also linear elastic relationships in Figure 6.14 over a small range at the start of both loading and unloading. As well there are again loading and unloading plateaus over which the load-deflection slope is lower and relatively constant forces are applied at the beam tip over a large elastic range.

Figures 6.15b-d illustrates the response along the beam with the bilinear shape memory material at the maximum load. In this case all of the high curvature material is near the fixed end and involves about 40% of the total

beam length. This high curvature region near the the fixed end allows the large tip movement to occur. Again, the smoothness of the moment at the curvature discontinuity can be clearly seen.

6.3.3 Orthodontic Retraction Appliances

Structures made of shape memory alloys have the ability to provide relatively constant forces over large elastic ranges as demonstrated in the previous two examples. As discussed in Chapter 5, these are properties which are desirable in orthodontic appliances which are required to apply specific force systems to reposition teeth in the dental arch. (A more detailed discussion is given in Chapter 5.) In the past orthodontists have attempted to obtain these desired characteristics using appliances with complex initial geometries to overcome some of the limitations inherent in the materials used.

In this section, two typical appliance designs will be reconsidered under the assumption that the material is a shape memory alloy and behaves according to the bilinear constitutive relationship used up to this point. The purpose is to investigate what benefits could be obtained using shape memory alloys for orthodontic retraction springs.

6.3.3.1 Vertical Loop

The first appliance considered is the simple vertical loop with the same initial geometry as Appliance #1 shown in Figure 5.6a. The boundary conditions for this problem are the same as those discussed in Section 5.3.1 so that a two parameter shooting procedure is involved.

Figure 6.16 shows the resulting behavior for the vertical loops constructed of each of the three materials considered. Note that the curves corresponding to the stainless steel vertical loop are identical to those shown in Figure 5.6b-d for Appliance #1 and are repeated here for comparison. The maximum elastic activation of the TMA vertical loop has increased to 2.3 mm compared to the 1.0 mm maximum activation for the stainless steel. As well, the force-activation and M_3 -activation curves have lower slopes for the TMA than for the stainless steel which can be explained by the lower modulus of elasticity of TMA. The M_3/F ratio is exactly the same for both of these materials apart from the fact that the curve for the TMA vertical loop extends further due to its increased elastic range. This is because, as explained in Chapter 5, the

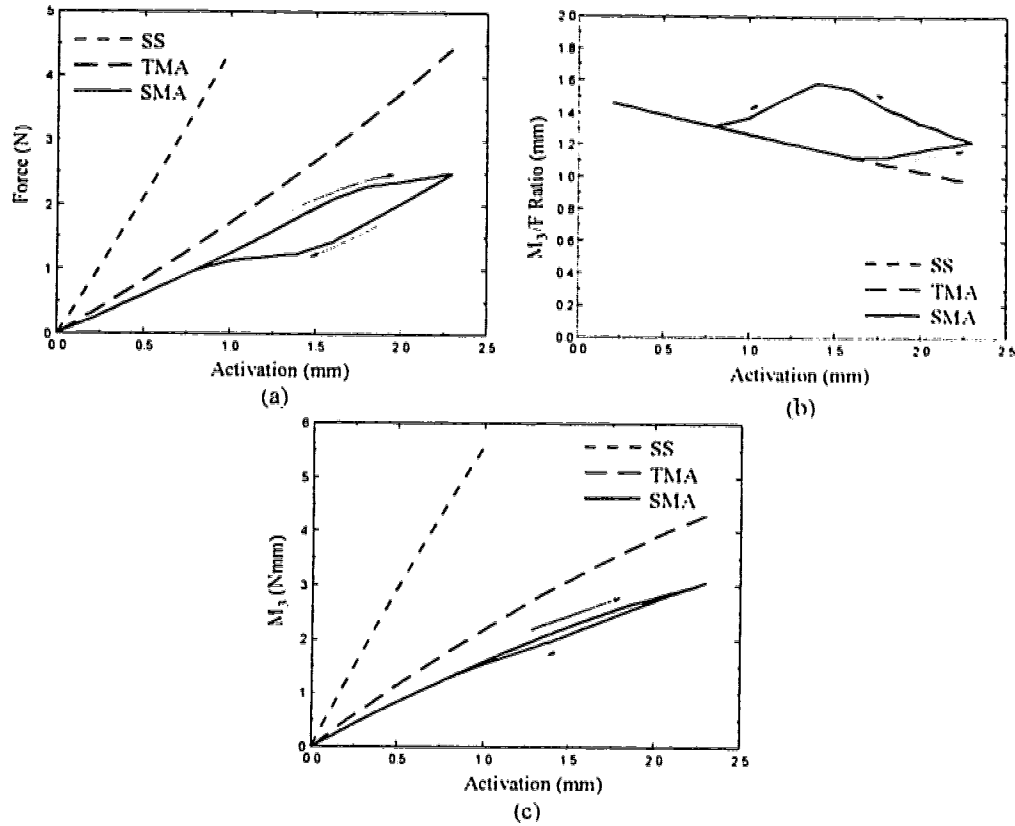


Figure 6.16: Results for Planar Vertical Loop Problem: (a) Force-Activation Relationship, (b) M_3/F Ratios, (c) M_3

M_3/F ratio depends only on the initial geometry for linear elastic materials and is independent of the modulus of elasticity.

The vertical loop made of the shape memory alloy was investigated up to an activation of 2.3 mm, which again was the largest elastic activation possible with the two linear elastic materials considered. This seems to be a reasonable assumption since these materials are typically able to experience large elastic deformations which should be at least as large as the TMA vertical loop. Figure 6.16 demonstrates behavior which is consistent with the results of the previous two examples. Although the maximum activation considered is the same as that of the TMA vertical loop (for comparison), the forces and moments produced at this activation are smaller which indicates lower force-deflection ratio. Further, on unloading there is hystere-

sis apparent which is more noticeable in the force relationship than for the moment. This results in the M_3/F ratio in Figure 6.16b initially increasing during unloading before eventually reducing and converging with the loading curve. These characteristics (softer force-deflection relationship and increased M_3/F ratios) are desirable in orthodontic appliances.

Figures 6.17a-d illustrate the moment and curvature distributions in the SMA vertical loop at the maximum activation considered. As can be seen from these figures, only a small amount of material near the top of the loop is in the high curvature region. This explains the limited amount of hysteresis apparent in Figure 6.16c.

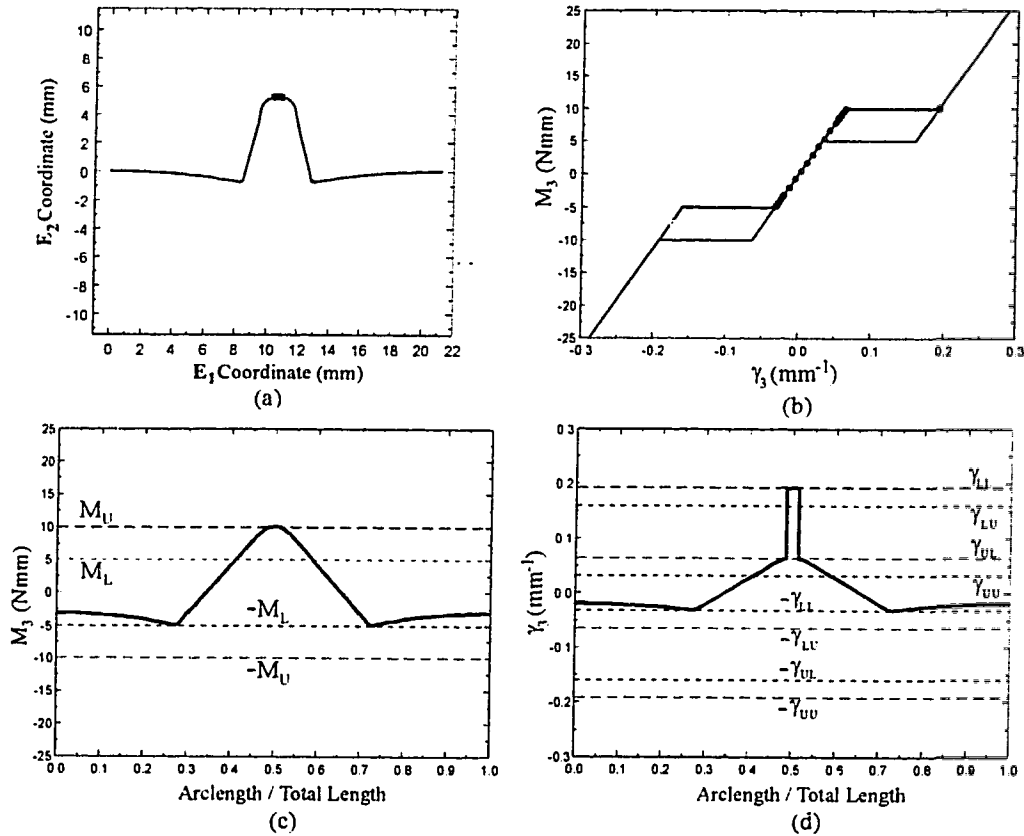


Figure 6.17: Moment and Curvature Distribution in Bilinear Vertical Loop Problem at the Maximum Activation 2.3mm: (a) Deflected Shape, (b) Constitutive Diagram, (c) Moment Distribution, (d) Curvature Distribution

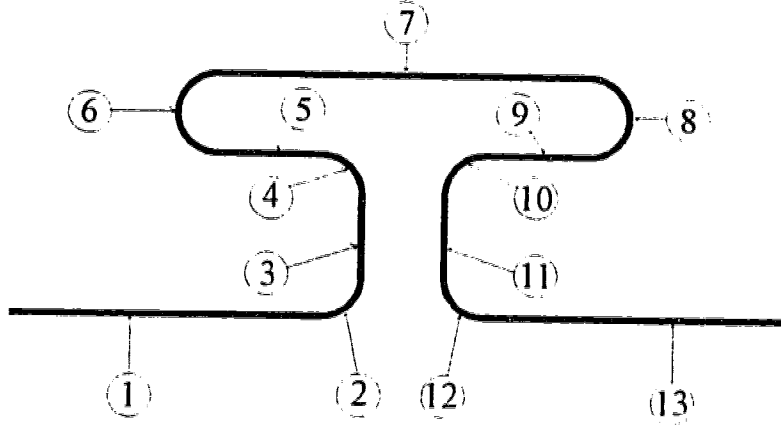


Figure 6.18: Geometry of Standard T-Spring

6.3.3.2 T-Spring

The final appliance considered is a standard T-spring. These T-springs are often initially preactivated (as shown in Figure 5.12) to increase M_3/F ratios. However, for simplicity the standard T-spring as shown in Figure 6.18 and with dimensions given in Table 6.2 will be considered. In this case only 1/2 of the spring is analyzed and symmetry is assumed. This is to help improve the convergence behavior and decrease computational effort. The boundary conditions for this problem are therefore the same as for the vertical loop except that the two known conditions required to use the shooting procedure are now at the center of the spring and are

$$X_{\text{center}} = \frac{\text{Neutral Length} + \text{Activation}}{2}, \quad \phi_{\text{center}} = 0. \quad (6.31)$$

Figure 6.19 shows the results obtained for each of the three materials considered. As before, the stainless steel T-spring produced higher forces and moments at a smaller maximum elastic activation than did the TMA T-spring indicating larger force-activation and moment-activation ratios. The maximum elastic activation for each of these materials increased over those of the vertical loops considered previously. This demonstrates that the initial geometry as well as the material used is important in determining this characteristic. As with the vertical loops, the M_3/F ratios for the linear elastic material are identical (apart from the larger range of the TMA T-spring) due to the fact that identical initial geometries were used.

Table 6.2: Details of Segments Used to Model Planar T-Spring

Segment	Type	Length (mm)	Angle (°)	Radius (mm)
1	Straight	7.5	—	—
2	Curved	—	90	1.0
3	Straight	2.0	—	—
4	Curved	—	90	1.0
5	Straight	2.5	—	—
6	Curved	—	180	1.0
7	Straight	9.0	—	—
8	Curved	—	180	1.0
9	Straight	2.5	—	—
10	Curved	—	90	1.0
11	Straight	2.0	—	—
12	Curved	—	90	1.0
13	Straight	7.5	—	—

The SMA T-spring was analyzed to an activation of 6.7 mm which was the maximum elastic activation of the two linear elastic T-springs considered. Figure 6.19 shows that the T-spring responds similarly to the vertical loops when SMA is used. The forces and moments produced at the maximum activation considered are lower than the stainless steel or TMA T-springs which indicates lower force-deflection ratios. Figures 6.19a and c show that the force and moment remain much more constant over a larger range than do the SMA vertical loops in Figure 6.16. When the appliance is de-activated, there is once again hysteresis which results in the M_3/F ratio in Figure 6.19c increasing initially during unloading before eventually converging with the activation curve. The M_3/F ratios produced with this appliance are somewhat higher than with the vertical loop for all of the materials considered. Note that they are still well below that suggested for tooth translation and some preactivation would still be required in order to achieve the suggested M_3/F ratio.

Figures 6.20a–d illustrate the moment and curvature distributions in the SMA T-spring at the maximum activation considered. As can be seen from these figures there are two distinct high curvature regions at the maximum

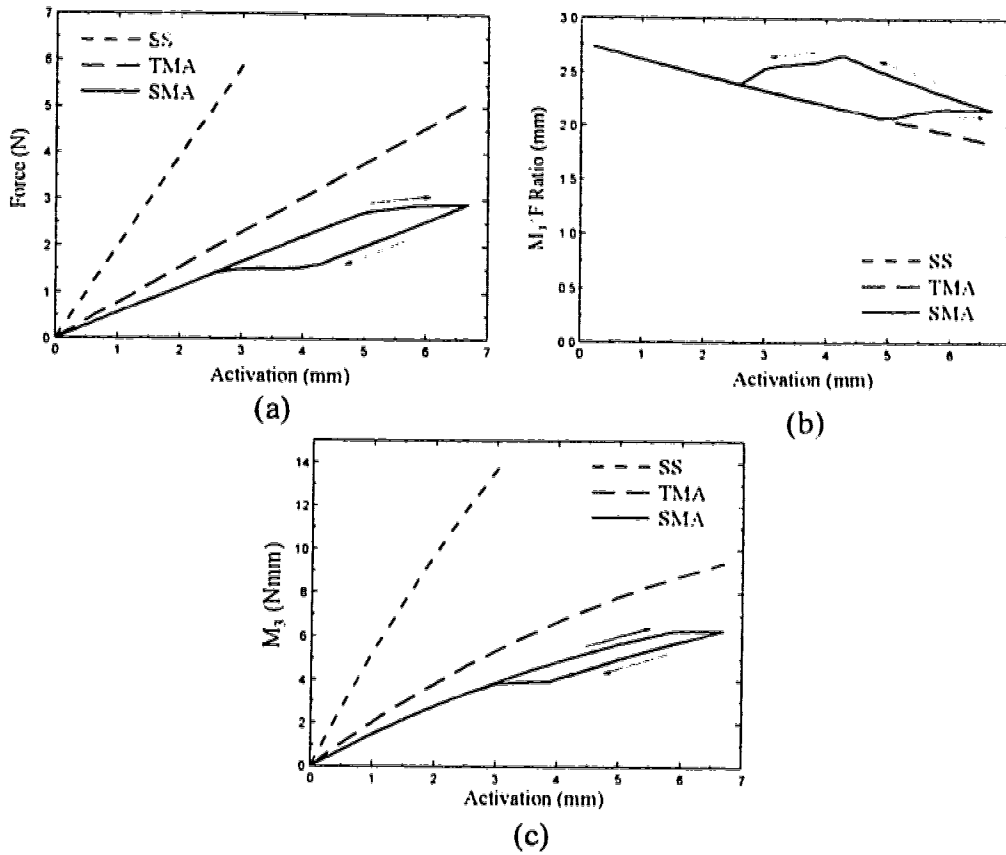


Figure 6.19: Results for Planar T-Spring Problem: (a) Force-Activation Relationship, (b) M_3/F Ratios, (c) M_3

activation. This results in a 'softer' appliance and explains the relative flatness of the force and moment curves in Figures 6.19a and c. The larger amount of material in the high curvature regions also explains the larger amount of hysteresis present than in the vertical loop considered previously.

Figure 6.21 illustrates the change in the curvature distribution along the appliance as it is de-activated. Upon unloading, the high curvature region A near the lower end of the appliance reverts back to the low curvature branch first. At a de-activation of 3.2 mm (reduced from 6.7 mm), the curvature distribution is as shown in Figure 6.21a. Region A has been reduced in length so that only a very small portion remains at the higher curvature

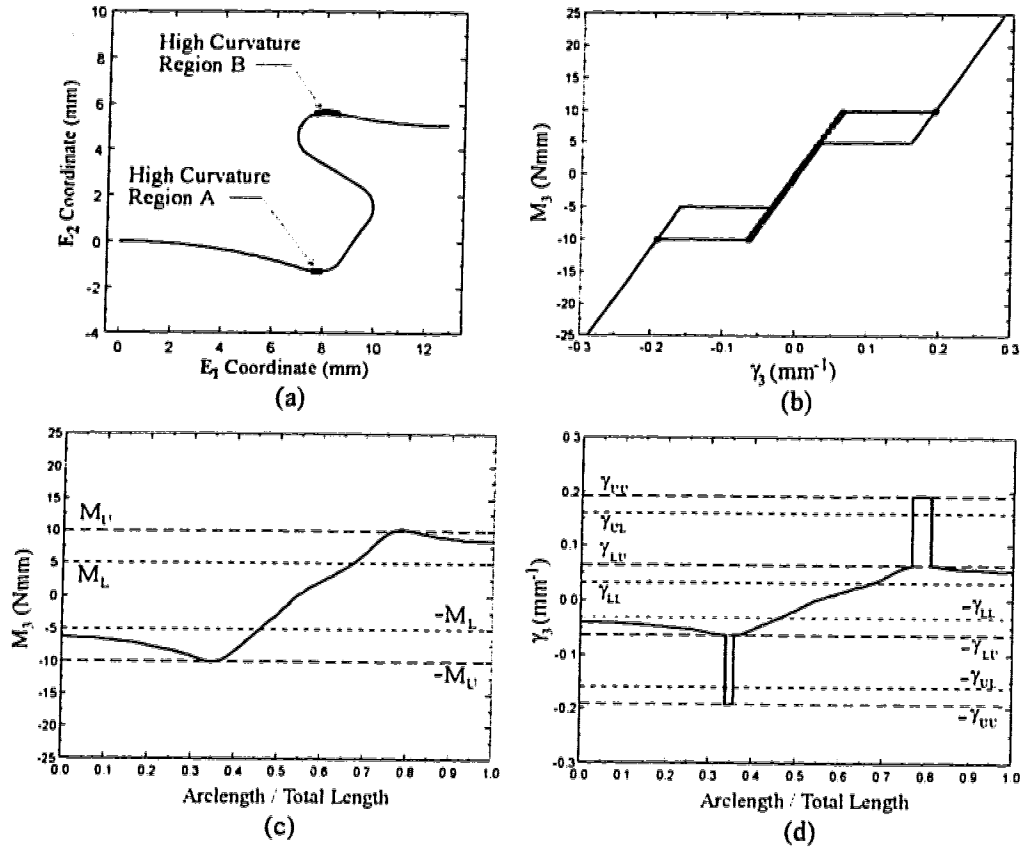


Figure 6.20: Moment and Curvature Distribution in Bilinear T-Spring Problem at the Maximum Activation 6.7mm: (a) Deflected Shape. (b) Constitutive Diagram. (c) Moment Distribution. (d) Curvature Distribution

(at γ_{UL}). The high curvature region B near the top of the appliance has also been reduced in both length and curvature values, although more of this high curvature region remains than in A. When the activation is then further reduced to 3.0 mm, all the material in A has returned to the lower curvature region as shown in Figure 6.21b. Region B has also been reduced again slightly as some of the high curvature material snaps to the low curvature region. When the activation reduces to 2.63 mm there is still a small amount of high curvature remaining which returns to the lower curvature region by a de-activation of 2.55 mm as shown in Figures 6.21c-d respectively.

If the material responds according to Maxwell's equal area rule then, as

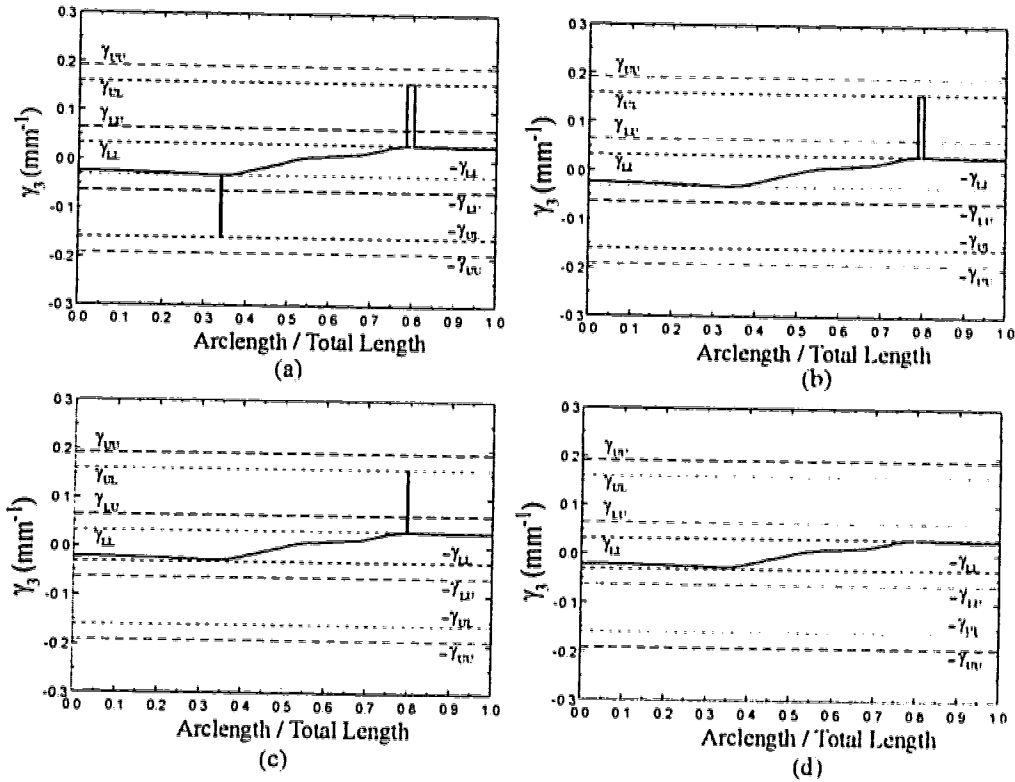


Figure 6.21: Curvature Distribution Along T-Spring During De-activation: (a) 3.2 mm, (b) 3.0mm, (c) 2.63mm, (d) 2.55mm

discussed previously, hysteresis will not be present but discontinuous curvatures are possible. Figure 6.22 illustrates such a relationship for a bilinear shape memory alloy. For illustration purposes, the moment at which the curvature discontinuity occurs is assumed to be 7.5 Nmm, halfway between the M_L and M_U values used for the above analysis. (A more detailed description of the unstable curvature region would be required to accurately determine this value.)

Figure 6.23 illustrates the response of the T-spring, made of this material (SMA-2) governed by Maxwell's equal area rule, activated to the same maximum activation as the original SMA material. These figures illustrate the point that hysteresis is not present in such a material (i.e. loading and unloading follows the same curve). However, discontinuous curvatures are possible which brings about very flat force-activation and moment-activation

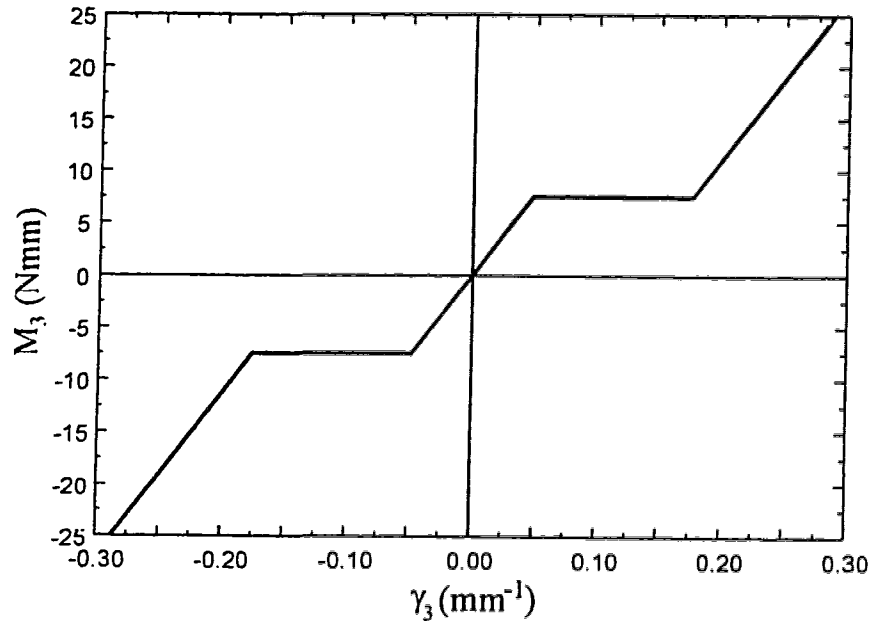


Figure 6.22: Moment-Curvature Relationship For Bilinear Material Governed by Maxwell's Equal Area Rule

relationships. The response of the new material seems to be approximately halfway between the loading and unloading curves for the SMA considered previously. This is not surprising considering the selection of parameters used to model the respective materials.

Figures 6.24a-d detail the moment and curvature distributions along the T-spring at the maximum activation considered. These figures show that, compared to the previous SMA T-spring, the main difference is that a larger portion of the material is now in the high curvature region. This is mainly due to the lower moment value at which transition occurs for the SMA-2 material. This increased amount of high curvature material accounts for the relative flatness of the force-activation and moment-activation curves.

Figures 6.19 and 6.23 illustrate the potential advantages of using shape memory alloys in the construction of orthodontic retraction appliances. The ability of these appliances to provide relatively constant forces, moments and M_3/F ratios is shown clearly. Although the M_3/F ratios shown for the particular appliances and materials considered are well below those suggested for translation, these can likely be increased with the use of an initial pre-

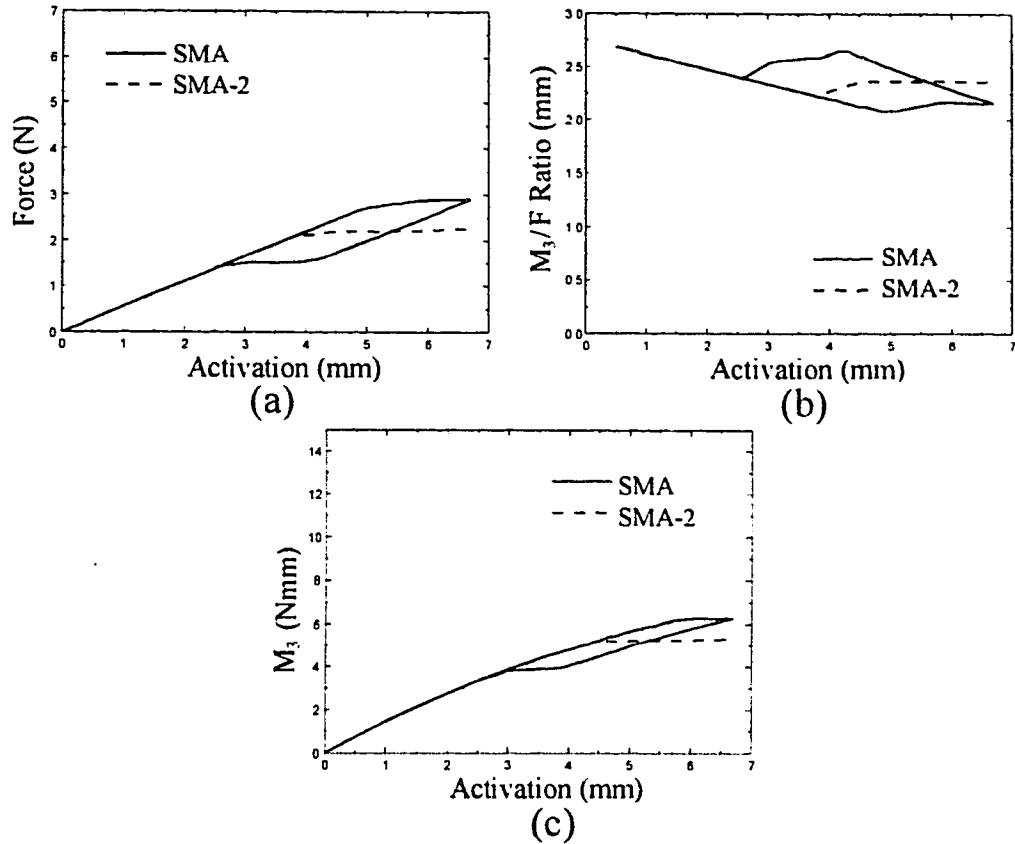


Figure 6.23: Results for Planar T-Spring Problem With Bilinear Material Following Maxwell's Equal Area Rule: (a) Force-Activation Relationship, (b) M_3/F Ratios, (c) M_3

activation as is done with the usual linear elastic materials. The forces, moments and M_3/F ratios eventually achievable will depend to a large extent on the exact properties of the shape memory alloy used in their construction for which there is little data at present. This can be seen in the difference in the response of the two materials shown in Figures 6.19 and 6.23.

Energy Integral A plot of the energy integral (equation (6.9)) for the new SMA (SMA-2) T-spring at the maximum activation considered (6.7 mm) is shown in Figure 6.25 without taking the constant of integration c_U into account. The energy integral, which should be a constant along a homogeneous

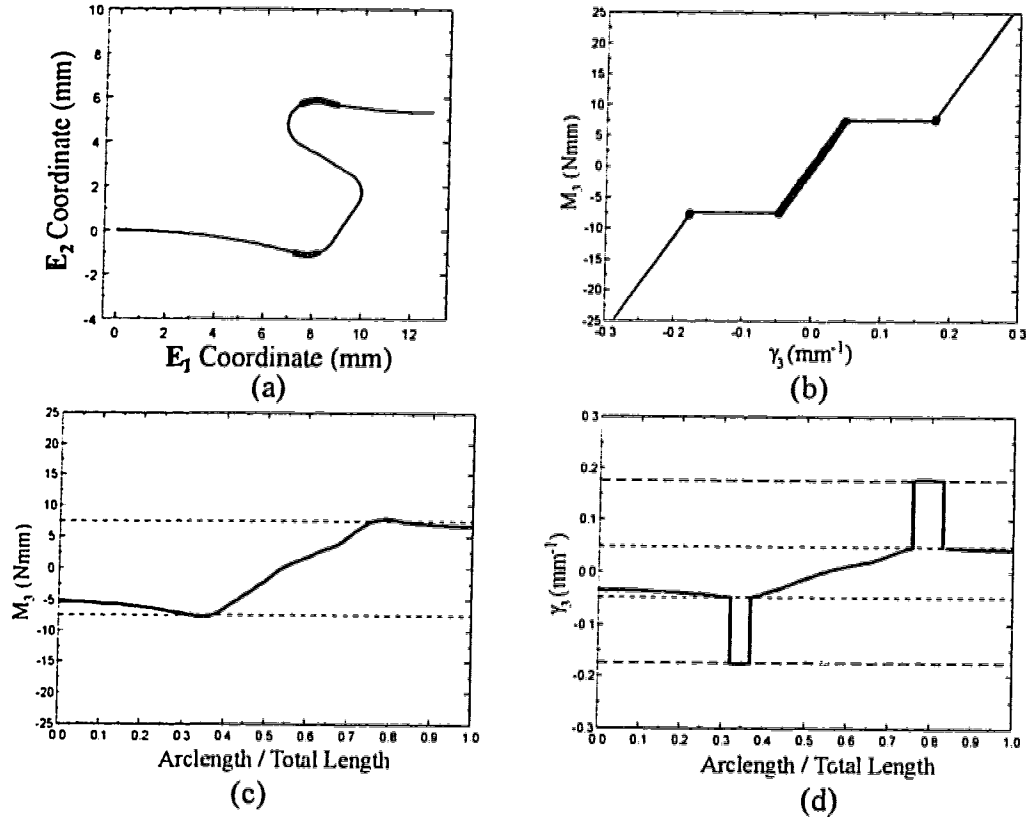


Figure 6.24: Moment and Curvature Distribution in Bilinear (Maxwell's Equal Area Rule) T-Spring Problem at the Maximum Activation 6.7mm: (a) Deflected Shape, (b) Constitutive Diagram, (c) Moment Distribution, (d) Curvature Distribution

rod (constant initial curvatures, uniform cross section and material properties), may have jump discontinuities at points where the initial curvatures change. Thus at the start of the segments (which alternate between straight and initially curved), where the initial curvatures change, discontinuities in the energy integral are allowed. However, along each segment the energy integral should maintain a constant value (which may be different for each segment). This can be seen to be the case except at the points where discontinuities in the curvature exists due to discontinuities in the $M_3 - \gamma_3$ material relationship. At these points discontinuities in the energy integral occur. As discussed earlier, material which follow Maxwell's equal area rule (which was

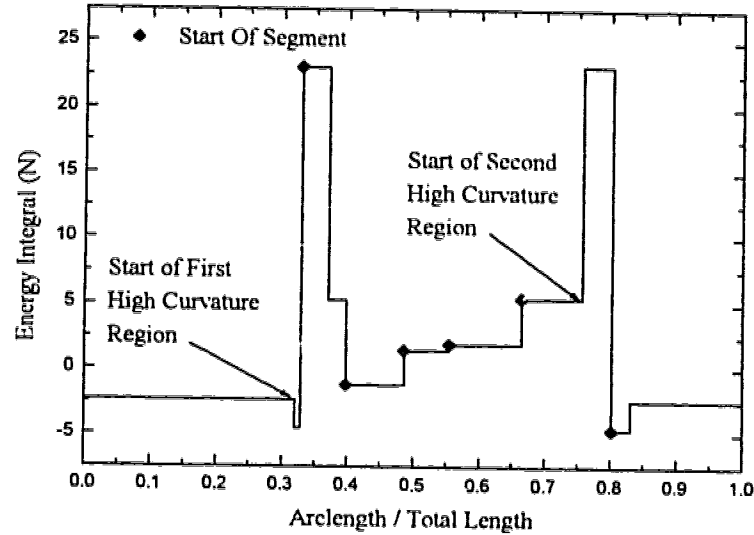


Figure 6.25: Energy Integral Along T-Spring with Bilinear Shape Memory Material

the material considered in Figure 6.25) should maintain a constant value of the energy integral even across these jumps in curvature due to discontinuous $M_3 - \gamma_3$ behavior. This does not appear to be the case in Figure 6.25. However, the constant of integration c_U (see equation (6.9)) has not been taken into account. The size of the jumps due to the discontinuous $M_3 - \gamma_3$ behavior are the same (20 N) at *both* instances where this occurs. Thus, in this case, a value of $c_U = 20$ N would result in the energy integral being constant over such discontinuities. Note that this result only applies for material which follow Maxwell's equal area rule and doesn't include the case when *initial* curvatures are discontinuous.

Chapter 7

Concluding Remarks

7.1 Summary

In this work a numerical procedure has been developed in an attempt to analyze problems involving large three-dimensional deformations of thin flexible rods. Since the deformations considered are large, these problems are governed by highly nonlinear equations which are difficult to solve analytically. This is further compounded by the wide variety of boundary conditions which may be involved. As a result numerical procedures are usually required to obtain approximate solutions to such problems.

The procedure developed is based upon the *segmental shooting technique* which is a numerical method previously found to be successful for planar elastica problems. The nonlinear equilibrium equations are applied to the rod and a solution is obtained from the initial values at one end using direct numerical integration. Some of these initial values will be unknown and must be initially estimated. A Newton-Raphson secant procedure is then used to iteratively modify the estimates of the initial unknowns to ensure that the required boundary conditions are satisfied. In this manner, the original two-point boundary value problem is solved as a sequence of initial value problems which converge to the appropriate boundary conditions.

The solution procedure also incorporated the ability to consider the rod as being comprised of a number of segments. There are several advantages to solving the rod in segments in this fashion. The most obvious is that many rod-like structures of interest (such as the orthodontic appliances considered in Chapter 5) have complicated geometries in the undeformed state.

Such rods can be idealized as a sequence of segments, each of which has a much simpler geometry (including straight, curved, twisted or possibly helical segments). Segmenting the rod in this manner allows a simple, physically intuitive method for modeling such rods. Complex loading conditions and changes in material or cross sectional properties can be handled in a similar manner. A further advantage of introducing new segments along the rod is the ability to reset all the Euler angles to zero and avoid the numerical problems caused by the singularity which occurs at $\theta = \pi/2$.

The initial value approach used here has its advantages and drawbacks. The most significant difficulty is the fact that good initial estimates of the unknowns are required to ensure that the procedure converges to a solution. This is especially true as the number of unknowns is increased. There are methods available to help alleviate these problems somewhat [so-called globally convergent root finding techniques (Press et al. 1992) or homotopy continuation methods (Keller 1968)], but good initial estimates are still usually required. However, this dependence on the initial estimates makes this approach well suited to finding multiple solutions when they exist. This is an important consideration since the equations being considered are highly nonlinear. This aspect of the initial value approach was used to advantage in Chapter 4 in investigating the multiplicity of solutions of cantilever beams under dead tip and uniform distributed loads.

The initial value approach presented is very accurate and efficient. In all cases where previous analytical, numerical or experimental results were available, the present method showed excellent agreement. As well, a number of checks on the accuracy of the solutions obtained were also similarly satisfied. Since each segment is analyzed separately, large computer memory is not required as with finite element procedures. Further, the loads and large deflections are handled in their entirety in one step. Thus incremental loading is avoided which speeds up the calculations significantly. The actual amount of time required to solve a particular boundary value problems depends heavily on the number of unknown quantities as well as the initial estimates. For example, the solutions for the preactivated T-spring considered in Chapter 5 at the maximum activation required 63 seconds on a Pentium 75 MHz personal computer. This problem involved a five parameter shooting procedure and required eight iterations to converge to the appropriate boundary conditions. Each iteration requires six passes of the numerical integrator (one to determine the end values and five required by the Newton Raphson secant method to compute the partial derivatives). The number

of iterations required depends heavily on the initial estimates, with better initial estimates resulting in fewer iterations and consequently less computer time. As well, problems with fewer unknowns show better convergence behavior and require considerably shorter computer time. For example, the initially curved cantilever beam loaded out of the initial plane (considered in Chapter 3), which was a two parameter shooting problem, required 9.0 seconds for six iterations to obtain the solution at the maximum load. The time required will also be affected by the tolerances used in the integration and shooting procedures, which in this work were typically 10^{-12} and 10^{-10} respectively.

The numerical technique was also modified to include materials which exhibit nonlinear elastic behavior. In particular, shape memory alloys were considered which allow discontinuities in the curvature to occur in equilibrium configurations. Constitutive models were proposed which qualitatively approximate the behavior of these materials in planar situations. The numerical results obtained demonstrated qualitative agreement with previous experimental results. Planar orthodontic appliances, assumed to be constructed of shape memory alloys, were revisited in an attempt to demonstrate some advantages of this material for this application.

7.2 Future Work

Shape memory alloys are seeing increasing use in a number of applications in which a numerical model of their behavior would be useful for design purposes. Before this can occur, a more complete experimental analysis of these materials is required to quantify their behavior. Although the constitutive relationships used to model shape memory alloys in this work demonstrated behaviors which show qualitative agreement with the limited results available, quantitative agreement is not possible to establish at this point due to a lack of experimental data to guide the selection of the appropriate constitutive model. This is especially true in the fully three dimensional case which includes a combination of bending, torsional and extensional deformations. No known work has been done to quantify these behaviors in combination where there may be a possible coupling of these deformation modes. Appropriate experimental data needs to be obtained to quantify the constitutive relationship for these materials.

As well, since these materials can undergo recoverable strains of up to

8%, a significant portion of the resulting deformation may be due to extension of the rod which is not considered in the present analysis. Therefore a modification to the numerical technique to account for the extensibility will likely need to be incorporated into the numerical procedure to accurately model shape memory alloys.

Further work can also be done in investigating the stability of the multiple equilibrium configurations which were found to exist. This could possibly be performed by using the shapes obtained numerically in this work to determine appropriate tangent stiffness matrices and investigating the signs of the eigenvalues. Another area which could see future development is utilizing the numerical procedure developed here as part of a dynamical analysis of flexible rods through a time stepping procedure where the inertia of the rod is treated as a (non-uniform) distributed load and the equivalent static problem is solved repeatedly.

References

- Alwar, R., N. R. Rao, and M. S. Rao (1974). An alternative procedure in dynamic relaxation. *Computers and Structures* 5, 271–274.
- Antman, S. S. (1968). General solutions for plane extensible elasticae having nonlinear stress-strain laws. *Quarterly Journal of Applied Mathematics* 26, 35–47.
- Antman, S. S. (1974). Kirchhoff's problem for nonlinearly elastic rods. *Quarterly of Applied Mechanics* 32(3), 221–240.
- Antman, S. S. (1995). *Nonlinear Problems of Elasticity*. Springer-Verlag.
- Banan, M., G. Karami, and M. Farshad (1991). Non-linear theory for elastic spatial rods. *International Journal of Solids and Structures* 27(6), 713–724.
- Belytschko, T. and T. Hughes (Eds.) (1983). *Computational Methods for Transient Analysis*. Chapter 5. pp. 245–265. Elsevier Science Publishers.
- Braun, S. and M. Marcotte (1995). Rationale of the segmented approach to orthodontic treatment. *American Journal of Orthodontics and Dentofacial Orthopedics* 108(1), 1–8.
- Burstone, C. J. (1982). The segmented arch approach to space closure. *American Journal of Orthodontics* 82(5), 361–378.
- Burstone, C. J. and J. Goldberg (1983). Maximum forces and deflections from orthodontic appliances. *American Journal of Orthodontics* 84(2), 95–103.
- Burstone, C. J. and H. A. Koenig (1974). Force systems from an ideal arch. *American Journal of Orthodontics* 65(3), 270–289.

- Burstone, C. J. and H. A. Koenig (1976). Optimizing anterior and canine retraction. *American Journal of Orthodontics* 70(1), 1-19.
- Chaconas, S. J., A. A. Caputo, and R. K. Hayashi (1974). Effects of wire size, loop configuration, and gabling on canine-retraction springs. *American Journal of Orthodontics* 65(1), 58-66.
- Chou, P. C. and N. J. Pagano (1967). *Elasticity: Tensor, Dyadic and Engineering Approaches*. Dover.
- Chucheepsakul, S., S. Buncharoen, and T. Huang (1995). Elastica of simple variable-arc-length beam subjected to end moment. *Journal of Engineering Mechanics* 121(7), 767-772.
- Cohen, H. (1966). A non-linear theory of elastic directed curves. *International Journal of Engineering Science* 4, 511-524.
- Dill, E. H. (1992). Kirchhoff's theory of rods. *Archive for History of Exact Sciences* 44(1), 1-23.
- Dowell, E. H., J. Traybar, and D. H. Hodges (1977). An experimental-theoretical correlation study of non-linear bending and torsion deformations of a cantilever beam. *Journal of Sound and Vibration* 50(4), 533-544.
- Duering, T. W., K. Melton, D. Stockel, and C. Wayman (1990). *Engineering Aspects of Shape Memory Alloys*. Butterworth-Heinemann.
- Falk, F. (1980). Model free energy, mechanics, and thermodynamics of shape memory alloys. *Acta Metallurgica* 28, 1773-1780.
- Faulkner, M. G., P. Fuchshuber, D. Haberstock, and A. Mioduchowski (1989). A parametric study of the force/moment systems produced by t-loop retraction springs. *Journal of Biomechanics* 22(6/7), 637-647.
- Faulkner, M. G., A. W. Lipsett, K. El-Rayes, and D. L. Haberstock (1991). On the use of vertical loops in retraction systems. *American Journal of Orthodontics and Dentofacial Orthopedics* 99(4), 328-336.
- Faulkner, M. G., A. W. Lipsett, and V. Tam (1993). On the use of a segmental shooting technique for multiple solutions of planar elastica problems. *Computer Methods in Applied Mechanics and Engineering* 110, 221-236.
- Faulkner, M. G. and D. J. Steigmann (1993). Controllable deformations of elastic spatial rods. *Acta Mechanica* 101, 31-43.

- Faulkner, M. G. and D. C. Stredulinsky (1976). Nonlinear bending of inextensible thin rods under distributed and concentrated loads. *Transactions of the CSME* 4(2), 77-82.
- Fosdick, R. L. and R. D. James (1981). The elastica and the problem of pure bending for a non-convex stored energy function. *Journal of Elasticity* 11, 165-186.
- Fried, I. (1981). Stability and equilibrium of the straight and curved elastica-finite element computation. *Computer Methods in Applied Mechanics and Engineering* 28, 49-61.
- Frisch-Fay, R. (1962). *Flexible Bars*. Butterworths.
- Goldstein, H. (1980). *Classical Mechanics* (Second ed.). Addison-Wesley.
- Gorski, W. (1976). A review of literature and a bibliography on finite elastic deflections of bars. *Civil Engineering Transactions* 18, 74-85.
- Green, A. and N. Laws (1966). A general theory of rods. *Proceedings of the Royal Society of London A293*, 145-155.
- Green, A. and N. Laws (1973). Remarks on the theory of rods. *Journal of Elasticity* 3(3), 179-184.
- Green, A., P. Naghdi, and M. Wenner (1974a). On the theory of rods i. derivations from the three-dimensional equations. *Proceeding of the Royal Society of London A337*, 451-483.
- Green, A., P. Naghdi, and M. Wenner (1974b). On the theory of rods ii: Developments by direct approach. *Proceedings of the Royal Society of London A337*, 485-507.
- Greif, R., M. Coltman, M. Gailus, and E. Shapiro (1982). Force generation from orthodontic appliances. *Transactions of the ASME* 104, 280-289.
- Hay, G. E. (1953). *Vector and Tensor Analysis*. Dover Publications.
- Hodges, D. H. and D. A. Peters (1975). On the lateral buckling of uniform cantilever beams. *International Journal of Solids and Structures* 11(12-A), 1269-1280.
- Isaacson, R. J., S. J. Lindauer, and L. K. Rubenstein (1993). Activating a 2×4 appliance. *The Angle Orthodontist* 63(1), 17-24.
- James, R. (1981). The equilibrium and post-buckling behavior of an elastic curve governed by a non-convex energy. *Journal of Elasticity* 11, 239-269.

- Jiang, L. and M. Chernuka (1993). A co-rotational formulation for geometrically nonlinear finite element analysis of spatial beams. *Transactions of the CSME* 18(1), 65-88.
- Kafadar, C. B. (1972). On the nonlinear theory of rods. *International Journal of Engineering Science* 10(4), 369-391.
- Kapila, S. K. and R. Sachdeva (1989). Mechanical properties and clinical applications of orthodontic wires. *American Journal of Orthodontics and Dentofacial Orthopedics* 96(2), 100-109.
- Keller, H. B. (1968). *Numerical Methods for Two-Point Boundary Value Problems*. Blaisdell.
- Koenig, H. A. and N. E. Bolle (1993). Non-linear formulation for elastic rods in three-space. *International Journal of Non-Linear Mechanics* 28(3), 329-335.
- Landau, L. D. and E. M. Lifshitz (1970). *Theory of Elasticity* (Second ed.). Pergamon Press.
- Lee, B. K., J. F. Wilson, and S. J. Oh (1993). Elastica of cantilevered beams with variable cross sections. *International Journal of Non-Linear Mechanics* 28(5), 579-589.
- Lipsett, A. W., M. G. Faulkner, and K. El-Rayes (1990). Large deformation analysis of orthodontic appliances. *Journal of Biomechanical Engineering* 112, 29-37.
- Lipsett, A. W., M. G. Faulkner, and V. Tam (1993). Multiple solutions for inextensible arches. *Transactions of the CSME* 17(1), 1-15.
- Love, A. E. H. (1944). *A Treatise on the Mathematical Theory of Elasticity* (fourth ed.). Dover.
- Mahadevan, L. and J. B. Keller (1993). The shape of a möbius band. *Proceedings of the Royal Society of London* 440, 149-162.
- Mitchell, T. (1959). The nonlinear bending of thin rods. *Journal of Applied Mechanics* 26, 40-43.
- Miura, F., M. Mogi, Y. Ohura, and H. Hamanaka (1986). The super-elastic properties of the japanese niti alloy wire for use in orthodontics. *American Journal of Orthodontics and Dentofacial Orthopedics* 90(1), 1-10.

- Navace, S. and R. E. Elling (1991). Large deflections of cantilever beams. *Transactions of the CSME* 15(1), 91-107.
- Navace, S. and R. E. Elling (1992). Equilibrium configurations of cantilever beams subjected to inclined end loads. *ASME Journal of Applied Mechanics* 59(3), 572-579.
- Pai, P. and A. Palazotto (1996). Large-deformation analysis of flexible beams. *International Journal of Solids and Structures* 33(9), 1335-1353.
- Papadrakakis, M. (1981). A method for the automatic evaluation of the dynamic relaxation parameters. *Computer Methods in Applied Mechanics and Engineering* 25, 35-48.
- Press, W. H., S. A. Teukolsky, W. T. Vetterling, and B. P. Flannery (1992). *Numerical Recipes* (Second ed.). Cambridge University Press.
- Quinn, R. S. and D. K. Yoshikawa (1985). A reassessment of force magnitude in orthodontics. *American Journal of Orthodontics* 88(3), 252-260.
- Raboud, D., M. G. Faulkner, and A. W. Lipsett (1996a). Multiple three-dimensional equilibrium solutions for cantilever beams loaded by dead tip and uniform distributed loads. *International Journal of Non-Linear Mechanics* 31(3), 297-311.
- Raboud, D., M. G. Faulkner, and A. W. Lipsett (1996b). A segmental approach for large three-dimensional rod deformations. *International Journal of Solids and Structures* 33(8), 1137-1155.
- Raboud, D., M. G. Faulkner, A. W. Lipsett, and D. L. Habersock (1996). Three dimensional effects in retraction appliance design. *American Journal of Orthodontics*, accepted for publication.
- Ramesh, G. and C. Krishnamoorthy (1993). Post-buckling analysis of structures by dynamic relaxation. *International Journal for Numerical Methods in Engineering* 36, 1339-1364.
- Rosen, A. (1991). Structural and dynamic behavior of pretwisted rods and beams. *Applied Mechanics Review* 44(12), 483-515.
- Schmidt, R. and D. A. DaDeppo (1971). A survey of literature on large deflections of nonshallow arches. bibliography of finite deflections of

- straight and curved beams, rings, and shallow arches. *Journal of the Industrial Mathematics Society* 21 (Part 2), 91–114.
- Shaw, J. A. and S. Kyriakides (1995). Thermomechanical aspects of shape memory alloys. *Journal of the Mechanics and Physics of Solids* 43(8), 1243–1281.
- Shigley, J. E. (1986). *Mechanical Engineering Design* (First Metric Edition ed.). McGraw-Hill.
- Steigmann, D. J. and M. G. Faulkner (1993). Variational theory for spatial rods. *Journal of Elasticity* 33, 1–26.
- Surana, K. S. (1983). Geometrically non-linear formulation for two dimensional curved beam elements. *Computers and Structures* 17(1), 105–114.
- Surana, K. S. and R. M. Sorensen (1989). Geometrically non-linear formulation for three dimensional curved beam elements with large rotations. *International Journal for Numerical Methods in Engineering* 28, 43–73.
- Tanne, K., H. A. Koenig, and C. J. Burstone (1988). Moment to force ratios and the center of rotation. *American Journal of Orthodontics and Dentofacial Orthopedics* 94, 426–431.
- Timoshenko, S. P. and J. N. Goodier (1970). *Theory of Elasticity* (Third ed.). McGraw-Hill.
- Wang, C. Y. (1986). A critical review of the heavy elastica. *International Journal of Mechanical Sciences* 28(8), 549–559.
- Whitman, A. and C. DeSilva (1974). An exact solution in a nonlinear theory of rods. *Journal of Elasticity* 4(4), 265–280.

Appendix A

Shooting Procedure

As mentioned in Section 3.1.2, the segmental technique requires that all of the conditions at the start of the rod be specified in order to obtain a solution. In most problems some of the initial values will be unknown while a corresponding number of conditions at the opposite end of the rod will be known. The unknowns at the start of the rod must be initially estimated to begin the solution procedure. The shooting procedure described here is a method used to modify the estimates of the initial unknowns iteratively to ensure that the known boundary conditions at the end of the rod are satisfied. In what follows it will be assumed that there are N unknown conditions at the start of the rod and N known boundary conditions at the other end.

Let \mathbf{A} be an $N \times 1$ vector containing the initial estimates of the unknown values at the start of the rod, \mathbf{B} be an $N \times 1$ vector containing the N known boundary conditions at the end of the rod and \mathbf{C} be an $N \times 1$ vector containing the values delivered by the segmental solution corresponding to the known boundary values at the end of the rod. The difference between the known boundary values and those obtained with the numerical solution is the vector difference between \mathbf{B} and \mathbf{C} , or

$$\mathbf{D}^k = \mathbf{B} - \mathbf{C}^k. \quad (\text{A.1})$$

\mathbf{D} is called the error function where the superscript k is an iteration counter. Note that \mathbf{B} has no iteration counter since the known boundary conditions will remain the same over each iteration and can be considered as constants for each separate rod problem. The components of \mathbf{C}^k (the computed values) depend on the initial guesses which are the components of \mathbf{A}^k . Therefore,

\mathbf{C}^k can be considered as being a function of the components of \mathbf{A}^k . Then from (A.1), the error function \mathbf{D}^k can be considered as also being a function of the components of \mathbf{A}^k and can be expressed as

$$\mathbf{D}^k = \mathbf{D}(\mathbf{A}^k) = \mathbf{D}(A_1^k, A_2^k, \dots, A_N^k). \quad (\text{A.2})$$

To obtain a solution to the original rod problem which satisfies the required boundary conditions it is necessary that each component of the error function \mathbf{D} approach zero simultaneously. Thus, the problem of determining the correct initial guesses involves solving a set of N nonlinear equations to determine the components of \mathbf{A} for which each component of the error function \mathbf{D} is approximately zero. A Newton-Raphson iterative procedure (secant method) is used to accomplish this objective. The Newton-Raphson method is based on a first order Taylor series expansion of (A.2) which can be written as

$$\mathbf{D}^{k+1} = \mathbf{D}^k + [\mathbf{J}]^k (\mathbf{A}^{k+1} - \mathbf{A}^k), \quad (\text{A.3})$$

where \mathbf{A}^{k+1} are the new values of the initial estimates for the $k+1^{\text{th}}$ iteration and \mathbf{D}^{k+1} are the corresponding values of the components of the error function. $[\mathbf{J}]^k$ is the $N \times N$ Jacobian matrix, the components of which are given by

$$J_{mn}^k = \frac{\partial D_m^k}{\partial A_n^k}, \quad m, n = 1, 2, \dots, N. \quad (\text{A.4})$$

In this case the functions \mathbf{D}_m^k are not analytical so the partial derivatives need to be evaluated numerically. A backward difference formulation is used to evaluate these derivatives. The approximate partial derivatives are then

$$J_{mn}^k = \frac{\partial D_m^k}{\partial A_n^k} \approx \frac{D_m(\mathbf{A}^k) - D_m(A_1^k, A_2^k, \dots, A_n^k - A_n^{k-1}, \dots, A_N^k)}{A_n^k - A_n^{k-1}}. \quad (\text{A.5})$$

Setting \mathbf{D}^{k+1} to zero in (A.3) (i.e. assuming that the next improvement to the initial estimates \mathbf{A}^{k+1} will produce a zero error function) and solving

for the new improved initial estimates of the unknown values at the start of the rod gives

$$[\mathbf{J}]\mathbf{H} = -\mathbf{D}^k, \quad \mathbf{H} = \mathbf{A}^{k+1} - \mathbf{A}^k, \quad (\text{A.6})$$

which can be solved for \mathbf{H} using standard methods such as Gauss elimination. Having obtained \mathbf{H} , the new initial guesses are then obtained from

$$\mathbf{A}^{k+1} = \mathbf{A}^k + \mathbf{H}. \quad (\text{A.7})$$

The new values of the initial estimates \mathbf{A}^{k+1} are then used to start the the solution over again for the $k + 1^{\text{th}}$ iteration. This procedure is continued until each component of the error function approaches zero to within some specified tolerance at the which point the boundary conditions are considered to be satisfied.

The backward finite difference formulation for the partial derivatives expressed in (A.5) is a simple but not very accurate approximation. More accurate methods are available (Press et al. 1992) which in turn require more function evaluations which require, in this instance, more solutions for the entire rod at a number of different initial conditions. Such a procedure is not very justifiable in the current situation since each evaluation of the rod at each different initial condition is rather expensive computationally. With the expression in (A.5), each iteration of the numerical procedure requires $N + 1$ solutions over the entire rod, one with the initial guesses \mathbf{A}^k and a further N to evaluate the partial derivatives. If a center difference formulation were used to evaluate to partial derivatives, then each iteration of the numerical procedure would now require $2N + 1$ solutions over the rod, which is a 50% increase in computation time for $N = 1$ and a 75% increase in computation time for $N = 3$. The possible gains in accuracy in evaluating the partial derivatives using such a procedure, which would only be beneficial very near the actual solution, would not offset this increased computational expense.

Appendix B

Analytical Solution for an Initially Straight Circular Rod Deformed into a Helix

In this appendix, the analytical solution to the problem of an initially straight isotropic rod bent and twisted into a helix and maintained in this deformed configuration by the application of moments and forces along the initial axis of the rod only. While this problem has been considered by several authors (Love 1944; Landau and Lifshitz 1970), the analysis is presented here for completeness. This is one of the few problems known to the author which combines bending and torsion and has a known analytical solution. Thus it will serve as a test case for the numerical procedure developed in Chapter 3.

Consider a straight rod with uniform material properties which is initially aligned with the global \mathbf{E}_3 axis as shown in Figure B.1. The rod is bent and twisted into a helix of radius R and pitch angle α where α is defined as the angle between the tangent to the helix and a plane perpendicular to \mathbf{E}_3 . The equation for such a helix is

$$\begin{aligned} \mathbf{r}(s) &= X\mathbf{E}_1 + Y\mathbf{E}_2 + Z\mathbf{E}_3, \\ X &= R \cos \zeta, \quad Y = R \sin \zeta, \quad Z = R \zeta \tan \alpha, \end{aligned} \tag{B.1}$$

which traces a curve around the surface of a cylinder of radius R aligned along \mathbf{E}_3 . ζ is a measure of the angle of rotation about the \mathbf{E}_3 axis. Differentiating (B.1) with respect to arclength gives an expression for the tangent

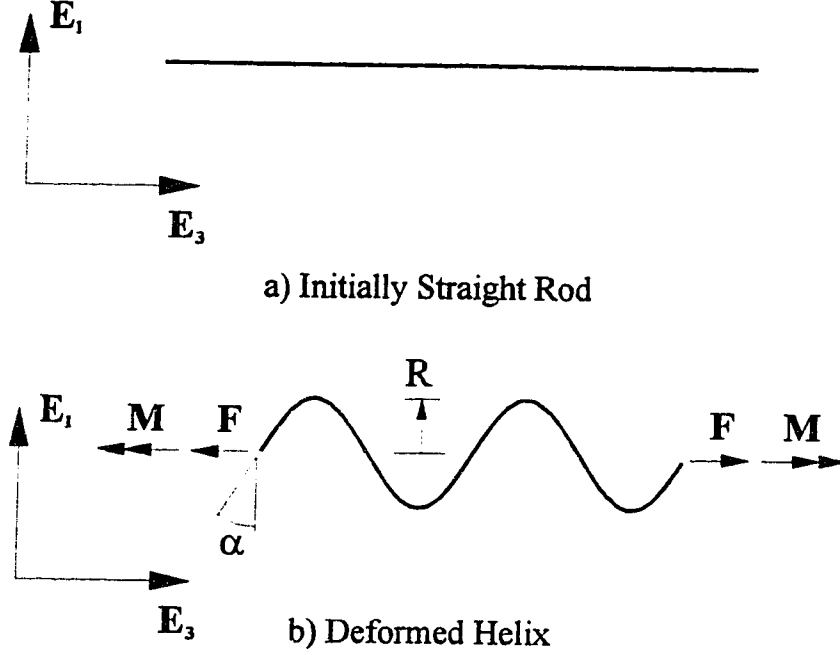


Figure B.1: Initially Straight Circular Rod Deformed Into a Helix

vector as

$$\mathbf{e}_1 = -R \frac{d\zeta}{ds} \sin \zeta \mathbf{E}_1 + R \frac{d\zeta}{ds} \cos \zeta \mathbf{E}_2 + R \frac{d\zeta}{ds} \tan \alpha \mathbf{E}_3. \quad (\text{B.2})$$

Since \mathbf{e}_1 is a unit vector its magnitude must be unity which along with (B.2) leads to the result

$$\frac{d\zeta}{ds} = \frac{\cos \alpha}{R}. \quad (\text{B.3})$$

which is a constant for the helix. Therefore (B.2) becomes

$$\mathbf{e}_1 = -\cos \alpha \sin \zeta \mathbf{E}_1 + \cos \alpha \cos \zeta \mathbf{E}_2 + \sin \alpha \mathbf{E}_3. \quad (\text{B.4})$$

Taking the derivative of (B.4) and again using (B.3) yields

$$\mathbf{e}'_1 = -\frac{\cos^2 \alpha}{R} \cos \zeta \mathbf{E}_1 - \frac{\cos^2 \alpha}{R} \sin \zeta \mathbf{E}_2. \quad (\text{B.5})$$

Substituting (B.4) and (B.5) into (2.13), which is the constitutive relation for initially straight transversely isotropic rods, gives

$$\begin{aligned} \mathbf{M} = & GJ\kappa_1 \left[\sin \alpha \mathbf{E}_3 + \cos \alpha \left(-\sin \zeta \mathbf{E}_1 + \cos \zeta \mathbf{E}_2 \right) \right] \\ & + \frac{EI}{R} \left[\cos^3 \alpha \mathbf{E}_3 + \sin \alpha \cos^2 \alpha \left(\sin \zeta \mathbf{E}_1 - \cos \zeta \mathbf{E}_2 \right) \right]. \end{aligned} \quad (\text{B.6})$$

Therefore, the moment required to maintain the deformed shape is

$$\mathbf{M} = M_z \mathbf{E}_3 + M_\zeta \mathbf{E}_\zeta. \quad (\text{B.7a})$$

where

$$M_z = GJ\kappa_1 \sin \alpha + \frac{EI}{R} \cos^3 \alpha, \quad (\text{B.7b})$$

$$M_\zeta = GJ\kappa_1 \cos \alpha - \frac{EI}{R} \cos^2 \alpha \sin \alpha, \quad (\text{B.7c})$$

and

$$\mathbf{E}_\zeta = -\sin \zeta \mathbf{E}_1 + \cos \zeta \mathbf{E}_2. \quad (\text{B.7d})$$

Note that M_ζ is directed along the tangent to the cylinder defined by the helix and M_z is directed along the axis of the cylinder. From equations (B.7a)-(B.7d) it can be seen that both M_z and M_ζ are constant but the orientation of M_ζ changes along the rod. At the start of the helix, ($\zeta = 0$) \mathbf{E}_ζ is equal to \mathbf{E}_2 .

To determine the force required, the derivative of (B.5) is given as

$$\mathbf{e}_1'' = \frac{\cos^3 \alpha}{R^2} \sin \zeta \mathbf{E}_1 - \frac{\cos^3 \alpha}{R^2} \cos \zeta \mathbf{E}_2, \quad (\text{B.8})$$

where (B.3) has again been used. Now substituting (B.5) and (B.8) into (2.16) gives the result

$$\mathbf{F} \times \mathbf{e}_1 = \left[\frac{EI}{R^2} \cos^3 \alpha \sin \alpha - \frac{GJ\kappa_1}{R} \cos^2 \alpha \right] \left(\cos \zeta \mathbf{E}_1 + \sin \zeta \mathbf{E}_2 \right). \quad (\text{B.9})$$

Comparing (B.9) with (B.4) gives the force \mathbf{F} as

$$\mathbf{F} = F_z \mathbf{E}_3, \quad F_z = \frac{GJ\kappa_1}{R} \cos \alpha - \frac{EI}{R^2} \cos^2 \alpha \sin \alpha. \quad (\text{B.10})$$

This is the force required to maintain the deformed shape. Note that the force vector is directed along the axis of the cylinder and is a constant. Comparing (B.10) with (B.7c) shows that

$$M_\zeta = F_z R. \quad (\text{B.11})$$

Therefore if no axial load is applied the resultant moment is purely along the helix axis.

Some further relations among these variables can be established. Taking the dot product of both sides of equation (2.13) with \mathbf{e}_1 gives

$$\mathbf{M} \cdot \mathbf{e}_1 = GJ\kappa_1 \quad (\text{B.12})$$

which is satisfied identically when \mathbf{M} is given by (B.7a)-(B.7d). For the special case where there is no axial force, $\mathbf{M} = M_z \mathbf{E}_3$ and equation (B.12) gives

$$\kappa_1 = \frac{M_z \sin \alpha}{GJ} \quad (\text{B.13})$$

and equations (B.10) and (B.13) combine to give the radius of the helix as

$$R = \frac{EI}{M_z} \cos \alpha. \quad (\text{B.14})$$

Appendix C

Use of Contour Maps For Two Parameter Shooting Problems

To begin the discussion and introduce the concept, consider a one parameter shooting problem, such as a cantilever with a dead tip load undergoing only planar deformations as described in Chapter 4. In this case, the unknown condition at the start (fixed end) of the rod is the M_3 component acting there, while the corresponding known condition is that M_3 must vanish at the free end. Thus, any M_3 value at the fixed end (input to the numerical integration procedure) which produces a zero M_3 at the free end corresponds to a solution to the problem.

Since this problem is geometrically nonlinear, more than one solution may exist and it is desirable to find all the solutions for a given load. In order to find these solutions, a plot of M_3 at the free end versus M_3 at the fixed end can be used. Such a plot is shown in Figure C.1 (which uses dimensionless moments defined by $\Lambda_3 = M_3 L / EI_3$) for a dimensionless load $\alpha = 5.0$. As can be seen, there are three solutions to the problem since there are three M_3 values at the fixed end which result in $M_3 = 0$ at the free end. Further, since possible values of M_3 at the fixed end are limited (can be no larger than the load multiplied by the length of the beam), the entire possible input range for M_3 has been considered. Therefore it can be concluded that three and only three equilibrium shapes exist at this load and the corresponding shapes are shown in Figure 4.3.

Now consider a two parameter shooting problem such as a cantilever beam with a dead tip load undergoing out-of-plane deformations. In this case, both M_1 and M_3 at the fixed end are unknown while both M_1 and M_3 at the free

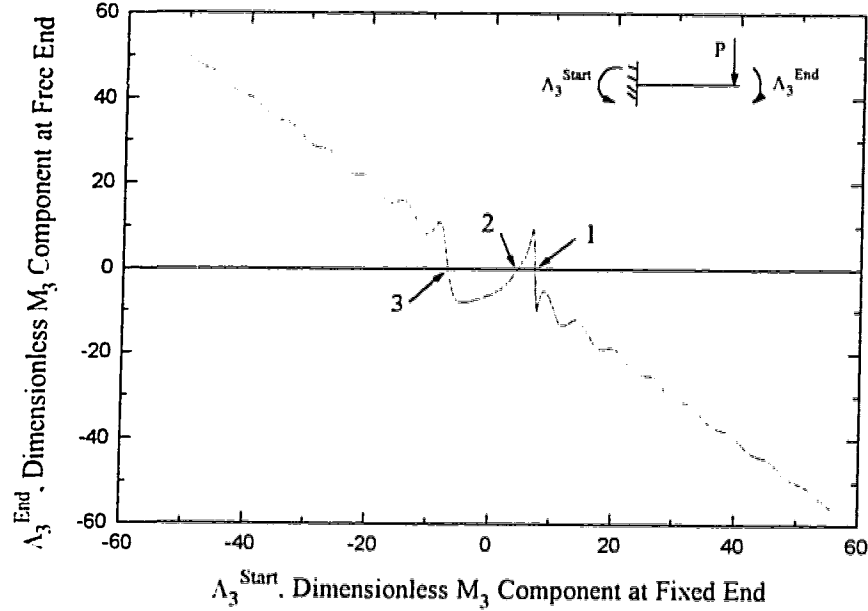


Figure C.1: Free End versus Fixed End Moment for a Cantilever Undergoing Planar Deformations for a Load $\alpha = 5.0$

end must be zero. Finding all of the possible solutions in this case is much more difficult since both conditions at the end of the rod must be satisfied simultaneously. One possible method to attempt this is through the use of contour maps. Basically, a contour is made of all the possible combinations of M_1 and M_3 at the fixed end which result in $M_1 = 0$ at the free end. These are not necessarily all solutions to the problem, they are only possible solutions. Then a similar contour is produced which satisfies $M_3 = 0$ at the free end. These two contours are then superimposed to find all the points at which the $M_1 = 0$ and $M_3 = 0$ contours cross therefore representing solutions to the problem. Note that shooting is not used in the generation of these contours, but rather only the integration portion of the numerical procedure.

Figure C.2 shows an example of part of a contour map for a deep cantilever beam (aspect ratio = 1/1.7) at a load of $\beta = 62$. (Note that these plots require large amounts of data to be generated and it is easier to consider the plots section by section.) As can be seen from this map there are two places where the contours cross so that both M_1 and M_3 are simultaneously zero at the free end which corresponds to the out-of-plane equilibrium solutions (Shape D and buckled Shape #2). However, as discussed in Chapter 4,

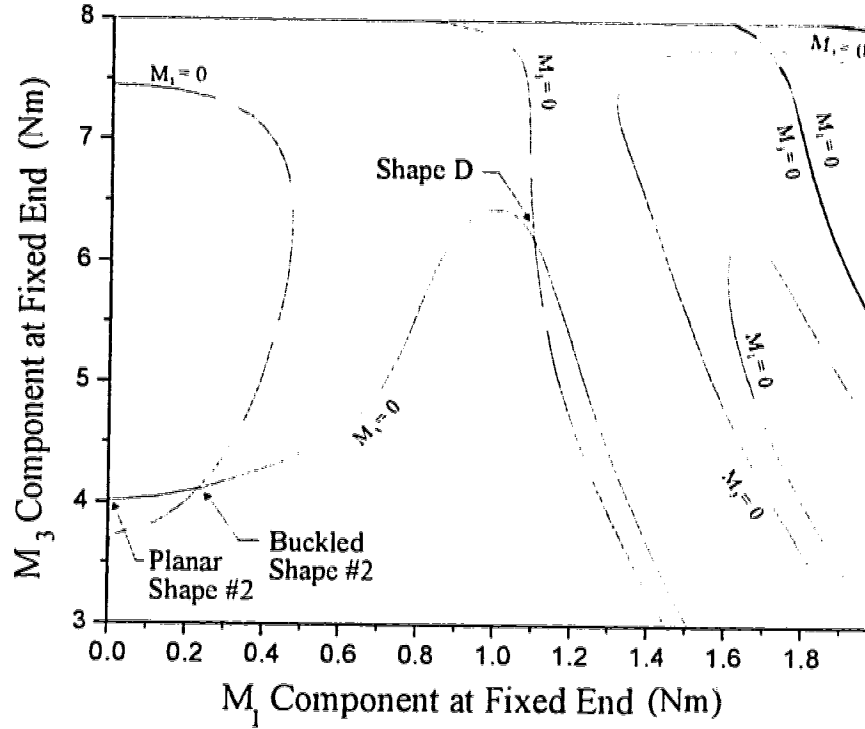


Figure C.2: Contour Map of Free End $M_1 = 0$ and $M_3 = 0$ as Functions of Fixed End M_1 and M_3 Components for a Cantilever Beam Undergoing Out-of-Plane Deformations for a Load $\beta = 62$

the case $M_1 = 0$ at the fixed end automatically corresponds to $M_1 = 0$ at the free end so that the vertical $M_1 = 0$ axis is also a contour. One other equilibrium shape, planar Shape #2, is therefore also shown in Figure C.2. Note that the load $\beta = 62$ in this case corresponds to a load of $\alpha = 4.60$ (see equations (4.5) and (4.6)) which, from Table 4.1, indicates that three planar equilibrium solutions exist at this load. Only one, Shape #2 is indicated in Figure C.2. The other two planar shapes have M_3 components at equilibrium outside of the range shown in Figure C.2 so that they do not appear.

Theoretically, in order to determine if all the solutions have been found, it is only necessary to consider all possible values for the inputs M_1 and M_3 at the fixed end (again, both M_1 and M_3 must be less than the load times the length of the cantilever). Several maps like the one in Figure C.2 must therefore be generated to consider all the possibilities. In practice, however,

this is not always a very practical approach. The functional dependence of the free end values on the fixed end values may be quite complex and a very large amount of data may need to be generated in order to determine if a solution actually exists or if the contours lines simply approach each other but do not cross. Also, as shown in the upper right portion of Figure C.2, there are places where the contours of $M_1 = 0$ and $M_3 = 0$ seem to run beside each other. It is very difficult to determine in these cases where (or if) the contours actually cross. These borderline cases are further complicated by the fact that interpolation from generated data is necessary to produce the contours. This interpolation is not exact and thus some error in locating the contour lines is introduced. Reducing this error requires a finer mesh of initial values to be evaluated which further increases the amount of time and numerical data needed. Therefore it seems reasonable to state that contour maps are very useful for finding solutions since they offer a systematic procedure for locating (approximately) the initial unknowns which satisfy the boundary conditions and result in a solution to the problem. However their use in determining whether or not all solutions have been found is somewhat limited.

It should be noted that it is not really necessary to find the exact points at which the contours cross. Contour maps best serve to locate the approximate initial M_1 and M_3 components which can be further improved using the shooting portion of the numerical procedure. However, since the success of the numerical procedure usually depends on having “good” initial estimates, it is still often necessary to generate fine meshes to obtain reasonably accurate initial estimates.

Appendix D

Evaluation of Elastic Limit

In this appendix, details are given about the method used to determine when yielding of the material has occurred. This information is used in Chapters 5 and 6 to determine the maximum elastic activations of a number of orthodontic retraction appliances. The appliances considered in Chapter 5 experience three-dimensional deformations which must be considered in determining the stress levels which exist.

The rods in this work are assumed to deform only through bending and twisting so these modes of deformation are the only ones which give rise to stresses in the material. In particular the stresses due to axial tension and to shear are ignored. While stresses due to these loads will exist in the actual material, these will be small in comparison to those due to bending and twisting.

Dill (1992) shows that the nonzero stresses over the cross section of the rod are given by¹

$$\tau_{12} = G(\kappa_1 - \kappa_1^0) \left(\frac{\partial \varphi}{\partial Y} - Z \right), \quad (\text{D.1})$$

$$\tau_{13} = G(\kappa_1 - \kappa_1^0) \left(\frac{\partial \varphi}{\partial Z} - Y \right), \quad (\text{D.2})$$

$$\sigma_{33} = E \left[(\kappa_2 - \kappa_2^0) Z - (\kappa_3 - \kappa_3^0) Y \right], \quad (\text{D.3})$$

where extensibility has been ignored, G and E are the shear modulus and Young's modulus of the material respectively, and Y and Z are the coordinates over the cross section in the \mathbf{e}_2 and \mathbf{e}_3 principal directions respectively.

¹Note that these stresses are the superposition of those given by elementary strength of materials results for bending and torsion.

φ is the warping function in torsion (see Timoshenko and Goodier 1970 for example) and depends only on the geometry of the cross section.

Yielding in the material occurs when the stress at some point exceeds a predetermined value for the specific material. There are a number of theories available which predict this stress value based on the yield strength of the material in simple tension tests. One of the simplest of these, the *maximum shear stress* criterion which states (Shigley 1986)

yielding begins whenever the maximum shear stress in any mechanical element becomes equal to the maximum shear stress in a tension-test specimen of the same material when that specimen begins to yield,

is used in this work. This is a relatively conservative estimate for the onset of yielding, but is sufficient for the present requirement of determining the approximate elastic range of orthodontic retraction appliances. The maximum shear stress at some point in the material is obtained using a Mohr's circle analysis with the normal and shear stresses given in equations (D.1)-(D.3).

To determine if yielding has occurred various points on the cross section are considered. The points on the rectangular cross sections ($b < a$) of the orthodontic springs are shown in Figure D.1. The maximum value for σ_{33} occurs at one of the corners (points 1-4) where the normal stresses due to bending about the \mathbf{e}_2 and \mathbf{e}_3 axes are superimposed. At these points the shear stress due to torsion is zero. Thus the maximum normal stress which

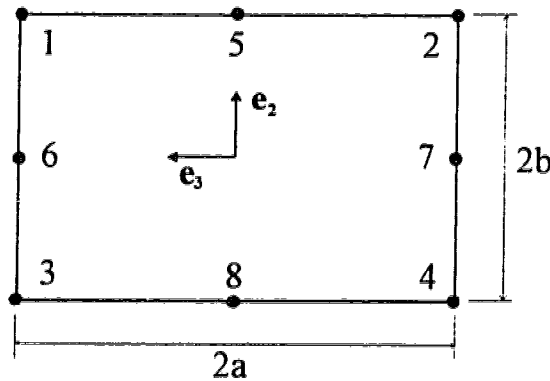


Figure D.1: Locations on the Cross Section Used to Evaluate the Yielding Criterion

exists in the cross section is given by

$$\sigma_{\max} = E \left[|(\kappa_2 - \kappa_2^0)|a + |(\kappa_3 - \kappa_3^0)|b \right] \quad (D.4)$$

and the maximum shear stress in the material is therefore

$$\tau_{\max} = \frac{\sigma_{\max}}{2}. \quad (D.5)$$

At the other points considered (5–8) the normal stress is due to only one bending component but the shear stresses due to torsion are a maximum for each side (with higher shear stresses at the points closer to the origin of the cross section). Thus at points 5 and 8, the normal stress is

$$\sigma_{33} = \pm E(\kappa_3 - \kappa_3^0)b \quad (D.6)$$

while the shear stress due to torsion is given by

$$\tau_{13} = \pm \frac{16G\gamma_1 b}{\pi^2} \sum_{n=1,3,5,\dots}^{\infty} \frac{(-1)^{\frac{n-1}{2}}}{n^2} \left[1 - \frac{\cosh \frac{n\pi Z}{2b}}{\cosh \frac{n\pi a}{2b}} \right] \cos \frac{n\pi Y}{2b} \quad (D.7)$$

(Chou and Pagano 1967) where $b < a$. The maximum shear stress is then given by

$$\tau_{\max} = \sqrt{\left[\frac{\sigma_{33}}{2} \right]^2 + \tau_{13}^2} \quad (D.8)$$

with σ_{33} and τ_{13} given by equations (D.6) and (D.7) respectively.

Similarly, at points 6 and 7 the normal stress is given by

$$\sigma_{33} = \pm E(\kappa_2 - \kappa_2^0)a \quad (D.9)$$

while the shear stress due to torsion is given by

$$\tau_{12} = \mp \frac{16G\gamma_1 b}{\pi^2} \sum_{n=1,3,5,\dots}^{\infty} \frac{(-1)^{\frac{n-1}{2}}}{n^2} \left[\frac{\sinh \frac{n\pi Z}{2b}}{\cosh \frac{n\pi a}{2b}} \right] \cos \frac{n\pi Y}{2b}. \quad (D.10)$$

The maximum shear stress at points 6 and 7 is then once again given by

$$\tau_{\max} = \sqrt{\left[\frac{\sigma_{33}}{2} \right]^2 + \tau_{12}^2} \quad (D.11)$$

with σ_{33} and τ_{12} now given by equations (D.9) and (D.10) respectively.

The shear stress used to determine if yielding has occurred is therefore given by the maximum of equations (D.5), (D.8) and (D.11). Each of these points on the cross section is evaluated at each arclength used by the numerical integrating procedure along the the appliance.